SILESIAN UNIVERSITY OF TECHNOLOGY

Faculty of Chemistry
Department of Physical Chemistry and Technology of Polymers

MSc Aleksandra Nyga

DOCTORAL DISSERTATION

Characterisation of donor-acceptor systems as materials for organic optoelectronics

Promoter: prof. dr hab. inż. Przemysław Data
Assistant promoter: dr hab. inż. Agata Blacha-Grzechnik

Gliwice 2022

POLITECHNIKA ŚLĄSKA

Wydział Chemiczny
Katedra Fizykochemii i Technologii Polimerów

Mgr inż. Aleksandra Nyga

ROZPRAWA DOKTORSKA

Charakterystyka układów donorowo-akceptorowych jako materiałów do optoelektroniki organicznej

Promotor pracy: prof. dr hab. inż. Przemysław Data
Promotor pomocniczy: dr hab. inż. Agata Blacha-Grzechnik

Gliwice 2022

Pragnę złożyć serdeczne podziękowania, Panu prof. dr hab. inż. Przemysławowi Dacie oraz Pani dr hab. inż. Agacie Blacha-Grzechnik, za zaangażowanie, wsparcie oraz motywację do dalszego rozwoju naukowego.

Składam również serdeczne podziękowania całej rodzinie za cierpliwość oraz wiarę w moje możliwości, a także przyjaciołom oraz wszystkim kolegom z Katedry Fizykochemii i Technologii Polimerów Politechniki Śląskiej, którzy swoją pomocą i życzliwością wspierali mnie oraz służyli cennymi radami w trakcie realizacji pracy doktorskiej.

The Foundation for Polish Science financed this work within project First TEAM no. POIR.04.04.00-00-4668/17-00.

Abstract

Organic optoelectronics is currently one of the fastest-growing fields of science. Thanks to the development of analytical techniques from the borderline of photophysics and photochemistry it is possible to perform research on increasingly efficient photoactive systems that are being used in organic luminescent diodes, flexible photovoltaic panels or organic transistors and sensors. In the last years, high attention has been paid to donor-acceptor systems applicable in such devices. These systems can be either single-molecule structures consisting of acceptor unit (A, accepting electrons) and donor unit (D, donating electrons) linked by a chemical bond or alternatively obtained by combining donor and acceptor molecules within a mixture or blend. The proper design of chemical structure and ratio of D-to-A units of such systems is important, which allows for optimisation of their physicochemical properties. Such a strategy can bring many possibilities to the research on organic light-emitting diodes (OLEDs) or organic photovoltaics (OPVs) with the aim to enhance the efficiency of processes standing behind their work. Moreover, a serious difficulty is a contribution of non-radiative processes that occur during the relaxation of excited systems. One of such processes, which can cause inefficient energy losses in optoelectronic devices, is the photogeneration of singlet oxygen. In this case excited photoactive molecule transfers its energy to an oxygen molecule resulting in a formation of singlet oxygen, $^1O_2$, which as a very strong oxidant is used both in a number of industry sectors as well as acute medicine or the wider healthcare sector, but is adverse in both OPVs and OLEDs.

Therefore, the main objective of this work is to investigate various acceptor-donor systems in regard to their multifunctionality and applicability in either organic optoelectronic devices or as a source of singlet oxygen. This research presents a new and unique approach to studying such D-A photoactive systems, taking into account not only their electrochemical and photophysical characteristics but also the photochemical ones. Understanding the competitive interactions between the radiative and non-radiative transitions occurring in photoactive molecules used as, i.e. photosensitizers or emitters, will result in a more conscious optimisation of a particular process and, thus, will allow releasing the hidden potential in the D-A photoactive materials.

Abstrakt

Optoelektronika organiczna jest obecnie jedną z najszybciej rozwijających się dziedzin nauki. Dzięki rozwojowi technik analitycznych z pogranicza fotofizyki i fizykochemii możliwe jest prowadzenie badań nad coraz wydajniejszymi układami fotoaktywnymi, które znajdują zastosowanie w organicznych diodach luminescencyjnych, elastycznych panelach fotowoltaicznych czy organicznych tranzystorach i czujnikach. W ostatnich latach dużą uwagę poświęca się układom donorowo-akceptorowym stosowanym w takich urządzeniach. Układy te mogą być zarówno strukturami jednocząsteczkowymi, składającymi się z rdzenia akceptorowego (A, przyjmującego elektrony) i rdzenia donorowego (D, oddającego elektrony), połączonych wiązaniem chemicznym, jak i mogą być otrzymane przez połączenie cząsteczek donora i akceptora w mieszaninie lub blendzie. Co ważne, odpowiednie zaprojektowanie struktury chemicznej oraz stosunku jednostek D do A takich układów pozwala na optymalizację ich właściwości fizykochemicznych. Taka strategia może otworzyć wiele możliwości dla badań nad organicznymi diodami elektroluminescencyjnymi (OLED) lub organicznymi ogniwami fotowoltaicznymi (OPV) w kontekście zwiększenia wydajności procesów związanych z ich działaniem. Ponadto, poważnym utrudnieniem jest udział procesów nieradiacyjnych, które zachodzą podczas relaksacji układów wzbudzonych. Jednym z takich procesów, który może powodować nieefektywne straty energii w urządzeniach optoelektronicznych, jest fotogeneracja tlenu singletowego. W tym przypadku wzbudzona cząsteczka fotoaktywna przekazuje swoją energię cząsteczce tlenu, w wyniku czego powstaje tlen singletowy, $^1O_2$, który jako bardzo silny utleniacz jest wykorzystywany zarówno w wielu sektorach przemysłu, jak i w medycynie, ale jest niekorzystny zarówno w OPV, jak i OLED.

Dlatego głównym celem tej pracy jest zbadanie różnych układów akceptorowo-donorowych pod kątem ich wielofunkcyjności i możliwości zastosowania w organicznych urządzeniach optoelektronicznych lub jako źródło tlenu singletowego. Badania te prezentują nowe i unikalne podejście do badania takich fotoaktywnych układów D-A, biorąc pod uwagę nie tylko ich charakterystykę elektrochemiczną i fotofizyczną, ale także fotochemiczną. Zrozumienie konkurencyjnych oddziaływań pomiędzy radiacyjnymi i nieradiacyjnymi przejściami zachodzącymi w fotoaktywnych cząsteczkach stosowanych jako fotouczulacze lub emitery pozwoli na bardziej świadomą optymalizację poszczególnych procesów, a tym samym uwolnienie ukrytego potencjału drzemiącego w fotoaktywnych materiałach D-A.

Table of contents

Abstract 5
Abstrakt 6
List of the main publications 8
List of other publications 10
Glossary 11
1. Introduction 13
2. Literature review 15
3. Aim and scope of the work 20
4. Research methodology 21
4.1. Electrochemical, spectroscopic and spectroelectrochemical characterisation of selected D-A systems 21
4.1.1. Cyclic voltammetry 21
4.1.2. EPR spectroelectrochemistry 21
4.1.3. UV-Vis-NIR spectroelectrochemistry 22
4.2. Photoactive layers formation 22
4.3. Singlet oxygen photogeneration 25
5. Results and discussion 26
5.1. Electrochemical, spectroscopic and/or spectroelectrochemical characterisation of selected D-A systems, and formation of photoactive layers 28
5.1.1. OLED systems 28
5.1.2. OPV systems 33
5.2. Singlet oxygen photogeneration 35
6. Conclusions 41
Bibliography 42
Main publications 45

List of the main publications

M1. *Multiaplicability of singlet oxygen – small molecule high impact in materials development.*

Nyga A., Gusev I., Blacha-Grzechnik A., Data P.,

Applied Materials Today., (2022), Manuscript under revision (IF_{2022}=10.04; MNiSW=140)

A.N. was responsible for conducting the literature review and writing the parts devoted to: *(i)* direct detection of singlet oxygen techniques, *(ii)* description of radiative and non-radiative transitions and *(iii)* discussion of photogeneration of singlet oxygen by organic systems applied in organic electronic devices. A.N. prepared figures: *Figure 2, Figure 3, Figure 5, Figure 6, Figure 7, Figure 9* and was co-author of the *graphical abstract.*

M2. *Dual-Photofunctional Organogermanium Compound Based on Donor-Acceptor–Donor Architecture*

Nyga, A., Kaihara, T., Hosono, T., Sipala, M., Stachelek, P., Tonai, N., Minakata, S. de Sousa, L., de Silva, P., Data, P., Takeda, Y..

Chem. Commun., (2022), vol. **58**, s. 5889-5892 (IF_{2021}= 6.22; MNiSW= 200)

A.N. was responsible for planning and conducing of the electrochemical analysis of compounds. Furthermore, A.N. conducted EPR as well as UV-Vis spectroelectrochemical characterisation of a investigated compounds.

M3. *Electrochemically deposited poly(selenophene)-fullerene photoactive layer: tuning of the spectroscopic properties towards visible light-driven generation of singlet oxygen*

Nyga A., Motyka R., Bussetti G., Calloni A., Sangarashettyhalli Jagadeesh M., Fijak S., Pluczyk-Małek S., Data P., Blacha-Grzechnik A.

Appl. Surf. Sci. **(**2020) vol. **525** s. 1-9 (IF_{2020}= 6.61; MNiSW= 140)

A.N. was responsible for planning and conducing the electrochemical analysis of $C_{60}Se$ and BisSe. A.N. was responsible for the electrochemical deposition of photoactive layers and the optimisation of the process parameters. The author was responsible for UV-Vis investigation of deposited films. Furthermore, A.N. examined the possibility of singlet oxygen photogeneration by the layers with α-terpinene trap. A.N. prepared figures: *Graphical abstract, Figure 1 and Figure S2*.

M4. *Singlet oxygen formation from photoexcited P3HT:PCBM films applied in oxidation reactions*

Nyga A., Blacha-Grzechnik A., Podsiadly P., Duda A., Kepska K., Krzywiecki M., Motyka R., Janssen R. A. J., Data P.

Mater. Adv. (2022) vol. **3**, nr 4, s.2063-2069 (IF_{2022}= n/a; MNiSW= 20)

A.N. was responsible for conducting a broad literature review on the topic and preparing a draft version of the manuscript. Moreover, the author was working on formation of photoactive layers and their further investigation with UV-Vis spectroscopy in cooperation with P. Podsiadly. A.N. conducted *in-situ* singlet oxygen photogeneration studies with 1,5-dihydroxynaphtalene. A.N. took part in the analysis of the obtained results.

M5. *Covalent immobilisation of organic photosensitizers on the glass surface: toward the formation of the light-activated antimicrobial nanocoating*

Nyga A., Dominika Czerwińska-Główka, Krzywiecki M., Przystaś W., Zabłocka-Godlewska E., Student S., Kwoka M., Data P., Blacha-Grzechnik A..

Materials (2021) vol. **14** iss. 11 s. 1-15 (IF_{2021}= 3.623; MNiSW= 140)

A.N. was responsible for the preparation of photoactive layers on glass substrate in a three-step procedure consisting in a covalent grafting and post-modifications. The author was also responsible for conducting UV-Vis characterisation and the investigation of the process of photogeneration of reactive oxygen species (ROS). A.N. prepared figures: *Graphical abstract and Scheme 2,* and the draft version of the *Introduction* part.

List of other publications

O1. *Thermally activated delayed fluorescent donor-acceptor-donor-acceptor π-conjugated macrocycle for organic light-emitting diodes*

Izumi S., Higginbotham H. F., **Nyga A.,** Stachelek P., Tohnai N., de Silva P., Data P., Takeda Y., Minakata S..

J. Am. Chem. Soc. (2020) vol. **142** iss. 3 s. 1482-1491, (IF_{2020}= 15.419; MNiSW=200)

O2. *Electrochemical and spectroelectrochemical comparative study of macrocyclic thermally activated delayed fluorescent compounds: molecular charge stability vs OLED EQE Roll-Off*

Nyga A., Izumi S., Higginbotham H. F., Stachelek P., Pluczyk S., de Silva P., Minakata S., Takeda Y., Data P..

Asian J. Org. Chem. (2020) vol. **9** iss. 12 s. 2153-2161. (IF_{2020}= 3.319; MNiSW=70)

O3. *Revealing topological influence of phenylenediamine unit on physicochemical properties of donor-acceptor-donor-acceptor thermally activated delayed fluorescent macrocycles*

Izumi S., **Nyga A.,** de Silva P., Tohnai N., Minakata S., Data P., Takeda Y.,

Chem. - Asian J. (2020) vol. **15** iss. 23 s. 4098-4103, (IF_{2020}= 4.568; MNiSW=100)

Glossary

$^1O_2$ – molecular oxygen in a singlet excited state

A - acceptor

AA – azure A

Ag – silver

APTES - 3-aminopropyltriethoxysilane

APTPP - 5-(4-aminophenyl)-10,15,20-(triphenyl)porphyrin

Au - gold

ax – axial conformation

BisSe – bis-selenophene

Bu_4NBF_4 - tetrabutylammonium tetrafluoroborate

$C_{60}Se$ – N-methyl-2-(2,5-di(selenophen-2-yl)thiophen-3-yl)fullero[3,4]pyrrolidine

D – donor

DCM – dichloromethane

DHN - 1,5-dihydroxynaphthalene

DPBF – 1,3-diphenylisobenzofurane

DSSC - Dye-Sensitized Solar Cells

EPR - electron paramagnetic resonance

eq – equatorial conformation

Fc/Fc^+ - ferrocene

HOMO - Highest Occupied Molecular Orbital

ISC - InterSystem Crossing

ITO - Indium-Tin Oxide

LUMO - Lowest Unoccupied Molecular Orbital

O_2 ($^3O_2$)– molecular oxygen in a triplet ground state

OFET - Organic Field-Effect Transistors

OLED - Organic Light-Emitting Diodes

OPV – Organic Photovoltaic

P3HT - poly(3-hexylthiophene-2,5-diyl)

PCBM - phenyl-C61-butyric acid methyl ester

PS – photosensitiser

Pt – platinum

PTB7 - poly [[4,8-bis[(2-ethylhexyl)oxy]benzo[1,2-b:4,5-b']dithiophene-2,6-diyl][3-fluoro-2-[(2-ethylhexyl)carbonyl]thieno[3,4-b]thiophenediyl]]

rISC - reverse InterSystem Crossing

S_n – singlet energy level

TADF -Thermally Activated Delayed Fluorescence

T_n – triplet energy level

αT - α-terpinene

Φ; PLQY – photoluminescence quantum yield

1. Introduction

Technological achievements of the XIX and XX centuries, especially the theories and accomplishments of scientists like Maxwell, Einstein, and Planck, allowed for the development of a new field of science called optoelectronics[1]. Generally, this area deals with all kinds of interactions of electrical devices with light, which may involve its production, control, or usage[2]. These breakthroughs allowed for the improvement of modern everyday life, laying the foundations for the expansion of such technological solutions as semiconductors, photomultipliers, optical fibers, light-emitting diodes or photovoltaics.

Back in 1955, André Bernanose published the first paper describing the electroluminescence effect in organic compounds: gonacrin, brilliant acridine, orange E and carbazole[3]. This paper had a huge impact on the scientific community and initiated a series of discoveries in the area of electroluminescence, leading to the development of the first OLED (organic light-emitting diodes) in the mid-80s by Ching Tang and Steven Slyke in Kodak[4]. Simplifying, one can say that the principle of electroluminescence lies in a continuous excitation of a molecule by an electric current. Afterwards, an excited molecule undergoing a relaxation process can produce light without any heat radiation. The huge advantage of organic optoelectronics is the possibility of obtaining flexible and elastic devices, which has led to a significant evolution of electronic devices[5–8]. Still, this technology leaves much to be desired in terms of the devices' performance and durability. One of the main problems of modern organic optoelectronic devices is their poor resistance to oxygen[9–11].

The unusual features of molecular oxygen arise from its electronic structure. Oxygen molecule, unlike other particles, occurs in a triplet ground state, $^3O_2$, exhibiting relatively low reactivity. However, the excitation of the O_2 molecule brings it to the excited singlet state, $^1O_2$, which possess marvellous oxidative abilities, e.g. toward π-conjugated organic compounds[12,13]. In consequence, the organic compounds, typically used in organic optoelectronic devices, might act as photosensitizers producing $^1O_2$ but also may undergo $^1O_2$ - induced degradation[14–16]. Understanding how closely related to each other are the desired radiative process occurring in optoelectronic devices and the process of singlet oxygen photogeneration seems to be of great importance for the research on novel photoactive materials. Improving the efficiency of optoelectronic devices or photosensitizers is intrinsically linked to understanding the nature of the mechanisms ruling the processes occurring in photoactive systems, especially those involving non-radiative transitions. That is why the presented thesis shows the novel, broader methodology in the investigation of photoactive organic materials,

in which to the classical electrochemical, spectroscopic and photophysical characterisation, the photochemical analysis is added in order to speed up the endless chase for more and more effective and efficient optoelectronic devices. Moreover, such an approach allows us to consider the duality of the photoactive organic systems in terms of their possible application.

2. Literature review

Nowadays, the most commonly developing fields of organic optoelectronics are organic light-emitting diodes (OLED), organic photovoltaics (OPV) and organic field-effect transistors (OFET). Thanks to the use of organic systems in those types of devices, it is possible to produce lightweight, flexible and easy to fast customisation modules that perfectly match the electronics market[17–19]. However, there is still much room for improvement, taking into account the stability and performance of organic optoelectronic devices. Due to the variety of types of optoelectronic devices, there are many different mechanisms involved in their organic backbone, but they all rely consistently on energy transfer. For example, in organic photovoltaic (OPV) devices, absorbed solar energy is transformed into electrical power. In OLED devices, the situation is quite the opposite – here, a current induces the photoluminescence process. Taking this into account, it might be stated that the basis of each of these systems lies in the Jabłoński diagram[11,20,21]. Considering the mechanisms occurring in all optoelectronic devices, it can be noted that the key feature that determines the processes occurring in photoactive compounds is the position of their energy levels. In OLED-type devices, the excess energy is emitted via luminescence[22]. In the first generation of organic devices – mainly phosphorescence occurs, while in the novel materials, so-called the third generation devices - a reverse InterSystem Crossing (rISC) process appear, which in turn leads to thermally activated delayed fluorescence (TADF)[21]. In the last type, the energy of the triplet state has to be high enough for reverse intersystem crossing to occur but not too high to avoid relaxation by non-radiative processes (Figure 1A). On the other hand, OPVs are designed

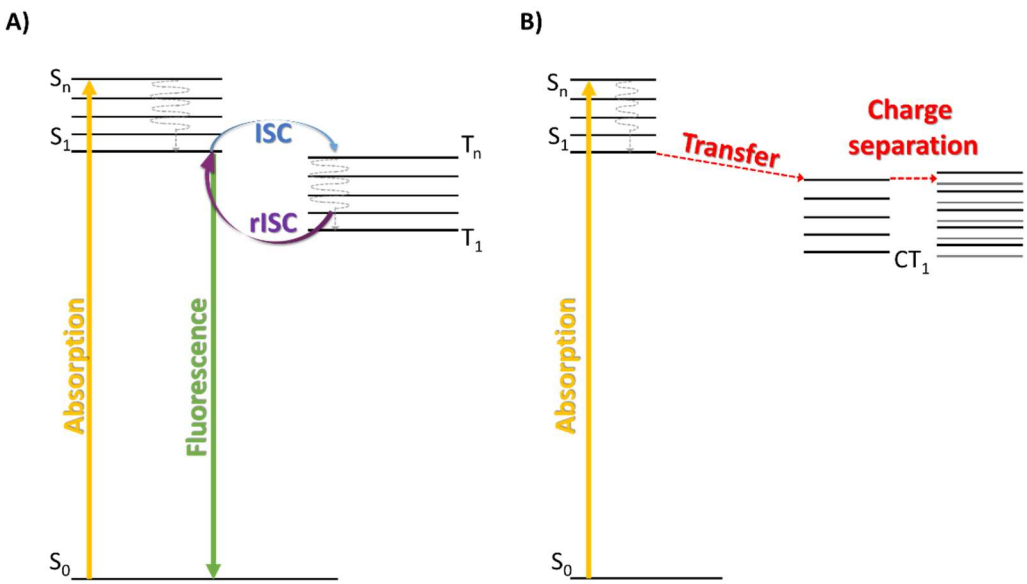

Figure 1. Energy transfer mechanisms occuring in A) TADF, B) OPV systems.

to have a charge separation process as large as possible. (Figure 1B). Thus, the triplet state has to be long-lived to increase the power conversion efficiency. Additionally, the energy of the triplet state has to be high enough to avoid relaxation without charge separation. Most of the currently developed optoelectronic technologies are based on further improvement of intermolecular interactions of organic units in photoactive compounds. These groups may have a donor (D) character when they are able to donate electrons, while in the case of groups hosting these electrons, we talk about acceptors (A). In such excited systems, the so-called charge transfer (CT) state is created. At this point, electrons rearrange themselves moving toward the acceptor while the holes are formed in the donor unit. As a result of recombination and radiative relaxation, emission of a photon (OLED) or the so-called free charge carriers generation (OPV) may take place. D-A systems can have a single molecule structure, but in this group of materials we also have polymers composed of different D-A units. Another possibility is so-called blends, mixtures of active compounds interacting with each other. The characteristic structure and the possibility of combining different types of donor and acceptor groups allow to boost the properties and features of new photoactive systems.

Due to their specific structure, the energy transfer process occurring in OLEDs and OPV devices is very sensitive to several internal and external factors. The disruption of energy transfer often leads to worse performance of optoelectronic devices. This happens by increasing the efficiency of the so-called non-radiative transitions at the expense of the radiative ones. Generally, three types of relaxation which can cause energy losses [23,24] can be named:

1. Radiative loss above bandgap/ energy gap
2. Radiative loss below bandgap/ energy gap
3. Non-radiative loss

While radiative losses (1) and (2) are traceable by suitable spectroscopic methods, investigating the non-radiative transition process isn't that straightforward. The non-radiative loss can be connected among all with a vibration-induced quenching, a concentration quenching, other energy transfers, and the most important from the topic point of view of this thesis - oxygen quenching[25]. Understanding the mechanisms behind the high contribution of non-radiative transitions in optoelectronic systems seems to be crucial in developing high-performance, state-of-the-art organic devices.

In the case of oxygen-caused non-radiative losses, the energy transfer from an excited organic moiety goes via Dexter Transfer. The energy from a conjugated domain is transferred to the oxygen molecule in the triplet ground state, $^3O_2$, which results in the formation of singlet

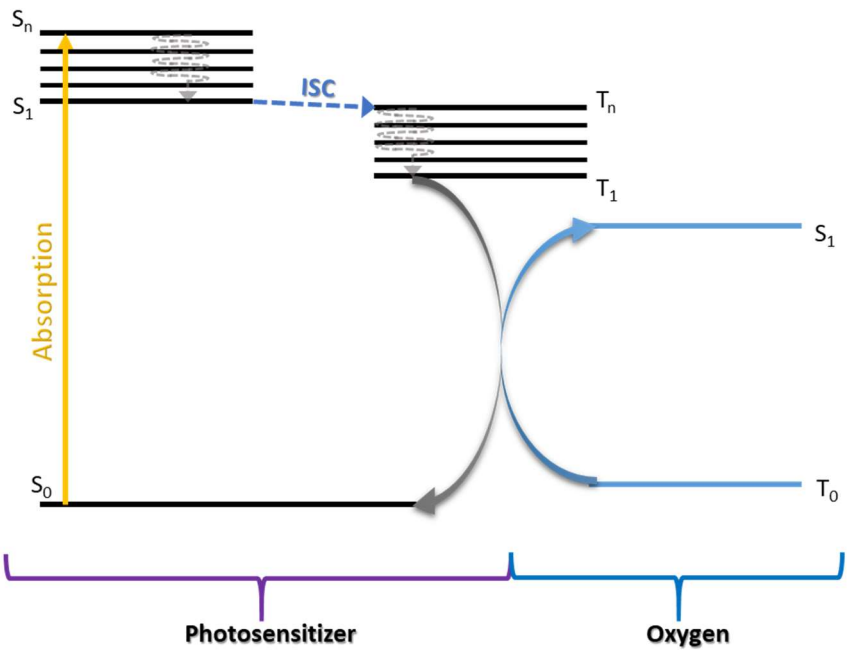

Figure 2. Singlet oxygen photogeneration involving the photosensitizer as energy donor

oxygen. Such process is so-called photosensitisation with organic compound acting as a so-called photosensitizer (Figure 2)[12,13].

The vast majority of organic compounds used in optoelectronic devices are conjugated ones. Generally, increasing the number of π bonds leads to an increase in the stability of bulky molecules by lowering their total energy and also causes the shift of the absorption maximum toward higher wavelengths. However, as mentioned above, the formation of $^1O_2$ by photoactive molecules, being a competitive process, results in lower efficiency of the devices. Moreover, the π-conjugated systems themselves can be oxidized by this reactive form of oxygen, that may lead to the degradation of the optoelectronic device. This can be avoided, for example, by encapsulation. When it comes to inhibiting the penetration of oxygen and water particles into devices, the type and quality of an encapsulation play a key role in the stability of optoelectronic devices[16,26]. Another aspect that significantly affects the choice of protective coating is the elasticity of the devices, which is one of the most important advantages of optoelectronic technology. For rigid devices - a glass encapsulation may be proposed, but the encapsulation should not affect the flexibility of the elastic devices. Currently, the most promising is the thin-film encapsulation method, which involves applying nanocomposites, resins or nanolaminates as protective coatings[27].

The chase for the best, the most effective, and the brightest photoactive molecules leaves no room for consideration of different possibilities of application of *less effective materials.* They may appear remarkably effective in another branch of industry, e.g. as photosensitizers.

The oxidative properties of singlet oxygen imply its application in various fields of industry, starting from the "green" synthesis, through environmental technologies and wastewater treatment up to biological applications such as photodynamic anticancer (PDT) and antimicrobial (PACT) therapies[12,28–33]. Thus, the ability of conjugated organic systems to photogenerate singlet oxygen can be considered an alternative application.

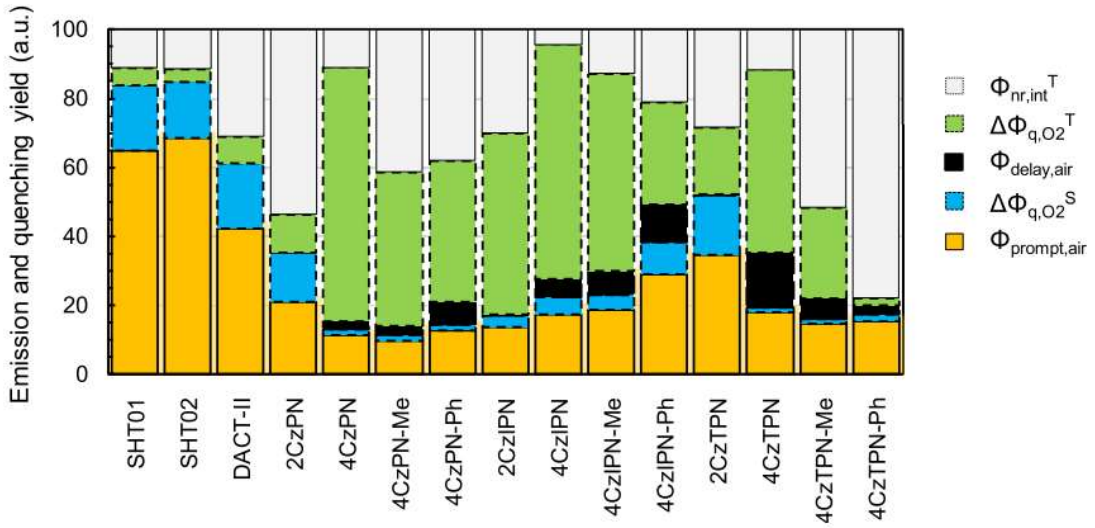

Figure 3. The contribution of deactivation processes from excited singlet and triplet states in photoactive molecules. $\Phi_{nr,\,int}^{T}$ - internal nonradiative deactivation pathways of: $\Delta\Phi_{q,\,O2}^{T}$ – PLQY triplet quenching, $\Phi_{delay,\,air}$ - PLQY of delayed component, $\Delta\Phi_{q,\,O2}^{S}$- PLQY singlet quenching, $\Phi_{prompt,\,air}$ – PLQY of prompt component

Reprinted (adapted) with permission from J. Phys. Chem. Lett. 2020, 11, 562−566. Copyright 2022 American Chemical Society.

The latest work of Notsuka et al. proved the potential photosensitising abilities of well-known TADF molecules typically used in organic devices. In this work, several compounds based on the cyanobenzene core were investigated. Depending on the chemical structure, the photogeneration of singlet oxygen had a different contribution to the non-radiative relaxation processes, as shown in Figure 3[25].

One of the most investigated groups of compounds for OPVs are fullerenes. Many fullerene derivatives, with the most recognizable - Phenyl-C61-butyric acid methyl ester (PCBM), have been studied [34]. In 2020 Bregnhøj et al. reported the results of photophysical and photochemical investigations of polymer-based electron donors and fullerene-based electron acceptors commonly used in OPV devices. It has been shown that both PCBM derivatives and polymers P3HT and PTB7 determined using subphthalocyanine (SubPc) as a reference show good quantum yields of photogeneration of singlet oxygen, both in liquid as well as in solid-phase [35].

Table 1. Quantum yield of singlet oxygen photogeneration process in saturated benzene solutions[35]

	Quantum yield of singlet oxygen photogeneration $\Phi^{a1\Delta g}$	
	Air	**O_2**
Compound	**Saturated**	**Saturated**
$PCBM5_0$	0.65 ± 0.04	0.68 ± 0.04
$PCBM_{70}$	0.90 ± 0.05	0.91 ± 0.05
P3HT	0.34 ± 0.04	0.40 ± 0.04
PTB7	0.24 ± 0.03	0.29 ± 0.03
SubPc	0.78 ± 0.06	0.88 ± 0.06

Undoubtedly, this type of research allows us to understand the effect of molecule structure on the efficiency of singlet oxygen photogeneration. This, in turn, may lead to a more conscious design of photoactive organic systems taking into account their target application. For example, understanding how to avoid non-radiative transitions by optimising chemical structure should lead to more efficient and stable organic electronic devices. Someday, it may also be possible to avoid production in an inert oxygen-free environment or the protection with dedicated coatings, which would strongly reduce the overall costs of such devices. On the other hand, such a broad approach can open doors to new opportunities in applying photoactive organic systems.

3. Aim and scope of the work

The main aim of the presented work is to broadly characterise donor-acceptor (D-A) systems, commonly applied in organic optoelectronics, taking into account both radiative and non-radiative processes. In such an approach, attention is paid to the duality of D-A systems, *i.e.,* their ability to act as an active layer in organic optoelectronic devices or as a singlet oxygen source. Thus, donor-acceptor systems commonly used in organic optoelectronics – either OLEDs or OPVs, were selected. Furthermore, the heteroatom-containing D-A compounds based on dibenzo[a,j]phenazine acceptor, which has been designed for their applicability in OLED devices, were investigated. Finally, in the group of OPVs D-A systems, a novel fullerene dyad with bis-selenophene, and well-known PCBM:P3HT and porphyrin-phenothiazine systems were selected.

The main novelty of the presented work lies in the undertaken approach, in which the investigation of singlet oxygen photogeneration is added to a standard analysis conducted on D-A organic systems. Hence, the selected D-A systems were firstly subjected to electrochemical, spectroscopic and/or spectroelectrochemical analysis and were, in the next step, deposited on solid support either *via* electrochemical polymerisation, spin-coating or chemical grafting. Finally, the photogeneration of singlet oxygen by the resulting layers was widely investigated, and the selected ones were tested in the industrial important oxidation process or as antimicrobial coatings.

4. Research methodology

4.1. Electrochemical, spectroscopic and spectroelectrochemical characterisation of selected D-A systems

4.1.1. Cyclic voltammetry

The goal of employing electrochemical methods in the analysis of the investigated systems was primarily to determine their oxidation and reduction processes, as well as to test their ability to undergo electrochemical polymerisation. The electrochemical analysis was performed using the SP-150 electrochemical workstation (Bio-Logic) and a conventional three-electrode cell. As a working electrode, a platinum disc electrode (Pt, EDAQ, 1 mm dia.), gold disc electrode (Au, EDAQ, 1mm dia.) or an Indium-Tin Oxide (ITO)/borosilicate glass (Präzisions Glas & Optik GmbH, PGO) were used. As a pseudo-reference electrode, the silver wire was chosen. Platinum wire acted as a counter electrode. The potential scale was calibrated using a typical internal standard, i.e. ferrocene (Fc/Fc^+). By default, measurements were performed with a 1 mM concentration of photoactive compounds in 0.1 M solutions of Tetrabutylammonium tetrafluoroborate (Bu_4NBF_4, 99% Sigma Aldrich), i.e. electrolyte, in dichloromethane (DCM; HPLC grade, Sigma Aldrich) at room temperature. Due to the significant effect of atmospheric oxygen on the measurements, the examined solutions were purged with an inert gas - argon, before starting the voltammetry measurements. Additionally, a gas was passed over the surface of the solution to prevent the impact of oxygen during the experiments.

The electrochemical analysis carried out by potentiodynamic methods with the use of cyclic voltammetry made it possible to determine such parameters as HOMO (Highest Occupied Molecular Orbital) as well as LUMO (Lowest Unoccupied Molecular Orbital), which were calculated using the following eqations[36]:

$$E_{HOMO} = -\left(E_{OX}{}^{onset\ vs\frac{Fc^+}{Fc}} + 5.1\right)[eV] \quad (1)$$

$$E_{LUMO} = -\left(E_{red}{}^{onset\ vs\frac{Fc^+}{Fc}} + 5.1\right)[eV] \quad (2)$$

4.1.2. EPR spectroelectrochemistry

Electron paramagnetic resonance (EPR) spectroelectrochemistry allowed us to detect unpaired electrons by examining the spin environment of the sample as a function of applied voltage. EPR measurements were performed using Jeol JES-FA 200 X-band CW-EPR

spectrometer and an AUTOLAB M101 potentiostat. The measuring cell was a thin glass tube narrowing to the bottom. A thin platinum wire was inserted as a working electrode, a silver wire as a pseudo-reference electrode, and a spirally coiled platinum wire as an auxiliary electrode. Measurements were carried out using 0.5 mM concentration of the test compound in 0.1 M solutions of Tetrabutylammonium tetrafluoroborate (Bu_4NBF_4, 99% Sigma Aldrich) in dichloromethane (DCM; HPLC grade, Sigma Aldrich) at room temperature. In addition, the concentration of photoactive molecules was adjusted to a particular test and procedure type.

4.1.3. UV-Vis-NIR spectroelectrochemistry

The absorption spectroelectrochemical measurements were performed in the ultraviolet (UV), visible (Vis) and near-infrared (NIR) spectral ranges. The measurements were carried out at static as well as dynamic potential changes. The obtained results were mainly analyzed to study the polaronic and bipolaronic bands. Similarly to previous spectroelectrochemical measurements, the silver and platinum wire were used as pseudo-reference and auxiliary electrodes. An ITO glass electrode in a thin quartz cuvette (Helma cells) was used as a working electrode. The measurements were performed with Ocean Optics QE6500 and NIRQuest apparatus. Measurements were performed within 0.5 mM concentration of photoactive compounds in 0.1 M solutions of Tetrabutylammonium tetrafluoroborate (Bu4NBF4, 99% Sigma Aldrich) in dichloromethane solvent (DCM; HPLC grade, Sigma Aldrich) at room temperature conditions.

4.2. Photoactive layers formation

Immobilizing photoactive molecules on a solid carrier can be done using either physical or chemical processes. Respectively, the application of these methods results in non-covalent interactions with surface atoms or covalent bonds. The first ones include such techniques as physical adsorption, blend/mixing in the matrix or trapping. Although, on the other hand, grafting is characteristic of covalently bonded formations, it does not matter whether it is obtained by chemical or electrochemical processes. The selection of a suitable method for the immobilisation of photosensitisers depends on the type of sensitiser, its structure and properties. Immobilisation of photoactive molecules usually increases photosensitiser stability but, unfortunately, decreases its photoactivity[37].

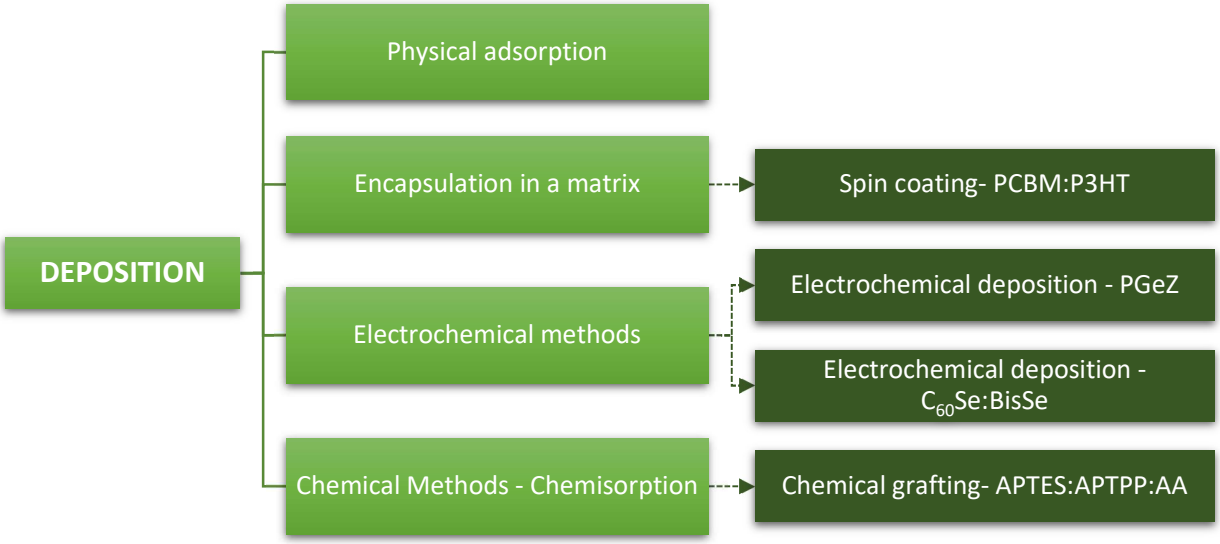

Figure 4. Diagram showing immobilisation techniques for photosensitizers on solid substrates. The dark green tiles represent the immobilisation techniques implemented to prepare the photoactive layers used in this work

Electrochemical polymerisation (M2 and M3)

The electrochemical polymerisation process, resulting in the formation of a polymeric layer on top of the working electrode, was performed analogically to electrochemical analysis. The same SP-150 electrochemical workstation (Bio-Logic) and three-electrode cells were employed to complete the process. Similarly, Indium-Tin Oxide (ITO)/borosilicate glass (Präzisions Glas & Optik GmbH, PGO) were used as a working electrode. As a pseudo-reference electrode, a silver wire was chosen. Platinum wire acted as a counter electrode. By default, measurements were performed in 0.1 M solutions of Tetrabutylammonium tetrafluoroborate (Bu_4NBF_4, 99% Sigma Aldrich) in dichloromethane (DCM; HPLC grade, Sigma Aldrich) in room temperature conditions. The concentration of monomers varied between experiments. In all trials, the concentration of the C_{60}Se dyad in M3 was kept constant (0.45 mM), while the concentration of BisSe was adjusted to obtain various molar ratios (5:1, 2:1, 1:1, 1:2 and 1:5). In the case of dibenzo[*a,j*]phenazine investigated in M2 and M3, the concentration was equal to 1 mM. Solutions were purged with intrinsic gas – argon prior to measurements.

Spin-coating (M4)

Rectangular glass substrates having identical UV-Vis absorbance were used as spin coating substrates. For the spin coating process, the glass substrates were washed and prepared as follows:

→ sonicated in acetone for 15 min,

→ manual washing in deionised water with sodium dodecylbenzosulfonate as detergent

→ sonicated with water and detergent for 15 minutes

→ rinse off the detergent and sonicated with deionised water for 15 minutes

→ sonicated with propan-1-ol for 15 minutes

→ drying under a fume hood

Cleaned and dried substrates were then coated using a Laurell WS-650M2-23 NPP/LITE spin coater to obtain thin films. One by one, pre-washed glasses were placed in the holder and fixed using a vacuum in the spin-coater chamber. An inert gas (nitrogen) was introduced into the chamber during the process. The 10 $\frac{mg}{mL}$ solution of photoactive molecules was applied by an automatic pipette. Centrifugation was turned on at selected parameters of speed and time and acceleration of 4000 $\frac{rpm}{s^2}$. After removing the plate from the device, it was left in a dark place for 24 hours.

Chemical grafting (M5)

Chemical grafting was done using a three-step procedure (M5). Firstly, the cleaned and pretreated with high concentrated sodium hydroxide (NaOH) and hydrochloric acid (HCl) glass substrates were placed in a 3-Aminopropyltriethoxysilane (APTES) solution in toluene. Then, after 24 h, glass substrates with chemically grafted APTES were rinsed with pure solvent and placed in the terephtaloyl chloride (TC) solution for post-modification and binding of the TC linker. Finally, functionalisation of the layer with the acyl chloride allows for the third stage of modification – chemical bonding of photosensitisers: azure A (AA) and 5-(4-aminophenyl)-10,15,20-(triphenyl)porphyrin (APTPP).

4.3. Singlet oxygen photogeneration

An indirect singlet oxygen detection can be performed in a homogeneous system where the photosensitizer is dissolved in the reaction medium. The process can also be carried out for photosensitizers deposited on different types of supports. In this case, we can speak of an conducted under heterogeneous conditions. Typically, a photoactive layer deposited on a solid substrate is placed in a 10 × 4 mm^2 quartz cuvette (Hellma Analytics, Müllheim, Germany). The glass cuvette is sealed with a Teflon cap to prevent solvent evaporation. The prepared layer is further illuminated either with a xenon lamp or with a diode laser. The xenon lamp is used as a broadband illumination source, while diode lasers (in presented work - Oxxius, Lannion, France, LBX-445- 100CSB-PP, LBX-532 and LBX-638-150-ELL-PP) are used as a light source exciting specifically chosen photosensitiser and its characteristic band. The light-activated production of reactive oxygen species (ROS) was followed *in situ* using Hewlett Packard (Palo Alto, CA, USA) 8452A UV–Vis spectrometer. The effectiveness of the investigated process is monitored by the drop in the absorbance of the specific marker used in the experiment, such as 1,3-diphenylisobenzofuran or α-Terpinene.

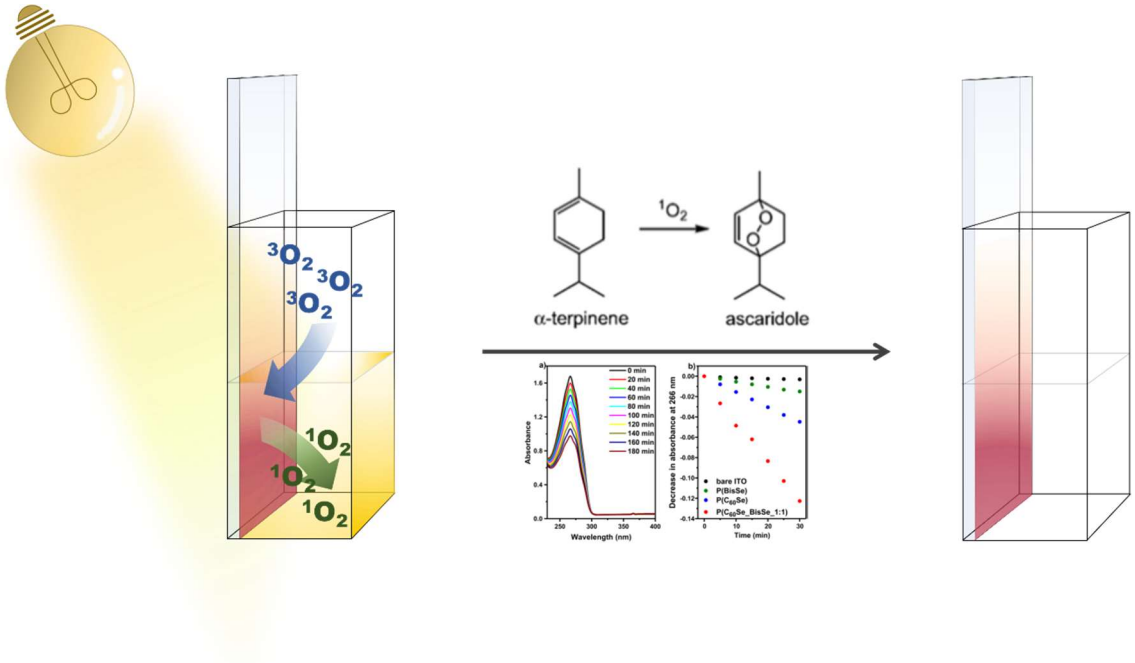

Figure 5. Schematic presentation of singlet oxygen photogeneration in heterogeneous experiment

5. Results and discussion

In the presented work, an extensive study of photoactive compounds commonly used in organic electronic devices has been carried out. Contrary to the classical approach, during the characterisation of photoactive systems, more attention was paid to investigating their ability to photosensitize singlet oxygen. The need for this research type is supported by a broad review (M1) of the topical literature that indicates the importance of non-radiative transitions affecting the performance of optoelectronic devices. The review mentioned above focuses on the photogeneration of singlet oxygen as one of the main causes of worsened performance of optoelectronic devices. Therefore, this work covers both the topic of non-radiative transitions in optoelectronic systems and also highlights the need for a broader perspective on the research on photoactive systems, their multi-purpose nature and potential versatile applications. Based on the literature review, it can be stated that only a limited number of works deal with the photoactive systems having a donor-acceptor structure which are applied in singlet oxygen photogeneration experiments. Thus, in order to fulfil this gap, the topic was undertaken in the presented work.

The selected systems studied in this work are summarized in Table 2. In the first part of the work (M2), a comprehensive electrochemical, spectroscopic and spectroelectrochemical analysis of the germanium derivative of dibenzo[a,j]phenazine was carried out, supplemented by studies conducted of respective heteroatomic silicon and phosphorus derivatives. Those compounds, with a donor-acceptor-donor structure, were designed as a potential TADF emitter for OLED devices. One of the investigated derivatives, which showed the highest tendency to undergo electropolymerisation, was in turn electrochemically deposited on a surface of an ITO electrode and further investigated in the form of a layer. Similarly, work M3 deals with the spectroscopic and electrochemical characterisation of novel compounds, in this case, fullerene dyads applicable in OPVs. Again, the investigated compounds were electrochemically deposited on an ITO surface. In this case, the donor-acceptor ratio was varied by conducting the electrochemical co-deposition of a bis-selenophene molecule - the donor form and a fullerene derivative, which acted as an acceptor.

Contrary to the above, works M4 and M5 present the results of the investigation of well-known systems that have been widely characterized for organic electronics applications. In the first case, the system of PCBM - a fullerene derivative that acted as an acceptor molecule – and a P3HT, which served as an energy donor was investigated. In this case, the photoactive layer was formed by spin-coating of solutions on top of the glass

substrates. All prepared active layers were then investigated as a potential source of singlet oxygen in an exemplary oxidation reaction. Finally, porphyrin and phenothiazine derivatives applicable in dye solar cells were covalently grafted to a glass surface and investigated as a potential photoactive antimicrobial layer.

Table 2. Overview of the examined molecules, their character and assignment.

		Title of work	Deposition technique	Investigated donor-acceptor systems
OLED	**M2**	*Dual-Photofunctional Organogermanium Compound Based on Donor–Acceptor–Donor Architecture*	Electrochemical polymerisation	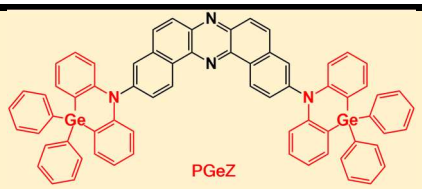
OPV	**M3**	*Electrochemically deposited poly(selenophene)-fullerene photoactive layer: tuning of the spectroscopic properties towards visible light driven generation of singlet oxygen*	Electrochemical polymerisation	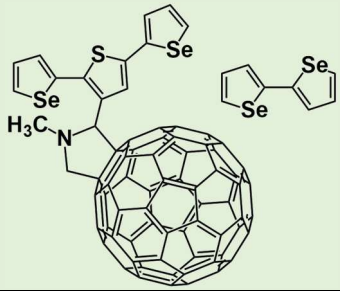
	M4	*Singlet oxygen formation from photoexcited P3HT:PCBM films applied in oxidation reactions*	Spin coating	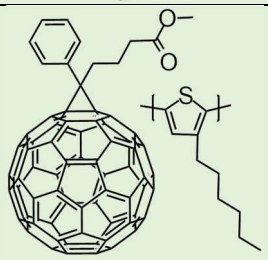
	M5	*Covalent Immobilization of Organic Photosensitizers on the Glass Surface: Toward the Formation of the Light-Activated Antimicrobial Nanocoating*	Chemical grafting	

5.1. Electrochemical, spectroscopic and/or spectroelectrochemical characterisation of selected D-A systems, and formation of photoactive layers

*Table 3. Absorption band, HOMO and LUMO values obtained during the conducted experiments. *Literature data are taken from reference [38]*

Compound	Absorption band [nm]	HOMO [eV]	LUMO [eV]
PGeZ	300 and 419	5.66	3.32
PSiZ	301 and 418	5.76	3.41
DPPZS	301 and 416	5.86	3.36
C_{60}Se	330	5.65	4.10
BisSe	500 ~ 400-600	5.22	-
PCBM	335	6.1*	3.7*
P3HT	510 ~ 400-600	5.0*	3.0*
APTPP	420	-	-
Azure A	628	-	-

The table presented above summarises the HOMO and LUMO values obtained during the research on the electrochemical properties of organic compounds presented in papers M2 and M3. Moreover, the absorption bands of particular photoactive compounds used in the study (M2-M5) are compared with each other. All the results correlate with the results of structurally similar molecules found in the literature regarding this topic.

5.1.1. OLED systems

At first, the objects of my investigations were compounds belonging to one of the better-known groups of compounds used in organic optoelectronics, especially in OLED devices, consisting of a dibenzo[a,j]phenazine acceptor core. A particular object of interest due to its properties was a derivative containing germanium as a heteroatom (PGeZ - phenazagermine), the characterization of which is presented in publication M2. Additionally, the electrochemical and spectroelectrochemical studies presented in this work have been carried out on the respective heteroatomic derivatives - silicon (PSiZ Phenazasilane) and phosphine (DPPZS dihydrophenophosphazine sulfide) presented in the Figure 6.

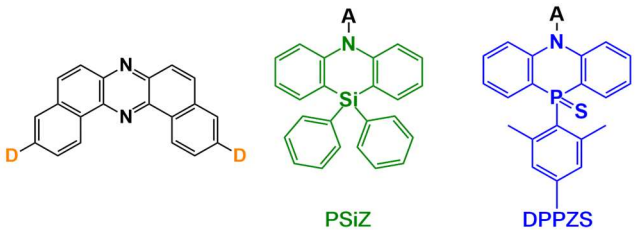

Figure 7. Phenazasilane (PSiZ) and dihydrophenophosphazine sulfide (DPPZS) derivatives.

The CV curves recorded for the investigated systems, shown in Figure 7, revealed that the examined germanium and silicon derivatives, in contrast to the phosphine derivative, tend to undergo electrochemical polymerisation on the platinum and gold electrode surface. A particularly distinctive polymerisation process was observed in the case of the germanium derivative. In the light of the obtained results, it can be suggested that the conformation of the molecule is key for understanding the ability of the studied D-A-D molecules to undergo the polymerisation processes. The equatorial-equatorial (eq-eq) conformers, i.e. germanium and silicon derivatives, have lower potentials of both oxidation and reduction. The opposite situation takes place for equatorial-axial (eq-ax) or axial-axial (ax-ax) conformers: higher values of oxidation and reduction potentials of these conformers indicate that those processes are more hindered [38]. Finally, it has to be noted that only the germanium derivative showed a tendency to form a stable polymeric layer on the Pt and Au electrodes surface. In contrast, in the case of silicon derivative – the forming layer was unstable. However, throughout the study, it was found that the PGeZ films formed on the ITO electrode become relatively unstable despite its tendency to undergo this process in the case of Pt and Au disc electrodes.

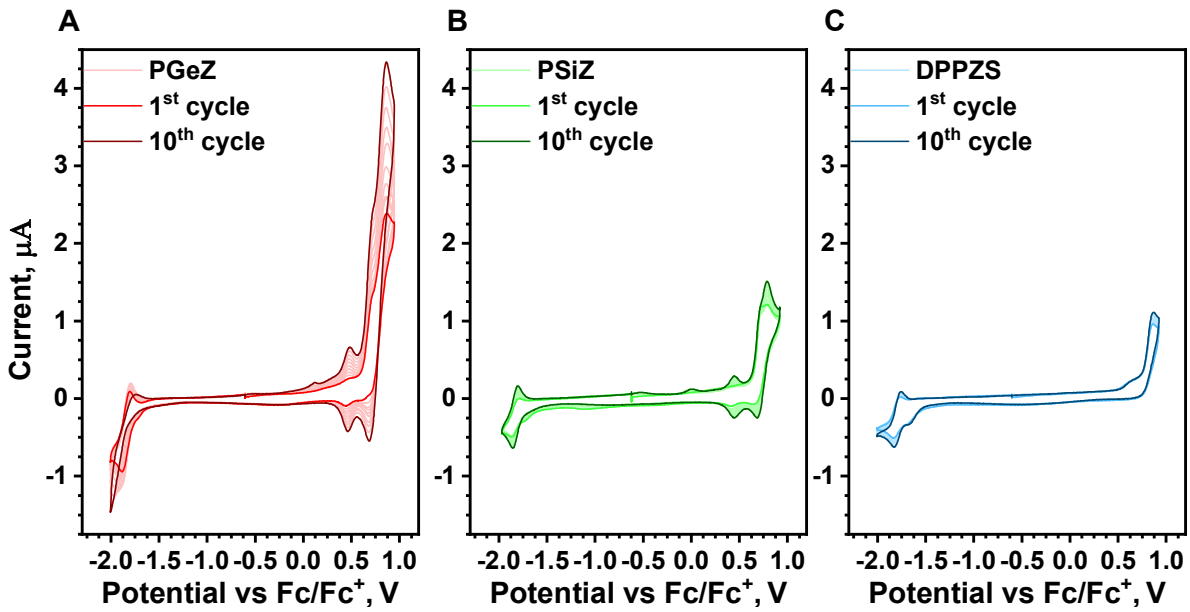

Figure 6. CV curves recorded for dibenzo[a,j]phenazine derivatives with heteroatomic dononor. A-PGeZ, B-PSiZ and C – DPPZS.

This could be due to the lower affinity of the forming polymer to the glass surfaces on the one hand. Still, on the other hand, ITO electrodes force the potential window to decrease while increasing the electrode area, which is not suitable for electrode processes in ranges above 1.5-1.6 V. However, increasing the scanning speed from the default 50 mV/s to 100 mV/s, allowed for limiting the influence of oligomer diffusion from the electrode surface and increasing the number of polymerisation cycles carried out to 30, resulting in a relatively stable polyPGeZ layer on the ITO electrode, which made it possible to study the photogeneration of singlet oxygen by the obtained photoactive layer. Both the EPR and UV-Vis-NIR spectroelectrochemical measurements performed for all dibenzo[a,j]phenazine photoactive derivatives, and presented in Figures 8 and 9 confirmed the redox character of the analyzed molecules. The observed changes in the EPR and UV-Vis spectra under varied applied potential correlated to the changes observed in the recorded CV curves. Potentiostatic UV-Vis-NIR spectroelectrochemistry of investigated monomers is presented in Figure. 8 reveals many differences in the spectroscopic behaviour of examined molecules. High electrochemical reactivity corresponds to the high spectroscopic answer of the PGeZ molecule. Already in low potential ranges, up to 1 V, the most visible changes are connected to increasing intensity of broad shoulder around 370 nm as well as 590 nm peak. Above 1 V, up to 1.7 V, a sudden growth of peaks near 350 465 and 590 nm occur, which might be associated with the formation of polarons. However, the biggest changes in spectra might be observed at a potential of 1.1-1.4 which then decreases for two broad bands localized between 700-850 nm and 1250-1500 nm. Since bipolarons are formed by oxidation of polarons it can be concluded that the behaviour of broad bands classifies them as bipolaronic. Only one, sharp peak around 420 nm seems to decrease as the oxidation process progresses. The oxidation processes which took place in the doping process seem to be irreversible. At the dedoping spectra of the PGeZ (Figure 8B) the sharp decrease of 590nm peak, as well as a broad band between 1200-1700 nm, was recorded.

Similar but much weaker behaviour can be described for PSiZ. Here, also after previous oxidation of the polarons, we might observe the increasing broad bands of bipolarons around 700-850 nm as well as 1200 – 1700 nm. The lack of the broad bands of bipolaronic moieties in the DPPSZ molecule could be related to its structure, conformation and the lack of redox behaviour. The most significant changes in absorption spectra, depending on the potential shift were observed for PGeZ monomer. For all the monomers, the biggest difference after the experiment occurs at 590 nm.

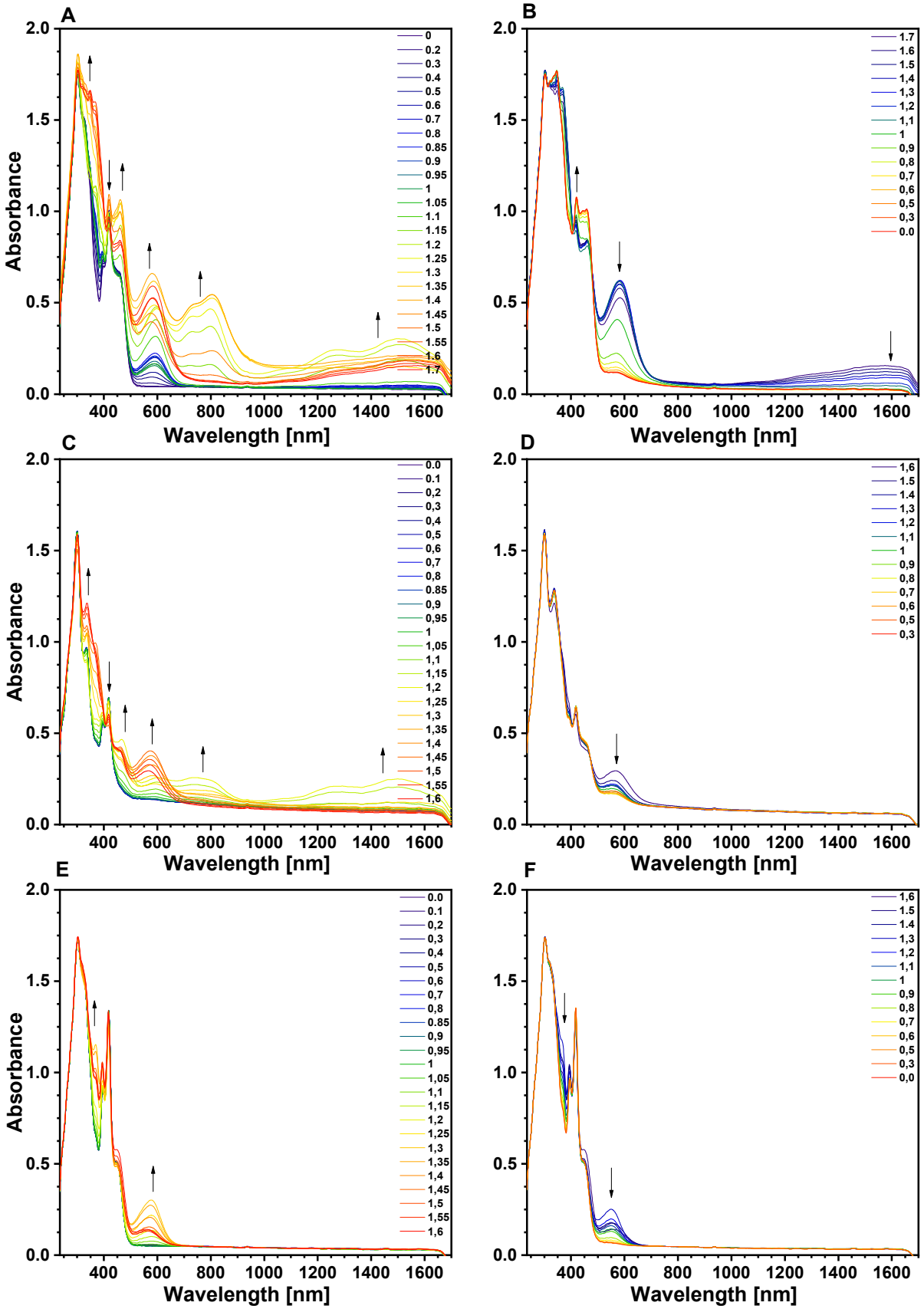

Figure 8. Spectroelectrochemichal measurements of examined photoactive molecules. A,C and E corresponds to doping and diagrams B, D and F to the dedoping processes.
A,B- PGeZ, C,D- PSiZ, and E,F- DPPZS

Due to understanding the formation of the reactive species on the electrode, the potentiostatic EPR spectroelectrochemistry was performed. In the case of PGeZ as well as PSiZ weak signals during the oxidation process were reported. The first visible signals for the EPR spectra were recorded at around 0.9 V for PGeZ and 0.8 V for PSiZ (vs. the Fc/Fc^{+} redox couple). The potential at which changes were observed for electron paramagnetic resonance spectra correlates with the results obtained for cyclic voltammetry - the EPR peak begins to increase at the potential at which the first oxidation peak for the monomer increases. By comparing these data with absorption spectroelectrochemistry results, it can be said that at this potential the formation of diradical dictation species occurs. Since it was not possible to obtain an oxidation EPR spectrum for the DPPZS monomer, it can be concluded that the reactive species are delocalized within the donor moiety of the analyzed compounds. The reduction of the analyzed molecules was only visible for the DPPZS. Here, the electrochemical reduction also corresponds to the obtained signal (-1.85 V). All the overmentioned processes are reversible.

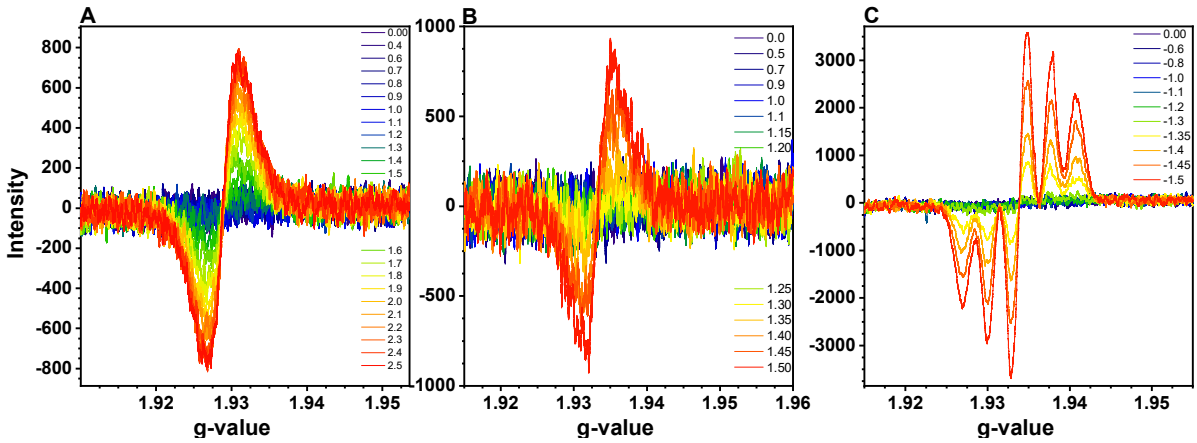

Figure 9.EPR results for analyzed photoactive molecule. A- PGeZ, B- PSiZ, and C- DPPZS

TADF-type compounds used in OLED devices that are capable of polymerisation possess several advantages compared to small molecules. First of all, they are characterized by high thermal stability and leave plenty of room for modification, especially in host-guest interactions. Second of all, their conjugated structure simplifies the devices' production process since printing can be used. On the other hand, the polymerisation of such compounds also might increase the efficiency of the non-radiative processes. A key feature here is the rigidity of the polymeric backbone: the more flexible structures show a significant decrease in the tested systems' performance due to increased non-radiative transitions [39].

5.1.2. OPV systems

In the work's second part, fullerene derivatives applicable in OPV devices were broadly investigated. Those carbon nanostructures possess an absorption band located mainly in the UV region of the spectra and significantly lower absorption in the visible range. Moreover, their characteristic cage-like structure allows for accepting electrons, which is extremely useful in OPVs when C_{60} is accompanied by an excellent electron donor that absorbs energy inthe visible spectrum, e.g. P3HT.

In the presented work, two types of fullerene derivatives were investigated: novel one - N-methyl-2-(2,5-di(selenophen-2-yl)thiophen-3-yl)fullero[3,4]pyrrolidine (C_{60}Se), and well-known Phenyl-C61-butyric acid methyl ester (PCBM). In the first case, the newly synthesized fullerene derivative C_{60}Se having a D-A structure, was further combined with BisSe units. Firstly, the electrochemical investigations of both monomers were conducted. As shown in Figure 10, irreversible oxidation was observed at 0.8 V (vs. Fc/Fc^+), which can be assigned to the oxidation of organic units in C_{60}Se and BisSe. Within the further scans, the steady increase in the redox couple at ca. 0.4 V (vs. Fc/Fc^+) was observed, indicating electroactive layer formation. Since the oxidation of both monomers occur at similar potentials, it can be stated that the forming layer contains both monomers. The electrochemical co-deposition was conducted in five different molar ratios with the aim to vary the ratio between donor and acceptor in the photoactive layer. This approach was further confirmed to be successful using CV (Figure 10A) and UV-Vis, and XPS spectroscopies.

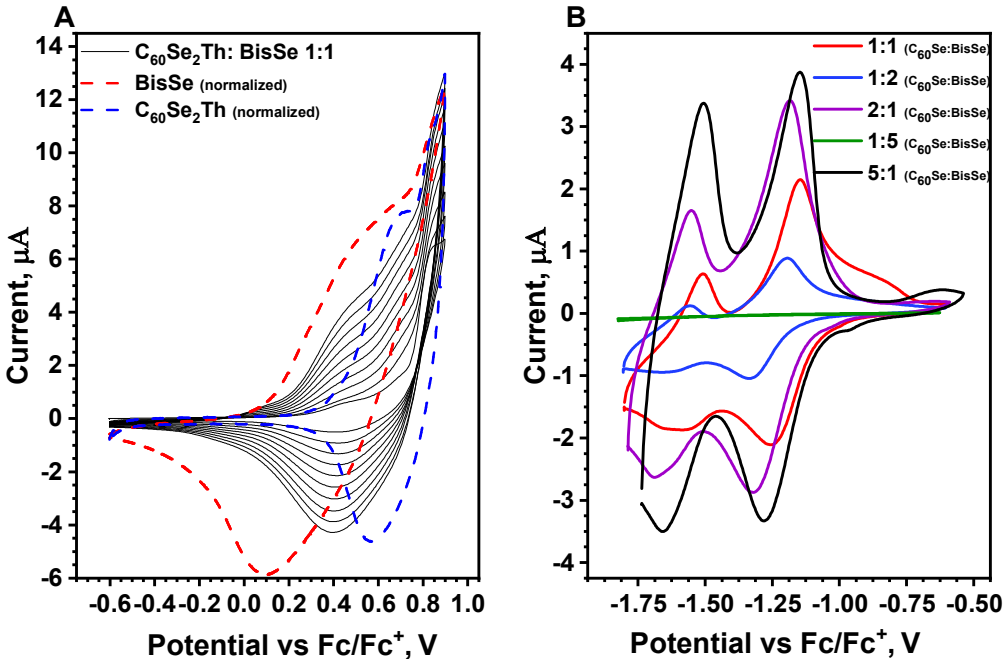

Figure 10. Electrochemical behaviour of fullerene-selenophene co-deposited layers in A) reduction and B) oxidation part of voltammogram.

In the second case in the group of OPVs materials, the PCBM:P3HT system was investigated. Here, poly(3-hexylthiophene-2,5-diyl) acts as an antenna and energy donor, while fullerene derivative acts as an electron acceptor. The values of HOMO and LUMO states presented in the literature for these two photoactive compounds are, respectively 6.1 and 3.7 for PCBM and 5.0 and 3.0 for P3HT[40]. Marvellous features predispose this blend as an active layer for OPV devices. In the presented study, PCBM:P3HT photoactive layers were formed using a spin-coating technique from solutions with varied molar ratios and were in the next step characterized by UV-Vis spectroscopy.

Figure 11 represents the UV-Vis spectra of obtained layers, confirming the composition of films. Borosilicate glass substrates with high UV transparency threshold (above 300 nm) were used as the substrate for obtaining the films. The strong and broad absorption band occurring between 400 and 600 nm belongs to P3HT and is due to pi-pi transitions. The small shoulder in the region of approximately 605 nm results from inter-chain stacking of this polymer and, as a result, its ordering. This band is clearly visible in the UV-Vis spectra of all layers containing the polymer. The characteristic fullerene absorption band is observed at ca. 330 nm.

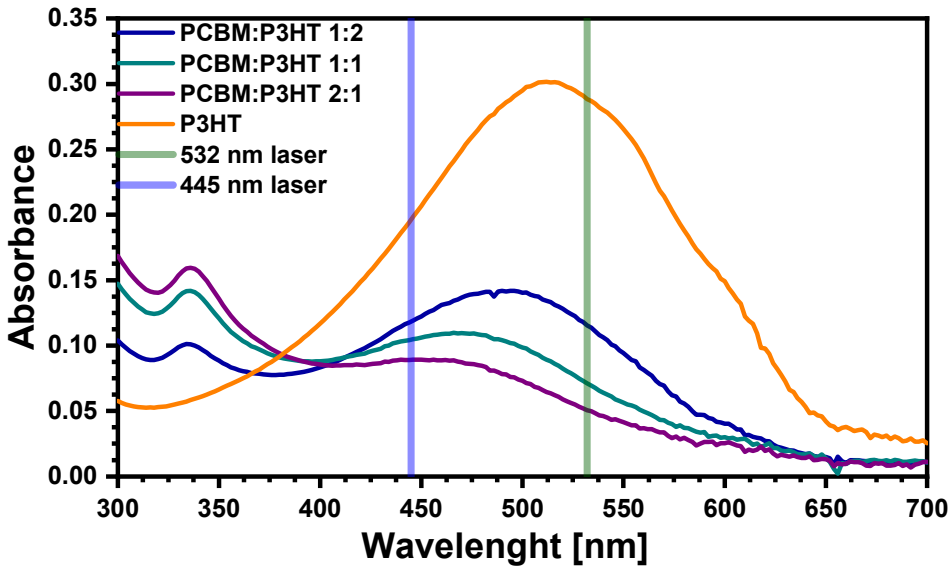

Figure 11. UV-Vis spectra of the thin layer absorption spectra for different concentration photoactive layers in comparison to pure P3HT layer.

Last but not least, the chemical grafting of porphyrin and phenothiazine derivatives on a glass surface was conducted. Both porphyrin and phenothiazine–containing materials are widely investigated for application as an active layer in Dye-Sensitized Solar Cells (DSSC). In this work, commercially available derivatives containing primary amino groups were selected. In the chosen modification strategy, the first step was a chemical grafting of the glass

surface with (3-Aminopropyl)triethoxysilane (APTES) and was followed by two post-modification steps based on the chemical reaction between $–NH_2$ and –COCl groups. Since the nanoscale layer was formed, the optical and physical properties of the glass substrate were not influenced. In the presented work, as in the case of donor-acceptor systems based on the photosensitising properties of fullerene derivatives, two photoactive molecules were applied in order to widen the absorption light spectrum. The chemical structure of the formed coating was confirmed using XPS and IR spectroscopies.

5.2. Singlet oxygen photogeneration

The ability of the photoactive compounds to act as a photosensitiser (PS) in the process of generation of singlet oxygen can be tested via direct or indirect methods. Direct methods involve monitoring the characteristic emission band at 1268 nm, which is challenging to observe due to its low intensity, stability, and position [41]. This issue was broadly discussed in M1, where different approaches, techniques and equipment were considered. In the presented work, the indirect method based on UV-Vis absorption spectroscopy and specific chemical traps was applied. The advantage of such an indirect method is its uncomplicated nature – it does not require advanced and expensive apparatus for research. Furthermore, it allows for a quick change of the experimental conditions by changing the light source, e.g. from a xenon lamp to a laser. Despite certain complication of the measuring system, the results obtained using the abovementioned methods are generally considered accurate and reliable. Nevertheless, it should be remembered that the ideal marker used during the measurements should not be sensitive to light itself, and its absorption peak should not overlap with the absorption peak of the tested photosensitiser. The most common chemical

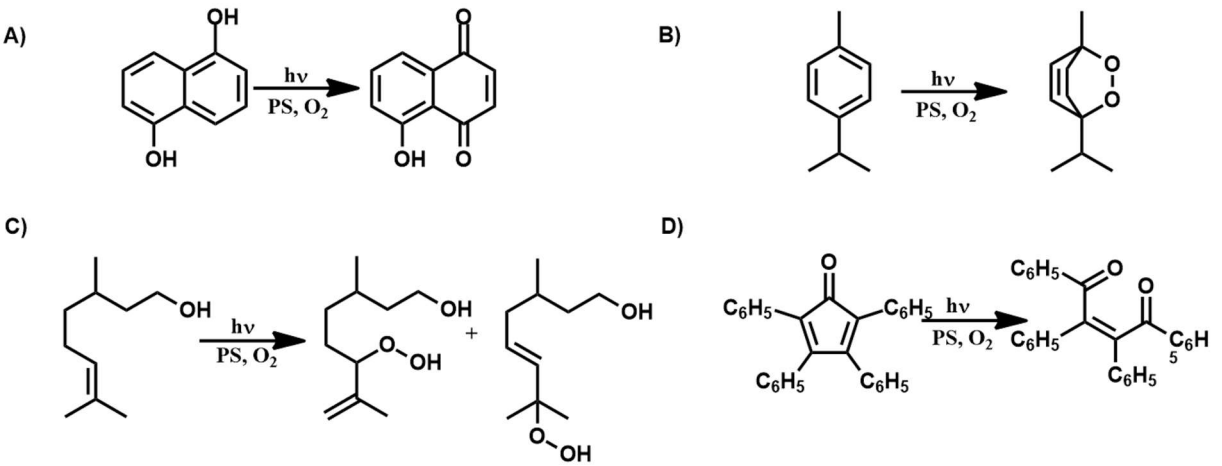

Figure 12. Singlet oxygen reactions with easily oxidizable with singlet oxygen materials such as A) 1,5-dihydroxynaphtalene, B) α-terpinen, C) citronellol and D) 2,3,4,5-tetraphenylcyclopentadienone

trap of singlet oxygen is 1,3-diphenylisobenzfurane (DPBF). Moreover, α-terpinene (αT) and 1,5-dihydroxynaphtalene (DHN) were applied in the conducted experiments (Figure 12). The principal goal of this work was to verify whether photoactive donor-acceptor systems dedicated to organic optoelectronics can effectively act as photosensitisers in the photogeneration of singlet oxygen.

In the case of the first of the investigated systems, i.e. PGeZ, the photogeneration experiment was carried out with α-terpinene in acetonitrile (ACN) with 445 nm laser as a light source. The choice of solvent was determined in this case for its weak affinity to the film and its lack of interaction with the polymeric layer, which was confirmed by stability studies. The results of photogeneration experiments are shown in Figure 13. Clear decrease in the absorption of α-terpinene at 266 nm was observed in time, indicating its reaction with singlet oxygen produced by PGeZ layer. Unfortunately, the film's sensitivity does not allow the same photoactive layer to be used repeatedly, and its performance decreases in successive trials.

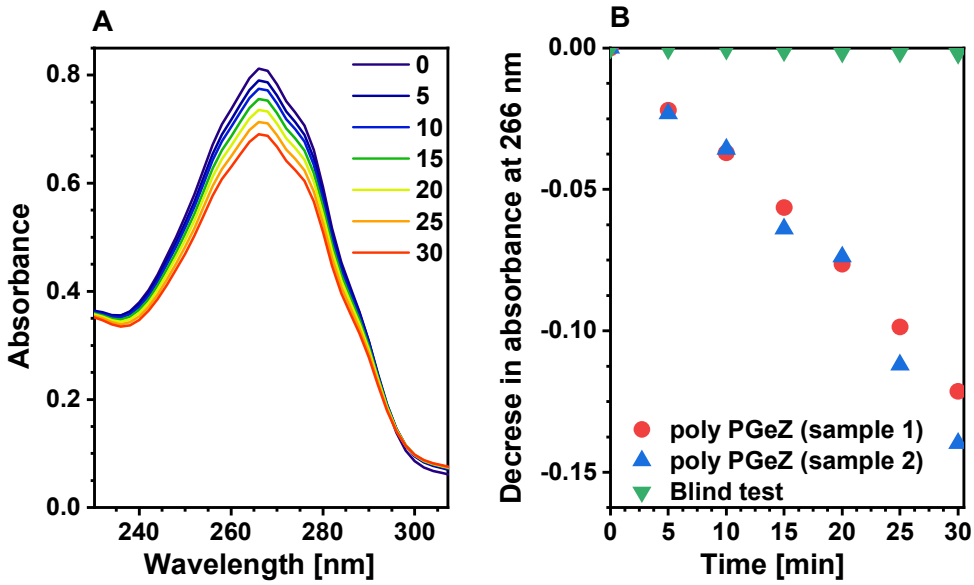

Figure 13. Oxidation of α-terpinene by PGeZ layer formed on top of ITO electrode.

Fullerenes and their derivatives have been already investigated as potential photosensitisers, especially for PDT therapy. Exposed to specific low wavelengths of light from the border of the UV and visible spectra, they show high quantum yields of singlet oxygen productions. However, when exposed to visible light, they are relatively useless. The situation can be changed by the introduction of organic units acting as donors. For example, a π-conjugated polymer absorbing in the visible range can act as an antenna transferring energy to fullerene. This idea was investigated in two works - M3 and M4, in which fullerene/organic

D-A systems were applied as a singlet oxygen source in the exemplary oxidation reactions used in fine chemicals synthesis.

The electrochemically co-deposited photoactive layers containing $C_{60}Se$ and BisSe with varied ratio were applied in α-terpinene oxidation to ascaridole (M3). The process can be followed by monitoring the decrease in the absorbance of α-terpinene 266 nm. The formation of $^1O_2$ was also confirmed with DPBF specific trap. The efficiency of energy transfer from the donor organic units to the fullerene acceptor was investigated by analyzing the oxygen photogeneration results for measurements with a xenon lamp as the light source. Some of the measurements were carried out using a filter transmitting only visible light above 400 nm so that mainly donor units in the studied layer were excited. Comparing the kinetics of the photooxidation reactions revealed that the P($C_{60}Se$_BisSe_1:1) layer was found to have the optimal balance between donor and acceptor unit and had the highest performance among the tested systems, which is shown in Table 4.

Table 4. Rate constants of singlet oxygen reaction photogenerated by layers with different concentrations of photosensitizer

Photoactive layer	**k** $\left[\frac{1}{mM \cdot min}\right]$
P($C_{60}Se$:BisSe 5:1)	$(1.72 \pm 0.01) \cdot 10^{-4}$
P($C_{60}Se$:BisSe 2:1)	$(2.85 \pm 0.01) \cdot 10^{-4}$
P($C_{60}Se$:BisSe 1:1)	**$(5.10 \pm 0.02) \cdot 10^{-4}$**
P($C_{60}Se$:BisSe 5:2)	$(2.52 \pm 0.01) \cdot 10^{-4}$
P($C_{60}Se$:BisSe 5:5)	$(1.30 \pm 0.01) \cdot 10^{-4}$
P($C_{60}Se$)	$(2.03 \pm 0.01) \cdot 10^{-4}$

Further, the PCBM:P3HT system was successfully applied as a singlet oxygen source in the oxidation of DHN to juglone. The process can be followed by monitoring the absorbance of DHN at 298 nm and the absorbance of juglone at 510 nm. Both tests conducted with 1,3-diphenylisobenzofuran (DPBF) as a specific marker and with DHN oxidation showed that the highest photogeneration efficiency was obtained for the layer consisting of a 2:1 PCBM:P3HT ratio. Furthermore, when the layer was illuminated with a xenon lamp, both PCBM and P3HT were activated thus, in order to investigate the energy transfer between the donor (P3HT) and the acceptor (PCBM), several tests were carried out, taking into account the light source used to illuminate the samples. In the case of the xenon lamp, both photoactive compounds were excited, while a laser with a 532 nm wavelength mainly excited the donor unit (Figure 14).

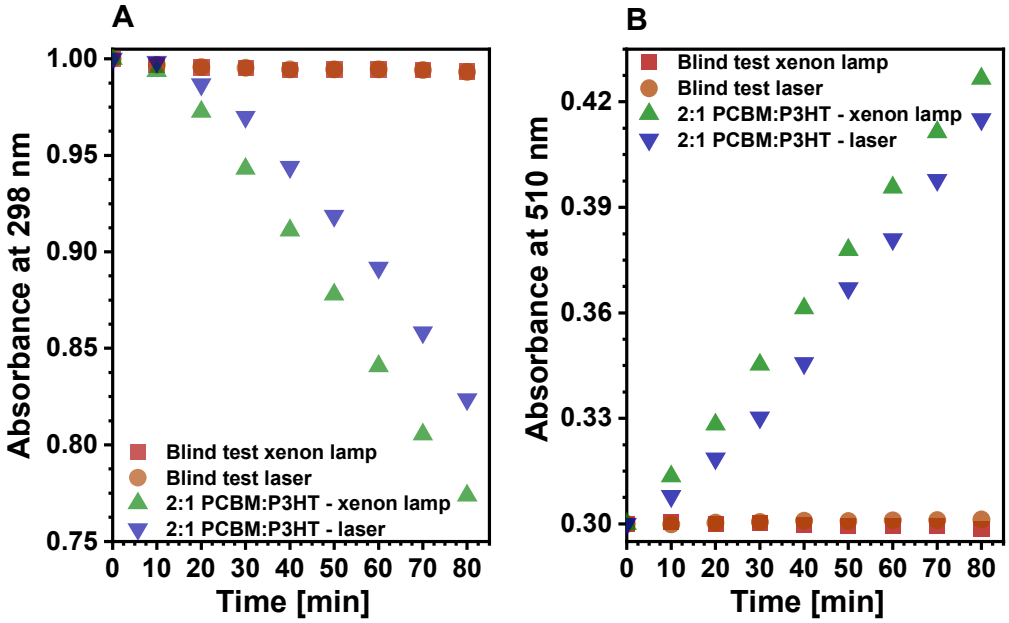

Figure 14. Comparison of two light sources used during oxidation of 1,5-DHN with singlet oxygen. The reaction rate observed by (A) decreasing absorption at 298 nm and (B) increasing absorption at 500 nm.

Both examined photoactive D-A systems based on fullerene derivatives showed good abilities to act as photosensitisers in the photogeneration of singlet oxygen. Two different approaches to layer formation were applied. On the one hand, the PCBM:P3HT system was deposited on glass in a completely mechanical way – through the spin coating technique. On the other hand, the C_{60}Se:BisSe units were electrochemically co-deposited on an ITO electrode surface. It was shown that the composition of the resulting layer, and thus its spectroscopic and photochemical properties, can be easily tuned in both methods. Moreover, in the case of both systems, introducing a donor unit with a strong absorption band in the visible range significantly increases the ability of the photoactive system to produce $^1O_2$ under broadband illumination. Based on the obtained results, it might also be said that the key feature defining the D-A system as a photosensitiser is the ratio between the donor and acceptor moieties, particularly if only one of them has sensitizing abilities. Thus, carefully optimising the ratio has to be done to avoid insufficient photosensitizer in the system or in the opposite situation - lack of low energy-absorbing donor units. Importantly, it has been proven that both systems initially designed and applied in organic optoelectronic devices can also act as an effective source of singlet oxygen.

Last but not least, the potential application of photoactive layers as the antibacterial coating was tested. Antibacterial and antiviral properties of singlet oxygen are well known in the literature. This phenomenon is related to the extremely strong oxidative properties of $^1O_2$. Pathogen cells are mainly composed of proteins and lipids, easily oxidized by $^1\Delta_gO_2$ molecules.

Therefore, bacterial colonies exposed to singlet oxygen in an aerobic environment cause the extermination of microbes. Going even further, it might be predicted that applying such antimicrobial coatings in medical centres and facilities allows for reducing nosocomial infections among patients.

Layers formed according to the scheme presented in the previous chapter were in the first step tested in a heterogeneous experiment. To investigate the performance of the mixed layers, a series of experiments were conducted with specific lasers at 445 nm (activating porphyrin, APTPP) and 638 nm (activating phenothiazine, AA) and a xenon lamp (activating both). The photogeneration was investigated with α-terpinene as a marker, thus, the involvement of other reactive oxygen species (ROS), not only singlet oxygen, cannot be excluded. It was confirmed that both photosensitizers retain their photoactivity towards ROS production and that the highest efficiency of the photoprocess under white light was observed for the mixed layer, as shown in Figure 15. The ability of the presented layers to exhibit antimicrobial action was confirmed in microbiological studies conducted by M. Sc. Dominikę Czerwińską-Główkę and presented in M5.

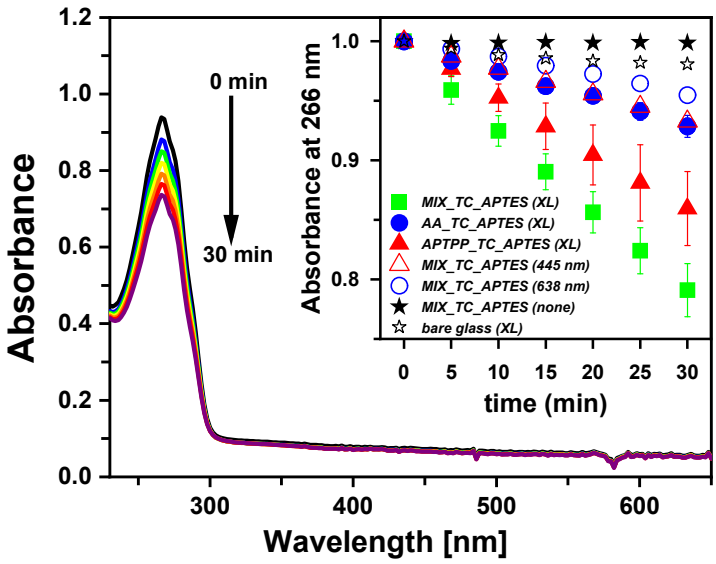

Figure 15. Decrease of 266 nm absorbance peak during photooxidation of α-terpinene by illumination of modified glasses respectively with AA, APTPP and mixed layers with xenon light (XL) and proper lasers (445 and 638 nm) (M5).

Worth mentioning that the applied modification does not interfere with the glass substrate's optical and physical features. Moreover, despite the outstanding stability of the covalently attached layers, glass substrates might be reused after proper cleaning and pretreatment in the modification process. These factors promote presented antimicrobial modification as an industry-friendly application of photosensitisers in manufacturing processes. Modified glass can be especially used in hospitals and medical facilities as windows, glass covers

for medical equipment or glass lightning elements. Considering how important the light is for the photoactive layers to fulfil their role, one should also consider applying these modifications during the production of optoelectronic systems, especially in OLED devices, which, by illuminating a glass screen, would enhance the antibacterial capabilities of the devices. It would have been an outstanding chance to overcome and reduce the influence of nosocomial and popular infections in medical centres and daily office work with monitors, smartphones, etc.

6. Conclusions

The presented work shows a broad approach to investigating conjugated organic systems, from classical spectroscopic/electrochemical studies of D-A-D-type molecules, throughout a rather unconventional part dealing with the analysis of $^1O_2$ photogeneration by those systems, up to the preliminary investigation of their potential application as photocatalysts or antimicrobial coatings. During the research, various approaches to forming photoactive layers were applied, such as electrochemical polymerisation, spin-coating, and the chemical modification and chemical grafting of photosensitisers. An integral part of science is the applicability of the investigated solutions. In this work, a system of photoactive compounds is applied due to its work as an antibacterial coating through its ability to photogenerate singlet oxygen.

It has been shown that the appropriate selection of two photoactive compounds, especially in donor-acceptor systems, can significantly boost the photoactive potential of the studied systems. This fact might be highly important from the organic optoelectronics perspective. Taking it one step further, the manipulation and skilful selection of co-existing photoactive systems might influence the ratio of radiative and non-radiative transition taking place in optoelectronic devices. Thus, understanding the processes occurring between the donor and acceptor in such systems is the key to improving known organic devices' efficiency. However, since the mechanism and structural changes that distinguish photoactive compounds as photosensitising materials or active materials for device manufacturing haven’t been determined, there remains much room for research into the nature of photoactive compounds.

Bibliography

1. Nosov, Y. R. History of optoelectronics: general review. in *Second Conference on Photonics for Transportation* vol. 4761 20–27 (2002).
2. Adams, F. & Barbante, C. *Nanotechnology and Analytical Chemistry*. *Comprehensive Analytical Chemistry* vol. 69 (2015).
3. Bernanose, A. Electroluminescence of organic compounds. *Br. J. Appl. Phys.* **6**, 54–56 (1955).
4. Forrest, S. R. & Thompson, M. E. Introduction: Organic electronics and optoelectronics. *Chem. Rev.* **107**, 923–925 (2007).
5. Lee, H. B., Jin, W. Y., Ovhal, M. M., Kumar, N. & Kang, J. W. Flexible transparent conducting electrodes based on metal meshes for organic optoelectronic device applications: A review. *J. Mater. Chem. C* **7**, 1087–1110 (2019).
6. Jeon, Y. *et al.* Parallel-stacked flexible organic light-emitting diodes for wearable photodynamic therapeutics and color-tunable optoelectronics. *ACS Nano* **14**, 15688–15699 (2020).
7. Im, H. G. *et al.* Flexible Transparent Crystalline-ITO/Ag Nanowire Hybrid Electrode with High Stability for Organic Optoelectronics. *ACS Appl. Mater. Interfaces* **12**, 56462–56469 (2020).
8. Xu, X., Sun, L., Shen, K. & Zhang, S. Organic and hybrid organic-inorganic flexible optoelectronics: Recent advances and perspectives. *Synth. Met.* **256**, 116137 (2019).
9. Lüer, L. *et al.* Oxygen-induced quenching of photoexcited states in polythiophene films. *Org. Electron.* **5**, 83–89 (2004).
10. Turak, A. Interfacial degradation in organic optoelectronics. *RSC Adv.* **3**, 6188–6225 (2013).
11. Kenry, Chen, C. & Liu, B. Enhancing the performance of pure organic room-temperature phosphorescent luminophores. *Nat. Commun.* **10**, 1–15 (2019).
12. Crutchley, R. J. & DeRosa, M. C. Photosensitized Singlet Oxygen and its Applications. *Coord. Chem. Rev.* **233–234**, 351–371 (2002).
13. Ogilby, P. R. Singlet oxygen: There is indeed something new under the sun. *Chem. Soc. Rev.* **39**, 3181–3209 (2010).
14. Schaer, M., Nüesch, F., Berner, D., Leo, W. & Zuppiroli, L. Water vapor and oxygen degradation mechanisms in organic light emitting diodes. *Adv. Funtional Mater.* **11**, 116–121 (2001).
15. Qin, Y. *et al.* Silicon and oxygen synergistic effects for the discovery of new high-performance nonfullerene acceptors. *Nat. Commun.* **11**, 1–10 (2020).
16. Lu, Q. *et al.* A Review on Encapsulation Technology from Organic Light Emitting Diodes to Organic and Perovskite Solar Cells. *Adv. Funct. Mater.* **31**, 1–41 (2021).

17. Yang, J., Yan, D. & Jones, T. S. Molecular Template Growth and Its Applications in Organic Electronics and Optoelectronics. *Chem. Rev.* **115**, 5570–5603 (2015).
18. Chen, M. *et al.* Anthracene-based semiconductors for organic field-effect transistors. *J. Mater. Chem. C* **6**, 7416–7444 (2018).
19. Zhang, Y., Chen, A., Kim, M. W., Alaei, A. & Lee, S. S. Nanoconfining solution-processed organic semiconductors for emerging optoelectronics. *Chem. Soc. Rev.* **50**, 9375–9390 (2021).
20. Han, G. & Yi, Y. Origin of Photocurrent and Voltage Losses in Organic Solar Cells. *Adv. Theory Simulations* **2**, 1900067 (1–17) (2019).
21. Bizzarri, C., Hundemer, F., Busch, J. & Bräse, S. Triplet emitters versus TADF emitters in OLEDs: A comparative study. *Polyhedron* **140**, 51–66 (2018).
22. Data, P. & Takeda, Y. Recent Advancements in and the Future of Organic Emitters: TADF- and RTP-Active Multifunctional Organic Materials. *Chem. - An Asian J.* **14**, 1613–1636 (2019).
23. Kohn, A. W., Lin, Z. & Van Voorhis, T. Toward Prediction of Nonradiative Decay Pathways in Organic Compounds I: The Case of Naphthalene Quantum Yields. *J. Phys. Chem. C* **123**, 15394–15402 (2019).
24. Li, S. *et al.* Asymmetric Electron Acceptors for High-Efficiency and Low-Energy-Loss Organic Photovoltaics. *Adv. Mater.* **32**, 1–10 (2020).
25. Notsuka, N., Nakanotani, H., Noda, H., Goushi, K. & Adachi, C. Observation of Nonradiative Deactivation Behavior from Singlet and Triplet States of Thermally Activated Delayed Fluorescence Emitters in Solution. *J. Phys. Chem. Lett.* **11**, 562–566 (2020).
26. Channa, I. A. *et al.* Solution processed oxygen and moisture barrier based on glass flakes for encapsulation of organic (opto-) electronic devices. *Flex. Print. Electron.* **6**, 025006 (2021).
27. Jeong, E. G., Kwon, J. H., Kang, K. S., Jeong, S. Y. & Choi, K. C. A review of highly reliable flexible encapsulation technologies towards rollable and foldable OLEDs. *J. Inf. Disp.* **21**, 19–32 (2020).
28. Blacha-Grzechnik, A. *et al.* Photogeneration of singlet oxygen by the phenothiazine derivatives covalently bound to the surface-modified glassy carbon. *Appl. Surf. Sci.* **371**, 151–159 (2016).
29. Zhuo, J. *Photoactive chemicals for antimicrobial textiles*. *Antimicrobial Textiles* (Elsevier Ltd, 2016). doi:10.1016/B978-0-08-100576-7.00011-0.
30. Ravikumar, M., Kathiravan, A., Neels, A. & Mothi, E. M. Tin(IV) Porphyrins Containing β-Substituted Bromines: Synthesis, Conformations, Electrochemistry and Photophysical Evaluation. *Eur. J. Inorg. Chem.* **2018**, 3868–3877 (2018).

31. Lin, L. *et al.* Singlet Oxygen Luminescence Image in Blood Vessels During Vascular-Targeted Photodynamic Therapy. *Photochem. Photobiol.* **96**, 646–651 (2020).
32. Page, K., Correia, A., Wilson, M., Allan, E. & Parkin, I. P. Light-activated antibacterial screen protectors for mobile telephones and tablet computers. *J. Photochem. Photobiol. A Chem.* **296**, 19–24 (2015).
33. Spagnul, C., Turner, L. C. & Boyle, R. W. Immobilized photosensitizers for antimicrobial applications. *J. Photochem. Photobiol. B Biol.* **150**, 11–30 (2015).
34. Collavini, S. & Delgado, J. L. Fullerenes: The stars of photovoltaics. *Sustain. Energy Fuels* **2**, 2480–2493 (2018).
35. Bregnhøj, M. *et al.* Oxygen-dependent photophysics and photochemistry of prototypical compounds for organic photovoltaics: inhibiting degradation initiated by singlet oxygen at a molecular level. *Methods Appl. Fluoresc.* **8**, 014001 (2020).
36. Cardona, C. M., Li, W., Kaifer, A. E., Stockdale, D. & Bazan, G. C. Electrochemical considerations for determining absolute frontier orbital energy levels of conjugated polymers for solar cell applications. *Adv. Mater.* **23**, 2367–71 (2011).
37. Spagnul, C., Turner, L. C. & Boyle, R. W. Immobilized Photosensitisers for antimicrobial applications. *J. Photochem. Photobiol. B Biol.* **150**, 11–30 (2015).
38. Goto, S. *et al.* Revealing the internal heavy chalcogen atom effect on the photophysics of the dibenzo[a,j]phenazine-cored donor-acceptor-donor triad. *J. Mater. Chem. C* **9**, 13942–13953 (2021).
39. Yin, X. *et al.* Recent Advances in Thermally Activated Delayed Fluorescent Polymer—Molecular Designing Strategies. *Front. Chem.* **8**, 1–23 (2020).
40. Kadem, B., Hassan, A. & Cranton, W. Efficient P3HT:PCBM bulk heterojunction organic solar cells; effect of post deposition thermal treatment. *J. Mater. Sci. Mater. Electron.* **27**, 7038–7048 (2016).
41. Khan, A. U. & Kasha, M. Direct spectroscopic observation of singlet oxygen emission at 1268 nm excited by sensitizing dyes of biological interest in liquid solution. *Proc. Natl. Acad. Sci. U. S. A.* **76**, 6047–6049 (1979).

Main publications

Multiaplicability of singlet oxygen – small molecule high impact in materials development.

Aleksandra Nyga [a], Ivan Gusev [a], Agata Blacha-Grzechnik [a], Przemyslaw Data [a]*

[a] *Faculty of Chemistry, Silesian University of Technology, Strzody 9, 44-100 Gliwice, Poland*

E-mail:
Prof. Przemyslaw Data, przemyslaw.data@polsl.pl.

Abstract

Singlet oxygen has been investigated for almost 60 years for medical application in photodynamic therapy, wastewater treatment, synthesis of fine chemicals and even in organic electronics . However, the main information about this species in organic electronics was a harmful degradation of the active layer but is that all, or maybe the knowledge of singlet oxygen behaviour could be helpful in the improvement of materials or find new applications? In this work, we would like to present the importance of singlet oxygen and the survey from basic understanding to particular application optoelectronics, for example in organic electronic devices like Organic Photovoltaics or Organic Light-Emitting Diodes.

Keywords

Singlet oxygen, photocatalysis, photosensitizers, organic electronics, photoactive layer, thermally activated delayed fluorescence.

1 Introduction

Singlet oxygen, $^1O_2$, is one of the Reactive Oxygen Species (ROS) that has been under high research interest since 1963, thanks to its remarkable features. It has been mainly considered for a potential application in medicine, wastewater treatment and synthesis of fine chemicals [1,2]. The number of research papers dealing with singlet oxygen has reached over 12000 works in the last ten years, confirming the attractiveness of this highly reactive species. On the other hand, it has been shown that the formation of $^1O_2$ and other ROS is rather undesirable in the case of organic electronics (OE) since it generally leads to the degradation of active material and the consecutive decrease in the efficiency of the device [3-5]. Many works reviewing the physical and chemical properties of singlet oxygen, so as the current significant development in its application, have been published till now [6-10]. However, the investigations of the role that $^1O_2$ plays in materials engineering and optoelectronics have not been summarised yet. Hence, this work aims to discuss the current state of knowledge on the influence of singlet oxygen, showing that the presence of $^1O_2$ needs to be taken into account in the materials engineering.

2 Singlet Oxygen – general information

What is singlet oxygen? Still, not many are familiar with the information that oxygen in its ground form is in its triplet state, unlike the typical organic molecules, in which the ground state is a singlet state. As for the basics, the electronic configuration of the molecular oxygen is KK $(1\sigma)^2(1\sigma*)^2(2\sigma)^2(2\sigma*)^2(3\sigma)^2(1\pi)^4(1\pi*)^2$, and it has three electronic states: $O_2(X_3\Sigma g^-)$, $O_2(a_1\Delta g)$, and $O_2(b_1\Sigma g^+)$.[14] Due to an even number of electrons on the antibonding π* orbital, oxygen has specific magnetic and chemical properties. The molecular oxygen in a triplet ground state $O_2(X_3\Sigma g)$ is a biradical with two electrons on the separate π* orbitals having parallel spins (**Figure 1**). The rearrangement of the electrons within these orbitals results in two possible singlet excited states: $O_2(a_1\Delta g)$ and $O_2(b_1\Sigma g^+)$. The first one is considered more stable, while $O_2(b_1\Sigma g^+)$ rapidly decays,

producing $O_2(a_1\Delta g)$. The energy of $O_2(a_1\Delta g)$ and $O_2(b_1\Sigma g^+)$ states is 92 kJmol^{-1} and 155 kJmol^{-1} higher than $O_2(X_3\Sigma g^-)$, respectively [11].

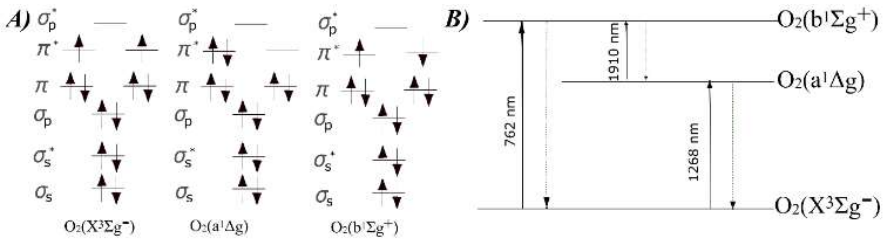

Figure 1. A) Molecular orbitals of triplet and singlet oxygen, B) Scheme of electronic transitions between the main and lower energy levels of the oxygen molecule.

The transition from the ground state to the singlet state is spin forbidden. However, singlet oxygen can be generated by direct excitation or via the energy transfer process. It is also possible to obtain singlet oxygen in a gas or condensed phase where oxygen concentration is very high, thanks to the interaction with other molecules causing perturbation of oxygen molecule leading to $O_2(X_3\Sigma g^-) \rightarrow O_2(a_1\Delta g)$ transition. The characteristic bands arising from the transitions between various oxygen states can be observed at the following wavelengths: $O_2(a_1\Delta g) \rightarrow O_2(X_3\Sigma g^-)$ at 1268 nm, $O_2(b_1\Sigma g^+) \rightarrow O_2(X_3\Sigma g)$ at 762 nm and $O_2(b_1\Sigma g^+) \rightarrow O_2(a_1\Delta g)$ at 1910 nm (**Figure 2**).

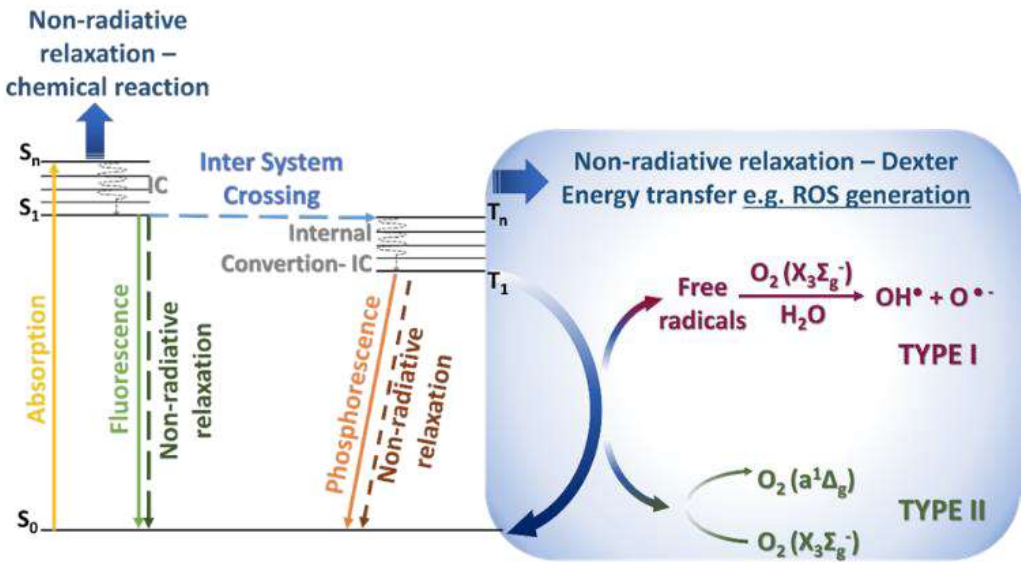

Figure 2. Type I and Type II photosensitisation Jablonski diagram concerning energy changes in photosensitiser and subsequent processes.

The triplet state oxygen has paramagnetic properties, unlike singlet oxygen form, which is diamagnetic. This corresponds to the arrangement of electrons of these three forms of molecular oxygen. Their chemical properties also vary significantly. Generally, $O_2(X_3\Sigma g^-)$ is considered less reactive due to the presence of the parallel electrons [12]. Singlet oxygen has approximately an order higher oxidising potential and significantly stronger electrophilic character than the ground state oxygen. The characteristic chemical reactions of singlet oxygen are [4+2] - cycloaddition to cis-dienes or aromatic hydrocarbons, [2+2] - cycloaddition to olefins. Because of its very high reactivity, the lifetime of singlet oxygen range from μs to ms in solutions, though in the diluted gas-phase, its lifetime can reach up to 72 minutes [13,14]. As indicated by the theoretical studies and later proven by the experiments, the lifetime of singlet oxygen is the lowest in water (about 2 μs) and the highest in deuterated or halogenated solvents (1 ms). The quenching efficiency of singlet oxygen determines the lifetime due to the inductive resonance energy transfer from the singlet oxygen to the vibrational sublevels of hydrogen and other atoms of solvent molecules.

3 Singlet oxygen production – Type 1 and Type 2 photosensitisation.

Singlet oxygen can be formed in various photochemical, chemical, and physical processes. The photochemical ones include photolysis [15,16], photosensitization [1] and direct light excitation of triplet-state oxygen molecules [17,18]. The latter occurs under irradiation with a wavelength of 1065 nm [19] or 1270 nm [20] but requires high oxygen pressures (up to 141.855 bar). The chemical methods consist of the decomposition of the selected oxygen-containing compounds [21,22]. Production of $^1O_2$ is also possible using gas-discharge tubes and tungsten incandescent lamps [23]. Even though various methods of singlet oxygen production have been introduced, still the most commonly used strategy is the photoexcitation of photosensitiser (PS) molecules [14]. In the

abovementioned process, after the light absorption, the photosensitiser molecules reaches its excited singlet state, from which it rapidly relaxes by the internal conversion to the first excited singlet state. The first excited singlet state of PS can be deactivated by the emission of a photon (fluorescence) or by intersystem crossing (ISC). The latter is the major pathway of the excited singlet state deactivation for many photoactive molecules and results in the formation of the PS's triplet state, T_1. The lifetime of the T_1 state is longer (ms) than that of the S_1 state (ns), allowing this excited state to further react in one of two possible ways, defined as Types I and II mechanisms, generating various Reactive Oxygen Species (ROS), including singlet oxygen (**Figure 3**).

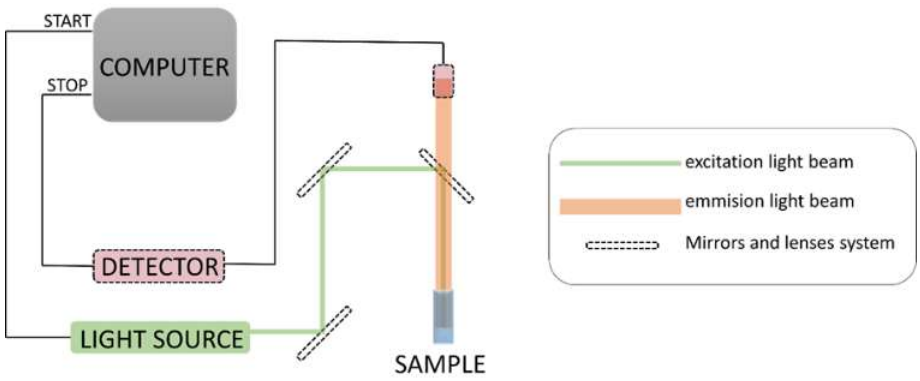

Figure 3. Simplified scheme of singlet oxygen direct detection setup.

Type I includes all photochemical reactions that go through the direct formation of free radicals, even when oxygen is not involved in the process. This mechanism involves hydrogen-atom abstraction or electron transfer between the excited sensitiser and a substrate, yielding free radicals. These radicals can react with oxygen to form reactive oxygen species, like superoxide radical anion. On the contrary, the Type II mechanism includes processes in which the primary interaction is the interaction of the excited photosensitiser molecule with ground state oxygen, yielding singlet oxygen [24,25]. In the Type II mechanism, singlet oxygen is generated by an energy transfer in a collision of the excited sensitiser with triplet oxygen. As a rule, both mechanisms occur simultaneously in the real chemical and biological systems, and their relative contribution strongly depends on the oxygen concentration, the concentration and nature of the reagents, the nature of photosensitisers, and many other factors

113 [26]. What's more, the relative contribution of Type I or Type II mechanisms can vary during the
114 photochemical process, too.

115

116

117 4 A typical application of singlet oxygen.

118 Singlet oxygen is applicable in the various fields of medicine, chemistry, and environmental sciences,
119 starting from photodynamic therapy up to chemical synthesis or wastewater treatment (**Table 1**). The
120 most widely investigated application of $^1O_2$ molecule is photodynamic therapy (PDT), including the
121 photodynamic inhibition of cancer tumours growth (i.e. lung [27], bladder [28], oesophagal [29],
122 breast [10], and brain [30] cancer), treatment of the bacterial, fungal, or viral infections [31,32] and
123 skin diseases [33] and sterilisation of blood or surfaces from bacteria or viruses [34]. Moreover, recent
124 works show the potential of singlet oxygen also in the treatment of Alzheimer's disease [35]. Next to
125 the medical applications, thanks to its tremendous oxidising capability, singlet oxygen is considered
126 as an attractive green reagent in the wastewater treatment [36] and in the selective oxidation of
127 aromatic alcohols [37], endoperoxides, dioxetanes, hydroperoxides, sulfoxides and phosphines
128 [38,39] that are of special interest in the production of fine chemicals.

129

130 **Table 1.** The selected examples of the application of singlet oxygen

Medicine		
Description of application	**Active species**	**Details of the process**
Treatment of Alzheimer's disease [35]	Various photosensitisers	The dissociation of Aβ self-assembled aggregates under illumination
Singlet oxygen-based chemodynamic therapy for selective tumour eradication [40]	Nanoparticulate hypochlorous ion (ClO^-)	Singlet oxygen initiating a complex genetic program, leading to cell death. There is a possibility of using intracellular singlet oxygen to treat

Singlet oxygen for treatment of skin melanoma [7]	Trisodium ferrous chlorophyllin (Fe-CHL) in nanoparticles 200 and 130 nm	tumours, but its effectiveness needs to be evaluated more precisely in the future. Nowadays, the most common technique of cancer treatment is photodynamic therapy. Photodynamic therapy (PDT) is a method of treating cancer, certain skin diseases, or infectious diseases based on the use of photosensitisers and light of a specific wavelength. The sensitiser is injected into the body most often intravenously but can be applied applicatively or orally. Generated singlet oxygen starts the cell death process of the target cells. Singlet oxygen and related techniques demonstrate outstanding potential in treating bladder cancer, skin cancer, lung cancer, bladder, prostate, oesophagal, breast, and brain cancer.
eatment of lung cancer [27]	Photofrin, laserphyrin	
Treatment of bladder and prostate cancer [28]	Hematoporphyrin derivatives: ALA, ALA-ester, Hypericin, Padeliporfin, Benzoporphyrin, Foscan	
Treatment of esophageal cancer [29]	Photofrin	
Treatment of breast cancer [10]	Photofrin, mTHPC (meso-tetra (m-hydroxyphenyl) chlorin), SnET2 (tin (II) ethyl etiopurpurin dichloride), and mote- xafin lutetium (MLu)	
Treatment of brain cancer [30]	Positive cofactor four on Au nanoparticles	
Medicine		
Treatment of the fungal infections [41]	Melanin	Isolated melanin irradiated with a laser at 532 nm produced singlet oxygen, which then reacted with fungal, caused cellular death
Singlet oxygen is essential for neutrophil extracellular traps formation [31]	Photofrin	Singlet oxygen can induce NET formation by a distinct system that generates singlet oxygen with photofrin in CGD neutrophils and healthy neutrophils. These results show that singlet oxygen is essential for the NET formation
Inactivation of SARS-CoV-2 through LED irradiation of visible spectrum wavelengths, production of singlet oxygen and another ROS [32]	Methylene blue, porphyrin derivatives	A LED device with a photosensitiser was tested on SARS- CoV-2 infected cells. Singlet oxygen showed the ability to inactivate SARS-CoV-2
Inactivation of hepatitis C virus in blood products [42]	Methylene blue	Treatment hepatitis C in blood plasma with methylene blue activated by the visible light and irradiation with shortwave ultraviolet generates singlet oxygen, leading to photooxidation of guanosine and destruction of the viral nucleic acid, thus preventing viral replication.
Wastewater treatment		

Disinfection of water [36]	Ru(II) complexes adsorbed on porous poly(dimethylsiloxane)	Photoinactivation of the microbiological contamination of water with singlet oxygen produced by the photosensitiser.
Degradation of organic pollutants [43]	Periclase (MgO) as peroxymonosulfate activator	Singlet oxygen acts as a highly selective reagent for the removal of electron-rich organic pollutants.
Degradation of Ciprofloxacin [44]	Sr-doped $BiFeO_3$ perovskites $Bi_{1-x}Sr_x FeO_3$ fabricated by sol-gel technique	The catalytic reaction of Sr-doping in the presence of oxygen induces the formation of singlet oxygen, which then acts as an oxidiser
Treatment of pharmaceutical wastewater [44]	Metal-free biochar derived from corn cob (CCBC) as peroxymonosulfate activator	CCBC obtained at 800□C showed the best adsorption capacity and catalytic activity towards typical organic pollutants. During peroxydisulfate activation with CCBC, singlet oxygen is produced.
Degradation of methyl orange [45]	Fe-Co bimetal-doped MCM-41 as peroxymonosulfate activator	Both radical and non-radical pathways were involved in the degradation of methyl orange in the FeCo-MCM-41/PMS system. Among ROS, singlet oxygen played a crucial role in the degradation.
Insecticidal activity		
Photoactivatable polycyclic aromatic dyes that absorb near-UV light wavelengths are used as insecticides [46]	Rose Bengal and erythrosine	Singlet oxygen generated by photosensitiser initiate necrosis, apoptosis of cells due to high membrane permeability.
Porphyrins and related compounds as photoactivatable insecticides with singlet oxygen as a key component of insecticide activity [47]	Porphyrins derivatives: meso-di(cis-4N- methyl-pyridyl)-cis-diphenyl-porphine ditosylate, hematoporphyrin, tri(4-N-methyl pyridyl)monophenyl-porphine trito- sylate	The photoinsecticidal activity increases with increasing hydrophobicity of the porphyrin molecule, Singlet oxygen generated by photosensitiser initiates cell death.
Fine chemical synthesis		
Selective oxidation of aromatic alcohols [48]	Pt/PCN-224(M), M: Zn, Ni, Co, Mn, H	Singlet oxygen is used as a mild oxidant for selective oxidation of aromatic alcohols to form corresponding aldehydes
Synthesis of racemic pandanusines A and B and pandalizine C, isolated from Pandanus amaryllifolius [49]	Methylene blue	Methylene blue plays a dual catalytic role of photosensitiser and redox catalyst.

Synthesis of substituted 2- oxindoles, 3-hydroxy-2-oxindoles, and isatins [50]	Methylene blue	Methylene blue generates singlet oxygen under irradiation. Singlet oxygen acts as an initiator of the cascade reaction
Synthesis of artemisinin, 1,2,4-Trioxanes, cyclic diperoxides, isonitriles [51]	Rose Bengal, eosin, methylene blue, porphyrin derivatives, fluorescein derivatives	Singlet oxygen produced by photosensitisers is used several of high-selectivity steps of artemisinin, 1,2,4-Trioxanes, cyclic diperoxides, isonitriles (ene reaction, Diels–Alder reaction, reaction with carbocyclic aromatic systems)
Synthesis CDE-ring system of the pectenotoxins via singlet oxygen [52]	Methylene blue	Singlet oxygen-mediated cascade reaction sequence creates the complete DE ring system

5 Detection of singlet oxygen

Indirect detection

Various techniques have been developed for the detection of singlet oxygen. Although the direct detection of near-infrared (NIR) luminescence near 1270 nm remains the most desired method for identifying $O_2(a_1\Delta g)$, it is technically challenging [53]. That's why, for the detection of singlet oxygen, indirect methods are more commonly used on a daily basis. They are usually based on the chemical reaction of $^1O_2$ with a specific trap causing an observable change in the absorption spectrum, fluorescence spectrum, or EPR spectrum [54,55]. Different commercially available traps can be used for the indirect detection of $O_2(a_1\Delta g)$. The most popular traps are: 2,2,6,6-tetramethylpiperidine (TEMP), 1,3-diphenylisobenzofuran (DPBF), Singlet Oxygen Sensor Green (SOSG), 9,10-dimethylanthracene, Tetracene or Rubrene (**Table 2**) [56].

Table 2. The most common traps for singlet oxygen detection.

Name	Structure	Comments
2,2,6,6-tetramethylpiperidine (TEMP)		The product of the reaction of $^1O_2$ with TEMP, i.e. TEMPO, exhibits an EPR spectrum consisting of three characteristic equally intense lines. Limitations: high cost, complicated operation
Singlet Oxygen Sensor Green (SOSG)	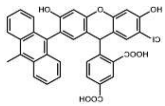	The SOSG working principle is based on luminescence, i.e. SOSG emits green fluorescence (excitation/emission maximum at ca. 504/525 nm) in the presence of singlet oxygen. These sensors are commonly used to monitor the singlet oxygen generation, e.g. photosynthetic organisms or medical applications. Limitations: high cost, limited range of detection systems, acts as photosensitiser itself.
1,3-diphenylisobenzofuran (DPBF)	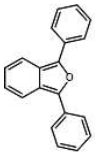	It is monitored with UV-Vis spectroscopy. DPBF has the absorption maximum in the region at ca. 410 nm. When oxidised with singlet oxygen, it forms a peroxide with no absorption bands in the Vis region. Limitations: also reacts with $O_2^{\bullet-}$, low photostability under illumination < 500 nm.
9,10-dimethylanthracene (DMA)	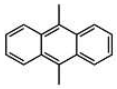	It is monitored with UV-Vis spectroscopy. DMA has an absorption maximum at ca. 380 nm. Limitations: also reacts with $O_2^{\bullet-}$, low photostability
Tetracene	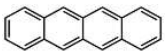	Monitored with UV-Vis spectroscopy. The tetracene absorption maximum is at ca. 474 nm Limitations: also reacts with $O_2^{\bullet-}$, low photostability
Rubrene		Monitored with UV-Vis spectroscopy. The rubrene absorption maximum is at ca. 525 nm, Limitations: also reacts with $O_2^{\bullet-}$, low photostability
2,5-diphenylfuran		They were monitored with UV-Vis spectroscopy. The 2,5-diphenylfuran absorption maximum is at ca. 370 nm. Limitations: also reacts with $O_2^{\bullet-}$, low photostability

Direct detection

The radiative relaxation pathway from the singlet excited state to the ground state, i.e. $^1\Delta_g \rightarrow X^3\Sigma_g$-, results in the fluorescent peak observed at the near-infrared region, around 1270 nm [57]. Nonetheless, as it was mentioned before, the characteristic features of singlet oxygen molecule, such as short lifetime (ns), high reactivity, as well as low emission probability (approx. 10^{-7}), make the direct photoluminescence detection methods very complicated and complex [57-62]. However, in the last years, the technique of the direct detection of $^1O_2$ has been widely developed to increase its

154 sensitivity and accessibility. One of the first groups reporting the indirect detection of $^1O_2$ was the
155 group of Ogilby. In their work, the NIR-sensitive InGaAs linear array detector combined with the
156 optical microscope was used during the heterogeneous experiment with the porphyrin derivative
157 present in the toluene/water mixture. The characteristic signals assigned to singlet oxygen were
158 observed only in the organic phase containing the photosensitiser. The spatial resolution of 2.5
159 um/pixel was reported [63]. InGaAs detectors stand out with a good photon detection efficiency and
160 large active areas. The consecutive modification introduced by Hu et al. based on the cooling of the
161 NIR InGaAs camera and adding two bandpass filters resulted in an improved signal-to-noise ratio
162 [64].

163 Another group of commonly used detectors are photomultiplier tubes (PMTs). Their main
164 disadvantages are low quantum efficiency, sensitive photocathode and moderate noises. However,
165 unlike InGaAs detectors, they can be used in time-resolved experiments [58,59]. Bregnhøj and Ogilby
166 used the described PMTs detector in the time-resolved luminescence traces of $^1O_2$ in the variety of
167 neat, sensitiser-free solvents. The presented results confirm that it is possible to directly excite the
168 ground state molecular oxygen, which is a broader perspective that may lead to the degradation of
169 the $^1O_2$-sensitive materials [66].

170 The direct time-resolved experiments are of high importance, especially for the biological and
171 medical applications, since they allow optimising the PDT processes. Moreover, real-time
172 measurement can be used to investigate the reactivity of $^1O_2$ and its interaction with other species
173 present in the biological environment [59, 66]. This issue was undertaken by Röder et al., and in their
174 work, the time-resolved fluorescence was used to monitor the oxygen saturation during the PDT
175 therapy [59]. Similar studies were also reported by Yamamoto et al. [66] and Lee et al. [67]
176 Furthermore, thanks to applying the direct detection of singlet oxygen, the optimisation of such
177 conditions as oxygen saturation, blood flow, local photobleaching, concentration and distribution of
178 photosensitiser as well as the laser power can be corrected and adjusted directly during therapy, which
179 gives the best and fastest results in the fight against tumours [61,66].

180 Another strategy allowing for the direct monitoring of PDT's is the Singlet Oxygen Luminescence
181 Dosimetry technique, the so-called SOLD. Based on the same phenomena of radiative decay of
182 energy from excited singlet molecules to the ground state, the SOLD is used to monitor luminescence
183 signals around 1270 nm. Among those mentioned above, the InGaAs and PMT's detectors, the
184 superconducting nanowire single-photon detector (SNSPD) is commonly used. However, this
185 detector works at cryostatic temperatures, which means that its advantages are in opposition to its
186 size and cost [58, 60, 61].

187 The bulky sizes and unwieldiness of traditional detectors cause more interest in developing more
188 innovative and more convenient systems. One of these is proposed by Boso et al., and it's called
189 negative feedback avalanche diode (NFAD). The applied setup achieved a good detection efficiency
190 (approx. 25%) with low noise and high collection efficiency [58]. The modern approach brings us
191 also to modifications of well-known systems. In their work, Gemmell et al. presented a combined
192 system based on InGaAs with semiconductor-based single-photon avalanche diodes (SPAD) detector.
193 SPAD are brilliant instruments with high detection efficiency, lower noise, compact form factor, and
194 the possibility of being gated. However, only in the spectral range 400-1000 nm, which makes them
195 unusable for singlet oxygen testing (**Figure 4**) [58,60]. One of the most promising methods of singlet
196 oxygen detection, especially in medical applications, is bioimaging [68-71]. Lin et al. presented the
197 results of singlet oxygen luminescence imaging during photodynamic therapy focused on blood
198 vessels. This group optimised the optical imaging system, which allowed for direct imaging of singlet
199 oxygen. The PDT therapy was done using different concentrations of Rose Bengal as a photosensitiser
200 [57].

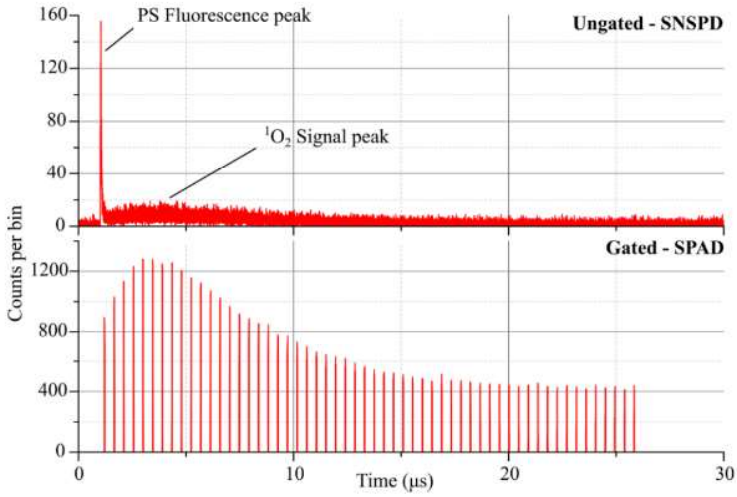

Figure 4. Difference in achieved luminescence signals of singlet oxygen between the gating in SPAD detector [60].

The significant issue is the determination of the photoluminescence quantum yield (Φ). By definition, the fluorescence quantum yield is the number of emitted photons relative to the number of absorbed photons. Other crucial properties of fluorophores are respective processes rate constants (κ) and corresponding emission lifetime (τ), which determine the time in which fluorescent molecule will interact with other, or relax [72,73]. For organic electronic devices such as organic light-emitting diodes (OLED) or organic photovoltaics (OPV), their general efficiency is based on fluorescence quantum yield but described as a relation between radiative and non-radiative rates [74]. As it was already mentioned, the photoluminescence quantum yield of singlet oxygen is extremely low, which demand the usage of highly sensitive detectors as described above. However, based on the fluorescence and time-resolved techniques, the photoluminescence quantum yield for singlet oxygen photogeneration can be determined in the simple indirect experiment, where the photosensitiser with a known Φ value can be used as a reference [75].

The direct method of quantum efficiency determination is by using the integrating sphere. The possibility of observing multiple reflections inside the sphere allows eliminating the noises from the environment and optical anisotropy. Furthermore, the specific behaviour of photons in the sphere also

220 provides for the most accurate and true quantum yield results. In their work, Hasebe et al. present the
221 instrumentation consisting of the integrating sphere, which can monitor the photoluminescence
222 quantum yield of singlet oxygen at emission 1270 nm and its lifetime. The absolute quantum yield of
223 the photosensitiser, here porphyrin in various solvents, can be calculated by knowing the ratio
224 between the absorbed amount of photons and the emission intensity of singlet oxygen radiative
225 relaxation process at around 1270 nm (**Figure 5**) [75].

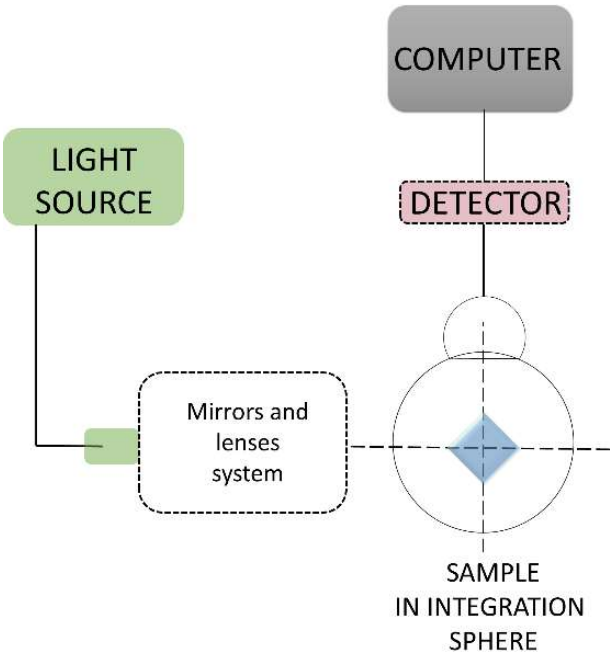

226

227 **Figure 5.** The scheme represents the simplified setup proposed by Hasebe et al. By combining two
228 multichannel optical detectors, the research group was able to measure absolute quantum yield [75].

229

230 Nonetheless, one of the most critical issues is the detailed understanding of the nature of radiation
231 and non-radiation transitions. Again, the high reactivity of oxygen with organic molecules causes a
232 high probability of relaxation through the non-radiative relaxation pathways (**Table 3**).

233

Table 3. Photophysical parameters measured for singlet oxygen photogeneration with porphyrin derivative as a PS for different solvents in a setup based on integration sphere constructed by Hasebe et al. Where the kr is the radiative and knr Is non-radiative rate constant.

Solvent	Quantum yield of singlet oxygen photogeneration $\Phi^{a1\Delta g}$	Absolute emission quantum yield $\Phi^{a1\Delta g}$	Radiative transition constant rate $k_r^{1\Delta}\ \left[\frac{1}{s}\right]$	Non-radiative transition constant rate $k_{nr}^{1\Delta}\ \left[\frac{1}{s}\right]$
Tetrachloromethane	1.00	8.1×10^{-3}	1.6	6.8×10^{1}
Benzene	0.98	3.2×10^{-5}	1.1	3.2×10^{4}
Benzene-d6	0.99	5.5×10^{-4}	0.9	1.6×10^{3}
Toluene	0.98	2.9×10^{-5}	0.93	3.2×10^{4}
Chloromethane	1.00	1.2×10^{-4}	0.69	5.8×10^{3}
Acetonitrile	0.98	2.2×10^{-5}	0.27	1.2×10^{4}
Acetonitrile-d3	0.96	4.6×10^{-4}	0.29	6.3×10^{2}
Ethanol	0.96	4.8×10^{-6}	0.32	6.6×10^{4}
EtOD	0.99	9.8×10^{-6}	0.30	3.1×10^{4}

6 Singlet oxygen and optoelectronic devices

Non-radiative pathways in organic devices

Organic electronics has been playing a significant role in our life for a few years now. The market for new technologies is highly receptive when it comes to innovative solutions that can potentially revolutionise certain areas of life. This new approach of developing the usability of devices based on organic compounds, such as smartphones and laptops displays, new types of sensors or lighting, causes more and more interest in this topic. The most common fields currently developing are organic light-emitting diodes (OLED), organic photovoltaics (OPV) and organic field-effect transistors (OFET) [76]. Their success on the market is mainly due to the possibility of producing flexible and lightweight devices characterised by an excellent potential for development and modification. The main drawback of organic optoelectronic devices is still low stability and not sufficient efficiency. Since the first discovery, there has been a constant struggle to obtain the most efficient and best organic systems for the applications mentioned above. For organic photovoltaics, the single-junction

solar cell maximum efficiency was described by The Shockley-Queisser limit, which is settled around 33.5% under AM1.5G illumination [77-80]. One of the most significant issues influencing the efficiency of organic optoelectronic devices is the energy loss directly bonded with the radiative and non-radiative relaxation pathways of excited organic molecules [81].

The efficiency of organic light-emitting diodes (OLEDs) depends directly on a photoluminescence quantum yield (Φ), and the maximum overall efficiency can be estimated based on photophysical analysis.

$$\boldsymbol{EQE = \eta_{out} \cdot \eta_{fl} \cdot \gamma \cdot \eta_{fr}} \qquad \textit{Equation 1.}$$

In a given equation, the $\boldsymbol{\eta_{out}}$ is the outcoupling factor. Usually, it is interpreted as a 20-30% maximum outcoupling efficiency. The $\boldsymbol{\eta_{fl}}$ is the photoluminescence quantum yield (PLQY, Φ). $\boldsymbol{\gamma}$ is so-called the charge balance factor, which usually is used as a 1. Considering that only 25% of singlet excitons are formed directly from charge recombination for fluorescence emitter, the $\boldsymbol{\eta_{fr}}$ parameter is accounted as 0.25, contributing to emission [82-84].

On the other hand, photoluminescence quantum yield (Φ) is the ratio of the number of emitted to the absorbed photons. It can be said that device EQE depends on both radiation and non-radiation electronic transitions as in the equation 2 [73,74]. Where the k_r stands for radiative transition constant rate, and k_{nr} non-radiative transition constant rate.

$$\boldsymbol{\Phi = \frac{emitted\ photons}{absorbed\ photons} = \frac{k_r}{k_r + k_{nr}}} \qquad \textit{Equation 2.}$$

However, the situation is not so clear and straightforward as it might seem. Non-radiative processes have a negative impact on the observed quantum efficiency and, consequently, the performance of the tested OLED devices. The non-radiative process is problematic not only on emissive devices but generally whenever the excitons are formed. In OPV, where solar light is forming the excitons within Bulk-Heterojunction (BHJ) layer, we can estimate the exciton lifetime by knowing the k_r and k_{nr} values. Generally, there are three types of relaxation which can cause energy losses [74,80]:

1. Radiative loss above bandgap/energy gap
2. Radiative loss below bandgap/energy gap
3. Non-radiative loss

The non-radiative energy losses may be correlated with vibration-induced quenching, concentration quenching, other energy transfers, and the most important, from our point of view, oxygen quenching [85]. Knowing all of this information, to correctly predict and measure the quantum yield, we need to understand this complicated phenomenon and its possible interaction and relaxation processes. Additional difficulties are caused by the fact that we cannot study this type of transition with any spectroscopic method due to their non-emissive nature [74]. One way to increase the efficiency of electronic devices based on organic compounds can be done by reducing or even eliminating the non-radiative transitions [81]. Due to the inability to observe non-radiation transitions, mathematical models allow calculating the possibility of this type of relaxations [9, 86, 87].

Influence of the k_r and k_{nr} ratio

We must understand all processes involved in exciton formation and singlet/triplet states to create new efficient OLED or OPV materials. Many reports describe the k_r and k_{nr} decay rate constant analysis and the influence of non-radiative relaxation processes in organic electronics [88-92]. One of the main reasons affecting the contribution of non-radiative transitions is the isomerisation of the molecule's structure. Li et al. draw attention to this phenomenon in materials for photovoltaic applications. In their work, the presented symmetrical (Y6) and asymmetrical (BTP-S1, BTP-S2) Acceptor-Donor-Acceptor (ADA) type of structures were characterised. This study showed that symmetrical molecule Y6 had worse results than the asymmetrical compounds due to the increase of the contribution of the non-radiative decay process. However, the comparison between the asymmetrical derivatives revealed that the molecule S2 decreased the non-radiative decay process compared to S1 by simply changing the chlorine to fluorine group (**Figure 6**) [80].

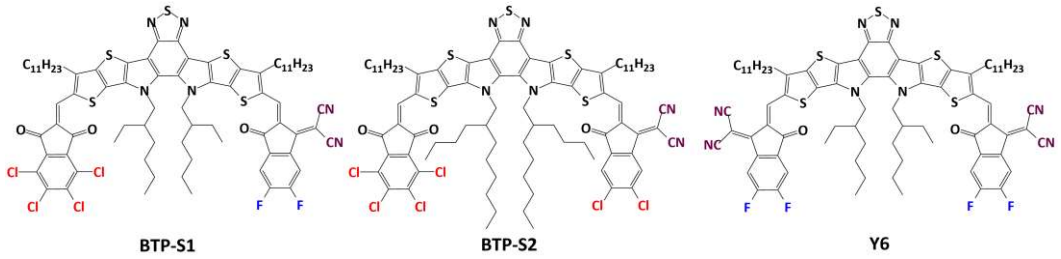

Figure 6. Structures of photoactive molecules synthesized by Li group [80].

A specific type of new generation of organic emitters exhibiting a thermally activated delayed fluorescence (TADF) process was developed. In TADF emitters, the transfer of excess energy from the emitter to the oxygen is considered a direct competition with delayed fluorescence. In delayed fluorescence, the energy should return to the singlet excited state by the reverse intersystem crossing (rISC) but is transferred to the oxygen molecule, thus inducing the formation of a reactive oxygen species - singlet form. A logical conclusion could be stated that limiting the transfer of energy to other molecules, e.g. oxygen, will increase the efficiency of the proposed emitters and, consequently, devices. Hall et al. report synthesis of novel TADF emitter called Mes_3DiKTa, and compared to the basic compound DiKTa increased EQE by about 50%. It was caused mainly by reducing the aggregation-induced quenching process. As the authors claim, slowing down the non-radiative processes can be correlated with stiffening the molecule's skeleton, which is related to weak coupling between the electronic excitations and the nuclei vibrations [6].

Similar studies were done by Serevičius et al., where they synthesised the donor-acceptor systems based on phenoxazine-pyrimidine structure. Two of four developed molecules are characterised by rapid non-radiative relaxation. The authors report a comparison of molecules with and without the methyl groups. Conclusions were those methyl units in *meta* position lower the non-radiative relaxation by ~17%, and the *ortho* substitution causes the increase of the non-radiative decay process. The researchers stated that the most significant influence had a molecule's rigidity, leading to higher quantum yield [93].

Considering the information included above, we can state that the structure of the molecule, its symmetry and flexibility, even slight differences in the position of substituent can have a significant effect on the ratio of radiative to non-radiative transitions in photoactive molecules. It's important to understand these phenomena by the scientific community involved in the study of photoactive compounds. Subtle changes in the structure of a compound can cause significant changes in emission efficiency. However, not only the organic emitters should be the main interest. Compounds used as hosts play an important role in the emission from the emitter and the OLED device efficiency. Abroshan et al. point out that OLED technology's critical issue is the interaction between the hosts and emitters. Hosts can highly influence the excited state relaxation transitions, both the radiative as well as non-radiative. Researchers presented how host CBP affects the radical emitter TTM-3NCz compared to the isolated emitter in the performed experiment. The results showed that the host-emitter system had around 30% smaller reorganisation energy than the geometrically optimised, isolated emitter. Authors assume that the host matrix binds the vibrations of the radical molecules by which the vibrational coupling and dynamic disorder are decreased [9].

In the prof. Lakowicz book - *Principles of Fluorescence Spectroscopy* is an example, based on Nad's and Pal's work, concerning the coumarin-151, where the nonpolar solvent causes the rotation of the amino group and leads to fast decay to the ground state. However, in the opposite situation, in the polar solvent, the rotation of the substituent is blocked due to the creation of an internal charge transfer state (ICT), and in consequence, by decreasing the non-radiative relaxation - increase the quantum yield. Therefore, the solvent effect on the non-radiative decay has a significant impact on quantum efficiency. Hence, the radiative decay and excitation coefficient seem insensitive to the polarity (**Table 4**) [73, 94].

Table 4. Set of photophysical properties of coumarin 151 depending on the used solvent.

Solvent	Fluorescence quantum yield Φ_f	Average fluorescence lifetime τ_f [ns]	Radiative transition constant rate $k_r^{1\Delta}$ $\left[\mathbf{x\ 10^7\ \frac{1}{s}}\right]$	Non-radiative transition constant rate $k_{nr}^{1\Delta}$ $\left[\mathbf{x\ 10^7\ \frac{1}{s}}\right]$
Hexane	0.19	0.68 (74), 1.35 (26) *	22.24	94.82
Cyclohexane	0.28	0.93 (60), 1.60 (40) *	23.37	61.72
Decalin	0.32	1.34 (35), 2.2 (65) *	16.85	35.81
1.4-dioxane	0.71	4.65	15.27	6.23
Ethyl acetate	0.62	4.67	13.27	8.14
Octanol	0.63	0.63	10.66	7.85
Hexanol	0.54	5.40	10.20	8.70
Butanol	0.48	5.24	9.16	9.92
DMSO	0.48	5.00	9.60	10.40
DMF	0.49	5.22	9.40	9.10
Isopropanol	0.52	5.28	9.84	9.10
Acetone	0.59	4.97	11. 87	8.25
Ethanol	0.49	5.38	9.10	9.48
Acetonitrile	0.57	5.13	11.11	8.38
Methanol	0.37	5.31	6.97	11.86

* for the short and long-lifetime component, the percentage contribution is presented in brackets.

Oxygen as an optoelectronics quencher

One of the most essential, critical phenomena correlated with non-radiative and radiative relaxation processes in optoelectronic devices is the side effect of singlet oxygen photogeneration. The excited molecule can act as a photosensitiser and, by Dexter energy transfer, pass it on to the oxygen ground state molecule (**Figure 7**) [59]. Oxygen sensitivity in organic electronics is a common problem and struggle with which the scientist has to deal. However, singlet oxygen photogeneration, which is considered an undesirable side effect in some circumstances, becomes a great advantage, e.g., *fine chemical* synthesis or medicine. The problem is not only that the transfer of energy to the oxygen molecule, i.e. one of the non-radiative processes, affects the efficiency of the designed and built devices, but also due to its extremely oxidising properties, singlet oxygen can have a destructive effect on organic materials used in these devices [95-99].

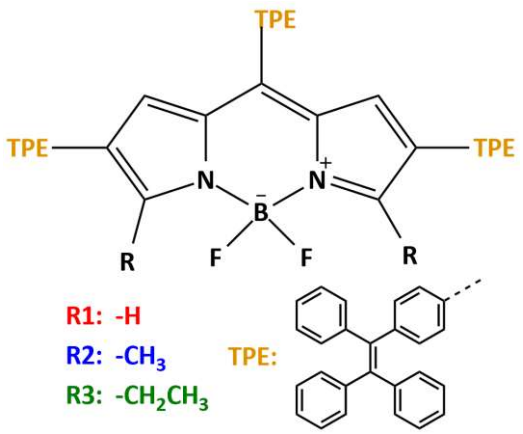

Figure 7. Scheme of BODIPY - based molecules presented by Scherf et al. By introducing into the BODYPI core, the TPE unit, researchers were able to overcome the Aggregation-Caused Quenching issue.

Organic photovoltaics

Organic photovoltaic development is focused mainly on conjugated polymers. Still, the significant impact on the development of organic solar cells was thanks to fullerene organic derivatives, which boosted device efficiency. The main advantage of fullerene is accepting and transferring the electrons, thanks to the cage-like structure. However, fullerenes' ability to absorb the light is somewhat limited to the UV region and slightly to the visible part of the spectra (below 400 nm), depending on the application's pros and cons. From a materials tailoring point of view, the advantage is modifying the structure using organic synthesis, both on the surface and inside the so-called "cage". The processing of organic compounds is an important factor, and fullerene solubility is limited in polar and aqueous solutions. Thus structure modification is also the way to influence their solubility. Thanks to its properties, fullerene derivatives gained interest in many fields of science such as industry, medicine and, most importantly, thanks to its photoactive properties in OPV technology. Its ability to photogenerate singlet oxygen is mainly owed due to stable and long-lived lowest triplet state (T_1) [8, 100 - 104]. However, the stability of such materials in ambient conditions leave much to be desired

[105], mainly because of the high sensitivity of fullerenes to oxygen in the air, which was proved by multiple reports [106, 107].

Bregnhøj et al. evaluated the possible singlet oxygen photogeneration and influence photophysical and photochemical results of molecules commonly used as an organic photovoltaic component. The work focuses on device degradation due to singlet oxygen. The tested fullerenes, both the $PCBM_{60}$ and $PCBM_{70}$, exhibit excellent potential for singlet oxygen photogeneration, and the quantum yield is very high, especially for $PCBM_{70}$. The polymers usually used as an OPV component showed the ability to produce $^1O_2$ with a good quantum yield. The time-resolved phosphorescence signals of singlet oxygen were recorded for the neat and blended film for both investigated fullerene, resulting in the decrease of the device's efficiency (**Table 5**) [3].

Table 5. Quantum yield of singlet oxygen production by fullerene and polymer materials often used as OPV compounds. The subphtalocyianine is used as a comparison.

Compound	Quantum yield of singlet oxygen photogeneration $\Phi^{a1\Delta g}$	
	Air	O2
PCBM60	0.65 ± 0.04	0.68 ± 0.04
PCBM70	0.90 ± 0.05	0.91 ± 0.05
P3HT	0.34 ± 0.04	0.40 ± 0.04
PTB7	0.24 ± 0.03	0.29 ± 0.03
SubPc	0.78 ± 0.06	0.88 ± 0.06

Lüer's research group investigated this problem, where the P3HT:PCBM and Si-PCPDTBT:PCBM system were tested over the photo-degradation process induced by oxygen. For both polymers, the degradation level was significant. However, the P3HT containing system showed a substantial reduction of the charge recombination coefficient. In consequence, it influenced the charge carrier mobility [4].

399 Another approach is presented by Soon et al., where the comparison between the stability of two
400 donor polymers was performed. Both the investigated PTB7 and DPP-TT-T have known donor
401 polymers often used as a blended film with fullerenes during the preparation of organic photovoltaic
402 devices. They are considering the exciton energies of investigated polymers and oxygen's singlet
403 energy of approx. 0.98 eV, it seems to be predictable that PTB7 has the potential to photogenerated
404 singlet oxygen, contrary to DPP-TT-T. Results discussed by the authors indicate that blended films
405 with PC71BM did not exhibit sensitivity to oxygen. However, both polymers demonstrated good
406 charge separation, which may lead to triplet state formation. Another interesting problem discussed
407 by researchers in the photodegradation of prepared films. As it was shown, the neat and blended films
408 containing PTB7 shows a high degradation rate with time. Together with the fluorescence outcome,
409 these results indicate that photogeneration of singlet oxygen by the photovoltaic device based on
410 fullerene and PTB7 is possible. Furthermore, it can cause irreversible degradation of the OPV system
411 [5]. In their follow-up work, Soon et al. highlighted that the crystallinity of polymeric materials used
412 in photovoltaic systems plays a crucial role in triplet states' lifetime and oxygen quenching efficiency
413 in investigated polymers. This issue should be considered when encapsulation as a method of
414 prevention of oxygen degradation is considered [108]. These examples lead to the statement that the
415 fullerene-based devices and systems, mainly used in organic photovoltaics, could be considered
416 efficient singlet oxygen photogenerators.

417 Characteristic, and unique types of OPV devices, are the dye-sensitised solar cells [109,110]. The
418 main component of such structures is the well-known group of singlet oxygen photosensitisers -
419 aromatics and dyes, in which we can particularly distinguish compounds such as porphyrins,
420 phenothiazines etc. For example, in the Qian et al. work, phenothiazine contained porphyrin
421 derivatives are studied to use as a component in dye-sensitised solar cells (DSSC) [111]. A similar
422 idea, where porphyrin derivatives for dye-sensitised solar cells were implemented by Grätzel and
423 Yella et al., presented a comprehensive overview on photovoltaic properties of synthesised

compounds [112, 113]. The importance of this field of science is confirmed by the fact that there are many reports on dye-sensitised solar cells [110. 114 - 116].

Another specific group of organic compounds that play an increasingly important role in organic electronics is boron-dipyrromethene derivatives (BODIPY). BODIPY organic structure is based on a dipyrromethene unit with boron difluoride attached in the centre. Since its discovery, the boron-based group of dyes has become the focus of interest in various fields related to photoactive compounds. They stand out with strong fluorescence signals and photostability. BODYPI's are also characterised by high absorption coefficient and narrow absorption and emission bands. Moreover, their chemical structure makes it easy to modify and influence both the chemical and physical properties of the derivatives obtained. This is because their versatility and the multitude of applications for which they are used is so large. Nonetheless, the promising properties showed by BODIPY molecules are balanced with small Stokes shifts and the tendency to aggregation and thus to quenching. These problems may be overcome by chemical tuning of the structure [68, 117 - 121].

The BODIPY molecule is willingly used as a core for developing new derivatives worth using in organic solar cells [119, 122 - 124]. One of such systems was proposed by Bucher et al. The A-π-D structured copolymers, based on BODIPY core and thiophene as well as porphyrin units (P(BdP-DEHT) and P(BdP/ Por-DEHT) respectively) were proposed as an element of the organic photovoltaic device. Thanks to incorporating the porphyrin unit into the polymer chain, the authors were able to increase the short-circuit current density (J_{sc}) while the open-circuit voltage (V_{oc}) wasn't affected. The investigation of the OPV devices revealed promising results. The power conversion efficiency (PCE) was relatively high for BODIPY-based devices [125].

The properly designed BODIPY derivatives may be excellent photosensitisers able to photogenerate singlet oxygen with high efficiency. This issue was highlighted by Ivaniuk et al. in their work, where they investigate the 1,7 – diphenyl-substituted derivatives based on BODIPY core. Presented molecules were examined over the OPV as well as OLED potential applications. The authors point out that the low-lying triplet excited state (T_1), around 1 eV, and known photostable properties of the

450 BODYPI molecules may cause the energy transfer from the excited molecule to oxygen by the non-
451 radiative process photogenerate the $^1O_2$ [126]. This conclusion is confirmed by a multitude of articles
452 presenting the topic of photosensitising properties of BODIPY, also in PDT and medical applications
453 [68, 127 - 132]. Enhancing the photosensitising abilities of discussed dyes may be achieved by
454 introducing to the molecule the heavy halogens (e.g. bromine, iodine). Thanks to that, by increasing
455 the contribution of triplet states in the processes, the quantum yield of photogeneration is also higher.
456 Similar conclusions were stated by Radunz et al. in publication on the pH-activable BODIPY
457 derivative for photodynamic therapy and Bioimaging. The authors present the pH-sensitive molecules
458 based on the BODIPY core used as photosensitisers during photodynamic therapy, exhibiting
459 efficient photogeneration of the singlet oxygen. This original concept worked thanks to the
460 incorporation of iodine units into pH-switchable fluorescent precursors [71].

461

462 **Organic Light-Emitting Diodes**

463 The most known singlet oxygen photosensitisers are organic dyes, phenothiazines such as methylene
464 blue, azure a or toluidine blue. A dozen groups of organic derivatives are widely described in
465 literature among their tremendous potential to singlet oxygen photogeneration, such as porphyrins,
466 phthalocyanines, xanthenes, etc. A lot of these derivatives were investigated and applied for medical
467 purposes. However, their photoactive properties let them be used in different applications such as
468 optoelectronics [1, 12]. Phenothiazine, with its uncommon optical and electronical properties, can act
469 as a hole transport layer but also as an efficient emitter. The combination of phenothiazine- porphyrin
470 molecule can cause an interesting system, where the exciton energy may be transferred to the
471 porphyrin ring. In an article presented by Qiu et al., two porphyrin-core molecules attached in *meso*-
472 position phenothiazines were synthesised. The fluorescence measurements revealed that both
473 synthesised molecules had a relatively high photoluminescence quantum yield around 0.40 in solution
474 and 0.35 in a thin film, promoting them as a potentially good red-light emitter [133]. Shahroosvand
475 et al. study propose the β-substituted zinc-porphyrin (ZnTCPP) with halogen atoms, where they could

476 enhance the Soret and Q-bands of the porphyrin derivative. Such change was possible by the
477 intensification of the splitting between the key filled and empty frontier orbitals. Synthesised
478 derivatives were successfully applied as an emitters in white-light emitting diode [134].

479 The previously mentioned in the OPV-related chapter, the BODIPY-based molecules are, among
480 others, often used as emitters for OLED applications [135, 136]. One of the most promising methods
481 to use the BODIPY as an emitter molecule in organic light-emitting diodes is turning its weakness
482 into an advantage. Through enhancing the aggregation tendency by tuning the chemical structure of
483 the BODIPY molecule, the researchers can develop the OLED emitters possessing Aggregation-
484 Induced Emission (AIE) [118]. A similar point of view had a research team under the lead of Ullrich
485 Scherf. They achieved that by incorporating into the BODIPY core, the tetraphenylethylene (TPE)
486 unit (**Figure 7**).

487 This operation should overcome the Aggregation-Caused Quenching (ACQ), which led to the
488 construction of the working, emissive device. What is worth to mention, the participation of the non-
489 radiative transition is relatively high in the neat films of presented BODIPY derivatives. The first
490 thing that comes to mind is that the AIE behaviour has not been amplified enough and, the k_{nr} is
491 mainly caused by aggregation quenching. However, we can't forget that the non-radiative processes
492 can be related to different issues (**Table 6**) [117].

493

494 **Table 6.** Fluorescence quantum yields and calculated values of k_r and k_{nr} of neat films and 0.1 and 1
495 w/w% 3TPEBDP1:F8BT blends.

Layer	Fluorescence quantum yield Φ_f	decay lifetime τ [ns]	Radiative transition constant rate $k_r^{1\Delta}$ $\left[\frac{1}{ns}\right]$	Non-radiative transition constant rate $k_{nr}^{1\Delta}$ $\left[\frac{1}{ns}\right]$
neat 3TPEBDP1	10	0.68	0.15	1.33
1 % 3TPEBDP1	47	2.7	0.17	0.20
neat 3TPEBDP2	39	1.01	0.39	0.60
1 % 3TPEBDP2	96	4.29	0.22	0.01
neat 3TPEBDP3	48	1.34	0.36	0.38
1 % 3TPEBDP3	100	4.56	0.22	0

In recent work, Ni et al. draw the reader's attention to the problem of sensitivity of the triplet state (T_1) of TADF molecules to ground-state oxygen. Luminescence imaging seems to be challenging for luminophores, considering the previous statement. Luminophores which can be applied in time-resolved luminescence imaging (TRLI), needs to have a long lifetime of the excited state (τ>10 ns). Therefore, it is necessary to distinguish their signals from the background, and one of the best choices is to apply the TADF molecules, which have long emission lifetimes. However, the phenomena of the TADF mechanism is based on the small energy gap between the singlet (S_1) and triplet (T_1) state and the molecule's excited state ability to perform the reverse intersystem crossing (rISC). The most sensitive issue here is the vulnerability of the excited triplet state to the oxygen environment. The excessive energy from the photoactive molecule can be transferred from the T_1 state to the ground state oxygen to produce singlet oxygen, which process is considered as a non-radiative transfer. One idea that can prevent energy transfer to an oxygen molecule is to use TADF molecules as phosphors in the TRLI, which tend to be aggregation-induced fluorescence. The aggregation process can perform as a shield, protecting the T_1 state [72].

One of the most important reports of last years, devoted to the non-radiative oxygen quenching, was published by the Adachi research group. The authors pointed out the need to research and determine non-radiative pathways during the evaluation of luminescent molecules, potentially useful emitters for OLED devices. Whereas in the case of traditional systems used in OLEDs, the balance between kr and knr seems relatively simple, but in the case of TADF compounds, we must also remember the delay in luminescence, which is the result of reverse intersystem crossing (rISC). We can define it in our divagation as k_{rISC}. Consequently, the non-radiative transition constant calculation requires us to distinguish the total quantum efficiency of luminescence from the prompt and delayed fluorescence. By monitoring changes in the photoluminescence decays observed in different conditions, the authors analysed the possibility of oxygen-induced quenching by widely known and discussed TADF type compounds. The detailed results could be stated that the singlet oxygen photogeneration process can be undoubtedly classified as a non-radiative process. Moreover, the molecules designed to perform good emitting properties such as TADF may have significant liability to photogenerate singlet oxygen (**Figure 8**) [85].

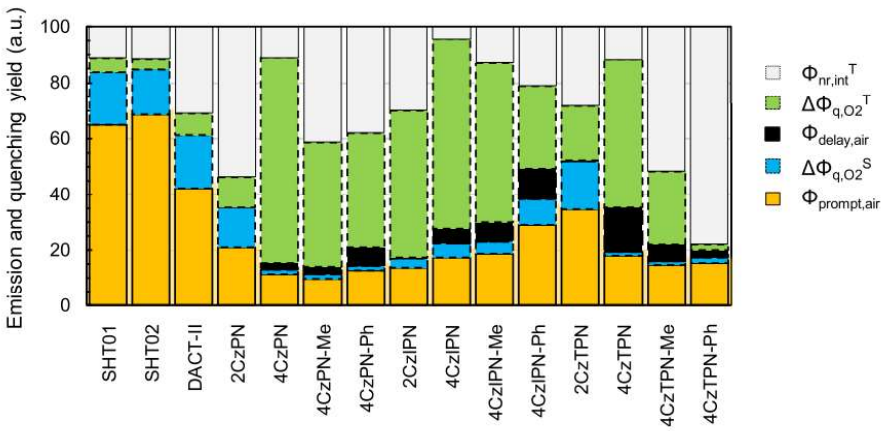

Figure 8. Graph showing the contribution of deactivation processes from excited singlet and triplet states [85], where:

$\Phi_{nr,\,int}^{T}$ - internal nonradiative deactivation pathways,

$\Delta\Phi_{q,\,O2}^{T}$ – PLQY triplet quenching,

$\Phi_{delay,\,air}$ - PLQY of delayed component,

532 $\Delta\Phi_{q,\,O2}^{S}$- PLQY singlet quenching,

533 $\Phi_{prompt,\,air}$ – PLQY of prompt component.

534

535 An interesting topic related to optoelectronic devices is OLED based sensors. Shinar et al. published
536 several materials based on an organic light-emitting platform able to sense oxygen. As a sensing
537 agent, the porphyrin derivatives such as Pt- or Pd-octaethylporphyrin (PtOEP or PdOEP) were
538 chosen. The principle of work of these sensors is relatively simple, porphyrin derivatives with a strong
539 red luminescence, when coming into contact with an oxygen molecule, are quenched. The oxygen
540 concentration can be correlated with those values by the Stern-Volmer equation (**Figure 9**) [137 -
541 139].

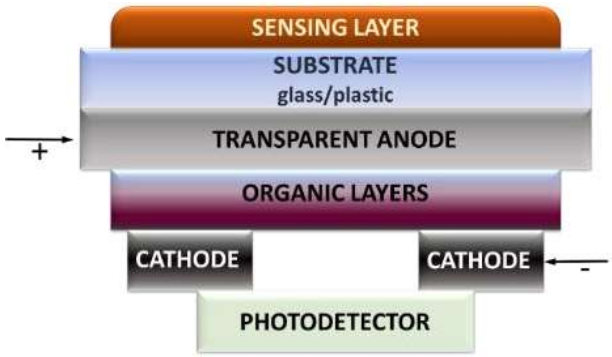

542

543 **Figure 9.** Structure of OLED-based sensor proposed by Shinar et al. [139].

544

545 The possibilities of synthesising a tremendous amount of photoactive organic and conjugated
546 molecules are limited only by the common sense of the synthetics and the requirements of the field
547 in which they are planned to be implemented. For this reason, it has to emphasise that the
548 understanding of the mechanisms behind the processes of both radiation transitions (used in OLED,
549 OPV, etc.) and, more challenging, the identification of the non-radiation transitions, including singlet
550 oxygen photogeneration, are remarkably important. One of such molecules is a perylene diimide
551 (PDI), which derivatives are often applied in non-fullerene organic photovoltaics [140 - 142], but also

in OLED devices [143 - 145]. Their molecular structure makes the PDI's very rigid. The unique π-conjugation lead to high charge-carrier mobility.

Moreover, the perylene diimides are characterised by thermal and photochemical stability, outstanding fluorescence efficiency, and self-assembly predisposition [146]. However, their properties also make them extraordinary candidates as photosensitisers in singlet oxygen photogeneration [147]. In their article, Aksakal et al. present the elaborate molecule based on a ruthenium(II) phenantrolene and bis(perylene diimide), which was able to photogenerate the $^1O_2$ with a good quantum yield of 0.30 [6].

Similar work on PID derivatives was presented by Ledwoń et al., showing the predisposition to photogenerate singlet oxygen with good efficiency [148]. Another interesting example is the work presented by Huang et al. concerned about porous organic cages (POCs) build by rylene-based units (**Figure 10**).

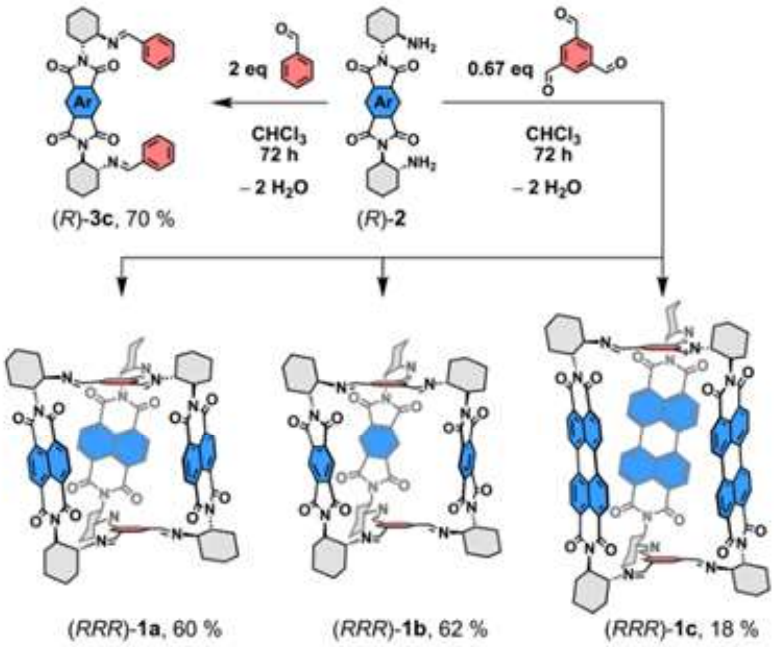

Figure 10. Schematic representation of POCs build based on rylene molecules [149].

POCs, due to their similarity to covalent organic frameworks, were designed and synthesised with a view of applications such as gas sorption and separation, molecular sieving, sensing, catalysis or ion transportation. POCs are also very efficient photosensitisers in the photogeneration of the singlet oxygen process. The research team draws our attention to the optoelectronic properties presented by them POCs are exhibiting. The presented rylene-based cage showed bright photoluminescence with good quantum yield [149, 150].

7 Conclusions

Singlet oxygen phenomena lie at the borders of modern knowledge in chemistry, physics and, biology. Over the entire period of study, several breakthroughs have been outlined and discovered. However, the vastness and mass use of this state of oxygen is precisely the point thanks to which science and technology will be able to make the necessary leap into the future: to see how cancer tumours will behave under different concentrations and impulses of singlet oxygen, to cope with the problem of wastewater treatment, which hangs over humanity every year more and more, and remember about various skin problems that have more impact on society than it usually seems. Singlet oxygen is precisely a physical phenomenon, but its impact can be visible in chemical processes in production and the control of cell proliferation, apoptosis, and necrosis. The singlet oxygen in an development of new materials for organic electronics on one side is a moiety which we would like to exclude in our working devices but on the other hand we could use this moiety for sensing or as the phenomena for photophysical analysis of the process kinetics. The authors of this review described only the most popular and recent applications of this phenomenon, while the reader is invited to be inspired and plunge into this "pandora's box".

Conflicts of interests

There are no conflicts of interest to declare.

Acknowledgments

A.N. I.G. & P.D. acknowledge the support received from the First Team program of the Foundation for Polish Science co-financed by the European Union under the European Regional Development Fund (project number: First TEAM POIR.04.04.00-00-4668/17-00). Publication supported under Rector's pro-quality grants. The Silesian University of Technology, no. 14/990/RGJ21/0154. ABG is grateful for the financial support from the Silesian University of Technology, Poland, under grant no. 04/040/BKM21/0171. The authors are thankful for the training actions funded by the European Union's Horizon 2020 research and innovation program under grant agreement No 952008. A.N. acknowledge the support received from the research project No. 2020/37/N/ST4/02435 financed by the National Science Centre. Authors acknowledge the supporting actions from EU's Horizon 2020 ERA-Chair project ExCEED, grant agreement No 952008.

8 References

[1] R.J. Crutchley, M.C. DeRosa, Photosensitized singlet oxygen and its applications, Coord. Chem. Rev. 233–234 (2002) 351–371. https://doi.org/10.1016/S0010-8545(02)00034-6.

[2] P.R. Ogilby, Singlet oxygen: there is indeed something new under the sun, Chem. Soc. Rev. 39 (2010) 3181–3209. https://doi.org/10.1039/B926014P

[3] M. Bregnhøj, M. Prete, V. Turkovic, A. Ugleholdt Petersen, N. Brøndsted Mogens, M. Madsen, P.R. Ogilby, Oxygen-dependent photophysics and photochemistry of prototypical compounds for organic photovoltaics: inhibiting degradation initiated by singlet oxygen at a molecular level, Methods Appl. Fluoresc. 8 (2020) 014001. https://doi.org/10.1088/2050-6120/ab4edc.

[4] S. Karuthedath, T. Sauermann, H.J. Egelhaaf, R. Wannemacher, C.J. Brabec, L. Lüer, The effect of oxygen induced degradation on charge carrier dynamics in P3HT:PCBM and Si-PCPDTBT:PCBM thin films and solar cells, J. Mater. Chem. A 3 (2015) 3399–3408. https://doi.org/10.1039/C4TA06719C

[5] Y.W. Soon, H. Cho, J. Low, H. Bronstein, I. McCulloch, J. R. Durrant, Correlating triplet yield, singlet oxygen generation and photochemical stability in polymer/fullerene blend films, Chem. Commun. 49 (2013) 1291–1293. https://doi.org/10.1039/C2CC38243A.

[6] D. Hall, S.M. Suresh, P.L. dos Santos, E. Duda, S. Bagnich, A. Pershin, P. Rajamalli, D.B. Cordes, A.M.Z. Slawin, D. Beljonne, A. Köhler, I.D.W. Samuel, Y. Olivier, E. Zysman-Colman, Improving Processability and Efficiency of Resonant TADF Emitters: A Design Strategy, Adv. Opt. Mater. 8 (2020) 1902627. https://doi.org/10.1002/adom.201901627.

[7] A.A. Sebak, I.E.O. Gomaa, A.N. El Meshad, M.H. Abdel Kader, Targeted photodynamic-induced singlet oxygen production by peptide-conjugated biodegradable nanoparticles for treatment of skin melanoma, Photodiagnosis Photodyn. Ther. 23 (2018) 181–189. https://doi.org/10.1016/j.pdpdt.2018.05.017.

[8] S. Wang, R. Gao, F. Zhou, M. Selke, Nanomaterials and singlet oxygen photosensitizers:

630 potential applications in photodynamic therapy, J. Mater. Chem. 14 (2004) 487–493.
631 https://doi.org/10.1039/B311429E.
632 [9] H. Abroshan, V. Coropceanu, J. L. Brédas, Thermally Activated Delayed Fluorescence
633 Sensitization for Highly Efficient Blue Fluorescent Emitters, Adv. Funct. Mater. 30 (2020)
634 1–10. https://doi.org/10.1002/adfm.202005898.
635 [10] A. Dimofte, T.C. Zhu, S.M. Hahn, R.A. Lustig, In vivo light dosimetry for motexafin
636 lutetium-mediated PDT of recurrent breast cancer, Lasers Surg. Med. 31 (2002) 305–312.
637 https://doi.org/10.1002/lsm.10115.
638 [11] G. Herzberg, S. Mrozowski, Molecular Spectra and Molecular Structure. I. Spectra of
639 Diatomic Molecules, Am. J. Phys. 19 (1951) 390–391. https://doi.org/10.1119/1.1932852.
640 [12] E.L. Clennan, New Mechanistic and Synthetic Aspects of Singlet Oxygen Chemistry,
641 Tetrahedron 56 (2000) 9151–9179. https://doi.org/10.1016/S0040-4020(00)00794-8.
642 [13] H.C. Miller, J.E. McCord, J. Choy, G.D. Hager, Measurement of the radiative lifetime of
643 $O_2(a^1\Delta_g)$ using cavity ring down spectroscopy, J. Quant. Spectrosc. Radiat. Transf. 69
644 (2001) 305–325. https://doi.org/10.1016/S0022-4073(00)00086-8.
645 [14] C. Schweitzer, R. Schmidt, Physical Mechanisms of Generation and Deactivation of Singlet
646 Oxygen, Chem. Rev. 103 (2007) 1685–1758. https://doi.org/10.1021/cr010371d.
647 [15] N. Gandra, A.T. Frank, O. Le Gendre, N. Sawwan, D. Aebisher, J.F. Liebman, K.N. Houk,
648 A. Greer, R. Gao, Possible singlet oxygen generation from the photolysis of indigo dyes in
649 methanol, DMSO, water, and ionic liquid, 1-butyl-3-methylimidazolium tetrafluoroborate,
650 Tetrahedron 62 (2006) 10771–10776. https://doi.org/10.1016/j.tet.2006.08.095.
651 [16] M. Gauthier, D. R. Snelling, Formation of singlet molecular oxygen from the ozone
652 photochemical system, Chem. Phys. Lett., 5 (1970) 220–223. https://doi.org/10.1016/0009-
653 2614(70)80011-2
654 [17] A. Blázquez-Castro, T. Breitenbach, P.R. Ogilby, Cell cycle modulation through subcellular
655 spatially resolved production of singlet oxygen *via* direct 765 nm irradiation: manipulating
656 the onset of mitosis, Photochem. Photobiol. Sci. 17 (2018) 1310–1318.

657 https://doi.org/10.1039/c8pp00338f.
658 [18] M. Bregnhøj, A. Blázquez-Castro, M. Westberg, T. Breitenbach, P.R. Ogilby, Direct 765
659 nm Optical Excitation of Molecular Oxygen in Solution and in Single Mammalian Cells, J.
660 Phys. Chem. B 199 (2015) 5422–5429. https://doi.org/10.1021/acs.jpcb.5b01727.
661 [19] L.B.C. Matheson, J. Lee, Reaction of chemical acceptors with singlet oxygen produced by
662 direct laser excitation, Chem. Phys. Lett. 7 (1970) 475–476. https://doi.org/10.1016/0009-
663 2614(70)80341-4.
664 [20] F. Anquez, E. Courtade, A. Sivéry, P. Suret, S. Randoux, A high-power tunable Raman fiber
665 ring laser for the investigation of singlet oxygen production from direct laser excitation
666 around 1270 nm, Opt. Express 18 (2010) 22928. https://doi.org/10.1364/OE.18.022928.
667 [21] E. Wasserman, R.W. Murray, M.L. Kaplan, W.A. Yager, Singlet oxygen sources in ozone
668 chemistry, J. Am. Chem. Soc. 90 (1968) 4160–4161. https://doi.org/10.1021/ja01004a085.
669 [22] M.V. Zagidullin, N.A. Khvatov, M.S. Malyshev, V.N. Azyazov, Dissociation of iodine
670 molecules and singlet oxygen generation in O_2–I_2 mixture induced by 1315-nm laser
671 radiation, Quantum Electron. 47 (2017) 932–934. http://dx.doi.org/10.1070/QEL16425.
672 [23] K. Furukawa, E.W. Gray, E.A. Ogryzlo, Singlet oxygen from discharge-flow systems, Ann.
673 N. Y. Acad. Sci. 171 (1970) 175–187. https://doi.org/10.1111/j.1749-6632.1970.tb39322.x.
674 [24] C.S. Foot, Definition of type I and type II photosensitized oxidation, Photochem. Photobiol.
675 54 (1991) 659. https://doi.org/10.1111/j.1751-1097.1991.tb02071.x.
676 [25] A. Wright, C.L. Hawkins, M.J. Davies, Photo-oxidation of cells generates long-lived
677 intracellular protein peroxides, Free Radic. Biol. Med. 34 (2003) 637–647.
678 https://doi.org/10.1016/S0891-5849(02)01361-8.
679 [26] J. Baier, T. Maisch, M. Maier, E. Engel, M. Landthaler, W. Bäumler, Singlet oxygen
680 generation by UVA light exposure of endogenous photosensitizers, Biophys. J. 91 (2006)
681 1452–1459. https://doi.org/10.1529/biophysj.106.082388.
682 [27] J. Usuda, H. Kato, T. Okunaka, K. Furukawa, K. Yamada, Y. Suga, H. Honda, Y.
683 Nagatsuka, T. Ohira, M. Tsuboi, T. Hirano, Photodynamic therapy (PDT) for lung cancers,

684 J. Thorac. Oncol. 1 (2006) 489–493. https://doi.org/10.1016/S1556-0864(15)31616-6.
685 [28] N. Yavari, S. Andersson-Engels, U. Segersten, P.U. Malmstrom, An overview on preclinical
686 and clinical experiences with photodynamic therapy for bladder cancer, Can. J. Urol. 18
687 (2011) 5778–5786. https://portal.research.lu.se/en/publications/an-overview-on-preclinical-
688 and-clinical-experiences-with-photodyn.
689 [29] K. Moghissi, K. Dixon, Photodynamic Therapy (PDT) in Esophageal Cancer: A Surgical
690 View of its Indications Based on 14 Years Experience, Technol. Cancer Res. Treat. 2 (2003)
691 319–326. https://doi.org/10.1177/153303460300200406.
692 [30] J.D. Meyers, Y. Cheng, A.M. Broome, R.S. Agnes, M.D. Schluchter, S. Margevicius, X.
693 Wang, M.E. Kenney, C. Burda, J.P. Basilion, Peptide-Targeted Gold Nanoparticles for
694 Photodynamic Therapy of Brain Cancer, Part. Part. Syst. Charact. 32 (2015) 448–457.
695 https://doi.org/10.1002/ppsc.201400119.
696 [31] Y. Nishinaka, T. Arai, S. Adachi, A. Takaori-Kondo, K. Yamashita, Singlet oxygen is
697 essential for neutrophil extracellular trap formation, Biochem. Biophys. Res. Commun. 413
698 (2011) 75–79. https://doi.org/10.1016/j.bbrc.2011.08.052.
699 [32] R. De Santis, V. Luca, J. Näslund, R.K. Ehmann, M. De Angelis, E. Lundmark, L. Nencioni,
700 G. Faggioni, S. Fillo, D. Amatore, E. Regalbuto, F. Molinari, G. Petralito, R. Wölfel, P.
701 Stefanelli, G. Rezza, A.T. Palamara, M. Antwerpen, M. Forsman, F. Lista, Rapid
702 inactivation of SARS-CoV-2 with LED irradiation of visible spectrum wavelengths, J.
703 Phoochem. Photobiol. 8 (2021) 100082. https://doi.org/10.1016/j.jpap.2021.100082.
704 [33] M. Kim, H.Y. Jung, H.J. Park, Topical PDT in the Treatment of Benign Skin Diseases:
705 Principles and New Applications, Int. J. Mol. Sci. 16 (2015) 23259–23278.
706 https://doi.org/10.3390/ijms161023259.
707 [34] E. Ben-Hur, N.E. Geacintov, B. Studamire, M.E. Kenney, B. Horowitz, The effect of
708 irradiance on virus sterilization and photodynamic damage in red blood cells sensitized by
709 phthalocyanines, Photochem. Photobiol. 61 (1995) 190–195. https://doi.org/10.1111/j.1751-
710 1097.1995.tb03959.x.

711 [35] B. Il Lee, Y.J. Chung, C.B. Park, Photosensitizing materials and platforms for light-
712 triggered modulation of Alzheimer's β-amyloid self-assembly, Biomaterials 190-191 (2019)
713 121–132. https://doi.org/10.1016/j.biomaterials.2018.10.043.
714 [36] D. García-Fresnadillo, Singlet Oxygen Photosensitizing Materials for Point-of-Use Water
715 Disinfection with Solar Reactors, ChemPhotoChem 2 (2018) 512–534.
716 https://doi.org/10.1002/cptc.201800062.
717 [37] Y.Z. Chen, Z.U. Wang, H. Wang, J. Lu, S.H. Yu, H.L. Jiang, Singlet Oxygen-Engaged
718 Selective Photo-Oxidation over Pt Nanocrystals/Porphyrinic MOF: The Roles of
719 Photothermal Effect and Pt Electronic State, J. Am. Chem. Soc. 139 (2017) 2035–2044.
720 https://doi.org/10.1021/jacs.6b12074.
721 [38] H. Wasserman, J.U. Yoo, R.W. DeSimone, Singlet Oxygen Reactions from the Adducts of
722 Ozone with Heterocyclic Substrates, J. Am. Chem. Soc. 117 (1995) 9772–9773.
723 https://doi.org/10.1021/ja00143a027.
724 [39] R. Kopecky. J.H. van de Sande, Deuterium isotope effects in the oxidation of 2,3-dimethyl-
725 2-butene via the bromohydroperoxide, by singlet oxygen and by triphenyl phosphite
726 ozonide, Can. J. Chem. 50 (1972) 4034–4049. https://doi.org/10.1139/v72-637.
727 [40] Y. Chen, J. Deng, F. Liu, P. Dai, Y. An, Z. Wang, Y. Zhao, Energy-Free, Singlet Oxygen-
728 Based Chemodynamic Therapy for Selective Tumor Treatment without Dark Toxicity, Adv.
729 Healthc. Mater. 8 (2019) 1900366. https://doi.org/10.1002/adhm.201900366.
730 [41] M.J. Beltrán-García, F.M. Prado, M.S. Oliveira, D. Ortiz-Mendoza, A.C. Scalfo, A. Pessoa,
731 M.H.G. Medeiros, J.F. White, P. Di Mascio, Singlet molecular oxygen generation by light-
732 activated DHN-melanin of the fungal pathogen Mycosphaerella fijiensis in black Sigatoka
733 disease of bananas, PLoS One 9 (2014) e91616.
734 https://doi.org/10.1371/journal.pone.0091616
735 [42] E. Steinmann, U. Gravemann, M. Friesland, J. Doerrbecker, T.H. Müller, T. Pietschmann,
736 A. Seltsam, Two pathogen reduction technologies—methylene blue plus light and shortwave
737 ultraviolet light—effectively inactivate hepatitis C virus in blood products, Transfusion, 53

(2013) 1010–1018. https://doi.org/10.1111/j.1537-2995.2012.03858.x.

[43] L. Kong, G. Fang, X. Xi, Y. Wen, Y. Chen, M. Xie, F. Zhu, D. Zhou, J. Zhan, A novel peroxymonosulfate activation process by periclase for efficient singlet oxygen-mediated degradation of organic pollutants, Chem. Eng. J. 403 (2021) 126445. https://doi.org/10.1016/j.cej.2020.126445

[44] C. Wang, S. Gao, J. Zhu, X. Xia, M. Wang, Y. Xiong, Enhanced activation of peroxydisulfate by strontium modified $BiFeO_3$ perovskite for ciprofloxacin degradation, J. Environ. Sci. (China) 99 (2021) 249–259. https://doi.org/10.1016/j.jes.2020.04.026.

[45] J. Zou, J. Yu, L. Tang, X. Ren, Y. Pang, H. Zhang, Q. Xie, Y. Liu, H. Liu, T. Luo, Analysis of reaction pathways and catalytic sites on metal-free porous biochar for persulfate activation process, Chemosphere 261 (2020) 127747. https://doi.org/10.1016/j.chemosphere.2020.127747

[46] X. Sun, D. Xu, P. Dai, X. Liu, F. Tan, Q. Guo, Efficient degradation of methyl orange in water via both radical and non-radical pathways using Fe-Co bimetal-doped MCM-41 as peroxymonosulfate activator, Chem. Eng. J. 402 (2020) 125881.

[47] J.R. Robinson, Photodynamic insecticides: A review of studies on photosensitizing dyes as insect control agents, their practical application, hazards, and residues, Residue Rev. 88 (1983) 69–100. https://doi.org/10.1007/978-1-4612-5569-7_2

[48] T.B. Amor, L. Bortolotto, G. Jori, Porphyrins and related compounds as photoactivatable insecticides. 3. Laboratory and field studies, Photochem. Photobiol. 71 (2000) 124. https://doi.org/10.1562/0031-8655(2000)071<0124:SIPPAR>2.0.CO;2.

[49] D. Kalaitzakis, K. Daskalakis, M. Triantafyllakis, M. Sofiadis, G. Vassilikogiannakis, Singlet-Oxygen-Mediated Synthesis of Pandanusine A and Pandalizine C and Structural Revision of Pandanusine B, Org. Lett. 21 (2019) 5467–5470. https://doi.org/10.1021/acs.orglett.9b01727.

[50] M. Triantafyllakis, K. Sfakianaki, D. Kalaitzakis, G. Vassilikogiannakis, The Power of Triplet and Singlet Oxygen in Synthesis: 2-Oxindoles, 3-Hydroxy-2-oxindoles, and Isatins

765 from Furans, Org. Lett. 20 (2018) 3631–3634. https://doi.org/10.1021/acs.orglett.8b01404.
766 [51] S. Malik, S.A. Khan, P. Ahuja, S. K. Arya, S. Sahu, K. Sahu, Singlet oxygen-mediated
767 synthesis of malarial chemotherapeutic agents, Med. Chem. Res. 22 (2013) 5633–5653.
768 https://doi.org/10.1007/s00044-013-0578-4.
769 [52] A. Kouridaki, T. Montagnon, D. Kalaitzakis, G. Vassilikogiannakis, Using singlet oxygen to
770 synthesise the CDE-ring system of the pectenotoxins, Org. Biomol. Chem. 11 (2013) 537–
771 554. https://doi.org/10.1039/C2OB27158C.
772 [53] S.J. Arnold, M. Kubo, E.A. Ogryzlo, Relaxation and Reactivity of Singlet Oxygen,
773 Oxidation of Organic Compounds, 70 (1968)133–142. DOI: 10.1021/ba-1968-0077.ch070.
774 [54] G. Nardi, I. Manet, S. Monti, M.A. Miranda, V. Lhiaubet-Vallet, Scope and limitations of
775 the TEMPO/EPR method for singlet oxygen detection: the misleading role of electron
776 transfer, Free Radic. Biol. Med. 77 (2014) 64–70.
777 https://doi.org/10.1016/j.freeradbiomed.2014.08.020.
778 [55] B.B. Fischer, É. Hideg, A. Krieger-Liszkay, Production, detection, and signaling of singlet
779 oxygen in photosynthetic organisms, Antioxidants Redox Signal. 18 (2013) 2145–2162.
780 https://doi.org/10.1089/ars.2012.5124.
781 [56] A. A. Krasnovsky, Problems of Regulation in Biological Systems, Research Institute of
782 Regular and Chaotic Dynamics, Moscow–Izhevsk, 2006, pp. 223–254.
783 [57] L. Lin, H. Lin, Y. Shen, D. Chen, Y. Gu, B. C. Wilson, B. Li, Singlet Oxygen
784 Luminescence Image in Blood Vessels During Vascular-Targeted Photodynamic Therapy,
785 Photochem. Photobiol. 96 (2020) 646–651. https://doi.org/10.1111/php.13264.
786 [58] G. Boso, D. Ke, B. Korzh, J. Bouilloux, N. Lange, H. Zbinden, Time-resolved singlet-
787 oxygen luminescence detection with an efficient and practical semiconductor single-photon
788 detector, Biomed. Opt. Express 7 (2016) 211. https://doi.org/10.1364/BOE.7.000211.
789 [59] M. Pfitzner, A. Preuß, B. Röder, A new level of in vivo singlet molecular oxygen
790 luminescence measurements, Photodiagnosis Photodyn. Ther. 29 (2020) 101613.
791 https://doi.org/10.1016/j.pdpdt.2019.101613.

[60] N.R. Gemmell, A. McCarthy, M.M. Kim, I. Veilleux, T.C. Zhu, G.S. Buller, B.C. Wilson, R.H. Hadfield, A compact fiber‐optic probe‐based singlet oxygen luminescence detection system, J. Biophotonics 10 (2017) 320–326. https://doi.org/10.1002/jbio.201600078.

[61] K. Tsimvrakidis, N.R. Gemmell, K. Erotokritou, S. Miki, M. Yabuno, T. Yamashita, H. Terai, R.H. Hadfield, Enhanced Optics for Time-Resolved Singlet Oxygen Luminescence Detection, IEEE J. Sel. Top. Quantum Electron. 25 (2019) 7000107. https://doi.org/10.1109/JSTQE.2018.2836962.

[62] L. Skuja, K. Smits, A. Trukhin, F. Gahbauer, R. Ferber, M. Auzinsh, L. Busaite, L. Razinkovas, M. Mackoit-Sinkevičiena, A. Alkauskas, Dynamics of Singlet Oxygen Molecule Trapped in Silica Glass Studied by Luminescence Polarization Anisotropy and Density Functional Theory, J. Phys. Chem. C 124 (2020) 7244–7253. https://doi.org/10.1021/acs.jpcc.9b11581.

[63] L.K. Andersen, Z. Gao, P.R. Ogilby, L. Poulsen, I. Zebger, A Singlet Oxygen Image with 2.5 μm Resolution, J. Phys. Chem. A 106 (2002) 8488–8490. https://doi.org/10.1021/jp021108z.

[64] B. Hu, N. Zeng, Z. Liu, Y. Ji, W. Xie, Q. Peng, Y. Zhou, Y. He, H. Ma, Two-dimensional singlet oxygen imaging with its near-infrared luminescence during photosensitization, J. Biomed. Opt. 16 (2011) 016003. https://doi.org/10.1117/1.3528593.

[65] M. Bregnhøj, P. R. Ogilby, Two-Photon Excitation of Neat Aerated Solvents with Visible Light Produces Singlet Oxygen, J. Phys. Chem. A 123 (2019) 7567–7575. https://doi.org/10.1021/acs.jpca.9b05517

[66] J. Yamamoto, S. Yamamoto, T. Hirano, S. Li, M. Koide, E. Kohno, M. Okada, C. Inenaga, T. Tokuyama, N. Yokota, S. Terakawa, H. Namba, Monitoring of Singlet Oxygen Is Useful for Predicting the Photodynamic Effects in the Treatment for Experimental Glioma, Clin. Cancer Res. 12 (2006) 7132–7139. https://doi.org/10.1158/1078-0432.CCR-06-0786.

[67] S. Lee, M.E. Isabelle, K.L. Gabally-Kinney, B.W. Pogue, S.J. Davis, Dual-channel imaging system for singlet oxygen and photosensitizer for PDT, Biomed. Opt. Express 2 (2011)

1233. https://doi.org/10.1364/BOE.2.001233.

[68] J. Zou, Z. Yin, P. Wang, D. Chen, J. Shao, Q. Zhang, L. Sun, W. Huang, X. Dong, Photosensitizer synergistic effects: D–A–D structured organic molecule with enhanced fluorescence and singlet oxygen quantum yield for photodynamic therapy, Chem. Sci. 9 (2018) 2188–2194. https://doi.org/10.1039/C7SC04694D.

[69] Q. Liu, M. Xu, T. Yang, B. Tian, X. Zhang, F. Li, Highly Photostable Near-IR-Excitation Upconversion Nanocapsules Based on Triplet-Triplet Annihilation for in Vivo Bioimaging Application, ACS Appl. Mater. Interfaces 10 (2018) 9883–9888. https://doi.org/10.1021/acsami.7b17929.

[70] Y. Mi, H.B. Cheng, H. Chu, J. Zhao, M. Yu, Z. Gu, Y. Zhao, L. Li, A photochromic upconversion nanoarchitecture: towards activatable bioimaging and dual NIR light-programmed singlet oxygen generation, Chem. Sci. 10 (2019) 10231–10239. https://doi.org/10.1039/C9SC03524A.

[71] S. Radunz, S. Wedepohl, M. Röhr, M. Calderón, H.R. Tschiche, U. Resch-Genger, pH-Activatable Singlet Oxygen-Generating Boron-dipyrromethenes (BODIPYs) for Photodynamic Therapy and Bioimaging, J. Med. Chem. 63 (2020) 1699–1708. https://doi.org/10.1021/acs.jmedchem.9b01873.

[72] F. Ni, N. Li, L. Zhan, C. Yang, Organic Thermally Activated Delayed Fluorescence Materials for Time-Resolved Luminescence Imaging and Sensing, Adv. Opt. Mater. 8 (2020) 1902187. https://doi.org/10.1002/adom.201902187.

[73] J.R. Lakowicz, Principles of Fluorescence Spectroscopy, 3rd edn., Springer Science Business Media, New York, 2006.

[74] A.W. Kohn, Z. Lin, T. Van Voorhis, Toward Prediction of Nonradiative Decay Pathways in Organic Compounds I: The Case of Naphthalene Quantum Yields, J. Phys. Chem. C 123 (2019) 15394–15402. https://doi.org/10.1021/acs.jpcc.9b01243.

[75] N. Hasebe, K. Suzuki, H. Horiuchi, H. Suzuki, T. Yoshihara, T. Okutsu, S. Tobita, Absolute phosphorescence quantum yields of singlet molecular oxygen in solution determined using

an integrating sphere instrument, Anal. Chem. 87 (2015) 2360–2366. https://doi.org/10.1021/ac5042268.

[76] G. De Miguel, L. Camacho, E.M. García-Frutos, 7,7′ -Diazaisoindigo: a novel building block for organic electronics, J. Mater. Chem. C 4 (2016) 1208–1214. https://doi.org/10.1039/C5TC03464G.

[77] S. Kim, J. A. Márquez, T. Unold, A. Walsh, Upper limit to the photovoltaic efficiency of imperfect crystals from first principles, Energy Environ. Sci. 13 (2020) 1481–1491. https://doi.org/10.1039/D0EE00291G.

[78] W. Shockley, H. J. Queisser, Detailed Balance Limit of Efficiency of p‐n Junction Solar CellsJ. Appl. Phys. 32 (1961) 510–519. https://doi.org/10.1063/1.1736034.

[79] O. Miller, E. Yablonovitch, S. Kurtz, Strong Internal and External Luminescence as Solar Cells Approach the Shockley–Queisser Limit, IEEE J. Photovoltaics 2 (2012) 303-311. https://doi.org/10.1109/JPHOTOV.2012.2198434.

[80] S. Li, L. Zhan, Y. Jin, G. Zhou, T. K. Lau, R. Qin, M. Shi, C. Z. Li, H. Zhu, X. Lu, F. Zhang, H. Chen, Asymmetric Electron Acceptors for High-Efficiency and Low-Energy-Loss Organic Photovoltaics, Adv. Mater. 32 (2020) 2001160. https://doi.org/10.1002/adma.202001160.

[81] S. Liu, J. Yuan, W. Deng, M. Luo, Y. Xie, Q. Liang, Y. Zou, Z. He, H. Wu, Y. Cao, High-efficiency organic solar cells with low non-radiative recombination loss and low energetic disorder, Nat. Photonics 14 (2020) 300–305. https://doi.org/10.1038/s41566-019-0573-5.

[82] R. Nagata, H. Nakanotani, C. Adachi, Near-Infrared Electrophosphorescence up to 1.1 μm using a Thermally Activated Delayed Fluorescence Molecule as Triplet Sensitizer, Adv. Mater. 29 (2017) 1604265. https://doi.org/10.1002/adma.201604265.

[83] V. Jankus, P. Data, D. Graves, C. McGuinness, J. Santos, M. R. Bryce, F. B. Dias, A. P. Monkman, Highly Efficient TADF OLEDs: How the Emitter–Host Interaction Controls Both the Excited State Species and Electrical Properties of the Devices to Achieve Near

100% Triplet Harvesting and High Efficiency, Adv. Funct. Mater. 24 (2014) 6178–6186. https://doi.org/10.1002/adfm.201400948.

[84] M. Furno, R. Meerheim, S. Hofmann, B. Lüssem, K. Leo, Efficiency and rate of spontaneous emission in organic electroluminescent devices, Phys. Rev. B - Condens. Matter Mater. Phys. 85 (2012) 115205. https://doi.org/10.1103/PhysRevB.85.115205.

[85] N. Notsuka, H. Nakanotani, H. Noda, K. Goushi, C. Adachi, Observation of Nonradiative Deactivation Behavior from Singlet and Triplet States of Thermally Activated Delayed Fluorescence Emitters in Solution, J. Phys. Chem. Lett. 11 (2020) 562–566. https://doi.org/10.1021/acs.jpclett.9b03302.

[86] A. Osipov, I. Kim, A. Odinokov, W. J. Son, A. Yakubovich, H. Choi, Tetradentate Pt(II) Phosphors: A Computational Analysis of Nonradiative Decay Rates and Luminescence Efficiency, J. Phys. Chem. C 124 (2020) 12039–12048. https://doi.org/10.1021/acs.jpcc.0c01754.

[87] Q. Peng, Y. Niu, C. Deng, Z. Shuai, Vibration correlation function formalism of radiative and non-radiative rates for complex molecules, Chem. Phys. 370 (2010) 215–222. https://doi.org/10.1016/j.chemphys.2010.03.004.

[88] Y.C. Chen, C.Y. Gao, K.L. Chen, T.H. Meen, C.J. Huang, Enhancement and Quenching of Fluorescence by Silver Nanoparticles in Organic Light-Emitting Diodes, J. Nanomater. 2013 (2013) 841436. https://doi.org/10.1155/2013/841436.

[89] F.D. Eisner, M. Azzouzi, Z. Fei, X. Hou, T.D. Anthopoulos, T.J.S. Dennis, M. Heeney, J. Nelson, Hybridization of Local Exciton and Charge-Transfer States Reduces Nonradiative Voltage Losses in Organic Solar Cells, J. Am. Chem. Soc. 141 (2019) 6362–6374. https://doi.org/10.1021/jacs.9b01465.

[90] J. Benduhn, K. Tvingstedt, F. Piersimoni, S. Ullbrich, Y. Fan, M. Tropiano, K.A. McGarry, O. Zeika, M.K. Riede, C. J. Douglas, S. Barlow, S.R. Marder, D. Neher, D. Spoltore, K. Vandewal, Intrinsic non-radiative voltage losses in fullerene-based organic solar cells, Nat. Energy 2 (2017) 17053. https://doi.org/10.1038/nenergy.2017.53.

[91] S.D. Stranks, Nonradiative Losses in Metal Halide Perovskites, ACS Energy Lett. 2 (2017) 1515–1525. https://doi.org/10.1021/acsenergylett.7b00239.

[92] K.H. Kim, S.J. Yoo, J.J. Kim, Boosting Triplet Harvest by Reducing Nonradiative Transition of Exciplex toward Fluorescent Organic Light-Emitting Diodes with 100% Internal Quantum Efficiency, Chem. Mater. 28 (2016) 1936–1941. https://doi.org/10.1021/acs.chemmater.6b00478.

[93] T. Serevičius, R. Skaisgiris, J. Dodonova, L. Jagintavičius, D. Banevičius, K. Kazlauskas, S. Tumkevičius, S. Juršėnas, Achieving Submicrosecond Thermally Activated Delayed Fluorescence Lifetime and Highly Efficient Electroluminescence by Fine-Tuning of the Phenoxazine–Pyrimidine Structure, ACS Appl. Mater. Interfaces 12 (2020) 10727–10736. https://doi.org/10.1021/acsami.9b21394.

[94] S. Nad, H. Pal, Unusual Photophysical Properties of Coumarin-151, J. Phys. Chem. A 105 (2001) 1097–1106. https://doi.org/10.1021/jp003157m.

[95] Q. Bao, X. Liu, S. Braun, M. Fahlman, Oxygen- and Water-Based Degradation in [6,6]-Phenyl-C61-Butyric Acid Methyl Ester (PCBM) Films, Adv. Energy Mater. 4 (2014) 1301272. https://doi.org/10.1002/aenm.201301272.

[96] W.R. Mateker, M.D. McGehee, Progress in Understanding Degradation Mechanisms and Improving Stability in Organic Photovoltaics, Adv. Mater. 29 (2017) 1603940. https://doi.org/10.1002/adma.201603940.

[97] M.P. Nikiforov, J. Strzalka, S.B. Darling, Delineation of the effects of water and oxygen on the degradation of organic photovoltaic devices, Sol. Energy Mater. Sol. Cells 110 (2013) 36–42. https://doi.org/10.1016/j.solmat.2012.06.028.

[98] J. Schafferhans, A. Baumann, A. Wagenpfahl, C. Deibel, V. Dyakonov, Oxygen doping of P3HT:PCBM blends: Influence on trap states, charge carrier mobility and solar cell performance, Org. Electron. 11 (2010) 1693–1700. https://doi.org/10.1016/j.orgel.2010.07.016.

[99] M. Schaer, F. Nüesch, D. Berner, W. Leo, L. Zuppiroli, Water Vapor and Oxygen

Degradation Mechanisms in Organic Light Emitting Diodes, Adv. Funct. Mater. 11 (2001) 116–121. https://doi.org/10.1002/1616-3028(200104)11:2<116::AID-ADFM116>3.0.CO;2-B.

[100] S. Collavini, J.L. Delgado, Fullerenes: the stars of photovoltaics, Sustain. Energy Fuels 2 (2018) 2480–2493. https://doi.org/10.1039/C8SE00254A.

[101] T. Xu, L. Yu, How to design low bandgap polymers for highly efficient organic solar cells, Mater. Today 17 (2014) 11–15. https://doi.org/10.1016/j.mattod.2013.12.005.

[102] B. Kadem, A. Hassan, W. Cranton, Efficient P3HT:PCBM bulk heterojunction organic solar cells; effect of post deposition thermal treatment, J. Mater. Sci. Mater. Electron. 27 (2016) 7038–7048. https://doi.org/10.1007/s10854-016-4661-8.

[103] Z. Markovic, V. Trajkovic, Biomedical potential of the reactive oxygen species generation and quenching by fullerenes (C60), Biomaterials 29 (2008) 3561–3573. https://doi.org/10.1016/j.biomaterials.2008.05.005.

[104] S.S.K. Iyer, V. Pagare, Effect of annealing on poly (3-hexylthiophene) and [6,6]-phenyl C 61-butyric acid methyl ester bulk heterojunction solar cells, Proceedings of the 14th International Workshop on the Physics of Semiconductor Devices (2007) 541-546. https://doi.org/10.1109/IWPSD.2007.4472571.

[105] N. Grossiord, J.M. Kroon, R. Andriessen, P.W.M. Blom, Degradation mechanisms in organic photovoltaic devices, Org. Electron. 13 (2012) 432–456. https://doi.org/10.1016/j.orgel.2011.11.027.

[106] A. Nyga, R. Motyka, G. Bussetti, A. Calloni, M. Sangarashettyhalli, S. Fijak, S. Pluczyk-malek, P. Data, A. Blacha-Grzechnik, Electrochemically deposited poly(selenophene)-fullerene photoactive layer: Tuning of the spectroscopic properties towards visible light-driven generation of singlet oxygen, Appl. Surf. Sci. 525 (2020) 146594. https://doi.org/10.1016/j.apsusc.2020.146594.

[107] A. Blacha-Grzechnik, M. Krzywiecki, R. Motyka, M. Czichy, Electrochemically Polymerized Terthiopehene–C60 Dyads for the Photochemical Generation of Singlet

953 Oxygen, J. Phys. Chem. C 123 (2019) 25915–25924.
954 https://doi.org/10.1021/acs.jpcc.9b06101.
955 [108] Y.W. Soon, S. Shoaee, R.S. Ashraf, H. Bronstein, B.C. Schroeder, W. Zhang, Z. Fei, M.
956 Heeney, I. McCulloch, J.R. Durrant, Material Crystallinity as a Determinant of Triplet
957 Dynamics and Oxygen Quenching in Donor Polymers for Organic Photovoltaic Devices,
958 Adv. Funct. Mater. 24 (2014) 1474–1482. https://doi.org/10.1002/adfm.201302612.
959 [109] M. Freitag, J. Teuscher, Y. Saygili, X. Zhang, F. Giordano, P. Liska, J. Hua, S.M.
960 Zakeeruddin, J.E. Moser, M. Grätzel, A. Hagfeldt, Dye-sensitized solar cells for efficient
961 power generation under ambient lighting, Nat. Photonics 11 (2017) 372–378.
962 https://doi.org/10.1038/nphoton.2017.60.
963 [110] Y. Hua, L.T. Lin Lee, C. Zhang, J. Zhao, T. Chen, W.Y. Wong, W.K. Wong, X. Zhu, Co-
964 sensitization of 3D bulky phenothiazine-cored photosensitizers with planar squaraine dyes
965 for efficient dye-sensitized solar cells, J. Mater. Chem. A 3 (2015) 13848–13855.
966 https://doi.org/10.1039/C5TA01665G.
967 [111] X. Qian, L. Lu, Y.Z. Zhu, H.H. Gao, J.Y. Zheng, Phenothiazine-functionalized push–pull Zn
968 porphyrin photosensitizers for efficient dye-sensitized solar cells, RSC Adv. 6 (2016) 9057–
969 9065. https://doi.org/10.1039/C5RA26754D.
970 [112] A. Yella, C.-L. Mai, S.M. Zakeeruddin, S.-N. Chang, C.-H. Hsieh, C.-Y. Yeh, M. Grätzel,
971 Molecular Engineering of Push–Pull Porphyrin Dyes for Highly Efficient Dye-Sensitized
972 Solar Cells: The Role of Benzene Spacers, Angew. Chemie 126 (2014) 3017–3021.
973 https://doi.org/10.1002/ange.201309343.
974 [113] A. Yella, H.-W. Lee, H.N. Tsao, C. Yi, A.K. Chandiran, M.K. Nazeeruddin, E.W.-G. Diau,
975 C.-Y. Yeh, S.M. Zakeeruddin, M. Grätzel, Porphyrin-sensitized solar cells with cobalt
976 (II/III)-based redox electrolyte exceed 12 percent efficiency, Science 334 (2011) 629–634.
977 https://doi.org/10.1126/science.1209688.
978 [114] J.M. Cole, G. Pepe, O.K. Al Bahri, C.B. Cooper, Cosensitization in Dye-Sensitized Solar
979 Cells, Chem. Rev. 119 (2019) 7279–7327. https://doi.org/10.1021/acs.chemrev.8b00632.

[115] Y. Ren, D. Sun, Y. Cao, H.N. Tsao, Y. Yuan, S.M. Zakeeruddin, P. Wang, M. Grätzel, A Stable Blue Photosensitizer for Color Palette of Dye-Sensitized Solar Cells Reaching 12.6% Efficiency, J. Am. Chem. Soc. 140 (2018) 2405–2408. https://doi.org/10.1021/jacs.7b12348

[116] K. Sharma, V. Sharma, S.S. Sharma, Dye-Sensitized Solar Cells: Fundamentals and Current Status, Nanoscale Res. Lett. 13 (2018) 381. https://doi.org/10.1186/s11671-018-2760-6

[117] S. Baysec, A. Minotto, P. Klein, S. Poddi, A. Zampetti, S. Allard, F. Cacialli, U. Scherf, Tetraphenylethylene-BODIPY aggregation-induced emission luminogens for near-infrared polymer light-emitting diodes, Sci. China Chem. 61 (2018) 932–939. https://doi.org/10.1007/s11426-018-9306-2.

[118] Z. Liu, Z. Jiang, M. Yan, X. Wang, Recent Progress of BODIPY Dyes With Aggregation-Induced Emission, Front. Chem. 7 (2019) 712. https://doi.org/10.3389/fchem.2019.00712.

[119] D. Ho, R. Ozdemir, H. Kim, T. Earmme, H. Usta, C. Kim, BODIPY-Based Semiconducting Materials for Organic Bulk Heterojunction Photovoltaics and Thin-Film Transistors, ChemPlusChem, 84 (2019)18–37. https://doi.org/10.1002/cplu.201800543.

[120] A.M. Bittel, A.M. Davis, L. Wang, M.A. Nederlof, J.O. Escobedo, R.M. Strongin, S.L. Gibbs, Varied Length Stokes Shift BODIPY-Based Fluorophores for Multicolor Microscopy, Sci. Rep. 8 (2018) 4590. https://doi.org/10.1038/s41598-018-22892-8

[121] M. Poddar, R. Misra, Recent advances of BODIPY based derivatives for optoelectronic applications, Coord. Chem. Rev.421 (2020) 213462. https://doi.org/10.1016/j.ccr.2020.213462.

[122] R.S. Rao, A. Bagui, G.H. Rao, V. Gupta, S.P. Singh, Achieving the highest efficiency using a BODIPY core decorated with dithiafulvalene wings for small molecule based solution-processed organic solar cells, Chem. Commun. 53 (2017) 6953–6956. https://doi.org/10.1039/C7CC03363J.

[123] J.J. Chen, S.M. Conron, P. Erwin, M. Dimitriou, K. McAlahney, M.E. Thompson, High-Efficiency BODIPY-Based Organic Photovoltaics, ACS Appl. Mater. Interfaces 7 (2015) 662–669. https://doi.org/10.1021/am506874k.

1007 [124] R.S. Rao, B. Yadagiri, G.D. Sharma, S.P. Singh, Butterfly architecture of NIR Aza-
1008 BODIPY small molecules decorated with phenothiazine or phenoxazine, Chem. Commun.
1009 55 (2019) 12535–12538. https://doi.org/10.1039/C9CC06300E.
1010 [125] L. Bucher, N. Desbois, P.D. Harvey, C.P. Gros, G.D. Sharma, Porphyrin Antenna-Enriched
1011 BODIPY–Thiophene Copolymer for Efficient Solar Cells, ACS Appl. Mater. Interfaces, 10
1012 (2018) 992–1004. https://doi.org/10.1021/acsami.7b16112.
1013 [126] K. Ivaniuk, Pidluzhna, P. Stakhira, G.V. Baryshnikov, Y.P. Kovtun, Z. Hotra, B.F. Minaev,
1014 H. Ågren, BODIPY-core 1,7-diphenyl-substituted derivatives for photovoltaics and OLED
1015 applications, Dye. Pigment. 175 (2020) 108123.
1016 https://doi.org/10.1016/j.dyepig.2019.108123.
1017 [127] M. Üçüncü, E. Karakuş, E. Kurulgan Demirci, M. Sayar, S. Dartar, M. Emrullahoglu,
1018 BODIPY–Au(I): A Photosensitizer for Singlet Oxygen Generation and Photodynamic
1019 Therapy, Org. Lett. 19 (2017) 2522–2525. https://doi.org/10.1021/acs.orglett.7b00791.
1020 [128] M.A. Filatov, S. Karuthedath, P.M. Polestshuk, H. Savoie, K.J. Flanagan, C. Sy, E. Sitte, M.
1021 Telitchko, F. Laquai, R.W. Boyle, M.O. Senge, Generation of Triplet Excited States via
1022 Photoinduced Electron Transfer in meso-anthra-BODIPY: Fluorogenic Response toward
1023 Singlet Oxygen in Solution and in Vitro, J. Am. Chem. Soc. 139 (2017) 6282–6285.
1024 https://doi.org/10.1021/jacs.7b00551.
1025 [129] R. Prieto-Montero, A. Prieto-Castañeda, R. Sola-Llano, A.R. Agarrabeitia, D. García-
1026 Fresnadillo, I. López-Arbeloa, A. Villanueva, M.J. Ortiz, S. de la Moya, V. Martínez-
1027 Martínez, Exploring BODIPY Derivatives as Singlet Oxygen Photosensitizers for PDT,
1028 Photochem. Photobiol. 96 (2020) 458–477. https://doi.org/10.1111/php.13232.
1029 [130] A. Turksoy, D. Yildiz, E.U. Akkaya, Photosensitization and controlled photosensitization
1030 with BODIPY dyes, Coord. Chem. Rev. 379 (2019) 47–64.
1031 https://doi.org/10.1016/j.ccr.2017.09.029.
1032 [131] X.F. Zhang, J. Zhu, BODIPY parent compound: Excited triplet state and singlet oxygen
1033 formation exhibit strong molecular oxygen enhancing effect, J. Lumin. 212 (2019) 286–292.

https://doi.org/10.1016/j.jlumin.2019.04.050.

[132] J. Jiang, Y. Qian, Z. Xu, Z. Lv, P. Tao, M. Xie, S. Liu, W. Huang, Q. Zhao, Enhancing singlet oxygen generation in semiconducting polymer nanoparticles through fluorescence resonance energy transfer for tumor treatment, Chem. Sci. 10 (2019) 5085–5094. https://doi.org/10.1039/C8SC05501G.

[133] X. Qiu, R. Lu, H. Zhou, X. Zhang, T. Xu, X. Liu, Y. Zhao, Synthesis of phenothiazine-functionalized porphyrins with high fluorescent quantum yields, Tetrahedron Lett. 49 (2008) 7446–7449. https://doi.org/10.1016/j.tetlet.2008.10.081.

[134] H. Shahroosvand, S. Zakavi, A. Sousaraei, E. Mohajeranic, M. Mahmoudic, Unusual near-white electroluminescence of light emitting diodes based on saddle-shaped porphyrins, Dalt. Trans. 44 (2015) 8364–8368. https://doi.org/10.1039/C4DT03975K.

[135] M. Chapran, E. Angioni, N.J. Findlay, B. Breig, V. Cherpak, P. Stakhira, T. Tuttle, D. Volyniuk, J.V. Grazulevicius, Y.A. Nastishin, O.D. Lavrentovich, P.J. Skabara, An Ambipolar BODIPY Derivative for a White Exciplex OLED and Cholesteric Liquid Crystal Laser toward Multifunctional Devices, ACS Appl. Mater. Interfaces 9 (2017) 4750–4757. https://doi.org/10.1021/acsami.6b13689.

[136] D.A. Merkushev, S.D. Usoltsev, Y.S. Marfin, A.P. Pushkarev, D. Volyniuk, J.V. Grazulevicius, E.V. Rumyantsev, BODIPY associates in organic matrices: Spectral properties, photostability and evaluation as OLED emitters, Mater. Chem. Phys. 187 (2017) 104–111. https://doi.org/10.1016/j.matchemphys.2016.11.053.

[137] Y. Cai, R. Shinar, Z. Zhou, J. Shinar, Multianalyte sensor array based on an organic light emitting diode platform, Sensors Actuators, B Chem. 134 (2008) 727–735. https://doi.org/10.1016/j.snb.2008.06.019.

[138] Z. Zhou, R. Shinar, A.J. Allison, J. Shinar, Enhanced Photoluminescence of Oxygen Sensing Films through Doping with High Dielectric Constant Particles, Adv. Funct. Mater. 17 (2007) 3530–3537. https://doi.org/10.1002/adfm.200700324.

[139] R. Shinar, Z. Zhou, B. Choudhury, J. Shinar, Structurally integrated organic light emitting

1061 device-based sensors for gas phase and dissolved oxygen, Anal. Chim. Acta 568 (2006)
1062 190–199. https://doi.org/10.1016/j.aca.2006.01.050.
1063 [140] Q. Zhang, A. Cirpan, T.P. Russell, T. Emrick, Donor−Acceptor Poly(thiophene-block-
1064 perylene diimide) Copolymers: Synthesis and Solar Cell Fabrication, Macromolecules, 42
1065 (2009) 1079–1082. https://doi.org/10.1021/ma801504e.
1066 [141] S. Rajaram, P.B. Armstrong, J.K. Bumjoon, J.M.J. Fréchet, Effect of Addition of a Diblock
1067 Copolymer on Blend Morphology and Performance of Poly(3-hexylthiophene):Perylene
1068 Diimide Solar Cells, Chem. Mater. 21 (2009) 1775–1777.
1069 https://doi.org/10.1021/cm900911x.
1070 [142] J. Zhang, Y. Li, J. Huang, H. Hu, G. Zhang, T. Ma, P. C. Y. Chow, H. Ade, D. Pan, H. Yan,
1071 Ring-Fusion of Perylene Diimide Acceptor Enabling Efficient Nonfullerene Organic Solar
1072 Cells with a Small Voltage Loss, J. Am. Chem. Soc. 139 (2017) 16092–16095.
1073 https://doi.org/10.1021/jacs.7b09998.
1074 [143] M. Matussek, M. Filapek, P. Gancarz, S. Krompiec, J. Grzegorz Małecki, S. Kotowicz, M.
1075 Siwy, S. Maćkowski, A. Chrobok, E. Schab-Balcerzak, A. Słodek, Synthesis and
1076 photophysical properties of new perylene bisimide derivatives for application as emitting
1077 materials in OLEDs, Dye. Pigment. 159 (2018) 590–599.
1078 [144] S.V. Dayneko, M. Rahmati, M. Pahlevani, G.C. Welch, Solution processed red organic
1079 light-emitting-diodes using an N-annulated perylene diimide fluorophore, J. Mater. Chem. C
1080 8 (2020) 2314–2319. https://doi.org/10.1039/C9TC05584C.
1081 [145] E. Kozma, W. Mróz, F. Villafiorita-Monteleone, F. Galeotti, A. Andicsová-Eckstein, M.
1082 Catellani, C. Botta, Perylene diimide derivatives as red and deep red-emitters for fully
1083 solution processable OLEDs, RSC Adv. 6 (2016) 61175–61179.
1084 https://doi.org/10.1039/C6RA10467C.
1085 [146] G. Li, Y. Zhao, J. Li, J. Cao, J. Zhu, X.W. Sun, Q. Zhang, Synthesis, Characterization,
1086 Physical Properties, and OLED Application of Single BN-Fused Perylene Diimide, J. Org.
1087 Chem. 80 (2015) 196–203. https://doi.org/10.1021/jo502296z.

[147] H. Dinçalp, Ş. KIzIlok, S. Içli, Targeted singlet oxygen generation using different DNA-interacting perylene diimide type photosensitizers, J. Fluoresc. 24 (2014) 917–924. https://doi.org/10.1007/s10895-014-1372-5.

[148] A. Blacha-Grzechnik, A. Drewniak, K.Z. Walczak, M. Szindler, P. Ledwon, Efficient generation of singlet oxygen by perylene diimide photosensitizers covalently bound to conjugate polymers, J. Photochem. Photobiol. A Chem. 388 (2020) 112161. https://doi.org/10.1016/j.jphotochem.2019.112161.

[149] H.-H. Huang, K.S. Song, A. Prescimone, A. Aster, G. Cohen, R. Mannancherry, E. Vauthey, A. Coskun, T. Šolomek, Porous shape-persistent rylene imine cages with tunable optoelectronic properties and delayed fluorescence, Chem. Sci. 12 (2021) 5275–5285. https://doi.org/10.1039/D1SC00347J.

[150] T. Šolomek, N.E. Powers-Riggs, Y.L. Wu, R.M. Young, M.D. Krzyaniak, N.E. Horwitz, M.R. Wasielewski, Electron Hopping and Charge Separation within a Naphthalene-1,4:5,8-bis(dicarboximide) Chiral Covalent Organic Cage, J. Am. Chem. Soc. 139 (2017) 3348–3351. https://doi.org/10.1021/jacs.7b00233.

ChemComm

COMMUNICATION

View Article Online
View Journal | View Issue

Check for updates

Cite this: *Chem. Commun.*, 2022, **58**, 5889

Received 18th March 2022,
Accepted 20th April 2022

DOI: 10.1039/d2cc01568d

rsc.li/chemcomm

Dual-photofunctional organogermanium compound based on donor–acceptor–donor architecture†

Aleksandra Nyga, ‡[a] Takahito Kaihara,‡[b] Takumi Hosono,[b] Massimiliano Sipala,[a] Patrycja Stachelek,[c] Norimitsu Tohnai,[b] Satoshi Minakata,[b] Leonardo Evaristo de Sousa,[d] Piotr de Silva,*[d] Przemyslaw Data*[a] and Youhei Takeda*[b]

A dual-photofunctional organogermanium compound based on a donor–acceptor–donor architecture that exhibits thermally activated delayed fluorescence and mechano-responsive luminochromism has been developed. The developed compound was successfully applied as an emitter for efficient organic light-emitting diodes.

Organogermanes have attracted attention in a wide variety of research fields such as organometallic chemistry,[1] biology,[2] and catalysis.[3] In sharp contrast, the utilization of organogermanium compounds and polymers as optoelectronic materials has been rarely exploited.[4–6] For example, tetraaryl germanes and related polymers have been used as host materials for organic light-emitting diodes (OLEDs), by utilizing the high triplet energy and adequate carrier transport capability.[4] Also, a systematic study of blue-emitters based on phenothiaborin-connected acridan analogues with group 14 elements including germanium for non-doped efficient OLEDs has been reported.[5] Given unique characteristics of organogermanes such as a large atomic radius (122 pm), electropositive nature (χ_p = 2.01), and capability of σ–π conjugation, the development of novel Ge-containing organic functional materials would offer us great opportunities to cultivate design principles for a new class of functional materials. Specifically, the diminished σ–π conjugation ability of Ge element when compared with Si allows for higher-energy triplet excited states than the corresponding silicon compounds.[4] Since the triplet energy is a limiting factor for determining the emission color of thermally activated delayed fluorescent (TADF),[7] donor–acceptor (D–A) type organogermanes are promising for realizing high-energy TADF (blue to green).[5]

Herein, we disclose the development of a dual-photofunctional Ge-containing donor–acceptor–donor (D–A–D) type compound **1** (Fig. 1a). Notably, the developed compound represents a rare example of luminescent organogermanium compounds,[5,8] and it nicely shows dual photofunctionality of TADF and mechano-responsive luminochromism.[9] Furthermore, compound **1** serves as the first example of green-TADF emitter based on organogermanium for an efficient OLED device.

The synthetic route to compound **1** is shown in Fig. 1b (for the details, see the ESI†). We initially developed a synthetic method for dihydrophenazagermine **4**, starting from *N*-protected dibromo diarylamine **2**. Dilithiation of **2** followed by trapping with Ph_2GeCl_2 and detaching the *N*-*p*-methoxybenzyl (PMB) group with DDQ afforded **4**. The X-ray diffraction analysis of the single crystal **4**

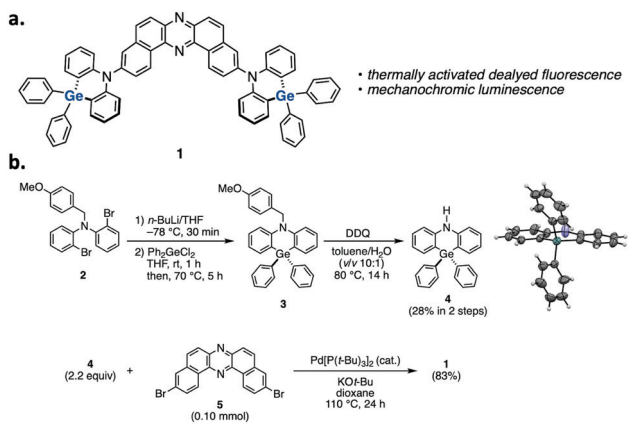

Fig. 1 (a) Structure and (b) synthetic route to compound **1**.

[a] Faculty of Chemistry, Silesian University of Technology, M. Strzody 9, 44-100, Gliwice, Poland. E-mail: przemyslaw.data@polsl.pl
[b] Department of Applied Chemistry, Graduate School of Engineering, Osaka University, Yamadaoka 2-1, Suita, Osaka 565-0871, Japan. E-mail: takeda@chem.eng.osaka-u.ac.jp
[c] Chemistry Department, Durham University, South Road, Durham DH1 3LE, UK
[d] Department of Energy Conversion and Storage, Technical University of Denmark, Anker Engelunds Vej 301, 2800 Kongens Lyngby, Denmark. E-mail: pdes@dtu.dk

† Electronic supplementary information (ESI) available: Experimental procedures for the syntheses of materials, spectroscopic data of new compounds, single crystal X-ray crystallographic data, cyclic voltammogram, thermogravimetric analysis (TGA) profiles, the copies of NMR spectra of new compounds, and theoretical calculation details. CCDC 2153796. For ESI and crystallographic data in CIF or other electronic format see DOI: https://doi.org/10.1039/d2cc01568d

‡ These authors contributed equally to this work.

revealed that the angle between two phenylene planes is 173° (the inset figure in Scheme S1, for the details, see Table S1, ESI†), which is larger than that of its Si analogue (*ca.* 133°) in a D–A system.[5] This planar structure of the donor would be ascribed to the longer Ge–C bond (*ca.* 1.93 Å) when compared to Si–C bond (*ca.* 1.85 Å).[5] D–A–D compound **1** was successfully synthesized through a Pd-catalyzed Buchwald–Hartwig amination of 3,11-dibromo-dibenzophenazine **5**[10] with donor **4** (Fig. 1b).

The steady-state UV-vis absorption spectra of diluted solutions ($c = 10^{-5}$ M) of **1** displayed a π–π* absorption at λ_{abs} 300–350 nm and weak vibronic absorption ascribed to the acceptor core at λ_{abs} 380–420 nm (Fig. 2a). Also, in the lower-energy region, a broad and weak absorption ascribed to charge-transfer (CT) transition was observed. In a non-polar solvent (*n*-hexane), compound **1** displayed a vibronically-shaped emission spectrum (λ_{em} 474 nm) with a moderate photoluminescence quantum yield (PLQY), which is ascribed to the emission from the locally excited state (^{1}LE). In contrast to the absorption spectra, the PL spectrum significantly red-shifted as a function of solvent polarity (Fig. 2a), suggesting the CT character of the excited states in those solvents. The Mataga–Lippert plot analysis corroborated the hybridized local and charge-transfer (HLCT) nature of compound **1** (Fig. S3, ESI†). An interesting phenomenon other than solvatochromism involves dual-emission in a polar solvent such as dichloromethane (DCM) and DMF (Fig. 2a). Comparison with a known D–A system

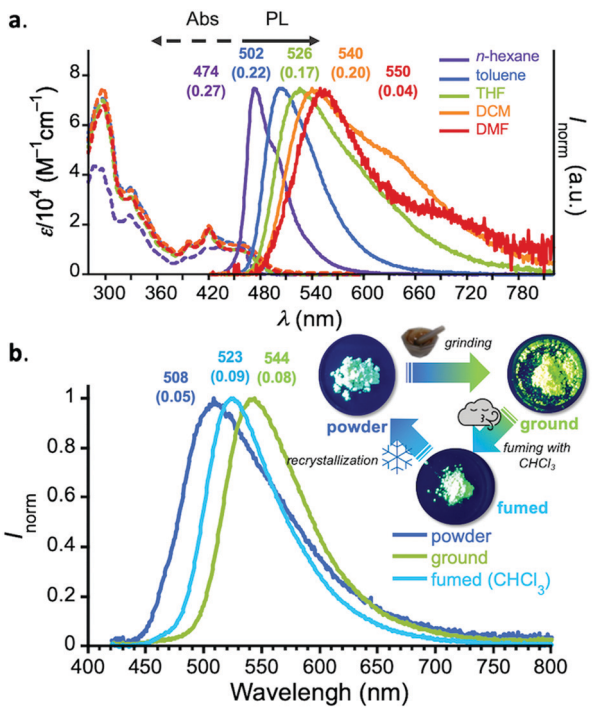

Fig. 2 (a) UV-vis absorption (dotted lines) and PL (solid lines) spectra of diluted solutions of **1** ($c = 10^{-5}$ M). Photoluminescence spectra were acquired with the excitation at λ_{ex} 400 nm. (b) PL spectra of power (blue), ground (moth green), and fumed sample (light blue) of **1** excited at λ_{ex} 400 nm. The photographs represent the image of the emission-color change cycle. All emoji designed by OpenMoji-the open-source emoji and icon project. License: CC BY-SA 4.0.

having a phenazagermin donor allows us to notice that the contribution of the emission ascribed to axial-axial conformer is little in our system.[5] The exclusive population of equatorial-equatorial conformer of compound **1** was supported by the theoretical calculations (*vide infra*).

It is noted that D–A–D compound **1** exhibited a significant change in emission color in the solid states, responding to external stimuli (Fig. 2b). When as-prepared powdery solid ("powder") was ground with a pestle and mortar ("ground"), the emission peak significantly shifted to the lower-energy regime (Δλ 1303 cm^{-1}). In contrast, when the ground was fumed with organic vapor such as $CHCl_3$ and CH_2Cl_2, the emission spectrum slightly reverted back (Δλ 738 cm^{-1}). The initial powder state was recovered by recrystallization. The powder X-ray diffraction (PXRD) analyses of the solids revealed that only the peak at 2θ = 23.4° (*d* = 3.8 Å) significantly decreased upon grinding and its intensity was reverted back upon exposing to chloroform vapor (Fig. S4, ESI†). This would suggest that the emission color change in response to stimuli would be ascribed to the fluctuation of intermolecular electronic interaction.[11] It is noted that such dual photofunctionality of TADF and mechano-responsive emission color change would offer opportunities for sensing applications.[12]

Time-resolved luminescence spectroscopy of compound **1** was performed in both inert non-polar cyclo olefin polymer host Zeonex®, 4,4′-bis(*N*-carbazoyl)-1,1′-biphenyl (CBP), and bis[(2-diphenylphosphino)phenyl]ether oxide (DPEPO) hosts, the latter two of which were used to mimic the chemical environment within an OLED device. Each material showed emission within two distinct time regions within all the hosts. The first, decaying with a lifetime within the nanosecond time regime in all materials, is attributed to prompt emission from the singlet excited state due to its temperature independence (Fig. 3). In all cases, spectral inspection at time delays (TD) = 5 ns shows a Gaussian charge transfer (^{1}CT) singlet peak that decays over longer times.

At longer delay times, in the microsecond/millisecond delay time regions, delayed emission was observed (Fig. 3). Depending upon the experimental temperature, both the singlet state delayed emission and triplet state emission was observed on similar millisecond timescales, and therefore, the emission from each state is most easily elucidated upon spectral inspection at different temperatures (Fig. 3). At room temperature (300 K), the delayed emission spectrum had the same shape and onset energy as the prompt emission in both CBP and DPEPO (Fig. 3c and e). Therefore, the delayed emission was identified as TADF. But, the delayed emission in Zeonex® was observed in a slightly lower-energy region (Fig. 3a), probably due to the structural relaxation in the excited state. Intriguingly, the triplet excited state emissions observed at low temperatures showed quite varied energies: 2.65 eV in Zeonex®, 2.14 eV in CBP, and 2.11 eV in DPEPO hosts (Fig. 3a, c, and e). Such fluctuation in the triplet energy is unusual for dibenzo[*a,j*]phenazine-cored D–A–D systems.[13] This observation could suggest a higher triplet state (T_2) was involved in the emission in Zeonex®. Such a scenario was partly supported by the theoretical calculations (*vide infra*). Such complications cause much weaker TADF emission in the CBP and DPEPO

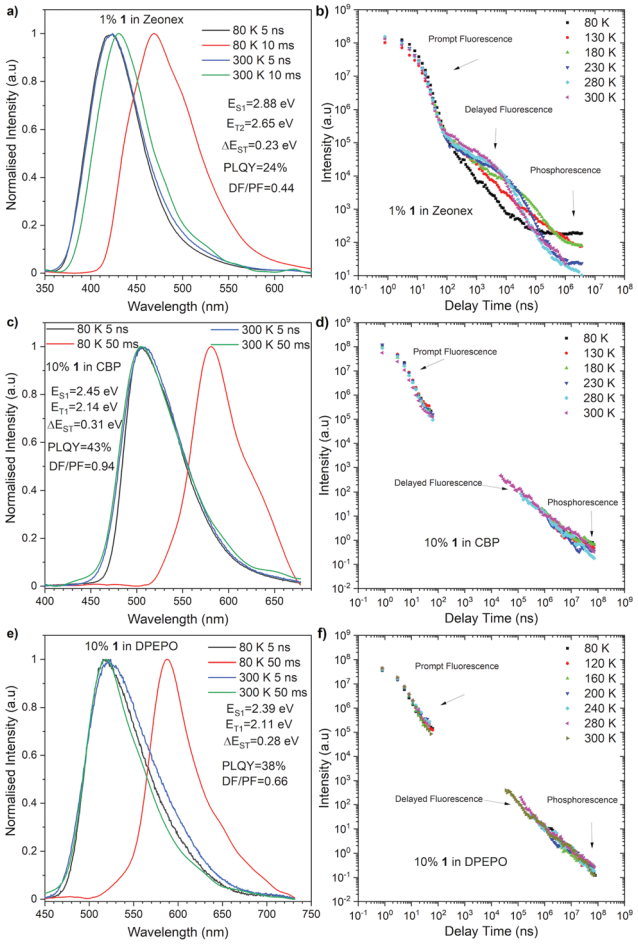

Fig. 3 Emission intensity of **1** against delay time measured in (a) Zeonex®, (c) CBP, and (e) DPEPO at different temperatures. Normalized emission spectra of **1** in (b) Zeonex®, (d) CBP, and (f) DPEPO at varying delay times at 300 K and 80 K.

matrices and a much lower rISC contribution than it was observed in the Zeonex® matrix. The polarity of the host affects the energy of both singlet and triplet excited states. Therefore, as the polarity increases, the ΔE_{ST} of the materials increases from 0.23 eV in Zenex® to 0.31 eV in CBP, and 0.28 in DPEPO, which weaken the rISC process. When compared with the photophysical properties of a phenothiaborine-connected phenazagermine compound[5] in a phosphineoxide host (diphenylphosphoryl)dibenzo[*b,d*]furan: PPF, the λ_{em} for **1** in DPEPO (518 nm) locates at the lower-energy region than that for the D–A dyad (468 nm), while the ΔE_{ST} of **1** (0.28 eV) is larger than that for the D–A dyad (0.11 eV).

The OLED devices were fabricated to investigate whether the Ge-containing compound is applicable to optoelectronic applications (Fig. 4). The HOMO and LUMO energy levels of **1** were determined by cyclic voltammetry (CV) to be −5.65 eV and −3.34 eV, respectively (Fig. S1, ESI†). Since the thermogravimetric analysis (TGA) indicated the high thermal stability of compound **1** [T_d (5 wt% loss under N_2) = 466 °C] (Fig. S2, ESI†), the devices were fabricated with thermal evaporation technique. As a result of an optimization study, the optimal configuration was obtained as follows: Device 1

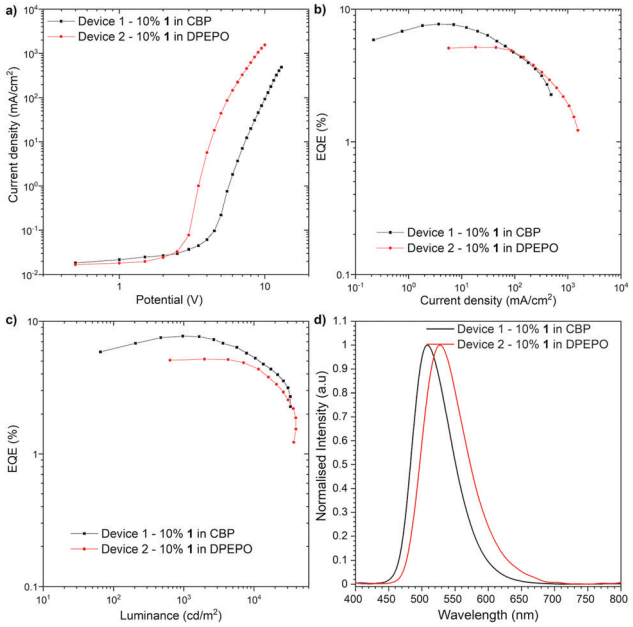

Fig. 4 Device characteristic.

[ITO/*N,N′*-di(1-naphthyl)-*N,N′*-diphenyl-(1,1′-biphenyl)-4,4′-diamine (NPB) (40 nm)/10% **1** in CBP (25 nm)/2,2′,2″-(1,3,5-benzinetriyl)-tris(1-phenyl-1*H*-benzimida-zole) (TPBi) (40 nm)/LiF (1 nm)/Al (100 nm)], Device 2 [ITO/NPB (40 nm)/tris(4-carbazoyl-9-ylphenyl)amine (TCTA) (10 nm)/10% **1** in DPEPO (20 nm)/TPBi (60 nm)/LiF (1 nm)/Al (100 nm)] (Fig. 4). The characteristics of the OLED structures revealed a good efficiency of Ge-containing TADF emitter **1** in CBP host OLED device (EQE *ca.* 7.7%, Fig. 4b), which exceeds the theoretical maximum of the OLED device fabricated with prompt fluorescent emitter (*ca.* 5%). On the one hand, the DPEPO host-based device showed lower efficiency (EQE *ca.* 5.1%). The luminance of the device in both hosts is quite high (more than 32 000 cd m^{-2} in CBP and 39 000 cd m^{-2} in DPEPO), which suggests good charge recombination in the device. The turn-on voltage was around 2.5 V in DPEPO and 4.0 V in CBP. In both structures, the OLED characteristic showed a moderate roll-off dependency (Fig. 4b and c). It is worth noting that the Ge-containing TADF emitter for OLEDs is quite limited so far,[5] and compound **1** represents the first example of green-TADF emitter based on organogermanium compound.

To obtain further insight into the behavior of compound **1**, density functional theory (DFT) calculations were performed and the nuclear ensemble method was used to estimate photophysical rates[14] (see the ESI† for details). A conformational analysis of **1** was conducted, revealing that the equatorial-equatorial conformation is the most stable one in ground, S_1 and T_1 states. A fluorescence spectrum simulation of compound **1** (Fig. S3, ESI†) predicts an emission peak at 516 nm (2.40 eV) and an emission rate of 1.2×10^7 s^{-1} (Table S5, ESI†), which matches well the experimental value (502 nm) in toluene (Fig. 2) but underestimates the S_1 emission energy in Zeonex® (Fig. 3a), though toluene and Zeonex® share similar dielectric constants (*ca.* 2.3). This suggests that the S_1 emission in this

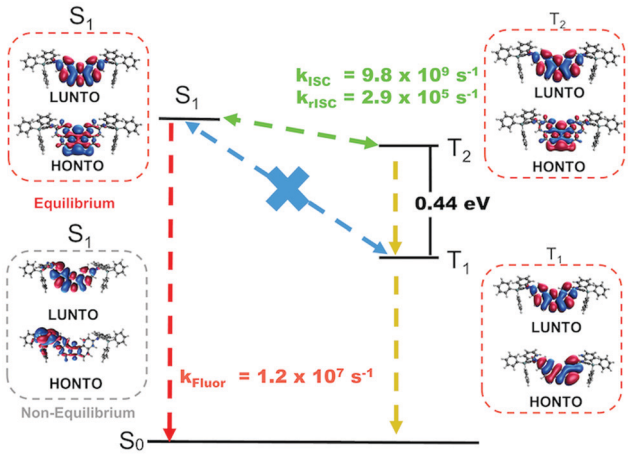

Fig. 5 NTOs for the S_1, T_1 and T_2 states and schematics of the TADF mechanism in compound **1** with DFT estimated rates in toluene. A CT S_1 state calculated at a non-equilibrium geometry is also shown.

case could result from another conformer being preferentially locked in place by solid-state effects specific to this host matrix, a hypothesis that is corroborated by emission energies of 2.83 eV and 2.75 eV calculated for the axial–axial and equatorial–axial conformers, respectively.

Estimated rates for ISC from S_1 (Table S4, ESI†) indicate that the preferred process takes place between the S_1 and T_2 states, due to a lower average energy gap (0.012 eV between S_1 and T_2 *versus* 0.421 eV between S_1 to T_1). The simulated phosphorescence spectra from T_1 and T_2 (Fig. S6 and Tables S4–S6, ESI†) predict one order of magnitude higher emission rate from T_2 than from T_1 with a T_1 peak at 579 nm (2.14 eV) and a T_2 peak at 475 nm (2.61 eV). The predicted energy of T_2 matches the phosphorescence energy measured in Zeonex® (2.65 eV), providing further evidence for the S_1 to T_2 ISC hypothesis. The T_1 energy, in turn, agrees well with phosphorescence energies in CBP and DPEPO (Fig. 3c and e), suggesting that in these host matrices, transfers to T_1 from S_1 may be more efficient due to higher solvatochromic shift or that internal conversion from T_2 can play an important role. In toluene, calculations indicate an average T_1–T_2 gap of 0.44 eV (Table S7, ESI†), enough to prevent rapid depopulation to T_1 if the competing processes (rISC, phosphorescence) are efficient enough. Calculated rISC rates from T_1 and T_2 states (Tables S5 and S6, ESI†) reveal that rISC to S_1 is the preferred transfer for both triplet states. The rISC rate from T_2 to S_1 is orders of magnitude higher than that from T_1, indicating more efficient TADF when T_2 is the state involved in the triplet harvesting mechanism. This agrees with the observed decrease in TADF performance in CBP and DPEPO, which, as mentioned above, have larger T_1 involvement.

Fig. 5 summarizes the proposed TADF mechanism based on the probabilities of each process (Table S8, ESI†). Natural transition orbitals (NTOs) for the S_1, T_1 and T_2 states have mostly localized character, explaining the mild red shift observed from CBP to DPEPO. On the other hand, stronger shifts in solution may result from the fact that vibrational effects can alter the electronic character of the excited states,[15,16] (see example of CT S_1 in Fig. 5) such that the actual picture is not fully captured by NTOs on optimized structures. In fact, this effect should be more prominent in solution than in solid-state, as the vibrational motion may be hindered in the latter case.

In summary, we have developed a dual-photofunctional organogermanium compound that exhibits TADF and mechanochromic behavior. The compound represents the first example of green-TADF emitter using organogermanium scaffold for efficient OLED devices. Theoretical calculations shed light on the importance of the higher triplet excited state to yield TADF *via* rISC process. This work opens up a new avenue for organogermanium-based multi-photofunctional materials in the future.

This work was partly supported by KAKENHI (JP19H05716, JP20H02813, and JP21K18960 to Y. T.), a grant from VILLUM FONDEN (00028053 to P. de Se. and L. E. S.) and the First Team program (POIR.04.04.00-00-4668/17-00 to P. D.). The full list for acknowledgement is included in the ESI.†

Conflicts of interest

There are no conflicts to declare.

Notes and references

1 C. S. Weinert, *Encycl. Inorg. Bioinorg. Chem.*, 2015, 1–18.
2 (*a*) J. S. Thayer, *Appl. Organomet. Chem.*, 1987, **1**, 227–234; (*b*) L. G. Menchikov and M. A. Ignatenko, *Pharm. Chem. J.*, 2013, **46**, 635–638.
3 C. Fricke and F. Schoenebeck, *Acc. Chem. Res.*, 2020, **53**, 2715–2725.
4 (*a*) C. Yao, Q. Cui, J. Peng, X. Xu, R. Liu, J. Wang, Y. Tian and L. Li, *J. Mater. Chem. C*, 2015, **3**, 5017–5025; (*b*) C. Yao, Y. Yang, L. Li, M. Bo, C. Peng and J. Wang, *J. Mater. Chem. C*, 2018, **6**, 6146–6152; (*c*) M.-K. Hung, K.-W. Tsai, S. Sharma, J.-Y. Wu and S.-A. Chen, *Angew. Chem., Int. Ed.*, 2019, **58**, 11317–11323; (*d*) M.-K. Hung, K.-W. Tsai, S. Sharma, J. Lei, J.-Y. Wu and S.-A. Chen, *ACS Appl. Mater. Interfaces*, 2019, **11**, 36895–36904.
5 K. Matsuo and T. Yasuda, *Chem. Sci.*, 2019, **10**, 10687–10697.
6 (*a*) N. Allard, R. B. Aïch, D. Gendron, P.-L. T. Boudreault, C. Tessier, S. Alem, S.-C. Tse, Y. Tao and M. Leclerc, *Macromolecules*, 2010, **43**, 2328–2333; (*b*) J. Ohshita, Y.-M. Hwang, T. Mizumo, H. Yoshida, Y. Ooyama, Y. Harima and Y. Kunugi, *Organometallics*, 2011, **30**, 3233–3236; (*c*) C. M. Amb, S. Chen, K. R. Graham, J. Subbiah, C. E. Small, F. So and J. R. Reynolds, *J. Am. Chem. Soc.*, 2011, **133**, 10062–10065.
7 H. Uoyama, K. Goushi, K. Shizu, H. Nomura and C. Adachi, *Nature*, 2012, **492**, 234–238.
8 (*a*) J. Ohshita, K. Murakami, D. Tanaka, Y. Ooyama, T. Mizumo, N. Kobayashi, H. Higashimura, T. Nakanishi and Y. Hasegawa, *Organometallics*, 2014, **33**, 517–521; (*b*) H. Arii, Y. Iwanami, D. Nakane, H. Masuda, J. Matsumoto, T. Shiragami, K. Mochida and T. Kawashima, *Organometallics*, 2021, **40**, 1363–1370.
9 Y. Sagara, S. Yamane, M. Mitani, C. Weder and T. Kato, *Adv. Mater.*, 2016, **28**, 1073–1095.
10 Y. Takeda, M. Okazaki and S. Minakata, *Chem. Commun.*, 2014, **50**, 10291–10294.
11 S. Goto, Y. Nitta, N. O. Decarli, L. E. de Sousa, P. Stachelek, N. Tohnai, S. Minakata, P. de Silva, P. Data and Y. Takeda, *J. Mater. Chem. C*, 2021, **9**, 13942–13953.
12 P. Data and Y. Takeda, *Chem. – Asian J.*, 2019, **14**, 1613–1636.
13 Y. Takeda, P. Data and S. Minakata, *Chem. Commun.*, 2020, **56**, 8884–8894.
14 L. E. de Sousa and P. de Silva, *J. Chem. Theory Comput.*, 2021, **17**, 5816–5824.
15 L. E. de Sousa and P. de Silva, *ChemRxiv*, 2022, DOI: 10.26434/chemrxiv-2022-pq978.
16 P. de Silva, C. A. Kim, T. Zhu and T. Van Voorhis, *Chem. Mater.*, 2019, **31**, 6995–7006.

Applied Surface Science 525 (2020) 146594

Contents lists available at ScienceDirect

Applied Surface Science

journal homepage: www.elsevier.com/locate/apsusc

Electrochemically deposited poly(selenophene)-fullerene photoactive layer: Tuning of the spectroscopic properties towards visible light-driven generation of singlet oxygen

Aleksandra Nyga[a], Radoslaw Motyka[a], Gianlorenzo Bussetti[b], Alberto Calloni[b], Madan Sangarashettyhalli Jagadeesh[b], Sylwia Fijak[a], Sandra Pluczyk-Malek[a], Przemyslaw Data[a], Agata Blacha-Grzechnik[a,*]

[a] Faculty of Chemistry, Silesian University of Technology, Strzody 9, 44-100 Gliwice, Poland
[b] Department of Physics, Politecnico di Milano, Piazza Leonardo Da Vinci, 32, 20133 Milan, Italy

ARTICLE INFO

Keywords:
Photoactive layers
Visible light-driven singlet oxygen generation
Fullerene dyads
Photosensitizers immobilization
Electrochemical polymerization

ABSTRACT

A selenophene-containing fullerene dyad (C_{60}Se) was electrochemically co-deposited with bis-selenophene (BisSe) to form a visible light absorbing poly(selenophene) layer with incorporated fullerene photosensitizers on platinum (Pt) or indium-tin oxide (ITO) substrates. The resulting photoactive films (P(C_{60}Se_BisSe)) were characterized by cyclic voltammetry, UV–Vis, IR, Raman and X-ray photoelectron spectroscopies. The efficiency of P(C_{60}Se_BisSe) towards singlet oxygen photogeneration was investigated by applying reactions with chemical traps, *i.e.* α-terpinene and 1,3–diphenylisobenzofuran (DPBF), monitored by UV–Vis spectroscopy. The composition of the electropolymerized layer was controlled by varying the monomers ratio in the feed solution and it had a strong influence on the spectroscopic and photosensitizing properties of the deposited film. It has been shown that the efficiency of the visible light-driven singlet oxygen generation can be increased by optimizing the ratio between C_{60} photosensitizers and organic units in the layer.

1. Introduction

Lately, carbon nanostructures, *i.e.* fullerenes, nanotubes and graphene, have attracted considerable attention in the photocatalysis, because of their high efficiency of singlet oxygen ($^1O_2$) production [1,2]. Since such photosensitizers absorb mainly in the ultraviolet region, their spectroscopic properties have to be optimized. This can be done using different strategies that are generally based on the covalent attachment of a chromophore or incorporation into organic matrix absorbing in the visible region [3-8]. The resulting visible light-harvesting structures can be effectively applied as a source of $^1O_2$ molecule. This active form of oxygen can be simply produced in the photosensitization process, in which a photosensitizer molecule is activated by light illumination and transfers energy to triplet state oxygen via collision (so called Type II mechanism) [9-11]. Next to carbon nanostructures, other organic or inorganic photosensitizers show high photosensitizing efficiency: dyes, porphyrins, inorganic transition metals complexes or semiconductors oxides [10,12].

Among Reactive Oxygen Species (ROS), singlet oxygen possess one of the highest oxidative properties and reacts rapidly with an unsaturated carbon–carbon bond or with neutral nucleophiles. Singlet oxygen is extremely attractive as an oxidizing agent in the light-activated synthesis of fine chemicals, *i.e.* production of ascaridole, juglone etc., or in the wastewater treatment [1,9,13]. The lifetime of $^1O_2$ strongly depends on the type of solvent [14] - it can vary from few μs in water and methanol, up to few hundreds μs in chlorinated or deuterated ones [15]. Still, this active form of oxygen is relatively short-lived, and thus, it has to be generated *in situ* in a reaction mixture. Though, typically higher efficiency is observed for the homogenous photosensitization, the heterogeneous approach has many advantages, like simplified operation, product separation or recycling of a photocatalyst. In some cases even higher stability of the latter can be observed [1,16,17]. Various approaches for the deposition of photoactive molecules have been reported, e.g. based on the covalent immobilization on a solid support or non-covalent incorporation into a polymeric matrix [1,18,19].

The investigation of new solid fullerene-based photosensitizers should take into account the type of precursor and the strategy of the

* Corresponding author at: 44-100 Gliwice, Strzody 9, Poland.
E-mail address: agata.blacha@polsl.pl (A. Blacha-Grzechnik).

https://doi.org/10.1016/j.apsusc.2020.146594
Received 13 January 2020; Received in revised form 3 May 2020; Accepted 3 May 2020
Available online 07 May 2020

layer deposition, that would allow controlling the properties of both – the fullerene photosensitizer and the visible light absorbing unit. In our previous work we have shown that the structure of terthiophene-fullerene dyad strongly influences the photosensitizing efficiency of the resulting photoactive layer [20]. Till now, the organic layers containing thiophene and selenophene units have been mainly investigated for the application in the organic electronics, especially in the fullerene or non-fullerene Organic Photovoltaic Devices (OPVs) [21-24]. Lately, it has been shown that fullerene – conjugate polymers blends are able to generate ROS, including singlet oxygen. This, however, is considered as a drawback in solar cells, since it may result in a device degradation [25-29].

Here, we continue our studies aiming to increase the visible light absorption of the photoactive layer by the introduction of selected organic-only units absorbing in the low energy region. Thus, a selenophene/thiophene-fullerene dyad (C_{60}Se), chosen as a photoactive precursor was co-deposited with bis-selenophene (BisSe) in the electrochemical polymerization process. The main aim of this study was to optimize the composition of the resulting photoactive layer in order to tune its spectroscopic properties, *i.e.* broadband absorption in the visible range, and the photosensitizing properties. The deposited layers were characterized by electrochemical and spectroscopic methods. The efficiency of the visible light-driven singlet oxygen photogeneration was tested in the process of α–terpinene oxidation leading to ascaridole formation, that was followed by UV–Vis spectroscopy. Quantum yields of $^1O_2$ production by the investigated layers were estimated with chemical quencher, *i.e.* 1,3–diphenylisobenzofuran (DPBF). The influence of the monomers ratio on the electrochemical, spectroscopic and photoactive properties of the layer was studied.

2. Experimental

2.1. Materials

C_{60}Se dyad and BisSe (Fig. 1) were synthesized applying previously reported procedures [20,30,31]. The synthetic routes and the product identification are given in the Supporting Information. The electrochemical co-deposition of the photoactive layers and their characterization was conducted in Tetrabutylammonium tetrafluoroborate ($TBABF_4$) (Sigma Aldrich, 99%) electrolyte solution in dichloromethane (HPLC grade, Sigma Aldrich). The photosensitizing properties were tested with α-Terpinene (TCI, purity 90%) in acetonitrile (Sigma Aldrich) or 1,3-diphenylisobenzofuran (DPBF) (Acros Organics, purity > 97%) in methanol (Acros Organics, 99.9%). Rose Bengal (Acros Organics) was used as a reference in the determination of the quantum yield of singlet oxygen photogeneration.

2.2. Electrochemical co-deposition of C_{60}Se and BisSe

The electrochemical co-deposition of C_{60}Se and/or BisSe monomers was conducted using SPI-150 electrochemical workstation (Bio-Logic).

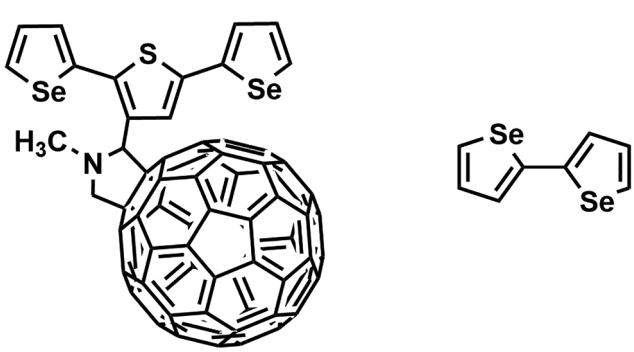

Fig. 1. Investigated monomers: C_{60}Se dyad and BisSe.

A three-electrode cell was used with a platinum disc electrode (Pt, EDAQ, 1 mm dia.) or an Indium-Tin Oxide (ITO)/borosilicate glass (Präzisions Glas & Optik GmbH, PGO) acting as a working electrode, a silver wire - as a pseudoreference electrode and a platinum wire - as a counter electrode. The potential was calibrated with respect to ferrocene (Fc/Fc^+) internal standard. The platinum disc electrode was cleaned with a diamond paste. All electrodes were washed with acetone and dichloromethane and were placed in a Teflon holder in 2 ml conical cell or 5 ml cell, if Pt or ITO were used as a working electrode, respectively. The electrochemical polymerization of C_{60}Se and BisSe was carried out by cyclic voltammetry (CV) within the potential range (-0.6 ; 0.9) V vs Fc/Fc^+ at the scan rate 0.05 V/s in the monomer-containing solution in 0.1 M $TBABF_4$ / dichloromethane. The layer was deposited within 10 scan cycles with the initial anodic polarization. The concentration of C_{60}Se dyad was kept constant at 0.45 mM in all the experiments, while the concentration of BisSe was varied, in order to obtain a different molar ratio of the monomers (5:1, 2:1, 1:1, 1:2 and 1:5). The solution was homogenized with ultrasonic mixing for 15 min and then it was bubbled with Argon (Ar) to remove oxygen prior to measurements.

2.3. Electrochemical and spectroscopic characterization of P(C_{60}Se:BisSe) layers

The electrochemical properties of the layers were investigated in a monomer-free electrolyte solution (0.1 M $TBABF_4$ /CH_2Cl_2 purged with Ar before measurements) using SPI-150 electrochemical workstation (Bio-Logic) and the above-mentioned three-electrode system. CV curves were recorded within (-1.8 ÷ -0.6) V or (-0.6 ÷ 0.9) V vs Fc/Fc^+ potential ranges at 0.05 V/s scan rate.

The content of fullerene in the deposited films was estimated using Equation (1) [32]:

$$\Gamma_{C60} = \frac{Q}{n \bullet F \bullet A} \tag{1}$$

where Q is a charge exchanged in a reversible reduction of C_{60} to $C_{60}^{\bullet -}$, n is a number of electrons, here: equal to 1, A is a platinum electrode surface area (0.785 mm^2) and F is Faraday constant.

Hewlett Packard 8452A UV–Vis spectrometer was used to record UV–Vis spectra of the photoactive layers deposited on ITO and UV–Vis spectra of 0.025 mM solution of C_{60}Se, C_{60} and BisSe in CH_2Cl_2.

IR spectra of the photoactive layers deposited on a platinum plate, powder C_{60}, BisSe and C_{60}Se dyad were collected using ATR mode with Perkin Elmer Spectrum Two IR spectrometer equipped with DTGS MIR detector in the range 2500 – 450 cm^{-1}. Additionally, Raman spectra of co-deposited films were acquired with Renishaw inVia Raman Microscope (Renishaw, Inc., New Mills, UK, with high sensitivity ultra-low noise RenCam CCD detector). A diode laser with the wavelength of 514 nm (maximum power of 12 mW, reduced to 5%), 2400-line/mm grating and 50x objective were used. Renishaw software was applied for spectra smoothing and baseline subtraction.

X-ray photoelectron spectroscopy (XPS) investigations of photoactive layers deposited on ITO utilized an Mg Kα radiation ($h\nu$ = 1253.6 eV), having an overall full width half maximum energy resolution of about 0.9 eV. The spectrometer is a 150 mm hemispherical analyzer from SPECS GmbH working in magnification mode at a pass energy of 20 eV. The samples were mounted on a flat plate with two wing clamps touching the upper part of the specimen, thus ensuring good mechanical and electric contact. Before each experiment, the sample resistance with respect to the ground was checked, the measured resistance was in the range from 5 to 15 Ohm. The fixed samples were placed in an ultra-high vacuum chamber (base pressure of about 1×10^{-10} mbar) [33]. The samples, coming from outside, were firstly inserted inside a fast-entry and, after a couple of hours of pumping, transferred inside the main chamber. No charging effects or sample detriments in vacuum have been detected during the measurements.

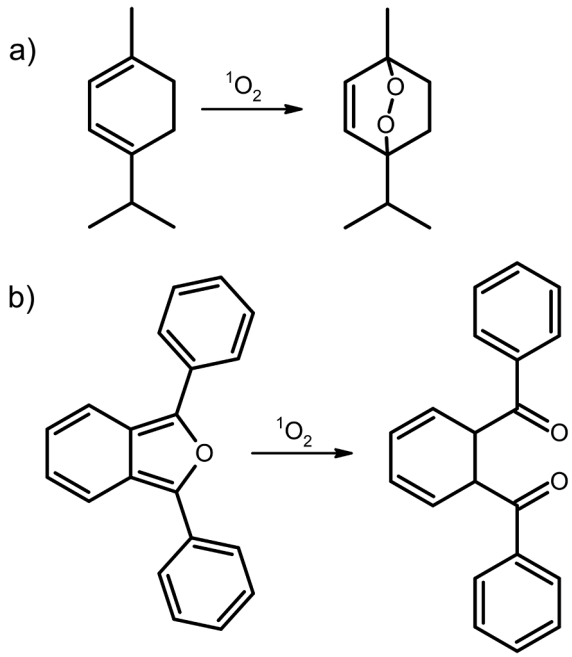

Fig. 2. Scheme of reaction of singlet oxygen with a) α-terpinene and b) DPBF.

2.4. Photogeneration of singlet oxygen by P(C_{60}Se:BisSe) layers

The photogeneration of singlet oxygen molecule was tested with α-terpinene in acetonitrile and 1,3–diphenylisobenzofuran (DPBF) in methanol. The reaction schemes are given in Fig. 2a and Fig. 2b, respectively.

The photosensitizing properties of the deposited layers under visible light illumination were tested with 0.05 mM α-terpinene in acetonitrile. The process was followed *in situ* in 10 × 4 mm quartz cuvette (Hellma Analytics) arranged as a thin layer cell, as in our previous works [20,34]. The setup scheme is given in Fig.S2. The UV–Vis spectra of α-terpinene were collected with Hewlett Packard 8452A UV–Vis spectrometer. Ca. 0.5 cm^2 of sample surface was illuminated with a xenon lamp equipped with a filter transmitting only the radiation above 400 nm, that was placed perpendicularly to the UV–Vis spectra acquisition. The yield and the kinetic parameters of the process were determined based on the decrease in the absorption of α-terpinene at 266 nm [20,34].

DPBF (0.05 mM in CH_3OH) was applied as $^1O_2$ specific quencher under green light illumination. The measurement set-up was arranged as for α-terpinene tests. In this case 532 nm diode laser (Oxxius, LCX-532L-150-CSB-PPA model, 150 mW maximum power, 50 mW power used) was applied as an excitation source. The quantum yields of singlet oxygen photogeneration, Φ, were estimated applying so-called DPBF-method and Rose Bengal (RB) as a reference with known Φ_{RB} equal to 0.80 in CH_3OH. The quantum yield of photochemical production of $^1O_2$ can be calculated using Equation (2).

$$\Phi_i = \Phi_{RB} \cdot \frac{m_i}{m_{RB}} \cdot \frac{\alpha_{RB}}{\alpha_i} \tag{2}$$

where Φ_i and Φ_{RB} are quantum yields of singlet oxygen photogeneration by unknown photosensitizer or RB, respectively; m_i and m_{RB} are rate constants of DPBF oxidation in the presence of an unknown photosensitizer or RB, respectively, and α is absorption correction factor given by $\alpha = 1 - 10^{-A}$ (A is absorbance at irradiation wavelength, here: 532 nm) [35-38].

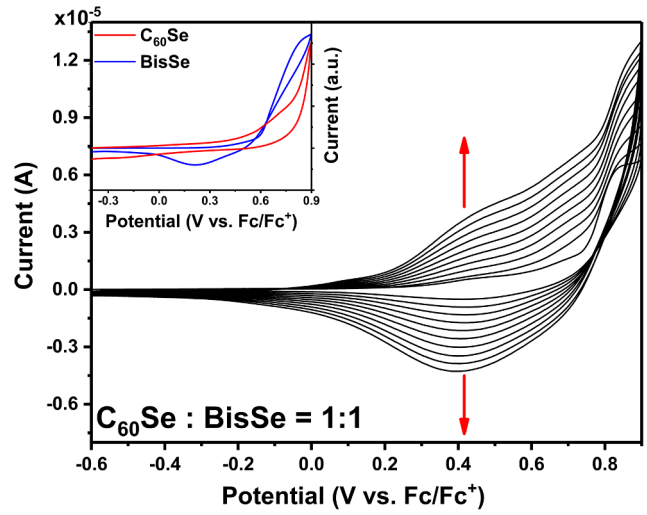

Fig. 3. CV curves recorded for Pt disc electrode in electrolyte solution containing C_{60}Se and BisSe in 1:1 M ratio; arrows indicating the trend of change in the recorded currents. Inset: CV curves recorded for Pt disc electrode in electrolyte solution containing C_{60}Se (red line) or BisSe (blue line).

3. Results and discussion

3.1. Electrochemical co-deposition of C_{60}Se and BisSe

The electrochemical polymerization of monomers was firstly investigated with the platinum disc electrode (Pt). As in our previous works [20,39] such strategy was chosen, since it allows to control the process of layer formation and the amount of the electroactive species being deposited. Fig. 3 presents CV curves recorded during continuous scanning in the equimolar solution of C_{60}Se and BisSe. In the first anodic scan an irreversible oxidation at 0.85 V (vs. Fc/Fc$^+$) is observed, that can be assigned to the oxidation of organic unit, namely selenophene group, to form radical cations [40]. In the consecutive scans the increase in the recorded current in the broad potential range can be observed, indicating the deposition of the electroactive layer on the platinum electrode surface. Similar CV curves were recorded for ITO acting as a working electrode. The electropolymerization process was conducted only in the anodic domain in order to activate organic units only and to ensure the stability of fullerene present in C_{60}Se monomer. Both, the current increase and the appearance of the new redox couple centered at ca. 0.4 V (vs. Fc/Fc$^+$), confirm the polymerization of the organic units to form conjugated polymeric layer [41]. It can be seen in the first scan cycle recorded in the single-component solutions (Fig. 3, inset) that the onset of the anodic oxidation, initiating electropolymerization process, is located at ca. 0.4 V (vs. Fc/Fc$^+$) for both monomers. Therefore, it can be stated that under applied conditions both C_{60}Se and BisSe undergo electrochemical polymerization [42].

3.2. Electrochemical and spectroscopic characterization of P(C_{60}Se:BisSe) layers

3.2.1. Cyclic voltammetry

The electrodeposited polymeric layers, consisting of selenophene and thiophene rings with incorporated fullerene photosensitizers, were in turn characterized by electrochemical and spectroscopic techniques.

The CV curve of P(C_{60}Se_BisSe_1:1) layer recorded in the pure electrolyte solution (Fig. 4) shows three redox couples located at ca. 0.4 V and −1.2 V and −1.5 V vs. Fc/Fc$^+$. The first signal, that arises from the redox process within the polymeric unit, occurs at potential that lies between the potentials of the corresponding signal in P(C_{60}Se) and P(BisSe) – that is ca. 0.6 V and 0.3 V vs. Fc/Fc$^+$, respectively. Hence, the presence of both monomer in the structure of the layer is

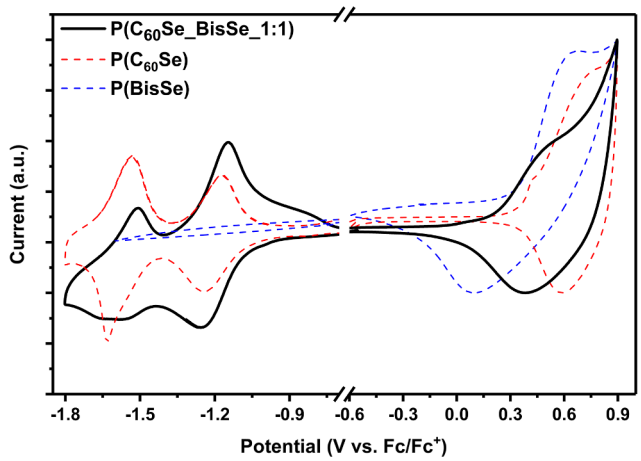

Fig. 4. CV curves recorded for P(C_{60}Se_BisSe_1:1) (black line), P(C_{60}Se) (red dashed line) and P(BisSe) (blue dashed line) deposited on Pt disc electrode in electrolyte solution.

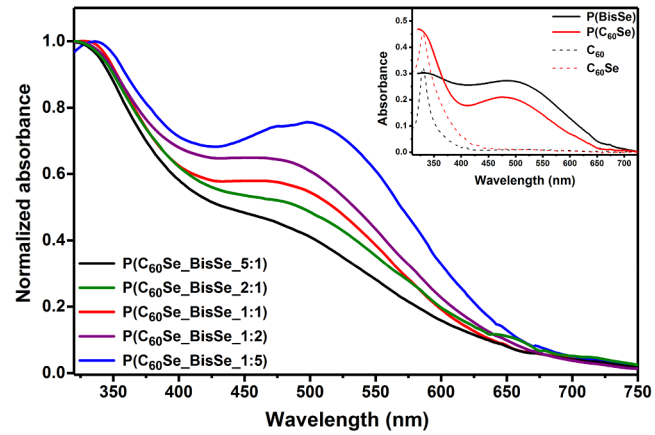

Fig. 5. UV–Vis spectra of P(C_{60}Se_BisSe) layers deposited on ITO from solutions with varied molar ratios of monomers. Inset: UV–Vis spectra of 0.025 mM solution of C_{60} (black dashed line), C_{60}Se in dichloromethane (red dashed line), P(C_{60}Se) (red line) and P(BisSe) (black line) layers deposited on ITO.

confirmed.

In the cathodic scan, two reversible redox couples centered at ca. −1.2 V and at ca. −1.5 V vs. Fc/Fc$^+$ are observed. Those signals, which are absent in the case of P(BisSe) layer, arise from the two-step reduction of C_{60} to $C_{60}^{\bullet-}$ and then to C_{60}^{2-}, respectively [40,43]. This confirms the presence of fullerene units in P(C_{60}Se_BisSe_1:1) layer. Similar CV curves were recorded for other polymeric films deposited from the solution with varied monomers ratio. Taking into account the area under first reduction peak arising from C_{60} to $C_{60}^{\bullet-}$ transition, the fullerene content in the formed layers was roughly estimated. As expected, the amount of C_{60} units in P(C_{60}Se_BisSe) films was decreasing by lowering the C_{60}Se – to – BisSe ratio in the feed solution (Table 1).

3.2.2. UV–Vis spectroscopy

The UV–Vis spectra of the electrochemically deposited layers (Fig. 5) show two distinctive absorption bands. The band with maximum at 330 nm corresponds to the fullerene absorption, that for pristine C_{60} in CH_2Cl_2 solution is located at 329 nm (Fig. 5, inset). The second band present in the low energy region can be linked to the absorption of conjugated polymeric unit, namely $\pi \rightarrow \pi^*$ transition. The UV–Vis spectrum of the fullerene-dyad monomer shows only one broad signal covering C_{60} and organic unit absorption (Fig. 5, inset), while in the UV–Vis spectra of P(C_{60}Se_BisSe) layers the band of selenophene/thiophene-containing matrix is batochromicaly shifted and well-separated from the C_{60} absorption band, which confirms that electrodeposition process results in the elongation of the conjugate organic chain [44]. The maximum of the above-mentioned band is located at ca. 490 nm and is slightly red-shifting with the increase in the BisSe content. In all cases, only one absorption maximum is observed in the visible region and it is located between the maxima of the corresponding homopolymers, *i.e.* 480 nm for P(C_{60}Se) and 500 nm for P(BisSe) (Fig. 5, inset). This may indicate that the electrochemical codeposition results in the formation of the copolymeric structure rather than the blend of homopolymers [45,46]. Since the onset of π-π* transition band is located at ca. 675 nm for all the films, it can be stated that the resulting photoactive layers possess comparable effective conjugation length [47]. Importantly, the absorbance in the Vis range is significantly increasing with respect to C_{60} absorption at 330 nm, with the increase in the content of BisSe. This confirms that the spectroscopic properties of the photoactive layer can be tuned by changing the monomers ratio in the feed solution.

Table.1
Fullerene content in P(C_{60}Se_BisSe) layers deposited from the solution with various molar ratio of monomers.

Photoactive layer	Fullerene content [mol/mm^2]
P(C_{60}Se_BisSe_5:1)	$5.7 \cdot 10^{-9}$
P(C_{60}Se_BisSe_2:1)	$4.2 \cdot 10^{-9}$
P(C_{60}Se_BisSe_1:1)	$2.5 \cdot 10^{-9}$
P(C_{60}Se_BisSe_1:2)	$1.2 \cdot 10^{-9}$
P(C_{60}Se_BisSe_1:5)	$4.9 \cdot 10^{-11}$

3.2.3. ATR-IR spectroscopy

Fig. 6 presents the IR spectra of both monomers and P(C_{60}Se_BisSe_1:1) layer recorded in the ATR mode. In the case of fullerene dyad spectrum, four characteristic C_{60} bands are observed at 524 cm^{-1}, 574 cm^{-1}, 1177 cm^{-1} and 1427 cm^{-1}, that can be assigned to the vibrations of pentagons and hexagons of the fullerene cage [48]. The presence of organic unit in the monomer dyad is confirmed by C-H out-of-plane vibrations of the monosubstituted selenophene ring located at 678 cm^{-1} [47]. The latter vibration is the most dominant in the IR spectrum of BisSe, together with the aromatic stretching band at 1427 cm^{-1} [47] and other signals in the fingerprint region at 748 cm^{-1} and 814 cm^{-1}, that can be assigned to the adjacent and isolated out-of-plane bending vibrations of the selenophene ring [49]. For P(C_{60}Se_BisSe_1:1) layer the aromatic stretching vibrations, namely

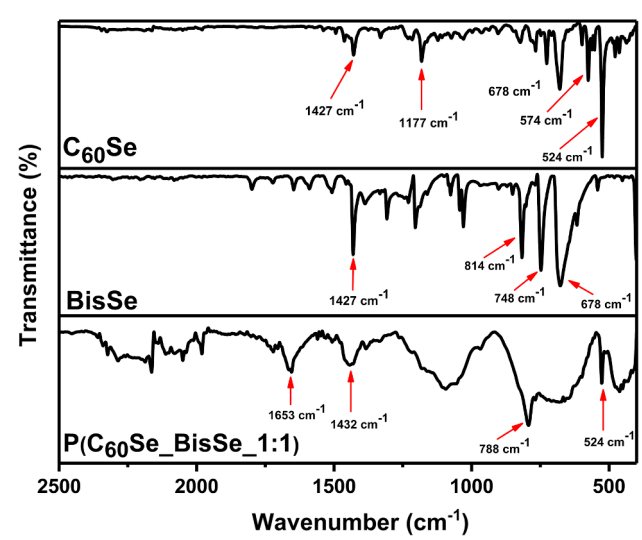

Fig. 6. ATR-IR spectra of C_{60}Se, BisSe and P(C_{60}Se_BisSe_1:1) layer deposited on Pt plate.

symmetric and asymmetric stretching of C = C in the selenophene ring, are observed at 1432 cm^{-1} and 1653 cm^{-1}, respectively [50]. Those bands are significantly broaden when compared to monomers spectra, which is typical for electrodeposited polymeric layers [44]. The effectiveness of the electropolymerization process is also confirmed by the decrease in the relative intensity of 678 cm^{-1} band being specific for the monosubstituted heterocyclic ring. The strong signal at 788 cm^{-1} arises from C-H out-of-plane vibrations in the 2,5-disubstituted selenophene rings, which indicates that the electrochemical polymerization occurs *via* α,α'-mechanism [51]. This is also supported by the absence of the band at ca. 820 cm^{-1} that is characteristic for polyselenophene obtained by α,β-coupling [50]. Moreover, the band located at 524 cm^{-1} confirms the presence of C_{60} units in the deposited photoactive polymeric layer. The position of the vibrations of the fullerene spheres, *i.e.* "pentagonal pinch" A_g mode, in the recorded Raman spectra (Fig. S3) gives the final check of the structure of the formed layer. The mentioned band is located at slightly lower wavenumbers (1455 cm^{-1}) than for the pristine C_{60}, but this can be a result of the additional contribution of the C = C stretching vibration of BisSe, rather than the oligomerization of the fullerene units [52,53].

3.2.4. X-ray phototoelectron spectroscopy

The structures of the electrochemically polymerized photoactive layers were further investigated by XPS (Fig. 7). In the survey spectra obtained for P(C_{60}Se_BisSe_1:1)/ITO layer, given in Fig. 6a, signals of Se 3*d*, S 2*p*, C 1 *s* and N 1 *s* appear at 56 eV, 165 eV, 286 eV and 399 eV, respectively [54,55]. While the presence of selenium, sulfur and nitrogen is specific for the deposited layer, the carbon signal arises from the deposited layer and the so-called adventitious carbon residues [56,57]. The O 1 *s* peak, placed at around 530 eV, has reasonably the same origin, even if the ITO substrate contribution cannot be excluded. Importantly, only weak signals coming from the electrolyte or solvent used during the electrodeposition process, like F 1 *s* at 686 eV, are observed. Similarly, only low-intensity peaks from the ITO substrate are recorded, *i.e.* Sn 3*d* at 485 eV, In 3*d* at 444 eV and Si *2p* at 100 eV [58], which confirms the homogeneity of the layer.

The high-resolution spectra recorded for P(C_{60}Se_BisSe_1:1) are shown in Fig. 7b – d. The experimental data (dashed lines) were fitted using CASA XPS with components given as a product of Gaussian and Lorentzian lines. The Shirley function was used for the background subtraction [20,59]. The decomposition of N 1 *s* region (Fig. 7b) gives one component at 399.4 eV arising from the amine-linker in the fullerene-organic dyad [60]. In the case of two partially overlapping regions, namely S 2*p* and Se 3*p* region (Fig. 7c) four components, *i.e.* Se $3p_{3/2}$ and S $2p_{3/2}$ with their spin–orbit split counterparts can be distinguished at 162.3 eV and 163.9 eV, respectively [54,55,61]. Moreover, for Se 3*d* region (Fig. 7d) two spin–orbit components Se $3d_{5/2}$ and Se $3d_{3/2}$ with 0.86 eV separation and ca. 1.4-ratio are observed [62,63]. The position of both S $2p_{3/2}$ and Se $3d_{5/2}$ confirms the presence of thiophene- and selenophene-containing organic layer on the ITO surface. Importantly, since no additional components are observed in S 2*p* or Se 3*d* regions, it can be stated that no oxidized species are present within 2–3 nm from the sample surface [55,61]. The analysis of the C 1 *s* spectrum (Fig.S4) reveals the presence of five components arising from both - the deposited layer and the adventitious carbon [64]. The ratio between the components (Tab.S1) is in good agreement with the stoichiometry of the layer, confirming that the contamination is not significant.

Taking into account that N 1 s signal recorded at 399.4 eV arises from the amine-linker that is present only in the C_{60}Se dyad, the high-

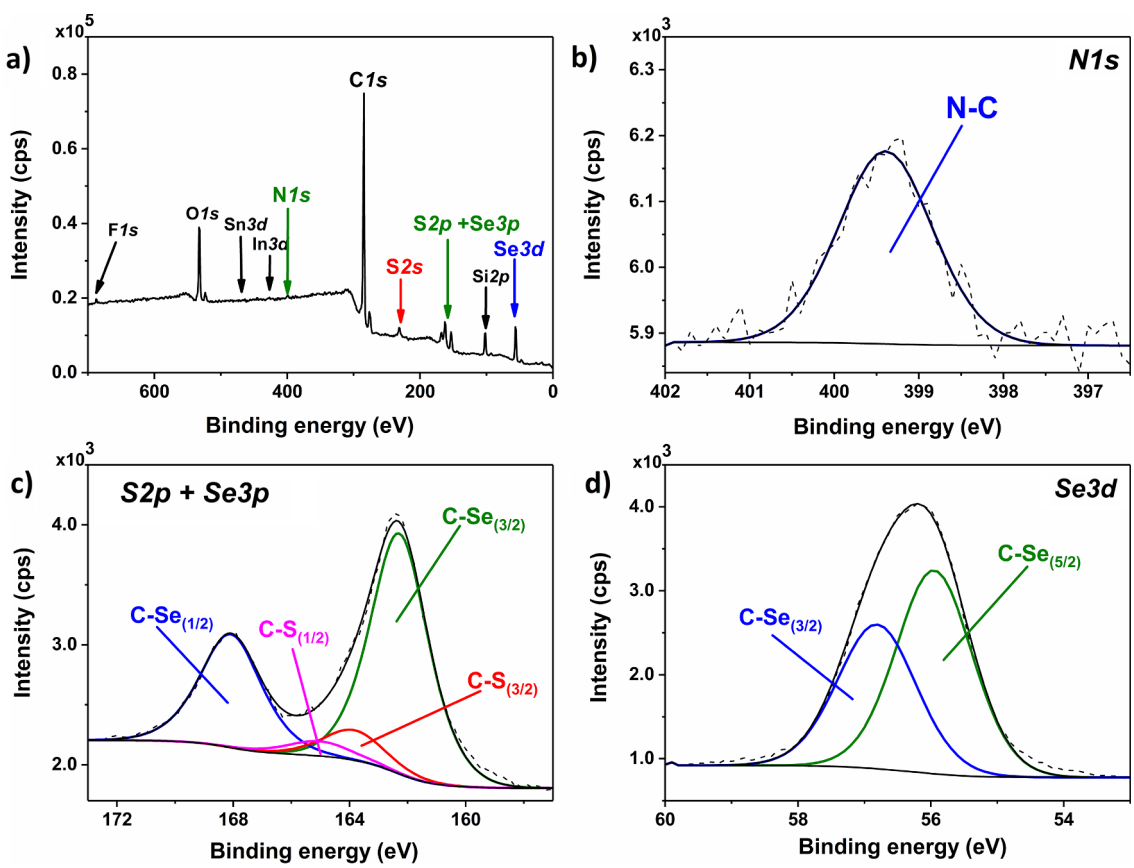

Fig. 7. XPS a) wide scan (pass energy 40 eV) and high resolution spectra b) N 1 s, c) S 2p + Se 3p and d) Se 3d recorded for P(C_{60}Se_BisSe_1:1) layer deposited on ITO.

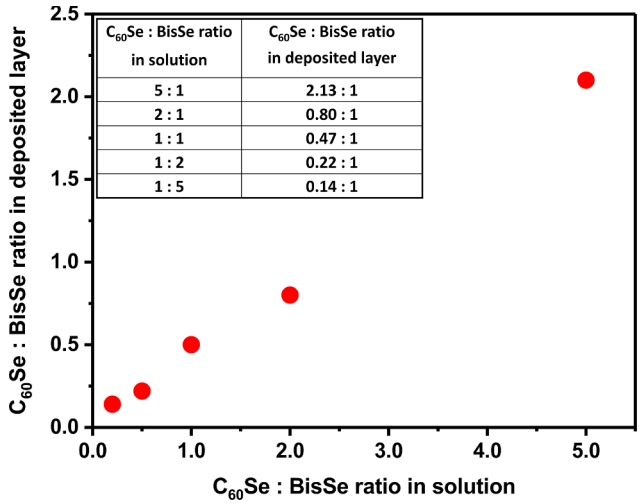

Fig. 8. Composition of photoactive layer as a function of monomers ratio in feed solution.

resolution N 1 *s* and Se 3*d* regions after correcting the signal intensity for the element and the transition specific photoemission cross sections, were in turn used to estimate the composition of the deposited P(C_{60}Se_BisSe) layers. Fig. 8 presents the relation between the composition of the feed solution and the monomers ratio in the resulting layer. As assumed, the monomers ratio in the solution strongly influences the deposited layer composition: the increase in the concentration of the fullerene-containing monomer yields layers with higher C_{60} content, with almost linear relation. This is in agreement with the above-mentioned CV and UV–Vis spectroscopy results. The estimated monomers ratios in the deposited layers are not equal to the ones in the feed solutions. The significantly higher content of BisSe units was observed, which suggests that, though both monomers undergo irreversible oxidation at similar potentials, the electropolymerization of BisSe monomer is more effective, probably because of the steric effect.

3.3. Singlet oxygen photogeneration by P(C_{60}Se:BisSe) layers

The photogeneration of singlet oxygen in homogenous and heterogeneous systems can be investigated directly, *i.e.* by measuring luminesce at ca. 1270 nm, or indirectly with chemical traps. Since the emission signal of singlet oxygen is quite weak, the second strategy is more common. Various chemical traps that can be monitored with UV–Vis or EPR spectroscopies have been proposed for the indirect detection of $^1O_2$ [65,66]. In this work, α-terpinene was used for the investigation of visible light photogeneration of ROS, while DPBF – specific singlet oxygen quencher, was applied under green-light illumination for the determination of the quantum yield.

The effectiveness of the visible light-induced photooxidation reaction was monitored by UV–Vis spectroscopy as the decrease in the absorption of α-terpinene at 266 nm [20]. Fig. 9a presents the UV–Vis spectra of α-terpinene recorded during illumination of P(C_{60}Se_BisSe_1:1) layer with the xenon lamp equipped with the filter transmitting only visible radiation. The decrease in the characteristic absorption band of α-terpinene observed at 266 nm indicates its reaction with ROS photogenerated by P(C_{60}Se_BisSe_1:1) layer. The photooxidation of α-terpinene results in the formation of ascaridole (Fig. 2a) [16,67]. Importantly, the deposited layer is not dissolving in the reaction medium, since no new bands are observed in the recorded spectra during the photoprocess.

Fig. 9b shows that almost no decrease in the substrate absorbance is observed when unmodified ITO is illuminated, which confirms that under applied conditions the process of α-terpinene self-decomposition can be excluded. Additionally, the decrease in the absorbance after 30 min of illumination is significantly higher for the electrochemically deposited polymeric layer containing fullerenes than for the layer containing only BisSe monomer. Thus, it can be stated that incorporated C_{60} photosensitizers are mainly responsible for the ROS photogeneration. As in our previous work, it is shown that the photosensitizers based on carbon nanostructures retain their photoactivity after deposition on a solid support [34].

The activity of P(C_{60}Se_BisSe_1:1) layer towards singlet oxygen was also tested applying DPBF - chemical quencher and 532 nm laser as an illumination source. Fig. S5 presents the UV–Vis spectra of DPBF in methanol recorded during irradiation of P(C_{60}Se_BisSe_1:1) layer with the green laser. The drop in the DPBF absorbance at 410 nm confirms that the energy transfer from the poly(selenophene) matrix to C_{60} can occur and it may result in the formation of $^1O_2$ species [4,6,7,68-71]. The quantum yield of singlet oxygen photogeneration was determined by the DPBF-method with Rose Bengal as a reference [36-38]. Φ is equal to ca. 0.7% for P(C_{60}Se_BisSe_1:1) and P(C_{60}Se) layers, suggesting that the efficiency of the above-mentioned energy transfer is comparable in both cases, even if the additional organic-only component (BisSe) acting mainly as a visible light antenna, is introduced into the deposited layer.

Further, as presented in Fig. 9b, the drop in α-terpinene absorbance at 266 nm is ca. 2.5-times higher for P(C_{60}Se_BisSe_1:1) layer than for the layer consisting of the fullerene dyad only - P(C_{60}Se). This can be explained by higher absorbance of the photoactive layer containing BisSe units in the visible range, which confirms the effectiveness of the assumed strategy.

In the next step, all electrochemically co-deposited layers were applied as a source of $^1O_2$ in the oxidation of α-terpinene, yielding similar set of spectra as presented in Fig. 9a. In order to compare the efficiency of the photoprocess, the rate constants were determined based on the drop of α-terpinene concentration. Assuming the pseudo-zero order kinetics [20], the rate constants were estimated with a linear regression as a slope of the line (c-$c_{initial}$) vs. time. As it can be seen in Table 2, the highest value of the rate constant was observed for the polymeric layer deposited from the feed solution with monomers ratio equal to 1. Further increase in the content of the organic unit or fullerene-dyad resulted in the drop of the reaction rate. This indicates that the ratio between the fullerene photosensitizer and the poly(selenophene) matrix, acting as an antenna for visible light, is the best optimized in the case of P(C60Se_BisSe_1:1) layer.

4. Conclusions

In the presented work, C_{60}Se fullerene-dyad was electrochemically co-deposited with bis-selenophene on Pt or ITO/glass, yielding the polymeric matrix with incorporated C_{60} photosensitizers. The proposed strategy resulted in the formation of the thin photoactive layer, which structure was confirmed with electrochemical and spectroscopic techniques. It was shown that the composition of the resulting layer can be simply varied by changing the monomers ratio in the feed solution. This, in turn, allows to tune the spectroscopic properties, namely the absorption in the visible range, and the photosensitizing properties of the deposited films. It was found that the layer with ca. 1:2 ratio between the fullerene dyad and bis-selenophene units, formed from the equimolar solution, shows the highest efficiency of singlet oxygen photogeneration under visible light illumination. The quantum yield of the photoprocess was comparable for C_{60}Se_BiSe and C_{60}Se-only layers. The presented results demonstrate that the efficiency of the visible light photogeneration can be simply enhanced by the introduction of the visible light-harvesting organic units into fullerene-containing photoactive layer.

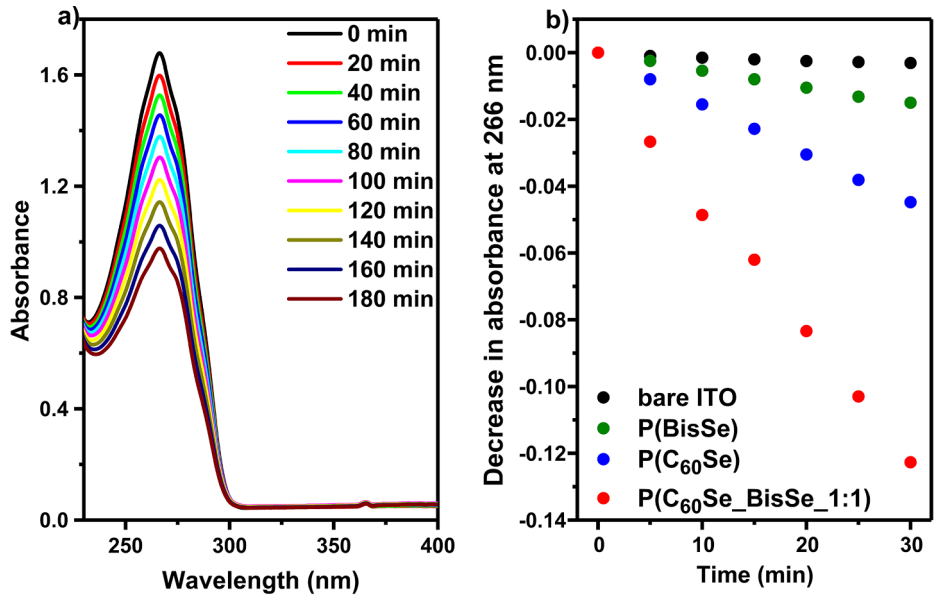

Fig. 9. a) UV–Vis spectra of α-terpinene recorded during illumination of P(C60Se_BisSe_1:1) layer with xenone lamp equipped with filter transmitting > 400 nm, b) decrease in the absorbance of α-terpinene at 266 nm during illumination of P(C60Se_BisSe_1:1), P(BisSe), P(C60Se) layers deposited on ITO and unmodified ITO.

Table.2
Rate constants of α-terpinene photooxidation reaction with singlet oxygen generated by P(C_{60}Se_BisSe) layers with various composition.

Photoactive layer	k [$mM^{-1}min^{-1}$]
P(C_{60}Se_BisSe_5:1)	$(1.72 \pm 0.01)\cdot10^{-4}$
P(C_{60}Se_BisSe_2:1)	$(2.85 \pm 0.01)\cdot10^{-4}$
P(C_{60}Se_BisSe_1:1)	$(5.10 \pm 0.02)\cdot10^{-4}$
P(C_{60}Se_BisSe_1:2)	$(2.52 \pm 0.01)\cdot10^{-4}$
P(C_{60}Se_BisSe_1:5)	$(1.30 \pm 0.01)\cdot10^{-4}$
P(C_{60}Se)	$(2.03 \pm 0.01)\cdot10^{-4}$

CRediT authorship contribution statement

Aleksandra Nyga: Investigation, Visualization. **Radoslaw Motyka:** Investigation. **Gianlorenzo Bussetti:** Investigation, Formal analysis, Writing - review & editing. **Alberto Calloni:** Investigation, Formal analysis. **Madan Sangarashettyhalli Jagadeesh:** Investigation. **Sylwia Fijak:** Investigation. **Sandra Pluczyk-Malek:** Validation, Writing - review & editing. **Przemyslaw Data:** Supervision, Funding acquisition. **Agata Blacha-Grzechnik:** Conceptualization, Methodology, Investigation, Formal analysis, Visualization, Writing - original draft, Writing - review & editing.

Acknowledgements

This work was supported by National Science Center, Poland (grand number: 2016/21/D/ST5/01641). A.N. & P.D. kindly acknowledge the support received from the First Team program of the Foundation for Polish Science co-financed by the European Union under the European Regional Development Fund (project number: First TEAM POIR.04.04.00-00-4668/17-00).

Appendix A. Supplementary data

Supplementary data (Synthesis and spectroscopic characterization of C_{60}Se and BisSe monomers. Scheme of setup for *in-situ* investigation of singlet oxygen photogeneration. Raman spectra of P(BisSe) and P(C_{60}Se:BisSe) layers. XPS high resolution spectrum C1s recorded for P(C_{60}Se_BisSe_1:1) layer deposited on ITO. UV–Vis spectra of DPBF recorded during illumination of P(C_{60}Se_BisSe_1:1) layer with 532 nm diode laser.) to this article can be found online at https://doi.org/10.1016/j.apsusc.2020.146594.

References

[1] J. Wahlen, D.E. de Vos, P.A. Jacobs, L. Alsters, Solid Materials as Sources for Synthetically Useful Singlet Oxygen, Adv. Synth. Catal. 346 (2004) 152–164, https://doi.org/10.1002/adsc.200303224.
[2] J. Wang, H. Huang, Z. Xu, J. Kou, C. Lu, The Potential of Carbon-based Materials for Photocatalytic Application The Potential of Carbon-based Materials for Photocatalytic Application, Curr. Org. Chem. 18 (2014) 1346–1364, https://doi.org/10.2174/1385272819666140424214022.
[3] F. Prat, R. Stackow, R. Bernstein, W. Qian, Y. Rubin, C.S. Foote, Triplet-State Properties and Singlet Oxygen Generation in a Homologous Series of Functionalized Fullerene Derivatives, J. Phys. Chem. A. 103 (1999) 7230–7235, https://doi.org/10.1021/jp991237o.
[4] B. Vileno, A. Sienkiewicz, M. Lekka, A. Kulik, L. Forro, In vitro assay of singlet oxygen generation in the presence of water-soluble derivatives of C60, Carbon N. Y. 42 (2004) 1195–1198, https://doi.org/10.1016/j.carbon.2003.12.042.
[5] T. Hamano, K. Okuda, T. Mashino, M. Hirobe, K. Arakane, A. Ryu, Singlet oxygen production from fullerene derivatives : effect of sequential functionalization of the fullerene core, Chem. Commun. (1997) 21–22, https://doi.org/10.1039/A606335G.
[6] L. Huang, X. Cui, B. Therrien, J. Zhao, Energy-Funneling-Based Broadband Visible-Light-Absorbing Bodipy–C60 Triads and Tetrads as Dual Functional Heavy-Atom-Free Organic Triplet Photosensitizers for Photocatalytic Organic Reactions, Chem. - A Eur. J. 19 (2013) 17472–17482, https://doi.org/10.1002/chem.201302492.
[7] Y. Wei, M. Zhou, Q. Zhou, X. Zhou, S. Liu, S. Zhang, B. Zhang, Triplet-triplet Annihilation Upconversion Kinetics of C60-Bodipy Dyads as Organic Triplet Photosensitizers, Phys. Chem. Chem. Phys. 33 (2017) 8689–8691, https://doi.org/10.1039/C7CP03840B.
[8] W. Wu, J. Zhao, J. Sun, S. Guo, Light-Harvesting Fullerene Dyads as Organic Triplet Photosensitizers for Triplet − Triplet Annihilation Upconversions, J. Org. Chem. 77 (2012) 5305–5312, https://doi.org/10.1021/jo300613g.
[9] M.C. DeRosa, R.J. Crutchley, Photosensitized singlet oxygen and its applications, Coord. Chem. Rev. 233–234 (2002) 351–371, https://doi.org/10.1016/S0010-8545(02)00034-6.
[10] S. Nonell, C. Flors, Singlet Oxygen: Applications in Biosciences and Nanosciences, Royal Society of Chemistry (2016), https://doi.org/10.1039/9781782622208.
[11] M.S. Baptista, J. Cadet, P. Di Mascio, A.A. Ghogare, A. Greer, M.R. Hamblin, C. Lorente, S.C. Nunez, M. Sim, H. Thomas, M. Vignoni, T.M. Yoshimura, Type I and Type II Photosensitized Oxidation Reactions : Guidelines and Mechanistic Pathways, Photochem. Photobiol. 93 (2017) 912–919, https://doi.org/10.1111/php.12716.
[12] H. Zou, F. Jin, X. Song, J. Xing, Singlet oxygen generation of photosensitizers effectively activated by Nd3+-doped upconversion nanoparticles of luminescence intensity enhancing with shell thickness decreasing, Appl. Surf. Sci. 400 (2017) 81–89, https://doi.org/10.1016/j.apsusc.2016.12.174.
[13] P.R. Ogilby, Singlet oxygen : there is indeed something new under the sun, Chem. Soc. Rev. 39 (2010) 3181–3209, https://doi.org/10.1039/b926014p.

[14] P.R. Ogilby, C.S. Foote, Chemistry of Singlet Oxygen. 42. Effect of solvent, Solvent Isotopic Substitution, and Temperature on the Lifetime of Singlet Molecular Oxygen, J. Am. Chem. Soc. 105 (1983) 3423–3430, https://doi.org/10.1021/ja00349a007.

[15] K.I. Salokhiddinov, I.M. Bytev, G.P. Gurinovich, Lifetime of singlet oxygen in various solvents, J. Appl. Scpectroscopy. 34 (1981) 561–564, https://doi.org/10.1007/bf00613067.

[16] J. Kyriakopoulos, M.D. Tzirakis, G.D. Panagiotou, M.N. Alberti, K.S. Triantafyllidis, S. Giannakaki, K. Bourikas, C. Kordulis, M. Orfanopoulos, A. Lycourghiotis, Highly active catalysts for the photooxidation of organic compounds by deposition of [60] fullerene onto the MCM-41 surface : A green approach for the synthesis of fine chemicals, Appl. Catal. B, Environ. 117–118 (2012) 36–48. doi:10.1016/j.apcatb.2011.12.024.

[17] S. Guo, H. Zhang, L. Huang, Z. Guo, G. Xiong, J. Zhao, Porous material-immobilized iodo-Bodipy as an efficient photocatalyst for photoredox catalytic organic reaction to prepare pyrrolo[2,1- a]isoquinoline, Chem. Commun. 49 (2013) 8689–8691, https://doi.org/10.1039/c3cc44486d.

[18] M. Condat, J. Babinot, S. Tomane, J.-P. Malval, I.-K. Kang, F. Spillebout, P.-E. Mazeran, J. Lalevee, S.A. Andalloussi, D.-L. Versace, Development of photo-activable glycerol-based coatings containing quercetin for antibacterial, RSC Adv. 6 (2016) 18235–18245, https://doi.org/10.1039/c5ra25267a.

[19] C. Piccirillo, S. Perni, J. Gil-Thomas, P. Prokopovich, M. Wilson, J. Pratten, I.P. Parkin, Antimicrobial activity of methylene blue and toluidine blue O covalently bound to a modified silicone polymer surface, J. Mater. Chem. 34 (2009) 6167–6171, https://doi.org/10.1039/b905495b.

[20] A. Blacha-Grzechnik, M. Krzywiecki, R. Motyka, Electrochemically Polymerized Terthiopehene − C60 Dyads for the Photochemical Generation of Singlet Oxygen, J. Phys. Chem. C. 123 (2019) 25915–25924, https://doi.org/10.1021/acs.jpcc.9b06101.

[21] S. Ren, M. Bernardi, R.R. Lunt, V. Bulovic, J.C. Grossman, S. Gradecak, Toward Efficient Carbon Nanotube / P3HT Solar Cells: Active Layer Morphology, Electrical and Optical Properties, Nano Lett. 11 (2011) 5316–5321, https://doi.org/10.1021/nl202796u.

[22] D. Meng, D. Sun, C. Zhong, T. Liu, B. Fan, L. Huo, Y. Li, W. Jiang, H. Choi, T. Kim, J.Y. Kim, Y. Sun, Z. Wang, A.J. Heeger, High-Performance Solution-Processed Non-Fullerene Organic Solar Cells based on Selenophene-Containing Perylene Bisimide Acceptor, J. Am. Chem. Soc. 138 (2016) 375–380, https://doi.org/10.1021/jacs.5b11149.

[23] Y. Lin, J. Wang, Z. Zhang, H. Bai, Y. Li, D. Zhu, X. Zhan, An Electron Acceptor Challenging Fullerenes for Efficient Polymer Solar Cells, Adv. Mater. 27 (2015) 1170–1174, https://doi.org/10.1002/adma.201404317.

[24] L. Zhong, H. Bin, I. Angunawela, Z. Jia, B. Qiu, C. Sun, X. Li, Z. Zhang, H. Ade, Y. Li, Effect of Replacing Thiophene by Selenophene on the Photovoltaic Performance of Wide Bandgap Copolymer Donors, Macromolecules. 52 (2019) 4776–4784, https://doi.org/10.1021/acs.macromol.9b00484.

[25] N. Grossiord, J.M. Kroon, R. Andriessen, P.W.M. Blom, Degradation mechanisms in organic photovoltaic devices, Org. Electron. 13 (2012) 432–456, https://doi.org/10.1016/j.orgel.2011.11.027.

[26] B.R. Pacios, A.J. Chatten, K. Kawano, J.R. Durrant, D.D.C. Bradley, J. Nelson, Effects of Photo-oxidation on the Performance of Poly[2-methoxy-5-(3',7'-dimethyloctyloxy)-1,4-phenylene vinylene]:[6,6] -PhenylC61-Butyric Acid Methyl Ester Solar Cells, Adv. Funct. Mater. 16 (2006) 2117–2126, https://doi.org/10.1002/adfm.200500714.

[27] M. Bregnhøj, M. Prete, V. Turkovic, A.U. Petersen, M.B. Nielsen, M. Madsen, P.R. Ogilby, Oxygen-dependent photophysics and photochemistry of prototypical compounds for organic photovoltaics: inhibiting degradation initiated by singlet oxygen at a molecular level, Methods Appl. Fluoresc. 8 (2020) 14001, https://doi.org/10.1088/2050-6120/ab4edc.

[28] A. Tournebize, M. Seck, A. Vincze, A. Distler, H. Egelhaaf, C.J. Brabec, A. Rivaton, H. Peisert, T. Chassé, Solar Energy Materials & Solar Cells Photodegradation of Si-PCPDTBT : PCBM active layer for organic solar cells applications : A surface and bulk investigation, Sol. Energy Mater. Sol. Cells. 155 (2016) 323–330, https://doi.org/10.1016/j.solmat.2016.06.026.

[29] A. Distler, P. Kutka, T. Sauermann, H. Egelhaaf, D.M. Guldi, D. Di Nuzzo, S.C.J. Meskers, R.A.J. Janssen, Effect of PCBM on the Photodegradation Kinetics of Polymers for Organic Photovoltaics, Chem. Mater. 24 (2012) 4397–4405, https://doi.org/10.1021/cm302623p.

[30] P. Data, M. Lapkowski, R. Motyka, J. Suwinski, Electrochimica Acta Influence of heteroaryl group on electrochemical and spectroscopic properties of conjugated polymers, Electrochim. Acta. 83 (2012) 271–282, https://doi.org/10.1016/j.electacta.2012.08.020.

[31] J.P. Parrish, V.L. Flanders, R.J. Floyd, K.W. Jung, Mild and efficient formation of symmetric biaryls via Pd (II) catalysts and Cu (II) oxidants, Tetrahedron Lett. 42 (2001) 7729–7731, https://doi.org/10.1016/S0040-4039(01)01691-4.

[32] D. Bonifazi, O. Enger, F. Diederich, Supramolecular [60] fullerene chemistry on surfaces, Chem. Soc. Rev. 36 (2007) 390–414, https://doi.org/10.1039/b604308a.

[33] G. Berti, A. Calloni, A. Brambilla, G. Bussetti, L. Duò, F. Ciccacci, Direct observation of spin-resolved full and empty electron states in ferromagnetic surfaces, Rev. Sci. Instrum. 85 (2014) 073901, , https://doi.org/10.1063/1.4885447.

[34] A. Blacha-Grzechnik, K. Piwowar, T. Zdyb, M. Krzywiecki, Formation of poly(Azure A) -C60 photoactive layer as a novel approach in the heterogeneous photogeneration of singlet oxygen, Appl. Surf. Sci. 457 (2018) 221–228, https://doi.org/10.1016/j.apsusc.2018.06.262.

[35] F. Lv, Y. Yu, E. Hao, C. Yu, H. Wang, L. Jiao, Highly Regioselective α -Formylation and α -Acylation of BODIPY Dyes via Tandem Cross-Dehydrogenative Coupling with in situ Deprotection, Org. Biomol. Chem. (2019) 1–44, https://doi.org/10.1016/j.cclet.2019.08.004.

[36] C.R. Lambert, I.E. Kochevar, Does Rose Bengal Triplet Generate Superoxide Anion ? J. Am. Chem. Soc. 118 (1996) 3297–3298, https://doi.org/10.1021/ja9600800.

[37] M.I. Burguete, F. Galindo, R. Gavara, S.V. Luis, M. Moreno, D.A. Russell, Singlet oxygen generation using a porous monolithic polymer supported photosensitizer : potential application to the photodynamic destruction of melanoma cells, Photochem. Photobiol. Sci. 8 (2009), https://doi.org/10.1039/b810921d.

[38] N. Epelde-Elezcano, V. Martinez-Martinez, E. Pena-Cabrera, C.F.A. Gomez-Duran, I.L. Arbeloa, S. Lacombe, Modulation of singlet oxygen generation in halogenated BODIPY dyes by substitution at their meso position : towards a solvent-independent standard in the vis region, RSC Adv. 6 (2016) 41991–41998, https://doi.org/10.1039/c6ra05820e.

[39] K. Piwowar, A. Blacha-Grzechnik, R. Turczyn, J. Zak, Electropolymerized phenothiazines for the photochemical generation of singlet oxygen, Electrochim. Acta. 141 (2014) 182–188, https://doi.org/10.1016/j.electacta.2014.07.052.

[40] J. Chen, G. Tsekouras, D.L. Officer, P. Wagner, C.Y. Wang, C.O. Too, G.G. Wallace, Novel fullerene-functionalised poly(terthiophenes), J. Electroanal. Chem. 599 (2007) 79–84, https://doi.org/10.1016/j.jelechem.2006.09.007.

[41] S. Pluczyk, W. Kuznik, M. Lapkowski, R.R. Reghu, J.V. Grazulevicius, The effect of the linking topology on the electrochemical and spectroelectrochemical properties of carbazolyl substituted perylene bisimides, Electrochim. Acta. 135 (2014) 487–494, https://doi.org/10.1016/j.electacta.2014.05.057.

[42] S. Pluczyk, P. Zassowski, C. Quinton, P. Audebert, V. Alain-Rizzo, M. Lapkowski, Unusual Electrochemical Properties of the Electropolymerized Thin Layer Based on a s-Tetrazine-Triphenylamine Monomer, J. Phys. Chem. C. 120 (2016) 4382–4391, https://doi.org/10.1021/acs.jpcc.5b11555.

[43] M. Czichy, P. Wagner, M. Lapkowski, D.L. Officer, Effect of π -conjugation on electrochemical properties of poly (terthiophene)s 3'-substituted with fullerene C60, J. Electroanal. Chem. 772 (2016) 103–109, https://doi.org/10.1016/j.jelechem.2016.04.009.

[44] B. Lu, S. Zhen, S. Ming, J. Xu, G. Zhao, RSC Advances (2015) 70649–70660, https://doi.org/10.1039/c5ra11849b.

[45] M. Ak, H. Ceti, L. Toppare, Blend or copolymer ? Spectroelectrochemical evidence of copolymerization and blending of two electrochromic monomers, Colloid Polym. Sci. 291 (2013) 767–772, https://doi.org/10.1007/s00396-012-2787-7.

[46] R. Holze, Copolymers — A refined way to tailor intrinsically conducting polymers, Electrochim. Acta. 56 (2011) 10479–10492, https://doi.org/10.1016/j.electacta.2011.04.013.

[47] B. Dong, Y. Xing, J. Xu, L. Zheng, J. Hou, F. Zhao, Electrosyntheses of free-standing and highly conducting polyselenophene films in an ionic liquid, Electrochim. Acta. 53 (2008) 5745–5751, https://doi.org/10.1016/j.electacta.2008.03.049.

[48] G. Rambabu, S.D. Bhat, Sulfonated fullerene in SPEEK matrix and its impact on the membrane electrolyte properties in direct methanol fuel cells, Electrochim. Acta. 176 (2015) 657–669, https://doi.org/10.1016/j.electacta.2015.07.045.

[49] C.Y. Park, Y.J. Kim, H.J. Lim, J.H. Park, M.J. Kim, S.W. Seo, C.P. Park, RSC Advances (2015) 4233–4237, https://doi.org/10.1039/C4RA12965B.

[50] J. Xu, J. Hou, S. Zhang, G. Nie, S. Pu, L. Shen, Q. Xiao, Electrosyntheses of high quality freestanding polyselenophene films in boron trifluoride diethyl etherate, J. Electroanal. Chem. 578 (2005) 345–355, https://doi.org/10.1016/j.jelechem.2005.01.016.

[51] Jean Roncali, Conjugated poly(thiophenes): synthesis, functionalization, and applications, Chem. Rev. 92 (4) (1992) 711–738, https://doi.org/10.1021/cr00012a009.

[52] H. Chadli, A. Rahmani, J.L. Sauvajol, Raman spectra of C60 dimer and C60 polymer confined inside a (10, 10) single-walled carbon nanotube, J. Phys. Condens. Matter. 22 (2010), https://doi.org/10.1088/0953-8984/22/14/145303.

[53] B. Sundqvist, Raman identification of C70 monomers and dimers, Diam. Relat. Mater. 73 (2017) 143–147, https://doi.org/10.1016/j.diamond.2016.09.001.

[54] N. Chanunpanich, A. Ulman, Y.M. Strzhemechny, S.A. Schwarz, J. Dornicik, M. Rafailovich, J. Sokolov, A. Janke, H.G. Braun, T. Kratzmüller, Polythiophene grafted on polyethylene film, Mater. Res. Soc. Symp. - Proc. 600 (2000) 203–208, https://doi.org/10.1557/proc-600-203.

[55] R.J. Thorn, K.D. Carlson, G.W. Crabtree, H.H. Wang, States determined by photoelectron spectroscopy in the perchlorate and perrhenate of TMTSF, J. Phys. C Solid State Phys. 18 (1985) 5501–5510, https://doi.org/10.1088/0022-3719/18/28/019.

[56] B.L. Hurley, R.L. Mccreery, Covalent Bonding of Organic Molecules to Cu and Al Alloy 2024 T3 Surfaces via Diazonium Ion Reduction, J. Electrochem. Soc. 151 (2004) B252–B259, https://doi.org/10.1149/1.1687428.

[57] P. Powroźnik, L. Grządziel, W. Jakubik, M. Krzywiecki, Sarin-simulant detection by phthalocyanine/palladium structures: from modeling to real sensor response, Sensors Actuators B. Chem. 273 (2018) 771–777, https://doi.org/10.1016/j.snb.2018.06.101.

[58] O. Gu-ping, G. Wen-ming, J. Shi-chao, Z. Fu-jia, Surface analysis for LiBq4 growing on ITO and CuPc film using atomic force microscopy (AFM) and X-ray photoelectron spectroscopy (XPS), Appl. Surf. Sci. 252 (2006) 3417–3427, https://doi.org/10.1016/j.apsusc.2005.01.042.

[59] M.S. Jagadeesh, G. Bussetti, A. Calloni, R. Yivlialin, L. Brambilla, A. Accogli, E. Gibertini, D. Alliata, C. Goletti, F. Ciccacci, L. Magagnin, C. Castiglioni, L. Duo, Incipient Anion Intercalation of Highly Oriented Pyrolytic Graphite Close to the Oxygen Evolution Potential : A Combined X - ray Photoemission and Raman Spectroscopy Study, J. Phys. Chem. C. 123 (2019) 1790–1797, https://doi.org/10.1021/acs.jpcc.8b09823.

[60] R.J.J. Jansen, H. van Bekkum, XPS of nitrogen-containing functional groups on activated carbon, Carbon N. Y. 33 (1995) 1021–1027, https://doi.org/10.1016/0008-6223(95)00030-H.

[61] T. Teslaru, I. Topala, M. Dobromir, V. Pohoata, L. Curecheriu, N. Dumitrascu, Polythiophene films obtained by polymerization under atmospheric pressure plasma conditions, Mater. Chem. Phys. 169 (2016) 120–127, https://doi.org/10.1016/j.matchemphys.2015.11.038.
[62] B. Canava, J. Vigneron, A. Etcheberry, J.F. Guillemoles, D. Lincot, High resolution XPS studies of Se chemistry of a Cu (In, Ga) Se 2 surface, Appl. Surf. Sci. 202 (2002) 8–14, https://doi.org/10.1016/S0169-4332(02)00186-1.
[63] I. Ikemoto, K. Kikuchi, K. Yahuski, H. Kuroa, K. Kobayashi, X-Ray Photoelectron Spectroscopy of Tetramethyltetraselenapulvalene (TMTSF) complexes, Solid State Commun. 42 (1982) 257–259, https://doi.org/10.1017/CBO9781107415324.004.
[64] G. Beamson, D. Briggs, XPS of Organic Polymers, John Wiley & Sons, Chichester, 1992.
[65] N. Miyoshi, G. Tomita, Production and Reaction of Singlet Oxygen in Aqueous Micellar Solutions Using Pyrene as Photosensitizer, Zeitschrift Fur Naturforsch. B. 33 (1978) 622–627, https://doi.org/10.1515/znb-1978-0612.
[66] M. Wainwright, K. Meegan, C. Loughran, R.M. Giddens, Phenothiazinium photosensitisers, Part VI: Photobactericidal asymmetric derivatives, Dye. Pigment. 82 (2009) 387–391, https://doi.org/10.1016/j.dyepig.2009.02.011.
[67] J. Cai, J. Huang, H. Yu, L. Ji, Synthesis, Characterization, and Photocatalytic Activity of TiO2 Microspheres Functionalized with Porphyrin, Int. J. Photoenergy. 2012 (2012) 1–10, https://doi.org/10.1155/2012/348292.
[68] M. Narutaki, K. Takimiya, T. Otsubo, Y. Harima, H. Zhang, Y. Arki, O. Ito, Synthesis and Photophysical Properties of Two Dual Oligothiophene-Fullerene Linkage Molecules as Photoinduced Long-Distance Charge Separation Systems, J. Org. Chem. 71 (2006) 1761–1768, https://doi.org/10.1021/jo051821v.
[69] T. Yamashiro, Y. Aso, T. Otsubo, H. Tang, Y. Harima, K. Yamashita, Intramolecular Energy Transfer of [60]Fullerene-linked Oligothiophenes, Chem. Lett. 28 (1999) 443–444, https://doi.org/10.1246/cl.1999.443.
[70] K. Matsumoto, M. Fujitsuka, T. Sato, S. Onodera, O. Ito, Photoinduced Electron Transfer from Oligothiophenes / Polythiophene to Fullerenes (C60 / C70) in Solution : Comprehensive Study by Nanosecond Laser Flash Photolysis Method, J. Phys. Chem. B. 104 (2000) 11632–11638, https://doi.org/10.1021/jp002228e.
[71] B. Vileno, M. Lekka, A. Sinekiewicz, P. Marcoux, A.J. Kulik, S. Kasas, S. Catsicas, G. Alfred, L. Forro, Singlet oxygen (1Δg) -mediated oxidation of cellular and subcellular components : ESR and AFM assays, J. Phys. Condens. Mater. 17 (2005) S1471–S1482, https://doi.org/10.1088/0953-8984/17/18/005.

Materials Advances

ROYAL SOCIETY OF CHEMISTRY

PAPER

View Article Online
View Journal | View Issue

Check for updates

Cite this: *Mater. Adv.*, 2022, 3, 2063

Singlet oxygen formation from photoexcited P3HT:PCBM films applied in oxidation reactions†

Aleksandra Nyga,[ab] Agata Blacha-Grzechnik,*[ab] Przemysław Podsiadły,[b] Alicja Duda,[b] Kinga Kępska,[a] Maciej Krzywiecki,[c] Radosław Motyka,[b] René A. J. Janssen[d] and Przemysław Data*[a]

Received 5th December 2021,
Accepted 13th January 2022

DOI: 10.1039/d1ma01151k

rsc.li/materials-advances

Poly(3-hexylthiophene) thin films containing carbon-based nanostructures, *i.e.* fullerenes such as buckminsterfullerene (C_{60}) or phenyl-C_{61}-butyric acid methyl ester (PCBM), or single-walled carbon nanotubes, were investigated as heterogeneous photosensitizers producing singlet oxygen ($^1O_2$) in aerated organic solvents. Thin films were deposited on borosilicate glass using spin coating and characterized by profilometry, UV-vis, Raman and XPS. Photogeneration of $^1O_2$ was confirmed by photooxidation of 1,3-diphenylisobenzofuran and by reaction of 1,5-dihydroxynaphthalene to juglone. The photochemical efficiency of the blends was found to depend on the carbon-based photosensitizer and can be increased by varying its concentration in the poly(3-hexylthiophene) matrix.

1. Introduction

Blends of conjugated polymers and carbon nanostructures, such as fullerenes and carbon nanotubes (CNTs), have been under high scientific interest for application in organic photovoltaic (OPV) devices[1–3] and have been extensively studied for their photophysical properties. In polymer:fullerene blends two competitive processes have been identified to occur from the initially-formed interfacial charge-transfer state: charge separation and charge recombination into a triplet state.[4] The efficiencies of these processes not only depend on the individual properties of the donor and acceptor in the blend, but also on their ratio and the layer morphology.[5,6] Triplet generation is considered as a significant drawback in OPV, because it reduces the short-circuit current density, open-circuit voltage, and power conversion efficiency, and in the presence of oxygen may lead to the formation of singlet oxygen ($^1O_2$) which is highly reactive and destructive for the photoactive layers.[7,8]

Though the formation of $^1O_2$ may be unfavorable for organic electronic devices, it received much scientific attention as an efficient oxidative agent in fine-chemicals synthesis, wastewater treatment, and in photodynamic therapy (PDT).[9–13] The direct optical excitation of triplet ground state oxygen to the singlet excited state is spin-forbidden, but $^1O_2$ formation is possible using photosensitizers. In such a process, a photosensitizer absorbs light, forming a singlet-excited state (S_1) and converts to a triplet-excited state (T_1) *via* intersystem crossing (ISC) that can subsequently transfer its energy in a spin-allowed reaction to ground state triplet oxygen ($^3O_2$) resulting in formation of singlet-state oxygen and the photosensitizer in the ground state.[9,13]

The most commonly studied photoactive molecules are organic dyes, transition metal complexes, and inorganic oxides.[9,10,13] In recent years, carbon-based photosensitizers have been shown to produce $^1O_2$ in good yields,[14] but practical applications are limited because these materials mainly absorb in the high-energy region. To circumvent this problem, additional organic chromophores can be introduced.[15–19] The high reactivity of $^1O_2$ causes its lifetime to be very short and it thus must be produced *in situ*, using either homogenous or heterogeneous photocatalysts. Immobilization of photosensitizers generally results in a decrease in their activity but may be beneficial for commercial applications.[10,20]

Reactive oxygen species (ROS), such as singlet oxygen, exhibit strong antimicrobial properties acting in a versatile way on bacteria, viruses, and fungi. The main advantage of photodynamic antimicrobial chemotherapy (PACT) is the absence of microbial resistance towards ROS, and that it does not cause the spread of drug-resistant bacteria.[19,21,22] High attention is put nowadays on the introduction of antimicrobial coatings in health-related areas to decrease the number of

[a] *Centre for Organic and Nanohybrid Electronics, Silesian University of Technology, Konarskiego 22b, 44-100 Gliwice, Poland. E-mail: przemyslaw.data@polsl.pl, agata.blacha@polsl.pl*
[b] *Faculty of Chemistry, Silesian University of Technology, Strzody 9, 44-100 Gliwice, Poland*
[c] *Institute of Physics – CSE, Silesian University of Technology, Konarskiego 22b, 44-100 Gliwice, Poland*
[d] *Molecular Materials and Nanosystems & Institute for Complex Molecular Systems, Eindhoven University of Technology P.O. Box 513, 5600 MB, Eindhoven, The Netherlands*

† Electronic supplementary information (ESI) available. See DOI: 10.1039/d1ma01151k

patients gaining nosocomial infections.[23] The introduction of photoactive antimicrobial coatings would allow also reduce the use of chlorinated, toxic disinfectants. Various approaches for the immobilization of photoactive molecules, mainly dyes, have been explored, *e.g.* the non-covalent immobilization in a polymer matrix, like cellulose acetate,[24] or covalent binding at a surface.[25] In the first case a high antimicrobial activity has been reported, however such materials may possess low stability, due to leaching of the photoactive molecule from the blend.[24,26] The covalent binding of dyes, *e.g.* Rose Bengal, to a polymer matrix, like polystyrene, polyamide, or poly(methyl methacrylate), can be achieved *via* chemical reaction between the matrix functional groups and the dyes.[27,28] The main disadvantage, however, is a more complicated multistep procedure.

In this study, we investigate the possibility of applying poly(3-hexylthiophene) (P3HT) layers containing carbon nanostructures, as a heterogeneous source of singlet oxygen. P3HT has been selected because it absorbs strongly in the visible region and its blends with carbon nanostructures can be easily deposited on solid supports. Moreover, their photophysical properties are well characterized in the literature. It has been shown that energy transfer from P3HT to fullerenes and carbon nanotubes occurs in solution[29,30] and in the solid-state,[31,32] and that such blends can produce singlet oxygen.[20] Here, P3HT is assumed to act both as support for the carbon-based photosensitizers and as a visible-light antenna. The blend layers were characterized with various spectroscopic techniques. Singlet oxygen photogeneration was investigated with 1,3-diphenylisobenzofuran (DPBF) in methanol under excitation with green light, which allowed for the determination of quantum yields of the photoprocess. On the other hand, oxidation of 1,5-dihydroxynaphthalene (DHN) to juglone in acetonitrile under white light illumination was demonstrated as an example of fine-chemical synthesis. The influence of the type of carbon photosensitizer and its content on the photoactive properties of the layer was studied.

2. Experimental

2.1. Materials

C60 (purity 99.9%) was purchased from Acros Organics. [6,6]-Phenyl-C_{61}-butyric acid methyl ester (PCBM) (purity 99.0%) and single-walled carbon nanotubes (SWCNTs) were obtained from Osilla Ltd. Regiorandom P3HT was synthesized following a well-established procedure (ESI†). Chlorobenzene (>99%, Acros Organics) was applied as a solvent for layer preparation. Sodium dodecyl sulfate (>98%, Sigma-Aldrich), isopropanol (99.5%), and acetone (95%) (both Acros Organics) were used for cleaning glass slides. 1,3-Diphenylisobenzofuran (DPBF, >97%) dissolved in methanol (99.9%, both Across Organic) was used as a singlet oxygen scavenger. The quantum yield of $^1O_2$ photogeneration was determined with Rose Bengal (Acros Organics) as a reference. Photooxidation under white light was tested with 1,5-dihydroxynaphthalene (DHN, 97%) in acetonitrile (≥99.9% both from Sigma-Aldrich).

2.2. Photoactive layers deposition and characterization

P3HT layers containing carbon nanostructures as photosensitizers were formed on borosilicate glass slides (1 × 1 cm^2 or 3 × 3 cm^2, Präzisions Glas & Optik GmbH, PG&O) *via* spin coating (Laurell spin-coater, WS-650 M2-23). Before layer deposition, the glass substrates were cleaned with sodium dodecyl sulfate aqueous solution and then sonicated in acetone, pure water, and finally isopropanol. Carbon nanostructures and P3HT were dispersed in chlorobenzene in a 1 : 2 mass ratio, and additionally in 1 : 1 and 2 : 1 mass ratios in case of PCBM, and sonicated for 15 min. 30 mm^3 of the solution was dropped on the glass slide and spin coated for 30 s at a spinning rate of 2000 rpm.

A Veeco, Dektak 150 profilometer was used to determination the layer thickness, employing 1200 μm scanning length, a needle with a diameter of 12.5 μm, and a pressure force of 5.00 mg.

UV-vis spectra of the films were recorded with a HP 8452A spectrometer Raman spectra were recorded using Renishaw inVia Raman Microscope (Renishaw, Inc., New Mills, UK) equipped with a 514 nm diode laser, a 2400 line per mm grating, and a 50× objective. All spectra were smoothened and the baseline was subtracted utilizing Renishaw software.

X-ray photoelectron spectroscopy (XPS) analysis was done with PREVAC EA15 hemispherical electron energy analyzer with 2D multi-channel plate detector. Al-K_α X-ray source (PREVAC dual-anode XR-40B, 1486.6 eV) was used for sample irradiation. The measurements were conducted under 9 × 10^{-9} Pa base pressure. Pass energy was equal to 200 eV pass energy for survey spectra (scanning step 0.9 eV) and 100 eV (scanning step 0.05 eV) for high-resolution spectra acquisition. The binding energy scale was calibrated with respect to C–C component in the C1s region (284.8 eV).[33] The spectra were analyzed applying CASA XPS® software. Shirley function was used as a background and the product of Gaussian and Lorentzian functions were used for components fitting.

2.3. Singlet oxygen photogeneration

The effectiveness of the photoactive layers containing carbon-based nanomaterials in the process of singlet oxygen photogeneration was determined using a 0.06 mM solution of DPBF as specific $^1O_2$ quencher in methanol.[34,35] The reaction progress was monitored with a Hewlett Packard 8452A UV-vis spectrometer as the change in the DPBF absorbance at 410 nm. The process was conducted *in situ* in a standard 10 mm × 4 mm quartz cuvette (Hellma Analytics) under 532 nm laser irradiation (Oxxius, LCX-532L-150-CSB-PPA model having 150 mW maximum power reduced to 50 mW).[35] The quantum efficiency of the light-induced $^1O_2$ production was determined with the DPBF method and Rose Bengal as a standard having Φ_{RB} equal to 0.80 in CH_3OH.[36–39]

2.4. Material photooxidation of DHN

Selected P3HT-fullerene layers deposited on borosilicate glass slides were applied as a source of singlet oxygen in the

oxidation of DHN. *In situ* measurements were conducted in the set-up as for DPBF tests with a 100 W xenon lamp acting as a source of light. The initial concentration of DHN in acetonitrile was equal to 0.14 mM. The reaction with $^1O_2$ was followed by monitoring the decrease in the absorbance of DHN at 298 nm and the increase of the absorbance of the oxygen adduct, juglone, at 406 nm.

Photooxidation of DHN was also done in a 100 ml photoreactor. Nine glass slides (9 cm^2 each) covered with P3HT:PCBM were introduced into the photoreactor filled with a 0.0146 M solution of DHN in acetonitrile and illuminated with a xenon lamp. During the reaction, the mixture was magnetically stirred and bubbled with oxygen. After 4 h the reaction mixture was evaporated and the crude product was purified by column chromatography with dichloromethane as eluent. The structure of the product was confirmed by ^{1}H-NMR spectroscopy (Varian Unity Inova 300 MHz Spectrometer, $CDCl_3$).

3. Results and discussion

3.1. Deposition and characterization of photoactive layers

P3HT layers containing various carbon-based photosensitizers were deposited on glass substrates by spin coating. The spin-coating parameters were optimized, *i.e.* various rotation speeds were tested in the range between 500 and 4000 rpm, to obtain layers with *ca.* 35 nm thickness. The average thickness of the deposited layers is given in Table S1 (ESI†). Deposited layers were not subjected to heat treatment, *i.e.* thermal annealing, to minimize phase segregation and crystallization of fullerene and polymer,[40,41] that is known to assist charge separation between donor and acceptor units.[5,42–44]

Deposited layers were first characterized by UV-vis spectroscopy (Fig. 1). For P3HT a broad absorption band is observed between 400 and 600 nm with a maximum at *ca.* 510 nm attributed to its π–π* transition[42] and a shoulder at *ca.* 605 nm assigned to inter-chain stacking of P3HT and thus polymer ordering.[42,45,46] For fullerene-containing layers, the distinct fullerene absorption is visible at 340 nm and 334 nm for P3HT:C_{60} and P3HT:PCBM, respectively.[47] The maximum of the P3HT π–π* absorption is blue-shifted to *ca.* 490 nm for P3HT:PCBM, and further to 455 nm for P3HT:C_{60}. Moreover, the significant decrease in the absorption of the shoulder at 605 nm is observed in the latter case suggesting less inter-chain interactions within P3HT upon addition of C_{60}.[48,49] On the other hand, the UV-vis spectrum of the P3HT:SWCNT film almost completely coincides with P3HT-only spectrum, indicating that at this concentration of SWCNTs the polymeric inter-chain interactions remain dominant over interactions of P3HT with SWCNTs.[31,48] The presence of carbon nanotubes in the blend is confirmed by weak absorption peak appearing close to 700 nm.[31]

The chemical composition of the layers was also analyzed with Raman spectroscopy (Fig. 2). For all spectra, characteristic bands of P3HT are observed. The deformation vibration of the C–S–C bond arises at *ca.* 720 cm^{-1}, the C–C skeletal stretching at 1379 cm^{-1}, while the C═C stretching vibrations occur at 1450 cm^{-1}.[43] The latter is broadened and slightly shifted to higher wavenumbers for fullerene-containing layers, which is due to the additional contribution of the "pentagonal pinch" A_g mode vibrations of C_{60} spheres[50] and may suggest the lower order and crystallinity of the P3HT.[51] Raman spectra of P3HT:SWCNT coating exhibit additional signal typically observed for CNTs, so-called G band at 1593 cm^{-1}.[2] However, in this case, the C═C stretching vibration band of thiophene ring, and thus order of polymeric matrix seems unaffected by the introduction of carbon nanotubes,[51] which is in agreement with above-mentioned UV-vis results.

A XPS survey spectrum recorded for the P3HT:PCBM film (Fig. S1a, ESI†) confirms full coverage of the glass substrate. Moreover, basing on survey spectra and C1s region (see Fig. S1c, ESI†), no signals of impurities coming from the solvent or reagents used for P3HT synthesis are observed. The position of $S2p_{3/2}$ component in S2p high-resolution spectrum

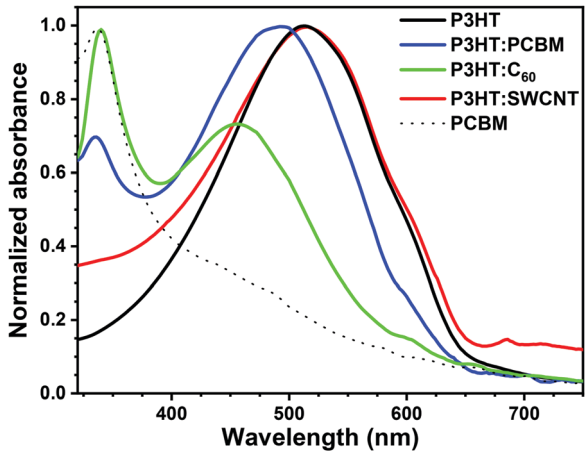

Fig. 1 UV-vis spectra of P3HT, P3HT : PCBM (2 : 1), P3HT : C_{60} (2 : 1), P3HT : SWCNT (2 : 1) and PCBM layers deposited on borosilicate glass.

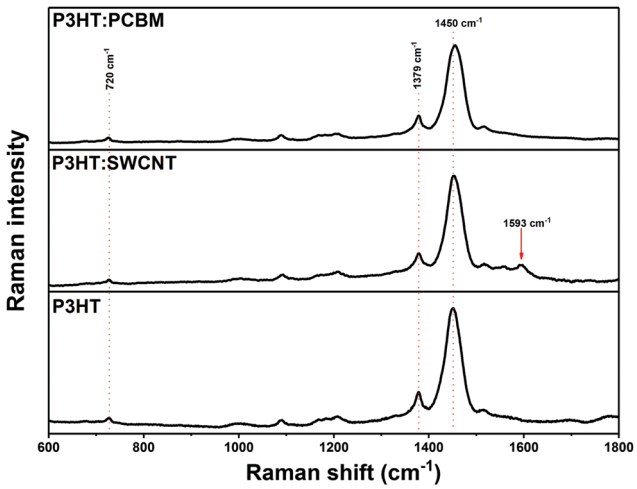

Fig. 2 Raman spectra of P3HT : PCBM (2 : 1), P3HT : SWCNT (2 : 1) and P3HT photoactive layers deposited on borosilicate glass.

(Fig. S1b, ESI†) suggests that polythiophene exists in its neutral form.[52,53]

3.2. Photogeneration of singlet oxygen

The photoactive layers were tested as a heterogeneous source of singlet oxygen in photooxidation reactions. As mentioned, P3HT plays a double role. First of all, it is used as a matrix for carbon-based photosensitizers and second, it may enhance absorption of visible light for $^1O_2$ production.

First, the process of singlet oxygen photogeneration was investigated with DPBF, which is a specific $^1O_2$ quencher.[34] The UV-vis spectra of a DPBF solution in methanol in contact with a P3HT:PCBM layer recorded during illumination with a green laser are shown in Fig. 3A. A clear decrease in the DPBF absorbance at 410 nm with time is observed, indicating that it is oxidized by singlet oxygen generated by irradiation of the P3HT:PCBM photoactive thin film.[17] This is further confirmed by control experiments, in which almost no drop in DPBF absorption is observed when the bare glass is illuminated or when the photoactive layer is in contact with the solution but not illuminated (Fig. 3B).

Fig. 3B shows the change of DPBF absorbance at 410 nm *vs.* time when various layers were illuminated. The largest drop in DPBF concentration after 25 min was observed for the P3HT layer containing PCBM. Under the applied conditions, P3HT itself exhibits poor photosensitizing properties.[20] Importantly, since no additional bands arise in the recorded UV-vis spectra in the course of the process (Fig. 3), the release of the fullerene into reaction mixture can be excluded. As shown in Fig. 4, the P3HT:PCBM photoactive layer retains its photoactivity towards singlet oxygen production in consecutive DPBF-tests, indicating that it can be effectively re-used. *Ca.* 10% decrease in the effectiveness of DPBF photooxidation was observed in the 7th run.

The quantum yield of singlet oxygen photogeneration (Φ) can be determined with respect to the well-known reference photosensitizers.[39,54] Here Rose Bengal was chosen. For

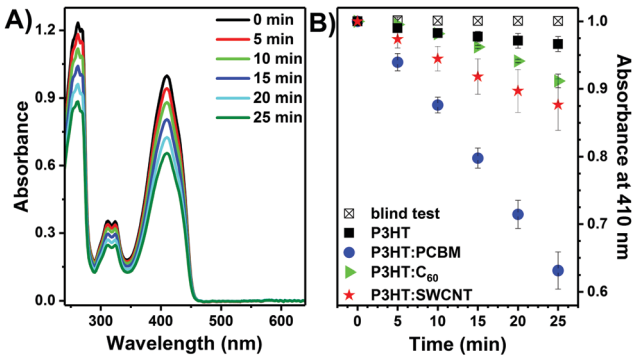

Fig. 3 (A) Representative set of UV-vis spectra of DPBF in methanol recorded during illumination of P3HT : PCBM (2 : 1) layer with a 532 nm laser. (B) Absorbance of DPBF at 410 nm as a function of time during illumination of P3HT, P3HT : PCBM (2 : 1), P3HT : C_{60} (2 : 1), P3HT : SWCNT (2 : 1) deposited on borosilicate glass and bare borosilicate glass (blind test) with a 532 nm laser.

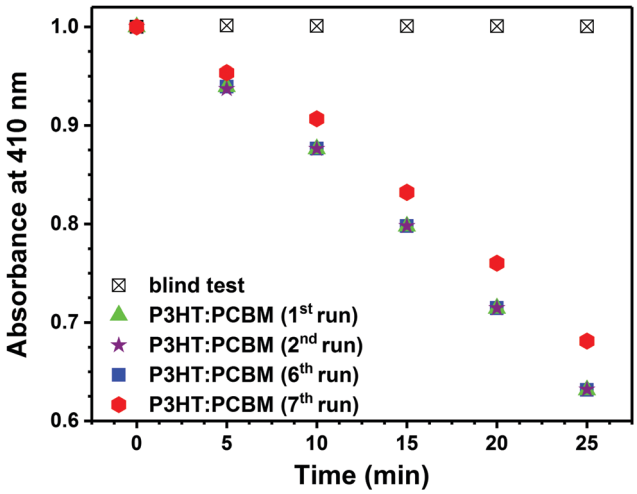

Fig. 4 The absorbance of DPBF at 410 nm as a function of time during consecutive illumination of P3HT : PCBM (2 : 1) deposited on borosilicate glass and bare borosilicate glass (blind test) with 532 nm laser.

P3HT:PCBM layers the quantum yield of singlet oxygen photogeneration was equal to 1.1% at a 2 : 1 mass ratio and increased to 4.2% at a 1 : 2 mass ratio (Table 1). Since the quantum yield of singlet oxygen photogeneration by the pristine PCBM layer (1.9%) is lower than that of P3HT : PCBM (1 : 2), energy transfer from P3HT to PCBM (which acts as the photosensitizer in the $^1O_2$ formation) is suggested.[17,31,32,55] We note that the energy of charge-separated state in P3HT:PCBM blends is at 1.14 eV and thus lower than the triplet energy of PCBM at 1.5 eV,[6,56] indicating that charge separation process is energetically favored. Nevertheless, it seems that in P3HT:PCBM blends energy transfer from P3HT to PCBM is efficient enough to form singlet the excited state of PCBM, which yields ^{3}PCBM* *via* intersystem crossing that reacts with $^3O_2$.

The drop in the absorbance of DPBF after 25 min and the corresponding quantum yields of singlet oxygen photogeneration are significantly lower for both P3HT:SWCNT and P3HT:C_{60} (Fig. 3B and Table 1), which is probably related to the low solubility of C_{60} and SWCNT and the thus higher tendency of the two to form agglomerates and clusters during deposition process.[57–59] It has already been shown that the lifetime of the triplet-excited state of the photosensitizer, and consequently the $^1O_2$ photogeneration efficiency, can be significantly reduced due to agglomeration. Moreover, it has been shown that carbon nanotubes can also effectively quench $^1O_2$, thus lowering its overall production yield.[60]

Table 1 Quantum yields of singlet oxygen photogeneration determined with the DPBF-method and Rose Bengal as reference

Photoactive layer	Φ_{CH_3OH} [%]
P3HT : C_{60} (2 : 1)	< 0.5
P3HT : SWCNT (2 : 1)	< 0.5
P3HT : PCBM (2 : 1)	1.1
P3HT : PCBM (1 : 1)	2.0
P3HT : PCBM (1 : 2)	4.2
Pristine PCBM	1.9

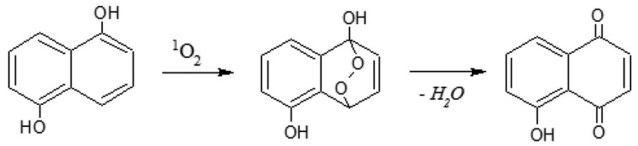

Scheme 1 Scheme of DHN reaction with $^1O_2$ to produce juglone.

Taking the above into account, the P3HT:PCBM composite was further investigated as a heterogeneous source of singlet oxygen. Since PCBM possesses significantly higher solubility than unmodified C_{60}, it is possible to increase its concentration in the polymeric matrix, while avoiding its aggregation.

3.3. Photooxidation of 1,5-dihydroxynaphthalene

1,5-Dihydroxynaphthalene (DHN) is a commonly used substrate in fine chemical reactions in the production of juglone (5-hydroxy-1,4-naphthoquinone) an anthelmintic drug (Scheme 1), which naturally occurs in plants, especially in black walnut.[61,62] Oxidation of DHN to juglone was used as a proof of concept for singlet oxygen generation by direct measurement of the formed species. The progress of DHN oxidation can be easily monitored by UV-vis spectroscopy as changes in absorbance at 298 and 406 nm.[63,64]

The DHN photooxidation was conducted *in situ* applying photoexcitation of P3HT:PCBM layers to generate singlet oxygen. A xenon lamp was used for illumination, to excite the P3HT:PCBM films. Fig. 5A presents a set of UV-vis spectra of a DHN solution collected during illumination of the P3HT : PCBM (1 : 2) layer. The absorbance of DHN at 298 nm decreases with time, indicating its reaction with $^1O_2$ to produce juglone, also indicated by the appearance of the specific absorption band with a maximum at *ca.* 406 nm that is gradually increasing as the reaction proceeds. Almost no decrease in DHN concentration is observed when the bare glass is illuminated (Fig. 5A inset). As in the case of the DPBF test, the dissolution of the layer in the reaction mixture can be excluded, since neither characteristic absorption bands of PCBM nor P3HT have been recorded.

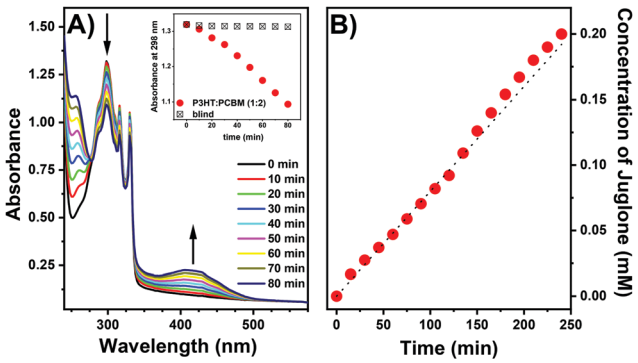

Fig. 5 (A) A representative set of UV-vis spectra of DHN in acetonitrile recorded during *in situ* illumination of P3HT : PCBM (1 : 2) layer with a xenon lamp. The inset shows the decrease in absorbance at 298 nm in time. (B) Change in the juglone concentration *vs.* time in the photoreactor reaction mixture during illumination of P3HT : PCBM (1 : 2) layer with a xenon lamp.

Table 2 Rate constants of DHN oxidation with singlet oxygen, photogenerated by P3HT:PCBM layers

Photoactive layer	$k \times 10^7$ (mol dm^{-3} min^{-1})
P3HT : PCBM (2 : 1)	0.90
P3HT : PCBM (1 : 1)	1.20
P3HT : PCBM (1 : 2)	3.25
Pristine PCBM	1.07

Similar sets of UV-vis spectra were collected for P3HT : PCBM layers with 1 : 1 and 2 : 1 ratio. The rate constants of DHN oxidation by singlet oxygen, which is pseudo-zero order reaction under applied conditions, are given in Table 2. As mentioned, during illumination of the photoactive layers with a xenon lamp also the PCBM photosensitizer is excited directly. As expected, an increase in PCBM content increases the value of rate constant of DHN oxidation. The relation is not linear and the trend corresponds to the quantum yield of $^1O_2$ generation (Table 1). The rate constant for DHN oxidation with pristine PCBM layer is about 3-times lower than for P3HT : PCBM (1 : 2), suggesting that P3HT absorbing in the visible region plays an additional role in the formation of singlet oxygen, either directly or indirectly by energy transfer to form C_{60} triplet excited state.

In a final step, DHN photooxidation was conducted in a self-constructed photoreactor equipped with a xenon lamp as illumination source using P3HT : PCBM (1 : 2) covered glass slides with a total active area of 81 cm^2. The reaction was carried out for 4 h and samples were taken every 15 min. and analyzed by UV-vis spectroscopy. Fig. 5B shows the increase in the concentration of juglone in the reaction mixture, calculated based on the absorbance at 406 nm. The structure of the reaction product juglone was further confirmed by ^{1}H-NMR spectroscopy (ESI†). The steady increase in the absorbance of juglone with time, confirms that P3HT:PCBM photoactive layers retain activity under prolonged illumination, and thus can be effectively applied as a heterogeneous source of singlet oxygen.

4. Conclusions

Photoactive layers based on a P3HT matrix containing carbon nanostructures as photosensitizers were investigated as photosensitizers to produce singlet oxygen. In these blends P3HT acts as a visible-light absorber and transfers energy to the carbon nanostructure, which is the actual photosensitizer that produces singlet oxygen. Singlet oxygen formation was monitored spectroscopically *in situ via* the oxidation of DPBF in methanol and was used synthetically to form juglone from DHN in acetonitrile. The efficiency of $^1O_2$ production depends on the photosensitizer and is significantly lower for blends of P3HT with C_{60} and single-walled carbon nanotubes than for blends of P3HT with PCBM. For P3HT:PCBM-based thin films, the quantum efficiency of $^1O_2$ photogeneration can be tuned by varying

the PCBM concentration in the P3HT layer. The results show that such easily-fabricated fullerene–polymer blends can be considered for singlet oxygen generation using visible-light and applied for fine chemicals synthesis.

Conflicts of interest

There are no conflicts to declare.

Acknowledgements

This work was supported by the National Science Center, Poland (Grand number: 2016/21/D/ST5/01641). The synthesis of P3HT was performed due to the financial support from the National Science Centre, Poland under the PRELUDIUM 11 program (Grant number: 2016/21/N/ST8/01871). A. N. acknowledges the support from the Silesian University of Technology (04/040/BKM21/0179). A. N., A. D. & P. D. kindly acknowledge the support received from the First Team program of the Foundation for Polish Science co-financed by the European Union under the European Regional Development Fund (Project number: First TEAM POIR.04.04.00-00-4668/17-00). Authors are grateful to the networking action funded from the European Union's Horizon 2020 research and innovation program under grant agreement no. 691684. Authors acknowledges the supporting actions from EU's Horizon 2020 ERA-Chair project ExCEED, grant agreement no. 952008.

References

1 S. Ren, M. Bernardi, R. R. Lunt, V. Bulovic, J. C. Grossman and S. Gradecak, *Nano Lett.*, 2011, **11**, 5316–5321.
2 V. C. Tung, J.-H. Huang, J. Kin, A. J. Smith, C.-W. Chu and J. Huang, *Energy Environ. Sci.*, 2012, **5**, 7810–7818.
3 R. M. Williams, H. Chen, D. Di Nuzzo, S. C. J. Meskers and R. A. J. Janssen, *J. Spectrosc.*, 2017, **2017**, 6867507.
4 A. J. Gillett, A. Privitera, R. Dilmurat, A. Karki, D. Qian, A. Pershin, G. Londi, W. K. Myers, J. Lee, J. Yuan, S. J. Ko, M. K. Riede, F. Gao, G. C. Bazan, A. Rao, T. Q. Nguyen, D. Beljonne and R. H. Friend, *Nature*, 2021, **597**, 666–671.
5 J. J. Benson-Smith, H. Ohkita, S. Cook, J. R. Durrant, D. D. C. Bradley and J. Nelson, *Dalton Trans.*, 2009, 10000–10005.
6 D. Di Nuzzo, A. Aguirre, M. Shahid, V. S. Gevaerts, S. C. J. Meskers and R. A. J. Janssen, *Adv. Mater.*, 2010, **22**, 4321–4324.
7 S. Cook, H. Ohkita, J. R. Durrant, Y. Kim, J. J. Benson-smith, J. Nelson and D. D. C. Bradley, *Appl. Phys. Lett.*, 2006, **89**, 101128.
8 A. Distler, P. Kutka, T. Sauermann, H.-J. Egelhaaf, D. M. Guldi, D. Di Nuzzo, S. C. J. Meskers and R. A. J. Janssen, *Chem. Mater.*, 2012, **24**, 4397–4405.
9 M. C. DeRosa and R. J. Crutchley, *Coord. Chem. Rev.*, 2002, **233–234**, 351–371.
10 J. Wahlen, D. E. De Vos, P. A. Jacobs and P. L. Alsters, *Adv. Synth. Catal.*, 2004, **346**, 152–164.
11 I. Pibiri, S. Buscemi, A. Palumbo Piccionello and A. Pace, *ChemPhotoChem*, 2018, **2**, 535–547.
12 A. A. Ghogare and A. Greer, *Chem. Rev.*, 2016, **116**, 9994–10034.
13 P. R. Ogilby, *Chem. Soc. Rev.*, 2010, **39**, 3181–3209.
14 P. Dallas, G. Rogers, B. Reid, R. A. Taylor, H. Shinohara, G. A. D. Briggs and K. Porfyrakis, *Chem. Phys.*, 2016, **465–466**, 28–39.
15 Q. Li, H. Guo, X. Yang, S. Zhang and H. Zhang, *Tetrahedron*, 2017, **73**, 6632–6636.
16 S. Guo, H. Zhang, L. Huang, Z. Guo, G. Xiong and J. Zhao, *Chem. Commun.*, 2013, **49**, 8689–8691.
17 L. Huang, X. Cui, B. Therrien and J. Zhao, *Chem. – Eur. J.*, 2013, **19**, 17472–17482.
18 A. Blacha-Grzechnik, M. Krzywiecki, R. Motyka and M. Czichy, *J. Phys. Chem. C*, 2019, **123**, 25915–25924.
19 E. Reynoso, A. M. Durantini, C. A. Solis, L. P. Macor, L. A. Otero, M. A. Gervaldo, E. N. Durantini and D. A. Heredia, *RSC Adv.*, 2021, **11**, 23519–23532.
20 M. Bregnhøj, M. Prete, V. Turkovic, A. U. Petersen, M. B. Nielsen, M. Madsen and P. R. Ogilby, *Methods Appl. Fluoresc.*, 2020, **8**, 014001.
21 M. Wainwright, *Photodiagn. Photodyn. Ther.*, 2009, **6**, 167–169.
22 N. E. Grammatikova, L. George, Z. Ahmed, N. R. Candeias, N. A. Durands and A. Efimov, *J. Mater. Chem. B*, 2019, **7**, 4379–4384.
23 S. Noimark, C. W. Dunnill and I. P. Parkin, *Adv. Drug Delivery Rev.*, 2013, **65**, 570–580.
24 V. Decraene, J. Pratten and M. Wilson, *Appl. Environ. Microbiol.*, 2006, **72**, 4436–4439.
25 C. Piccirillo, S. Perni, J. Gil-Thomas, P. Prokopovich, M. Wilson, J. Pratten and I. P. Parkin, *J. Mater. Chem.*, 2009, **19**, 6167–6171.
26 G. B. Hwang, E. Allan and I. P. Parkin, *ACS Appl. Mater. Interfaces*, 2016, **8**, 15033–15039.
27 M. Krouit, R. Granet and P. Krausz, *Eur. Polym. J.*, 2009, **45**, 1250–1259.
28 C. Ringot, V. Sol, M. Barrière, N. Saad, P. Bressollier, R. Granet, P. Couleaud, C. Frochot and P. Krausz, *Biomacromolecules*, 2011, **12**, 1716–1723.
29 E. A. Lukina, I. P. Pozdnyakov, A. S. Mereshchenko, M. N. Uvarov and L. V. Kulik, *J. Photochem. Photobiol., A*, 2015, **311**, 193–198.
30 R. A. J. Janssen, N. S. Sariciftci and A. J. Heeger, *J. Chem. Phys.*, 1994, **100**, 8641–8645.
31 A. J. Ferguson, J. L. Blackburn, J. M. Holt, N. Kopidakis, R. C. Tenent, T. M. Barnes, M. J. Heben and G. Rumbles, *J. Phys. Chem. Lett.*, 2010, **1**, 2406–2411.
32 A. R. S. Kandada, G. Grancini, A. Petrozza, S. Perissinotto, D. Fazzi, S. S. K. Raavi and G. Lanzani, *Sci. Rep.*, 2013, **3**, 2073.
33 G. Beamson and D. Briggs, *XPS of Organic Polymers*, John Wiley & Sons, Chichester, 1992.
34 M. Wainwright, *Dyes Pigm.*, 2007, **73**, 7–12.

35 K. Piwowar, A. Blacha-Grzechnik, R. Turczyn and J. Zak, *Electrochim. Acta*, 2014, **141**, 182–188.
36 F. Lv, Y. Yu, E. Hao, C. Yu, H. Wang and L. Jiao, *Org. Biomol. Chem.*, 2019, **17**, 1–44.
37 C. R. Lambert and I. E. Kochevar, *J. Am. Chem. Soc.*, 1996, **118**, 3297–3298.
38 M. I. Burguete, F. Galindo, R. Gavara, S. V. Luis, M. Moreno and D. A. Russell, *Photochem. Photobiol. Sci.*, 2009, **8**, 37–44.
39 N. Epelde-Elezcano, V. Martinez-Martinez, E. Pena-Cabrera, C. F. A. Gomez-Duran, I. L. Arbeloa and S. Lacombe, *RSC Adv.*, 2016, **6**, 41991–41998.
40 R. A. Marsh, J. M. Hodgkiss, S. Albert-Seifried and R. H. Friend, *Nano Lett.*, 2010, **10**, 923–930.
41 U. Zhokhavets, T. Erb, G. Gobsch, M. Al-Ibrahim and O. Ambacher, *Chem. Phys. Lett.*, 2006, **418**, 347–350.
42 B. Kadem, A. Hassan and W. Cranton, *J. Mater. Sci.: Mater. Electron.*, 2016, **27**, 7038–7048.
43 F. Otieno, B. K. Mutuma, M. Airo, K. Ranganathan and R. Erasmus, *Thin Solid Films*, 2017, **625**, 62–69.
44 Y.-C. Huang, Y.-C. Liao, S.-S. Li, M.-C. Wu, C.-W. Chen and W.-F. Su, *Sol. Energy Mater. Sol. Cells*, 2009, **93**, 888–892.
45 B. Y. Kadem, M. K. Al-hashimi and A. K. Hassan, *Energy Procedia*, 2014, **50**, 237–245.
46 Y. Yang, S. Feng, M. Li, Z. Wu, X. Fang, F. Wang, D. Geng, T. Yang, X. Li, B. Sun and X. Gao, *ACS Appl. Mater. Interfaces*, 2015, **7**, 24430–24437.
47 R. V. Bensasson, E. Bienvenue, M. Dellinger, S. Leach and P. Seta, *J. Phys. Chem.*, 1994, **98**, 3492–3500.
48 P. J. Goutam, D. K. Singh and P. K. Iyer, *J. Phys. Chem. C*, 2012, **116**, 8196–8201.
49 J. U. Lee, A. Cirpan, T. Emrick, T. P. Russell and W. H. Jo, *J. Mater. Chem.*, 2009, **19**, 1483–1489.
50 H. Chadli, A. Rahmani and J.-L. Sauvajol, *J. Phys.: Condens. Matter*, 2010, **22**, 145303.
51 C.-Y. Su, A.-Y. Lu, Y.-L. Chen, C.-Y. Wei, P.-C. Wang and C.-H. Tsai, *J. Mater. Chem.*, 2010, **20**, 7034–7042.
52 A. P. P. Alves, J. P. C. Trigueiro, H. D. R. Calado and G. G. Silva, *Electrochim. Acta*, 2011, **209**, 111–120.
53 G. J. H. Melvin, Q.-Q. Ni, Y. Suzuki and T. Natsuki, *J. Mater. Sci.*, 2014, **49**, 5199–5207.
54 W. Li, L. Li, H. Xiao, R. Qi, Y. Huang, Z. Xie, X. Jing and H. Zhang, *RSC Adv.*, 2013, **3**, 13417–13421.
55 M. Narutaki, K. Takimiya, T. Otsubo, Y. Harima, H. Zhang, Y. Arki and O. Ito, *J. Org. Chem.*, 2006, **71**, 1761–1768.
56 K. Vandewal, K. Tvingstedt, A. Gadisa, O. Inganäs and J. V. Manca, *Phys. Rev. B: Condens. Matter Mater. Phys.*, 2010, **81**, 125204.
57 S. Wang, R. Gao, F. Zhou and M. Selke, *J. Mater. Chem.*, 2004, 487–493.
58 R. S. Ruoff, D. S. Tse, R. Malhotra and D. C. Lorents, *J. Phys. Chem.*, 1993, **97**, 3379–3383.
59 S. Berson, R. De Bettignies, S. Bailly, S. Guillerez and B. Jousselme, *Adv. Funct. Mater.*, 2007, **17**, 3363–3370.
60 N. Gandra, P. L. Chiu, W. Li, Y. R. Anderson, S. Mitra, H. He and R. Gao, *J. Phys. Chem. C*, 2009, **113**, 5182–5185.
61 S. Cosmulescu, I. Trandafir, G. Achim and A. Baciu, *Not. Bot. Horti Agrobot. Cluj-Napoca*, 2011, **39**, 237–240.
62 S. Sugie, K. Okamoto, K. M. W. Rahman, T. Tanaka, K. Kawai, J. Yamahara and H. Mori, *Cancer Lett.*, 1998, **127**, 177–183.
63 S. Takizawa, R. Aboshi and S. Murata, *Photochem. Photobiol. Sci.*, 2011, **10**, 895–903.
64 M. Luiz, A. T. Soltermann, A. Biasutti and N. A. Garcia, *Can. J. Chem.*, 2006, **74**, 49–54.

materials

MDPI

Article

Covalent Immobilization of Organic Photosensitizers on the Glass Surface: Toward the Formation of the Light-Activated Antimicrobial Nanocoating

Aleksandra Nyga [1], Dominika Czerwińska-Główka [1], Maciej Krzywiecki [2], Wioletta Przystaś [3,4], Ewa Zabłocka-Godlewska [3,4], Sebastian Student [4,5], Monika Kwoka [5,6], Przemysław Data [1] and Agata Blacha-Grzechnik [1,*]

[1] Faculty of Chemistry, Silesian University of Technology, Strzody 9, 44-100 Gliwice, Poland; aleksandra.nyga@polsl.pl (A.N.); dominika.czerwinska-glowka@polsl.pl (D.C.-G.); przemyslaw.data@polsl.pl (P.D.)
[2] Center for Science and Education (CSE), Institute of Physics, Silesian University of Technology, Konarskiego 22B, 44-100 Gliwice, Poland; maciej.krzywiecki@polsl.pl
[3] Faculty of Energy and Environmental Engineering, Silesian University of Technology, 44-100 Gliwice, Poland; wioletta.przystas@polsl.pl (W.P.); ewa.zablocka-godlewska@polsl.pl (E.Z.-G.)
[4] Biotechnology Centre, Silesian University of Technology, 44-100 Gliwice, Poland; sebastian.student@polsl.pl
[5] Faculty of Automatic Control, Electronics and Computer Science, Silesian University of Technology, 44-100 Gliwice, Poland; monika.kwoka@polsl.pl
[6] Institute of Electronics, Silesian University of Technology, Akademicka 16, 44-100 Gliwice, Poland
* Correspondence: agata.blacha@polsl.pl; Tel.: +48-322371024

Citation: Nyga, A.; Czerwińska-Główka, D.; Krzywiecki, M.; Przystaś, W.; Zabłocka-Godlewska, E.; Student, S.; Kwoka, M.; Data, P.; Blacha-Grzechnik, A. Covalent Immobilization of Organic Photosensitizers on the Glass Surface: Toward the Formation of the Light-Activated Antimicrobial Nanocoating. *Materials* **2021**, *14*, 3093. https://doi.org/10.3390/ma14113093

Received: 11 May 2021
Accepted: 2 June 2021
Published: 4 June 2021

Abstract: Two highly efficient commercial organic photosensitizers—azure A (AA) and 5-(4-aminophenyl)-10,15,20-(triphenyl)porphyrin (APTPP)—were covalently attached to the glass surface to form a photoactive monolayer. The proposed straightforward strategy consists of three steps, i.e., the initial chemical grafting of 3-aminopropyltriethoxysilane (APTES) followed by two chemical postmodification steps. The chemical structure of the resulting mixed monolayer (MIX_TC_APTES@glass) was widely characterized by X-ray photoelectron (XPS) and Raman spectroscopies, while its photoactive properties were investigated in situ by UV–Vis spectroscopy with α-terpinene as a chemical trap. It was shown that both photosensitizers retain their activity toward light-activated generation of reactive oxygen species (ROS) after immobilization on the glassy surface and that the resulting nanolayer shows high stability. Thanks to the complementarity of the spectral properties of AA and APTPP, the effectiveness of the ROS photogeneration under broadband illumination can be optimized. The reported light-activated nanocoating demonstrated promising antimicrobial activity toward *Escherichia coli* (*E. coli*), by reducing the number of adhered bacteria compared to the unmodified glass surface.

Keywords: chemical grafting; photoactive layer; antimicrobial coating; reactive oxygen species (ROS); phenothiazines; porphyrins

1. Introduction

Hospital-acquired infections, also called nosocomial infections, happen to more than 8.0% of patients and result in approximately 37k and 99k deaths each year in Europe and the USA, respectively, as stated by the World Health Organization (WHO). The medical complications due to these nosocomial infections may cause serious health problems and/or prolonged stay in hospitals, which also has an economic impact on the healthcare system [1]. Moreover, excessive use of antibiotics results in the decrease of their effectiveness, which in turn will lead to the development of a generation of pathogens resistant

even to novel-class antimicrobial medicines [2]. Nowadays, due to the COVID-19 pandemic, even more attention is focused on the sterilization of various surfaces mainly, but not only, in the healthcare-related areas. One of the possible strategies is the application of the antimicrobial coatings on surfaces [3]; these can be generally divided into passive ones (lowering bacterial adhesion, such as poly(ethylene glycol)) and active materials with silver or copper nanoparticles, quaternary ammonium salts, cations of fluorinated polymers, etc. [4,5]. Lately, the light-activated layers that can produce reactive oxygen species (ROS) are being intensely investigated, since ROS show tremendous antibacterial, antiviral, and antifungal properties [6]. ROS, such as singlet oxygen or superoxide radicals, have been studied for more than 50 years now [7]. Their cytotoxicity against microbes is a base of photodynamic antimicrobial chemotherapy (PACT). ROS are highly effective against microorganisms, and they act in a nonselective way (e.g., oxidation of enzymes, increase in ions' cell-wall permeability, etc.). The ability to denature antioxidant enzymes is specific to the singlet oxygen molecule [8–12].

The modification of the surfaces with photoactive compounds can be done through either physical or chemical methods [13]. The physical ones, which result in the noncovalent binding, are typically based on the deposition of a matrix, e.g., resin or polymer [14], which acts as a carrier for the photoactive substances, or on the physical adsorption of the photosensitizer molecule [2,15]. In the first case, cellulose acetate or polyurethanes, e.g., have been used as a polymeric matrix for the photosensitizers, and the resulting layers showed high antimicrobial activity against *Staphylococcus aureus, Escherichia coli, Clostridium difficile, Candida albicans,* and *Pseudomonas aeruginosa* [2,3,6,9,15–22]. However, such coatings usually possess limited long-term stability, due to various factors, e.g., bleaching. This can be overcome by forming a covalent bond between the photosensitizer molecule and the surface atoms. One of the most popular methods allowing for the chemical immobilization of the (photoactive) organic molecules is grafting [3,23–26] or, in the case of conductive surfaces, electrografting [27,28]. The main advantage of this process is the formation of a strong covalent bond between the immobilized molecule and surface atoms resulting in higher stability of the thin films, which is crucial for their practical use.

The formation of the antimicrobial layers on glassy surfaces seems an important issue since glass is an indispensable element of the equipment of operating rooms, wards, and personal electronics (windows, glass surfaces of light sources, monitor screens or phone screens) and, thus, can be a great source of pathogens, causing nosocomial infections. Thus, in this work, two commercially available organic photosensitizers (PS)—Azure A (AA) and 5-(4-aminophenyl)-10,15,20-(triphenyl)porphyrin (APTPP) (Scheme 1)—were immobilized on the glass surface, in order to form a light-activated antimicrobial nanocoating. The proposed straightforward deposition strategy, yielding the photoactive layer covalently bound to the surface, consists in the grafting of 3-aminopropyltriethoxysilane (APTES) and the consecutive postfunctionalization of the resulting monolayer based on the reactivity of the primary amino groups present in the APTES structure [29,30]. Importantly, since AA and APTPP photosensitizers show complementary spectral properties, the deposited mixed monolayer is characterized by broadband absorbance, which is crucial to get high efficiency of the ROS photogeneration under daylight. The structure of the monolayer was confirmed using spectroscopic methods. The light-activated ROS production was tested with α-terpinene. The preliminary investigations of the antimicrobial properties of the presented MIX_TC_APTES@glass were done against the Gram-negative strain of *Escherichia coli* (*E. coli*). The scanning electron microscopy (SEM) enabled to assess the density of bacterial cells, and their viability was exhibited via fluorescent confocal microscopy.

2. Materials and Methods

2.1. Materials

Azure A (AA) (Fluka, Charlotte, North Carolina, US, purity >90%) and 5-(4-aminophenyl)-10,15,20-(triphenyl)porphyrin (APTPP, purity >98%, PorphyChem, Dijon, France) (Scheme 1) were selected for the formation of a photoactive layer on the glass surface. 3-Aminopropyltriethoxysilane (APTES, purity 99%), used for the chemical grafting of glass, was obtained from Acros Organics (Geel, Belgium), while terephthaloyl chloride (TC, purity ≥99%, Sigma Aldrich, Darmstadt, Germany) was used as a linker molecule. Triethylamine, analytical grade, was purchased from POCh, Gliwice, Poland. The reactive oxygen species trap—α-terpinene (purity >90%)—was obtained from TCI (Tokyo, Japan). The organic solvents, tetrahydrofuran (99.5%), toluene (99.85%), isopropanol (99.5%), ethanol (99.8%), and acetone (95%), were obtained from Acros Organics (Geel, Belgium). Acetonitrile was purchased from Honeywell (Charlotte, NC, USA) (≥99.9%). Sodium hydroxide (Acros Organics, Geel, Belgium, 1N standard solution) and hydrochloric acid (Chempur, Piekary Slaskie, Poland, 35–38% pure per analysis) were used for pretreatment of the glass substrates. The antimicrobial activity of MIX_TC_APTES@glass surface was examined using a bacterial strain of Gram-negative *Escherichia coli* (DSMZ, 30083, U5/41), which was cultivated in 23 g/L agar broth (BTL, Warsaw, Poland) at 35 °C for 24 h in an incubator. Subsequently, a suspension of bacteria (10.5×10^8 CFU/mL according to the McFarland scale) in physiological saline (0.85% water solution of NaCl) (Acros Organics, Geel, Belgium) was prepared. Glutaraldehyde (Fisher Bioreagents, Waltham, MA, USA) was used for the SEM imaging of the bacteria.

2.2. Formation and Characterization of the Photoactive Layer

2.2.1. Glass Substrate Pretreatment

The glass pretreatment procedure was done according to the literature [31,32]. Firstly, the substrates were sonicated in an ultrasound cleaner in acetone for 15 min and then in deionized water also for 15 min. Further, the glasses were soaked in 1 M NaOH in a Teflon beaker for an hour. After re-sonication in deionized water for 15 min, the substrates were placed in 36% HCl for an hour. After that, the glass was re-sonicated in deionized water for 15 min. In the end, the substrates were sonicated in isopropanol.

2.2.2. Photoactive Monolayer Formation

The selected photosensitizers were bound to the glass surface in the three-step process (Scheme 1). In the first step, the freshly prepared glassy slides were immersed in 10% APTES solution in toluene for 24 h at room temperature [31–36]. The resulting APTES@glass substrates were copiously rinsed with toluene. In the second step, the freshly deposited layer was postmodified by immersion in 0.1 M TC/THF solution with the few drops of triethylamine. After 24 h, the modified glass slides (TC_APTES@glass) were taken out and rinsed with THF. In the final step, linker_APTES@glass surfaces were immersed in 0.1 M PS/THF (PS: AA, APTPP, or AA + APTPP) with a few drops of triethylamine for 24 h. The resulting AA_TC_APTES@glass, APTPP_TC_APTES@glass, and MIX_TC_APTES@glass layers were copiously rinsed with THF, methanol, and water to remove any weakly adsorbed species.

2.2.3. X-Ray Photoelectron Spectroscopy

X-ray photoelectron spectroscopy (XPS) was done using the PREVAC (Rogów, Poland) EA15 hemispherical electron energy analyzer with the 2D multichannel plate detector and Al-Kα X-ray source (PREVAC dual-anode XR-40B source, 1486.60 eV). The system base pressure was equal to 9×10^{-9} Pa. Pass energy equal to 200 eV (scanning step 0.9 eV) or 100 eV (scanning step 0.05 eV) was set for survey spectra and for high-resolution spectra, respectively. For the charging effect compensation, the electron flood gun was applied

working in a low-energy range (in order to avoid electron-beam-induced degradation effects). The binding energy scale was calibrated with respect to C–C component of C1s spectra (284.8 eV) [37]. The acquired spectra were fitted using CASA XPS® software (version 2.3, Cheshire, UK).

2.2.4. Raman Spectroscopy

Raman spectra of both the photosensitizers, i.e., AA and APTPP; MIX_TC_APTES@glass; and the unmodified glass substrate were registered using a Renishaw inVia Raman Microscope (Renishaw, Inc., New Mills, UK), 514 nm diode excitation laser, and 2400 lines/mm grating. The Renishaw software (WiRE version 3.2, New Mills, UK) was used for smoothing and baseline subtraction.

2.3. Photogeneration of Reactive Oxygen Species (ROS)

The ability of the prepared layers to generate singlet oxygen was tested with α-terpinene in acetonitrile (0.05 mM solution). A modified glass plate was placed in a 10 × 4 mm^2 quartz cuvette (Hellma Analytics, Müllheim, Germany) and illuminated either with a xenon lamp or with a diode laser. The xenon lamp was used as a broadband illumination source. In contrast, 445 and 638 nm diode lasers (Oxxius, Lannion, France, LBX-445-100CSB-PP and LBX-638-150-ELL-PP) were used as a light source exciting specifically APTPP or AA, respectively. The light-activated ROS generation was followed in situ using a Hewlett Packard (Palo Alto, CA, USA) 8452A UV–Vis spectrometer. The course of the investigated process was observed by the drop in the absorbance of α-terpinene at 266 nm.

2.4. Microbiological Analysis

2.4.1. Bacterial Strain and Culture Conditions

Both MIX_TC_APTES@glass and unmodified glass slides were sterilized by immersion in 70% ethanol in a sterile 12-well plate for an hour in the dark. In the next step, the well plates were washed three times with distilled water and left to dry in the dark. The bacterial suspension (0.1 mL) in culture medium (2 mL), composed of 10 g/L tryptone (BTL), 5 g/L yeast extract (BTL), and 10 g/L NaCl, pH = 7, was dropped on the sterilized samples. The bacterial culture was carried out for 48 h; for the whole time, samples were exposed to conventional indoor lighting (fluorescent ceiling lamp with two 60 watts bulbs). The analysis of bacteria was performed at two time points, i.e., at 3 and 48 h of culture. To assess the reliability and repeatability of the results, all the experiments were conducted three times, and the mean value of the results (with ± standard deviation) was presented. The statistical significance ($p < 0.05$) was determined with the t-test.

2.4.2. Bacterial Cell Staining and Imaging

To assess the viability of bacteria on selected surfaces of glass and MIX_TC_APTES@glass, the LIVE/DEAD® BacLight Bacterial Viability Kit (Life Technologies, Thermo Fisher Scientific, Waltham, MA, USA) assay was done. Live or dead bacterial cells were labeled in green (SYTO9 stain) or in red (D-propidium iodide), respectively. Confocal fluorescence microscopy (Olympus FluoView FV1000, FV1000, Tokyo, Japan) was applied in the visualization and analysis of the percentage of living and dead bacterial cells. The image analysis was performed with ImageJ (NIH, Bethesda, MD, USA) software. In the case of SEM (Phenom ProX) analysis, *E. coli* on the substrates were fixed with 3% glutaraldehyde solution during 24 h, following by the washing with the distilled water and exposition to ethanol having concentration equal to 30%, 50%, 70%, 80%, 90%, 95%, and 99.8%, for 10 min. Then, the samples were dried in the oven (24 h, 50 °C) and they were sputtered-coated with a thin gold film for 20 min at 20 mA (Q150R Quorum Technologies). The images were acquired using following parameters: accelerating voltage—

15 kV and magnification—5000×. The average density, given by the number of bacterial cells/200 μm², was determined with the ImageJ 1.8.0 (NIH, Bethesda, MD, USA) software.

3. Results and Discussion

3.1. Chemical Grafting and Spectroscopic Characterization of the Photoactive Mixed Monolayer (MIX_TC_APTES@glass)

3.1.1. Chemical Grafting and XPS Spectroscopy

For the formation of the grafted mixed monolayer, a three-step procedure was applied, shown in Scheme 1. The chemical structures of the deposited layers were checked after each modification step by XPS spectroscopy. The analysis of the high-resolution XPS spectra was done using CASA XPS software with the Shirley function applied for background subtraction and the Gaussian (70%)–Lorentzian (30%) lines product for the component's representation.

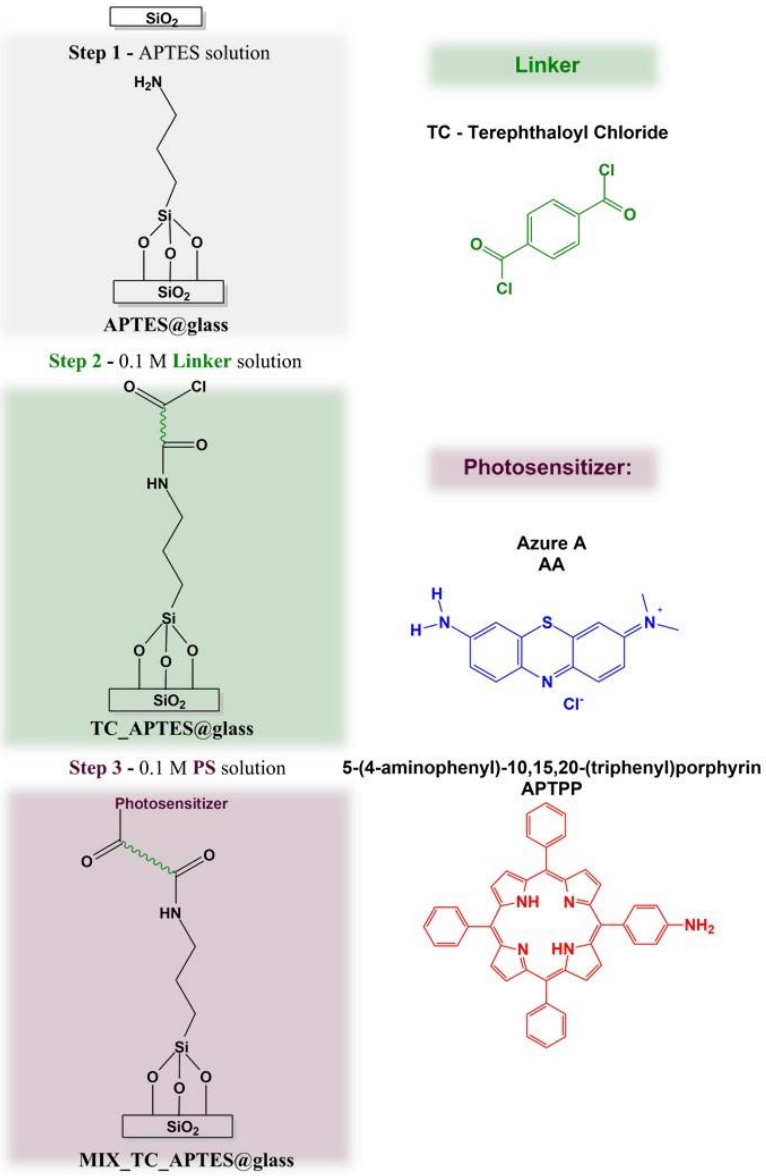

Scheme 1. General scheme of the chemical grafting of the light-activated mixed monolayer on the glass surface.

In the first step, the APTES molecule was chemically grafted on the glass surface to form a self-assembled monolayer [35]. A nonpolar environment was used in order to reduce the possibility of the formation of the hydrogen bonding between $–NH_2$ present in APTES and OH groups present at the glass surface [33,36]. In the survey scan recorded for APTES@glass (Figure 1a), O1s, N1s, C1s, and Si2p peaks are observed at approximately 530, 400, 285, and 102 eV, respectively. While the presence of oxygen, carbon, and silicon signals is due to both APTES and the glass substrate, the nitrogen N1s peak is specific to the grafted organic layer.

The decomposition of the high-resolution C1s spectrum (Figure 1b) shows five components at 282.9, 284.8, 285.5, 286.2, and 287.5 eV attributed to C–Si, C–C, C–N, C–O, and C=O, respectively. C–N and C–Si components, being in the ratio close to 1, are characteristic for the APTES monolayer [33,34,38], while C–C and C–O come from the grafted organic layer and the adventitious carbon residues [38]. Low content of the C–O component, approximately 3.4%, suggests that almost all $–OC_2H_5$ groups present in the APTES molecule are involved in the grafting process, forming a covalent bond either with the glass surface atoms or with each other [33].

The analysis of the N1s region (Figure 1c) reveals the presence of one component at 398.2 eV that can be assigned to $–NH_2$ group present in the APTES molecule bound to the glass surface. Importantly, no signal at approximately 402 eV was observed, indicating that neither $–NH_3^+$ nor $–NH_2$/OH hydrogen bonding was formed during the SAM deposition [33,38]. This is of particular importance, since the consecutive postmodification steps are based on the accessibility of the "free" amino groups. Finally, only one asymmetric component at 103.5 eV was observed for the Si2p high-resolution spectrum (Figure 1d). The major contribution to this region is by Si–O component originating from glass substrate. The contribution from the examined layer is represented by asymmetry (low binding energy side) and by region energy shift from the expected 104.0 eV for the clean glass to 103.5 eV due to the presence of the C–Si–O component [33,35].

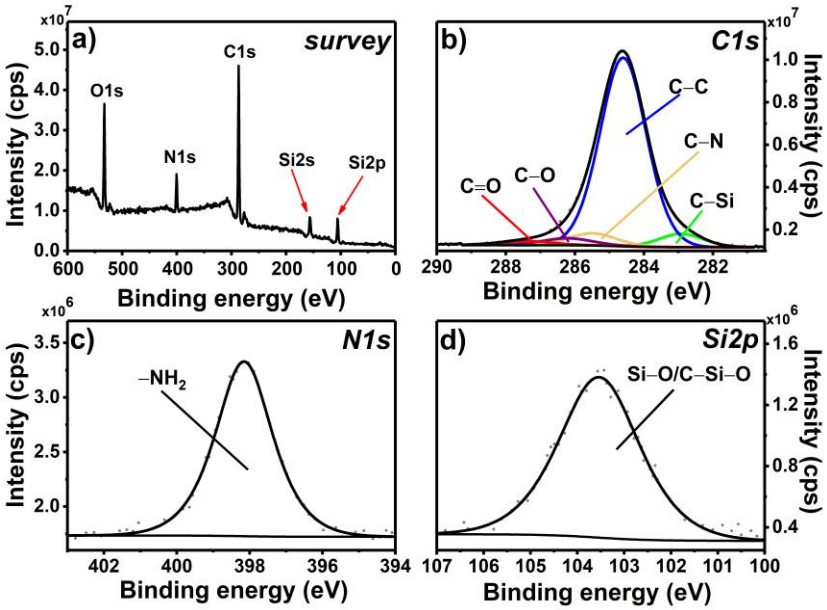

Figure 1. XPS survey spectrum (**a**) and high-resolution spectra of C1s (**b**), N1s (**c**), and Si2p (**d**) regions registered for the APTES@glass monolayer.

The chemically grafted APTES monolayer was, in the next step, modified in the consecutive chemical reactions. The first step of postfunctionalization was based on the reactivity of the primary amine present in the APTES@glass layer. Thus, the slides were immersed in a solution of diacyl chloride (TC linker) in order to form an amide group

(Scheme 1, Step 2). The XPS survey spectrum of the resulting TC_APTES@glass coating (Figure 2a) reveals the presence of the peaks that occurred also in the APTES@glass spectrum, i.e., O1s, N1s, C1s, and Si2p spectral lines at approximately 530, 400, 285, and 102 eV, with an additional signal of chlorine—Cl2p at 199 eV. The presence of the latter is also visible in the C1s high-resolution spectrum (Figure 2b) as the C–Cl component occurring at 288.5 eV from acyl chloride groups in TC linker. The other components previously observed in the C1s region for APTES@glass, i.e., C–Si, C–C, C–N, C–O, and C=O, are also observed in this case, though in slightly different ratios.

The most significant changes can be observed in the N1s high-resolution spectrum (Figure 2c). In the case of TC_APTES@glass, two clearly visible components can be distinguished: $–NH_2$ at 398.8 eV and –NH–CO– at 400.6 eV [38], which confirms the occurrence of the reaction between surface-bound $–NH_2$ groups and –COCl groups in the TC-linker molecule. The presence of the unreacted amine units is probably related to the steric hindrance of this surface-based reaction. The percentage contribution of –NH–CO– component to N1s signal is in agreement with the C–Cl/C–N ratio in C1s. The analysis of the Cl2p region (Figure 2d) confirms that only one component, with its spin-orbit splitting counterpart, is observed—$Cl2p_{3/2}$ at 198.3 eV, which can be assigned to chlorine present in the unreacted acyl chloride groups in TC-linker. The ratio of –NH–CO– component in N1s region and $Cl2p_{3/2}$ component in Cl2p region is close to 1 (taking into account the corresponding relative sensitive factors), indicating that only one –COCl group (per TC molecule) takes part in the reaction with the amine group, while the other –COCl group remains "available" for the consecutive functionalization.

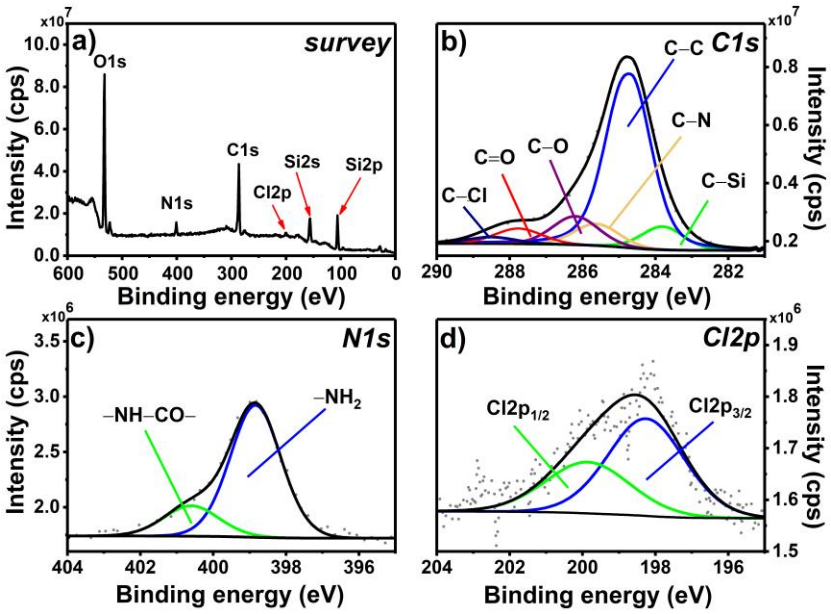

Figure 2. XPS survey spectrum (**a**) and high-resolution spectra of C1s (**b**), N1s (**c**), and Cl2p (**d**) regions registered for the TC_APTES@glass monolayer.

The last step of the formation of the photoactive layer was, as seen in Step 2, based on the reactivity of the acyl chloride and the amine group. Here, the remaining unreacted acyl chloride groups bound to the glass surface (TC_APTES@glass, Scheme 1) were reacted with the primary amine groups present in the selected photosensitizers, i.e., AA and APTPP. The recorded survey spectrum of MIX_TC_APTES@glass (Figure 3a) reveals the presence of the same characteristic signals as for the TC_APTES@glass sample with an additional signal of S2p at approximately 168 eV. The decomposition of the C1s high-resolution spectrum (Figure 3a) shows the presence of six components: C–Si, C–C, C–N/C–S, C–O, C=O, and C–Cl at 283.5, 284.8, 285.8, 286.4, 287.4, and 288.6 eV, respectively. The

significantly higher contribution of the C–N/C–S component can be observed, which is related to the attachment of phenothiazine (AA) and porphyrin (APTPP) rings. Moreover, the decrease in the content of the C–Cl component compared to the C1s spectrum of TC_APTES@glass, indicates the breakage of the C–Cl bond present in the attached TC linker in Step 3 due to the formation of the amide bond in the reaction between acyl chloride of TC and primary amine present in AA or APTPP.

Clear changes can be also observed in the N1s region recorded for the MIX_TC_APTES@glass sample (Figure 3b)—two components can be distinguished, located at 398.8 and 400.7 eV, that can be assigned to $–NH_2$/N-pyridinic ring and –NH–CO–/N-pyrrolic ring, respectively. The first one is present in the phenothiazine structure, i.e., AA photosensitizer, while the second one is found in porphyrin, APTPP [39,40], which together confirms the efficacy of the third step of the applied procedure of the mixed monolayer formation. Additionally, further proof of the attachment of the AA photosensitizer to the glassy surface is the presence of the S2p line in XPS spectrum of MIX_TC_APTES@glass. The decomposition of the registered S2p region (Figure 3c) gives $S2p_{3/2}$ component at 168.0 eV with its spin-orbit coupling counterpart, $S2p_{1/2}$, that can be assigned to the sulfur atom present in the central ring of AA. The slightly higher than expected energy of $S2p_{3/2}$ [41] may be connected to the charging of the phenothiazine ring.

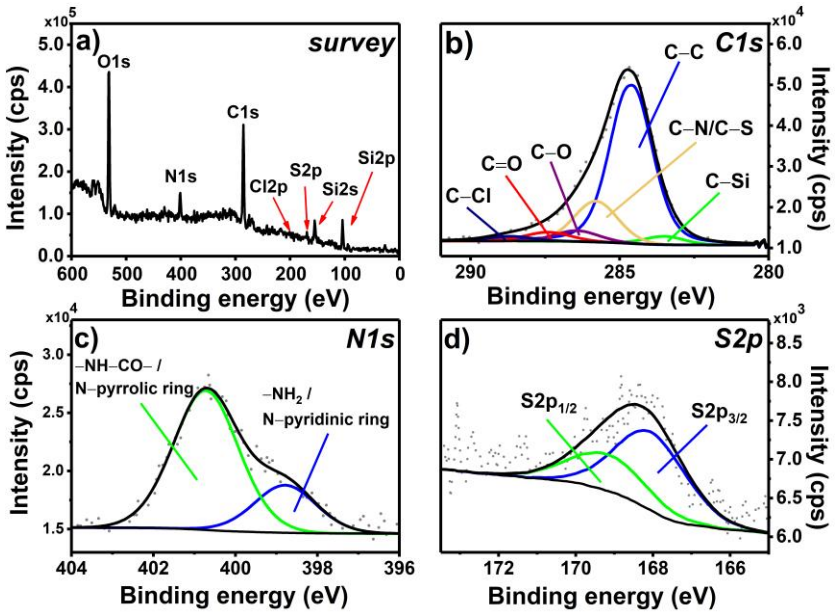

Figure 3. XPS survey spectrum (**a**) and high-resolution spectra of C1s (**b**), N1s (**c**), and S2p (**d**) regions registered for the MIX_TC_APTES@glass monolayer.

3.1.2. Raman Spectroscopy

The final check of the chemical structure of the deposited photoactive mixed layer was done by Raman spectroscopy. The Raman spectra of the two photosensitizers (AA and APTPP), the MIX_TC_APTES@glass layer, and the unmodified glass (Figure 4) were recorded with the 514 nm laser. The spectrum recorded for MIX_TC_APTES@glass shows signals coming from the inorganic glass substrate and the immobilized organic layer. The broadband located at 810 cm^{-1} arises from the symmetric stretching of the O–Si–O bond, while the signal at 929 cm^{-1} comes from the Si–O stretching vibrations of the glass substrate [42]. The second one is not clearly seen in the spectrum of MIX_TC_APTES@glass but probably leads to an overall increase in the intensity of the modes observed in the 900–950 cm^{-1} range. The presence of the chemically grafted APTES molecules in the deposited layer is confirmed by specific signals at 950, 1047, and 1455 cm^{-1} observed in the spectrum of MIX_TC_APTES@glass, which can be assigned to the vibrations of CH_2, the skeletal

stretching, and the bending vibrations of the CH_2 units attached to Si atom, respectively [43,44]. The formation of the amide groups with TC linkers in the postmodification steps is supported by the occurrence of the C–N stretching together with the N–H bending at 1311 cm^{-1} and the C=O stretching vibration mode at 1660 cm^{-1} [45].

Finally, the characteristic signals of both immobilized photosensitizers are present in the acquired Raman spectrum of the mixed photoactive layer (see the Raman spectrum of MIX_TC_APTES@glass layer presented in the limited range in Figure S1. For AA, the signals arising from the C–S–C vibrations, C–N–C stretching vibrations, and the C–C stretching within the phenothiazine ring are observed at 900, 1384, and 1634 cm^{-1}, respectively [46]. The specific bands coming from APTPP are located at 1002, 1240, 1331, and 1555 cm^{-1} and correspond to the in-plane bending deformation of the phenyl rings, the C_m–H bending, the symmetric stretching of the pyrrole half-ring, and the symmetric stretching of C_β–C_β, respectively [47,48].

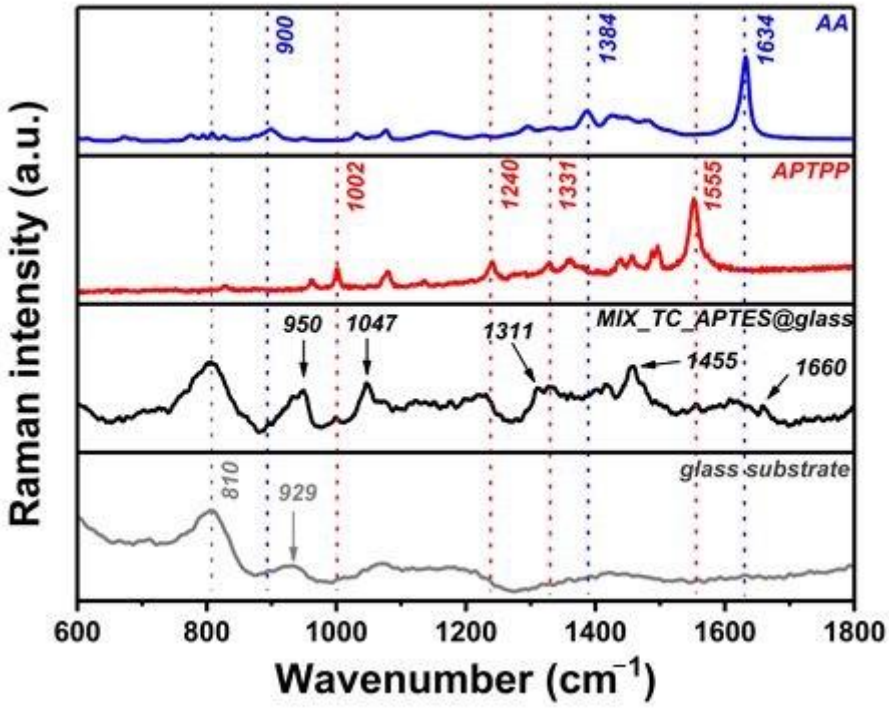

Figure 4. Raman spectra recorded for AA, APTPP, modified (MIX_TC_APTES@glass), and unmodified glass substrate.

3.2. Reactive Oxygen Species (ROS) Photogeneration by the Chemically Grafted Mixed Monolayer

As in our previous works [49,50], α-terpinene was used as a chemical trap for the indirect detection of ROS by means of UV–Vis spectroscopy. Since α-terpinene is more stable under white-light illumination than other more common testing systems, such as DPBF in methanol, it was selected as a trap for this study.

Figure 5 presents an exemplary UV–Vis spectrum recorded for the α-terpinene solution in acetonitrile in contact with the MIX_TC_APTES@glass coating during illumination with the xenon lamp (XL). The clear decrease in the α-terpinene absorbance at 266 nm with time indicates its oxidation by ROS species being produced by the MIX_TC_APTES@glass monolayer. Notably, under applied conditions, only a small drop in the absorbance of α-terpinene, due to its autooxidation, was observed when the unmodified glass was irradiated (Figure 5 inset). As no new bands appear in the UV–Vis spectra at approximately 400 or 600 nm, the degradation of the photoactive layer, resulting

in the release of the bound photosensitizers into the solution of the chemical trap, can be excluded. The consistency of the results obtained for the ROS production by the MIX_TC_APTES@glass monolayer under xenon lamp illumination indicates the reproducibility of the layer formation process. Moreover, almost no changes in the UV–Vis spectra during the so-called dark test were detected (Figure 5 inset), which confirms that ROS are produced only when the chemically grafted photosensitizers, i.e., AA and APTPP, are activated by the light.

The photogeneration process was also investigated under the illumination with the 445 or 638 nm diode laser. Use of the blue laser allows to selectively excite APTPP molecules present in the MIX_TC_APTES@glass layer, while the red laser acts mainly on AA (UV–Vis of photosensitizers given in Figure S2). In both tests, a steady drop in the absorbance of α-terpinene at 266 nm occurred (Figure 5 inset) showing that both photosensitizers composing the MIX_TC_APTES@glass layer, retain their photoactivity toward ROS production after immobilization on the glass substrate.

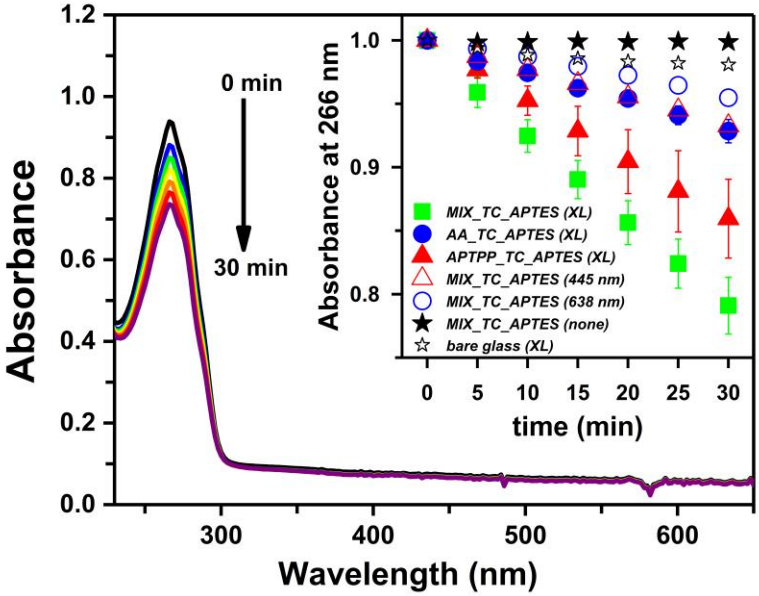

Figure 5. The set of UV–Vis spectra of α-terpinene (ACN solution) registered in the presence of AA_TC_APTES@glass illuminated by the xenon lamp; inset: the absorbance of α-terpinene at 266 nm during illumination of MIX_TC_APTES@glass (**green square**), AA_TC_APTES@glass (**blue circle**), APTPP_TC_APTES@glass (**red triangle**) monolayers, and bare glass (**empty star**) with Xenon lamp (XL); and MIX_TC_APTES@glass monolayer without illumination (**black star**) or under illumination with 445 nm (**empty triangle**) or 638 nm lasers (**empty circle**).

Importantly, in the photogeneration process activated with the xenon lamp, the drop in the α-terpinene concertation observed for the MIX_TC_APTES@glass coating is significantly higher than in the case of the single-component monolayers, i.e., AA_TC_APTES@glass or APTPP_TC_APTES@glass (Figure 5 inset). This proves that in the case of the two-component layer, thanks to the complementarity of the spectral properties of the immobilized photosensitizers, a broader range of light wavelengths can be effectively utilized in the production of the antimicrobial reactive oxygen species.

3.3. Antimicrobial Properties of the Chemically Grafted Mixed Monolayer

The bactericidal activity of the MIX_TC_APTES@glass monolayer has been investigated against a Gram-negative *E. coli* strain, which is a common cause of nosocomial infections [51–53]. The bacterial culture was carried out under conventional indoor lighting, and the samples for the analysis were collected after 3 and 48 h. The choice of the second

time point was based on the possibility of monitoring the prolonged antibacterial action of the investigated layers [54]. SEM was chosen for monitoring the bacterial growth, since it allows to conduct detailed quantitative and qualitative analysis, and thus the influence of the deposited layer on the bacterial cells structure, size, shape, etc. was observed [55]. The average number of bacteria adhering to the surfaces assessed using SEM microscopy and the corresponding calculated densities are shown in Figure 6a,b, respectively. The bacterial viability analysis performed by the Live/Dead assay allowed observation of live (green color) and dead (red color) cells on the surfaces of the MIX_TC_APTES@glass observed with a fluorescent microscope (Figure 6c). The bacterial cells were counted using the ImageJ (FIJI) software and are presented on a graph (Figure 6d).

The bacterial adhesion results observed after 3 h of culture indicate a significantly lower (45.3%) number of the bacterial cells adhered on the MIX_TC_APTES@glass (4.1 ± 0.7 cells/200 μm²) compared to the reference unmodified glass slides (7.5 ± 0.9 cells/200 μm²). Simultaneously, it is visible that the only 36.3% ± 6.8% of cells present on the unmodified glass during the phase of adhesion are dead, in contrast to cells on the light-activated functionalized surface reaching 53.9% ± 1.2%, which also indicates that the bactericidal action of the layer. Similar results proving the long-term antibacterial character of the MIX_TC_APTES@glass layer were obtained after 48 h of culture (Figure S3). Consequently, as in the SEM micrographs and the same on fluorescent images, the number of live bacterial cells was considerably lower on the light-activated mixed monolayer than on the uncoated glass surface, which confirms the antimicrobial properties of the MIX_TC_APTES@glass coating.

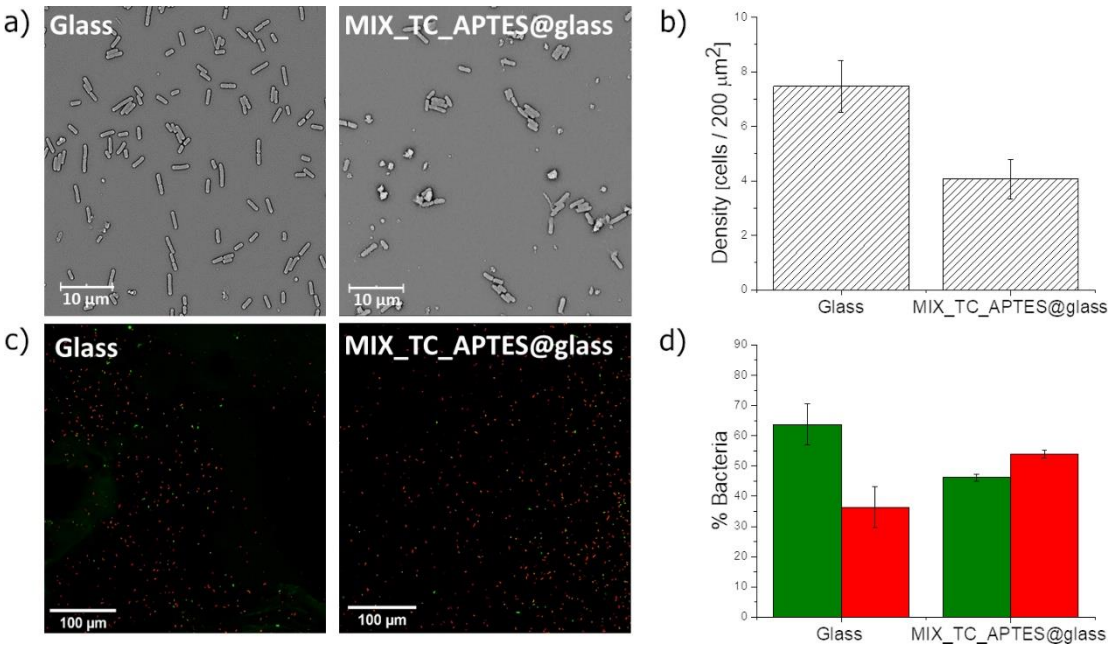

Figure 6. (**a**) SEM images showing *E. coli* present on the unmodified glass surface and MIX_TC_APTES@glass after 3 h; (**b**) the density of bacterial cells after 3 h determined from SEM for the unmodified glass and MIX_TC_APTES@glass surfaces; $p < 0.05$, $n = 3$; (**c**) confocal fluorescent microscope images showing *E. coli* on the unmodified glass and MIX_TC_APTES@glass surfaces after 3 h; (**d**) live and dead bacteria percentages after 3 h for the unmodified glass and MIX_TC_APTES@glass surfaces; $p < 0.05$, $n = 8$.

The obtained results confirm that the deposited mixed monolayer, MIX_TC_APTES@glass, possesses antimicrobial properties. Though, the light-activated production of ROS is believed to have the highest contribution to the above-mentioned bactericidal effect [56], it cannot be excluded that the presence of the organic moiety itself influences the adhesion of the bacteria to the surface. Such a beneficial synergic effect, including dark biocide activity [57], has been already reported [58]. It has been already

shown that the concentration of the PS in the layer has a high influence on the light-activated antimicrobial efficiency [5,58]. In this work, approximately 0.3 log reduction was obtained for the MIX_TC_APTES@glass nanocoating with respect to the control, i.e., unmodified glass, after 3 h under illumination by the conventional indoor lighting. This is in agreement with the results reported by other groups for coatings with a lower concentration of PS incorporated in the organic matrix [5,59] or for covalently attached PSs [54,60–62]. Though, the chemically grafted photoactive layers generally suffer from a lower antimicrobial response, their main advantage is the covalent bond between PS and the surface, which ensures high stability, thus preventing leakage of the PS into the environment (as often observed for the incorporated PS [5]), high adhesion to the surface, and also usually long-term stability. Since such modification occurs at the nanoscale, the coatings usually do not interfere with features such as color, transparency, etc., which is of great importance for the covering of computer screens, windows, etc. Finally, the presented strategy relies on the straightforward processes and commercially available reagents, which makes it easily accessible for the modification of the glassy surfaces regardless of their shape and size.

4. Conclusions

In the presented work, AA and APTPP photoactive molecules were chemically grafted on the glass surface in a straightforward three-step procedure. The chemical composition of the deposited layer was confirmed after each step by applying the XPS method, and at the very end, by Raman spectroscopy. The described approach resulted in the formation of the covalently bound mixed monolayer showing photoactivity toward ROS generation. It was shown that the efficiency of the ROS production under white-light illumination of the two-component film is significantly higher than that for the corresponding single-component ones, and that the layer remains inactive in dark conditions. Though, the MIX_TC_APTES layer modifies the glass surface only at the nanoscale, its deposition allows reducing the number of the adhered *E. coli* bacteria, as shown with the microbiological tests. The presented results demonstrate that the undertaken approach allows obtaining a stable, light-activated, antimicrobial nanocoating that may be considered as a promising alternative for the modification of glassy surfaces, where the accumulation of pathogenic material is problematic. The proposed strategy is straightforward and can be applied to various objects regardless their size or shape, without the usage of sophisticated equipment. The strong linkage with the surface atoms ensures that the photoactive molecules will not be released into the environment (as commonly used disinfectants are) and that the layers show long-term antimicrobial response. Finally, such monolayers, due to their nanoscale character, will not interfere with the features, e.g., color, of the modified objects. It is believed that the presented strategy can be further developed using other photosensitizers, in order to increase the broadband absorbance of the layer and, thus, the antimicrobial efficiency.

Supplementary Materials: The following are available online at www.mdpi.com/article/10.3390/ma14113093/s1, Figure S1. Raman spectrum of MIX_TC_APTES@glass layer in the range 1350–1700 cm^{-1}. Figure S2. UV–Vis spectra of 0.1 mM solution of AA and APTPP, Figure S3. (**a**) SEM images showing *E. coli* present on the unmodified glass surface and MIX_TC_APTES@glass after 48 h; (**b**) the density of bacterial cells after 48 h determined from SEM for the unmodified glass and MIX_TC_APTES@glass surfaces; $p < 0.05$, $n = 3$; (**c**) confocal fluorescent microscope images showing *E. coli* on the unmodified glass and MIX_TC_APTES@glass surfaces after 48 h; (**d**) live and dead bacteria percentages after 48 h for the unmodified glass and MIX_TC_APTES@glass surfaces; $p < 0.05$, $n = 8$.

Author Contributions: Conceptualization, A.B.-G.; methodology, A.B.-G., W.P., and E.Z-G.; formal analysis, A.B.-G., D.C.-G., and M.K. (Maciej Krzywiecki); investigation, A.N., A.B.-G., D.C.-G., M.K. (Maciej Krzywiecki), S.S., and M.K. (Monika Kwoka); writing—original draft preparation, A.B.-G., A.N., and D.C.-G.; writing—review and editing, A.B.-G.; visualization, A.B.-G., A.N., M.K. (Monika

Kwoka), S.S. and D.C.-G.; supervision, A.B.-G., W.P., E.Z.-G., and P.D.; funding acquisition, A.B.-G. and P.D. All authors have read and agreed to the published version of the manuscript.

Funding: This research was funded by the Polish Budget Founds for Scientific Research in 2020 as a core funding for R&D activities in the Silesian University of Technology—funding for young researchers (grant number 04/040/BKM20/0123). A.B.-G is grateful for the financial support from the Silesian University of Technology, Poland, under grand no. 04/040/RGH20/0141. A.N. and P.D. kindly acknowledge the support received from the First TEAM program of the Foundation for Polish Science co-financed by the European Union under the European Regional Development Fund (project number: First TEAM POIR.04.04.00-00-4668/17-00). D.C.-G. kindly acknowledges the financial support by the National Science Center, Poland (2016/23/D/ST5/01306). Authors are grateful to the training actions funded by the European Union's Horizon 2020 research and innovation program under grant agreement no. 952008. The authors acknowledge ESpeFuM laboratory for access to the XPS setup.

Institutional Review Board Statement: Not applicable.

Informed Consent Statement: Not applicable.

Data Availability Statement: Data are presented in the article and supplementary materials.

Conflicts of Interest: The authors declare no conflict of interest.

References

1. Allegranzi B., Bagheri S. N., Castillejos G. G., Kilpatrick C., Kelley E., Mathiai E. Report on the Burden of Endemic Health Care-Associated Infection Worldwide-Clean Care is Safer Care, **2011**, *3*, 1–34.
2. Grammatikova, N.E.; George, L.; Ahmed, Z.; Candeias, N.R.; Durandin, N.A.; Efimov, A. Zinc phthalocyanine activated by conventional indoor light makes a highly efficient antimicrobial material from regular cellulose. *J. Mater. Chem. B* **2019**, *7*, 4379–4384, doi:10.1039/c9tb01095e.
3. Noimark, S.; Dunnill, C.W.; Parkin, I.P. Shining light on materials — A self-sterilising revolution. *Adv. Drug Deliv. Rev.* **2013**, *65*, 570–580, doi:10.1016/j.addr.2012.07.003.
4. Sautrot-Ba, P.; Malval, J.-P.; Weiss-Maurin, M.; Paul, J.; Blacha-Grzechnik, A.; Tomane, S.; Mazeran, P.-E.; Lalevée, J.; Langlois, V.; Versace, D.-L.; Paprika, Gallic Acid, and Visible Light: The Green Combination for the Synthesis of Biocide Coatings. *ACS Sustain. Chem. Eng.* **2017**, *6*, 104–109, doi:10.1021/acssuschemeng.7b03723.
5. Hwang, G.B.; Allan, E.; Parkin, I.P. White Light-Activated Antimicrobial Paint using Crystal Violet. *ACS Appl. Mater. Interfaces* **2015**, *8*, 15033–15039, doi:10.1021/acsami.5b06927.
6. Walker, T.; Canales, M.; Noimark, S.; Page, K.; Parkin, I.; Faull, J.; Bhatti, M.; Ciric, L. A Light-Activated Antimicrobial Surface Is Active Against Bacterial, Viral and Fungal Organisms. *Sci. Rep.* **2017**, *7*, 15298, doi:10.1038/s41598-017-15565-5.
7. DeRosa, M.C. Photosensitized singlet oxygen and its applications. *Co-ord. Chem. Rev.* **2002**, *233-234*, 351–371, doi:10.1016/s0010-8545(02)00034-6.
8. Wainwright, M.; Crossley, K.B. Photosensitising agents—circumventing resistance and breaking down biofilms: A review. *Int. Biodeterior. Biodegradation* **2004**, *53*, 119–126, doi:10.1016/j.ibiod.2003.11.006.
9. Spagnul, C.; Turner, L.C.; Boyle, R.W. Immobilized photosensitizers for antimicrobial applications. *J. Photochem. Photobiol. B: Biol.* **2015**, *150*, 11–30, doi:10.1016/j.jphotobiol.2015.04.021.
10. Mangoni, M.L.; Epand, R.F.; Rosenfeld, Y.; Peleg, A.; Barra, D.; Epand, R.M.; Shai, Y. Lipopolysaccharide, a Key Molecule Involved in the Synergism between Temporins in Inhibiting Bacterial Growth and in Endotoxin Neutralization. *J. Biol. Chem.* **2008**, *283*, 22907–22917, doi:10.1074/jbc.m800495200.
11. Dahl, T.A.; Midden, W.R.; Hartman, P.E. PURE SINGLET OXYGEN CYTOTOXICITY FOR BACTERIA. *Photochem. Photobiol.* **1987**, *46*, 345–352, doi:10.1111/j.1751-1097.1987.tb04779.x.
12. Laurentius, L.; Stoyanov, S.R.; Gusarov, S.; Kovalenko, A.; Du, R.; Lopinski, G.P.; McDermott, M. Diazonium-Derived Aryl Films on Gold Nanoparticles: Evidence for a Carbon–Gold Covalent Bond. *ACS Nano* **2011**, *5*, 4219–4227, doi:10.1021/nn201110r.
13. De Bruin, A. Surface Treatments for Biological, Chemical and Physical Applications. *Johns. Matthey Technol. Rev.* **2018**, *62*, 259–262, doi:10.1595/205651318x696873.
14. Namba, N.; Yoshida, Y.; Nagaoka, N.; Takashima, S.; Matsuura-Yoshimoto, K.; Maeda, H.; Van Meerbeek, B.; Suzuki, K.; Takashiba, S. Antibacterial effect of bactericide immobilized in resin matrix. *Dent. Mater.* **2009**, *25*, 424–430, doi:10.1016/j.dental.2008.08.012.
15. Page, K.; Correia, A.; Wilson, M.; Allan, E.; Parkin, I.P. Light-activated antibacterial screen protectors for mobile telephones and tablet computers. *J. Photochem. Photobiol. A: Chem.* **2015**, *296*, 19–24, doi:10.1016/j.jphotochem.2014.08.011.
16. Peveler, W.J.; Noimark, S.; Al-Azawi, H.; Hwang, G.B.; Crick, C.R.; Allan, E.; Edel, J.B.; Ivanov, A.; MacRobert, A.J.; Parkin, I.P. Covalently Attached Antimicrobial Surfaces Using BODIPY: Improving Efficiency and Effectiveness. *ACS Appl. Mater. Interfaces* **2018**, *10*, 98–104, doi:10.1021/acsami.7b13273.

17. Piccirillo, C.; Perni, S.; Gil-Thomas, J.; Prokopovich, P.; Wilson, M.; Pratten, J.; Parkin, I.P. Antimicrobial activity of methylene blue and toluidine blue O covalently bound to a modified silicone polymer surface. *J. Mater. Chem.* **2009**, *19*, 6167–6171, doi:10.1039/b905495b.
18. Sehmi, S.K.; Noimark, S.; Pike, S.; Bear, J.C.; Peveler, W.J.; Williams, C.K.; Shaffer, M.S.P.; Allan, E.; Parkin, I.P.; MacRobert, A.J. Enhancing the Antibacterial Activity of Light-Activated Surfaces Containing Crystal Violet and ZnO Nanoparticles: Investigation of Nanoparticle Size, Capping Ligand, and Dopants. *ACS Omega* **2016**, *1*, 334–343, doi:10.1021/acsomega.6b00017.
19. Decraene, V.; Pratten, J.; Wilson, M. Cellulose Acetate Containing Toluidine Blue and Rose Bengal Is an Effective Antimicrobial Coating when Exposed to White Light. *Appl. Environ. Microbiol.* **2006**, *72*, 4436–4439, doi:10.1128/aem.02945-05.
20. Decraene, V.; Pratten, J.; Wilson, M. Novel Light-Activated Antimicrobial Coatings Are Effective Against Surface-Deposited Staphylococcus aureus. *Curr. Microbiol.* **2008**, *57*, 269–273, doi:10.1007/s00284-008-9188-7.
21. Ballatore, M.B.; Durantini, J.; Gsponer, N.S.; Suarez, M.B.; Gervaldo, M.; Otero, L.; Spesia, M.B.; Milanesio, M.E.; Durantini, E.N. Photodynamic Inactivation of Bacteria Using Novel Electrogenerated Porphyrin-Fullerene C60 Polymeric Films. *Environ. Sci. Technol.* **2015**, *49*, 7456–7463, doi:10.1021/acs.est.5b01407.
22. Page, K.; Wilson, M.; Parkin, I.P. Antimicrobial surfaces and their potential in reducing the role of the inanimate environment in the incidence of hospital-acquired infections. *J. Mater. Chem.* **2009**, *19*, 3819–3831, doi:10.1039/b818698g.
23. Sangermano, M.; Periolatto, M.; Castellino, M.; Wang, J.; Dietliker, K.; Grützmacher, J.L.; Grützmacher, H. A Simple Preparation of Photoactive Glass Surfaces Allowing Coatings via the "Grafting-from" Method. *ACS Appl. Mater. Interfaces* **2016**, *8*, 19764–19771, doi:10.1021/acsami.6b05822.
24. Ringot, C.; Sol, V.; BarrièreM.; Saad, N.; Bressollier, P.; Granet, R.; Couleaud, P.; Frochot, C.; Krausz, P. Triazinyl Porphyrin-Based Photoactive Cotton Fabrics: Preparation, Characterization, and Antibacterial Activity. *Biomacromolecules* **2011**, *12*, 1716–1723, doi:10.1021/bm200082d.
25. Ribeiro, S.M.; Serra, A.C.; Gonsalves, A.R. Covalently immobilized porphyrins as photooxidation catalysts. *Tetrahedron* **2007**, *63*, 7885–7891, doi:10.1016/j.tet.2007.05.084.
26. Krouit, M.; Granet, R.; Krausz, P. Photobactericidal films from porphyrins grafted to alkylated cellulose – synthesis and bactericidal properties. *Eur. Polym. J.* **2009**, *45*, 1250–1259, doi:10.1016/j.eurpolymj.2008.11.036.
27. Bélanger, D.; Pinson, J. Electrografting: A powerful method for surface modification. *Chem. Soc. Rev.* **2011**, *40*, 3995–4048, doi:10.1039/c0cs00149j.
28. Blacha-Grzechnik, A.; Piwowar, K.; Kościelniak, P.; Kwoka, M.; Szuber, J.; Zak, J. Phenothiazines grafted on the electrode surface from diazonium salts as molecular layers for photochemical generation of singlet oxygen. *Electrochimica Acta* **2015**, *182*, 1085–1092, doi:10.1016/j.electacta.2015.10.017.
29. Lv, Y.; Liu, H.; Wang, Z.; Hao, L.; Liu, J.; Wang, Y.; Du, G.; Liu, D.; Zhan, J.; Wang, J. Antibiotic glass slide coated with silver nanoparticles and its antimicrobial capabilities. *Polym. Adv. Technol.* **2008**, *19*, 1455–1460, doi:10.1002/pat.1138.
30. Saravanan, P.; Jayamoorthy, K.; Anandakumar, S. Fluorescence quenching of APTES by Fe2O3 nanoparticles – Sensor and antibacterial applications. *J. Lumin.* **2016**, *178*, 241–248, doi:10.1016/j.jlumin.2016.05.031.
31. Metwalli, E.; Haines, D.; Becker, O.; Conzone, S.; Pantano, C. Surface characterizations of mono-, di-, and tri-aminosilane treated glass substrates. *J. Colloid Interface Sci.* **2006**, *298*, 825–831, doi:10.1016/j.jcis.2006.03.045.
32. Howarter, J.A.; Youngblood, J.P. Optimization of Silica Silanization by 3-Aminopropyltriethoxysilane. *Langmuir* **2006**, *22*, 11142–11147, doi:10.1021/la061240g.
33. Acres, R.; Ellis, A.V.; Alvino, J.; Lenahan, C.E.; Khodakov, D.A.; Metha, G.F.; Andersson, G. Molecular Structure of 3-Aminopropyltriethoxysilane Layers Formed on Silanol-Terminated Silicon Surfaces. *J. Phys. Chem. C* **2012**, *116*, 6289–6297, doi:10.1021/jp212056s.
34. Cui, N.-Y.; Liu, C.; Yang, W. XPS and AFM characterization of the self-assembled molecular monolayers of a 3-aminopropyltrimethoxysilane on silicon surface, and effects of substrate pretreatment by UV-irradiation. *Surf. Interface Anal.* **2010**, *43*, 1082–1088, doi:10.1002/sia.3698.
35. Chang, C.-C.; Imae, T.; Chen, L.-Y.; Ujihara, M. Efficient surface enhanced Raman scattering on confeito-like gold nanoparticle-adsorbed self-assembled monolayers. *Phys. Chem. Chem. Phys.* **2015**, *17*, 32328–32334, doi:10.1039/c5cp05490g.
36. Vashist, S.K.; Lam, E.; Hrapovic, S.; Male, K.B.; Luong, J. Immobilization of Antibodies and Enzymes on 3-Aminopropyltriethoxysilane-Functionalized Bioanalytical Platforms for Biosensors and Diagnostics. *Chem. Rev.* **2014**, *114*, 11083–11130, doi:10.1021/cr5000943.
37. Beamson, G.; Briggs, D. *XPS of Organic Polymers*; John Wiley & Sons: Chichester, UK, 1992.
38. Shircliff, R.A.; Stradins, P.; Moutinho, H.; Fennell, J.; Ghirardi, M.L.; Cowley, S.W.; Branz, H.M.; Martin, I. Angle-Resolved XPS Analysis and Characterization of Monolayer and Multilayer Silane Films for DNA Coupling to Silica. *Langmuir* **2013**, *29*, 4057–4067, doi:10.1021/la304719y.
39. Marbach, H. Surface-Mediated in Situ Metalation of Porphyrins at the Solid–Vacuum Interface. *Accounts Chem. Res.* **2015**, *48*, 2649–2658, doi:10.1021/acs.accounts.5b00243.
40. Sun, Z.; Li, J.; Zheng, H.; Liu, X.; Ye, S.; Du, P. Pyrolyzed cobalt porphyrin-modified carbon nanomaterial as an active catalyst for electrocatalytic water oxidation. *Int. J. Hydrogen Energy* **2015**, *40*, 6538–6545, doi:10.1016/j.ijhydene.2015.03.103.
41. Thi, N.; Hoan, V.; Minh, N.N.; Thi, T.; Nhi, K.; Thang, N. Van; Tuan, V.A.; Nguyen, V.T.; Thanh, N.M.; Hung, N. Van TiO 2 / Diazonium / Graphene Oxide Composites : Synthesis and Visible-Light-Driven Photocatalytic Degradation of Methylene Blue. *J. Nanomater.* **2020**, 2020, doi: https://doi.org/10.1155/2020/4350125

42. Manghnani, M.H.; Hushur, A.; Sekine, T.; Wu, J.; Stebbins, J.F.; Williams, Q.; Raman, Brillouin, and nuclear magnetic resonance spectroscopic studies on shocked borosilicate glass. *J. Appl. Phys.* **2011**, *109*, 113509, doi:10.1063/1.3592346.
43. Sun, Y.; Yanagisawa, M.; Kunimoto, M.; Nakamura, M.; Homma, T. Depth profiling of APTES self-assembled monolayers using surface-enhanced confocal Raman microspectroscopy. *Spectrochim. Acta Part. A: Mol. Biomol. Spectrosc.* **2017**, *184*, 1–6, doi:10.1016/j.saa.2017.04.036.
44. Gunda, N.S.K.; Singh, M.; Norman, L.; Kaur, K.; Mitra, S. Optimization and characterization of biomolecule immobilization on silicon substrates using (3-aminopropyl)triethoxysilane (APTES) and glutaraldehyde linker. *Appl. Surf. Sci.* **2014**, *305*, 522–530, doi:10.1016/j.apsusc.2014.03.130.
45. Foggia, M. Di; Taddei, P.; Torreggiani, A.; National, I.; Dettin, M. Self-assembling peptides for biomedical applications: IR and Raman spectroscopies for the study of secondary structure. *J. Proteome Res.* **2012**, *2*, 231–272.
46. Snehalatha, M.; Joe, I.H.; Ravikumar, C.; Jayakumar, V.S. Azure A chloride: Computational and spectroscopic study. *J. Raman Spectrosc.* **2009**, *40*, 176–182, doi:10.1002/jrs.2102.
47. Lokesh, K.S.; De Keersmaecker, M.; Adriaens, A. Self Assembled Films of Porphyrins with Amine Groups at Different Positions: Influence of Their Orientation on the Corrosion Inhibition and the Electrocatalytic Activity. *Molecules* **2012**, *17*, 7824–7842, doi:10.3390/molecules17077824.
48. Aydin, M. DFT and Raman spectroscopy of porphyrin derivatives: Tetraphenylporphine (TPP). *Vib. Spectrosc.* **2013**, *68*, 141–152, doi:10.1016/j.vibspec.2013.06.005.
49. Nyga, A.; Motyka, R.; Bussetti, G.; Calloni, A.; Jagadeesh, M.S.; Fijak, S.; Pluczyk-Malek, S.; Data, P.; Blacha-Grzechnik, A. Electrochemically deposited poly(selenophene)-fullerene photoactive layer: Tuning of the spectroscopic properties towards visible light-driven generation of singlet oxygen. *Appl. Surf. Sci.* **2020**, *525*, 146594, doi:10.1016/j.apsusc.2020.146594.
50. Blacha-Grzechnik, A.; Piwowar, K.; Zdyb, T.; Krzywiecki, M. Formation of poly(Azure A)-C60 photoactive layer as a novel approach in the heterogeneous photogeneration of singlet oxygen. *Appl. Surf. Sci.* **2018**, *457*, 221–228, doi:10.1016/j.apsusc.2018.06.262.
51. Toval, F.; Köhler, C.-D.; Vogel, U.; Wagenlehner, F.; Mellmann, A.; Fruth, A.; Schmidt, M.A.; Karch, H.; Bielaszewska, M.; Dobrindt, U.; et al. Characterization of Escherichia coli Isolates from Hospital Inpatients or Outpatients with Urinary Tract Infection. *J. Clin. Microbiol.* **2014**, *52*, 407–418, doi:10.1128/jcm.02069-13.
52. Peleg, A.Y.; Hooper, D.C. Hospital-Acquired Infections Due to Gram-Negative Bacteria Anton. *J Med. N. Engl.* **2010**, *362*, 1804–1813, doi:10.1056/NEJMra0904124.Hospital-Acquired.
53. Nagarjuna, D.; Mittal, G.S.; Dhanda, R.; Verma, P.; Gaind, R.; Yadav, M. Faecal Escherichia coli isolates show potential to cause endogenous infection in patients admitted to the ICU in a tertiary care hospital. *New Microbes New Infect.* **2015**, *7*, 57–66, doi:10.1016/j.nmni.2015.05.006.
54. Wang, K.-K.; Kim, B.-J.; Heo, I.-; Jung, S.-J.; Hwang, J.-W.; Kim, Y.-R. Fabrication and characterization of antimicrobial surface-modified stainless steel for bio-application. *Surf. Coatings Technol.* **2017**, *310*, 256–262, doi:10.1016/j.surfcoat.2016.12.088.
55. Zhou, X.; Chen, Z.; Wang, Y.; Guo, Y.; Tung, C.-H.; Zhang, F.; Liu, X. Honeycomb-patterned phthalocyanine films with photoactive antibacterial activities. *Chem. Commun.* **2013**, *49*, 10614–10616, doi:10.1039/c3cc42085j.
56. Ringot, C.; Sol, V.; Granet, R.; Krausz, P. Porphyrin-grafted cellulose fabric: New photobactericidal material obtained by "Click-Chemistry" reaction. *Mater. Lett.* **2009**, *63*, 1889–1891, doi:10.1016/j.matlet.2009.06.009.
57. Modjinou, T.; Versace, D.L.; Andaloussi, S.A.; Langlois, V.; Renard, E. Co-Networks Poly(hydroxyalkanoates)-Terpenes to Enhance Antibacterial Properties. *Bioengineering* **2020**, *7*, 13, doi:10.3390/bioengineering7010013.
58. Mobeen, A.; Magdalane, C.M.; Shahina, S.J.; Lakshmi, D.; Sundaram, R.; Ramalingam, G.; Raja, A.; Madhavan, J.; Letsholathebe, D.; Bashir, A.; et al. Investigation on antibacterial and photocatalytic degradation of Rhodamine-B dye under visible light irradiation by titanium molybdate nanoparticles prepared via microwave method. *Surfaces Interfaces* **2019**, *17*, 100381, doi:10.1016/j.surfin.2019.100381.
59. Nuñez, J.A.P.; Salapare, H.S.; Villamayor, M.M.S.; Siringan, M.A.T.; Ramos, H.J. Antibacterial efficiency of magnetron sputtered TiO 2 on poly(methyl methacrylate). *Surfaces Interfaces* **2017**, *8*, 28–35, doi:10.1016/j.surfin.2017.04.003.
60. Cardoso, V.; Rittmeyer, T.; Correa, R.J.; Brêda, G.C.; Almeida, R.V.; Simões, G.; de França, B.M.; de Azevedo, P.N.; Forero, J.S.B. Photoactive cotton fabric: Synthesis, characterization and antibacterial evaluation of anthraquinone-based dyes linked to cellulose. *Dye. Pigment.* **2019**, *161*, 16–23, doi:10.1016/j.dyepig.2018.09.029.
61. Tu, Q.; Zhang, Q.; Wang, Y.; Jiao, Y.; Xiao, J.; Peng, T.; Wang, J. Antibacterial properties of poly(dimethylsiloxane) surfaces modified with graphene oxide-catechol composite. *Prog. Org. Coatings* **2019**, *129*, 247–253, doi:10.1016/j.porgcoat.2019.01.011.
62. Ferreira, A.M.; Carmagnola, I.; Chiono, V.; Gentile, P.; Fracchia, L.; Ceresa, C.; Georgiev, G.; Ciardelli, G. Surface modification of poly(dimethylsiloxane) by two-step plasma treatment for further grafting with chitosan–Rose Bengal photosensitizer. *Surf. Coatings Technol.* **2013**, *223*, 92–97, doi:10.1016/j.surfcoat.2013.02.035.